# OPTICORR Guide Book

Optimisation of in-service performance of boiler steels by modelling high temperature corrosion

# OPTICORR Guide Book

## Optimisation of in-service performance of boiler steels by modelling high temperature corrosion

Edited by

David Baxter

JRC Institute for Energy

Liisa Heikinheimo

VTT Industrial Systems

# Abstract

This Guide Book is intended to assist the prospective user of a novel range of corrosion modelling software that has been designed to assess potential corrosion under high temperature combustion process conditions. The models described have been developed through the course of the European-funded materials research project, OPTICORR, G5RD-CT-2001-00593.

The corrosion models were based on existing ChemSheet and InCorr software systems. These tools addressed two separate parts of the corrosion process, molten salt corrosion on the surface and internal oxidation/corrosion. The ChemSheet modelling development consists of models for salt-induced high temperature corrosion using the thermodynamic data from within the project. The approach has been to model the salt/gas and salt/metal interfaces. Interaction between the salt and the metal seems to be dependant on the interaction between the salt and the gas.

In the case of internal oxidation/corrosion, the objective was to simulate high temperature corrosion processes under near-service conditions, which requires both a thermodynamic model to predict phase stability for given conditions and a mathematical description of the process kinetics, i.e. solid-state diffusion. The simulation has been achieved by integrating the existing thermodynamic program library ChemApp into a numerical finite difference diffusion calculation. In order to illustrate the application of the modelling tools a number of examples are contained in this Guide Book, including: use of stability diagrams, modelling of internal oxidation / corrosion, modelling of hot salt corrosion and results from the gas precipitation model.

# Contents

# Details of the authors

**Project Coordinator**

Liisa Heikinheimo
VTT Industrial Systems, Espoo, Finland

**Partners**

Klaus Hack
GTT Technologies, Aachen, Germany

Ulrich Krupp
University Siegen, Germany

Michael Spiegel
Max Planck Institute, Düsseldorf, Germany

David Baxter
European Commission, JRC, Institute for Energy, JRC Petten, The Netherlands

Marko Hämäläinen
Helsinki University of Technology, Finland

Mikko Arponen
Rautaruukki Oyj, Raahe, Finland

**Other Partner Contributors**

Pertti Koukkari
VTT Processes, Espoo, Finland

Karri Penttilä
VTT Processes, Espoo, Finland

Hans-Jürgen Christ
University Siegen, Germany

Vicente B. da Trindade Filho
University Siegen, Germany

Andreas Ruh
Max Planck Institute, Düsseldorf, Germany

Szymon Sroda
European Commission, JRC, Institute for Energy, JRC Petten, The Netherlands

# 1. Introduction

This Guide Book is intended to assist the prospective user of a novel range of corrosion modeling software that has been designed to assess potential corrosion under high temperature combustion process conditions. The models described have been developed through the course of the European-funded materials research project, OPTICORR, under contract G5RD-CT-2001-00593. It is anticipated that the data and models developed during the course of the project will be of particular use for the following tasks:

- Design of new materials for used well-defined high temperature combustion processes

- Evaluation of process conditions for the purpose of selecting appropriate materials

- Study of failure cases

- Education and training.

The project set out to gather existing thermodynamic for all the main compounds taking part in the corrosion of engineering alloys under conditions typical of those found in energy from waste or biomass combustion plants. To enable thermodynamic stability calculations to simulate real process conditions as closely as possible, the project also worked to verify data for compounds whose basic thermodynamic data was previously not available. The formulation of data files (Fe-Cr-O-H, Fe-K-Zn-Cl-O, etc.) and construction of thermodynamic stability diagrams (for example for the chlorination of Fe in the presence of NaCl-KCl [10 wt%] with variable Cl potential and variable temperature) using the integrated thermodynamic databank system FactSage[1] Software are described and examples pertinent to waste and biomass combustion are given in this Guide Book. The diagrams cover metal-gas, metal-oxide, metal-salt and salt-gas systems.

In order to build models to simulate corrosion processes the time factor had to be taken into account. As a consequence, corrosion kinetic data had to be collected, in the first instance from the literature, but also from specifically designed laboratory tests that simulate particular aspects of a corrosion process. The laboratory tests were carried out under conditions defined by the former TESTCORR[2] European project with selection of corrosion environments guided by the PREWIN European network[3]. Thanks to the industrial calibration exercises that had been carried out in relation to the European pro-

---

[1] FactSage: C.W. Bale, P. Chartrand, S.A. Degterov, G. Eriksson, K. Hack, R. Ben Mahfoud, J. Melancon, A.D. Pelton and S. Petersen, CALPHAD, 26(2), (2002), pp. 189–228.

[2] TESTCORR European Project: SMT4-CT95-2001.

[3] PREWIN: Performance, Reliability and Emissions Reduction in Waste Incinerators.

ject and network, corrosion data collected using the TESTCORR- and PREWIN-supported tests could also be used for verification of the corrosion models. Examples of data used in the design, development and verification of the model are included in this Guide Book for illustration purposes.

The corrosion models were based on existing ChemSheet[4] and InCorr[5] software systems. In essence, these tools addressed two separate parts of the corrosion process, molten salt corrosion on the surface and internal oxidation/corrosion, respectively. The ChemSheet modelling consists of models for salt-induced high temperature corrosion using the thermodynamic data from within the project. A typical data-file consists of a system comprising seven components: Zn-K-Fe-He-O-Cl-H. It contains the gas phase, liquid salt phase, which is composed of four constituents: $KCl$, $ZnCl_2$, $FeCl_2$, $FeCl_3$, and several condensed phases (oxides, chlorides and etc.). The approach has been to use ChemSheet to model the salt/gas and salt/metal interfaces, allowing interaction between the salt and the metal seems to be dependant on the interaction between the salt and the gas.

In the case of internal oxidation/corrosion, the objective of OPTICORR was to simulate high temperature corrosion processes under near-service conditions, which requires both a thermodynamic model to predict phase stability for given conditions and a mathematical description of the process kinetics, i.e. solid-state diffusion. The simulation has been achieved by integrating the thermodynamic program library ChemApp[6] into a numerical finite difference diffusion calculation to treat internal oxidation and nitridation of Ni-base alloys at high temperatures.

In order to illustrate the application of the modelling tools a number of examples, in the form of case studies are contained in this Guide Book. These include:

- Use of stability diagrams

- Modelling of internal oxidation/corrosion

- Modelling of hot salt corrosion

- Results from the gas precipitation model.

---

[4] ChemSheet[TM]: P. Koukkari, K. Pentillä, K. Hack and S. Petersen, Microstructure, Mechanical Properties and Processes Computer Simulation and Modelling, EUROMAT 99 – Volume 3, (2000), 323, Wiley-VCH, Weinheim.

[5] InCorr is a product of University Siegen, Germany.

[6] ChemApp: G. Eriksson, K. Hack, and S. Petersen, Werkstoffwoche '96, Symposium 8, Simulation, Modellierung, Informationssysteme Herausgeber: J. Hirsch, DGM Informationsgesellschaft Verlag, 1997.

Finally, data from the various oxidation and corrosion tests carried out within the project for the purpose of assisting model development and verification are included.

As a first impression of what can be gained from a thermochemical approach two examples are given below. The first is a calculated phase diagram with associated experimental information (Figure 1.1). Note how the link is made between the data that can be read from the Fe-Cr-Mo-C phase diagram and the information that is contained in the experimental thermogravimetric (TG)/differential scanning calorimeter (DSC) curves. The second example shows the Fe-Cr-O phase diagram and associated inner/outer oxide layer morphology (Figure 1.2). In the latter case of the low-alloy steels, inward oxide growth contributes substantially to the overall oxidation process in the temperature range between 500 and 600°C. Figure 1.2a shows the cross-section of an oxide scale formed on a low-alloy steel during exposure at 550°C to air. Gold markers deposited on the surface of the sample by sputtering prior to exposure represent the position of the original metal surface. The layered structure of the oxide scale can be predicted from the Fe-Cr-O phase diagram in Figure 1.2b (for $T = 550°C$). For high oxygen potentials $Fe_2O_3$ (hematite) and $Cr_2O_3$ are formed. For lower oxygen potentials $Fe_3O_4$ (magnetite), $FeCr_2O_4$ (spinel) and finally for lowest oxygen potentials $Cr_2O_3$ are formed. FeO (wustite) is not expected, since it is not stable at temperatures below 570°C. Generally, the oxide scale as it is depicted in Figure 1.2a consists of a coarse-grained outer scale ($Fe_2O_3 + Fe_3O_4$), growing by outward iron diffusion, and a fine-grained, porous inner scale, growing by inward oxygen transport ($Fe_3O_4 + FeCr_2O_4$).



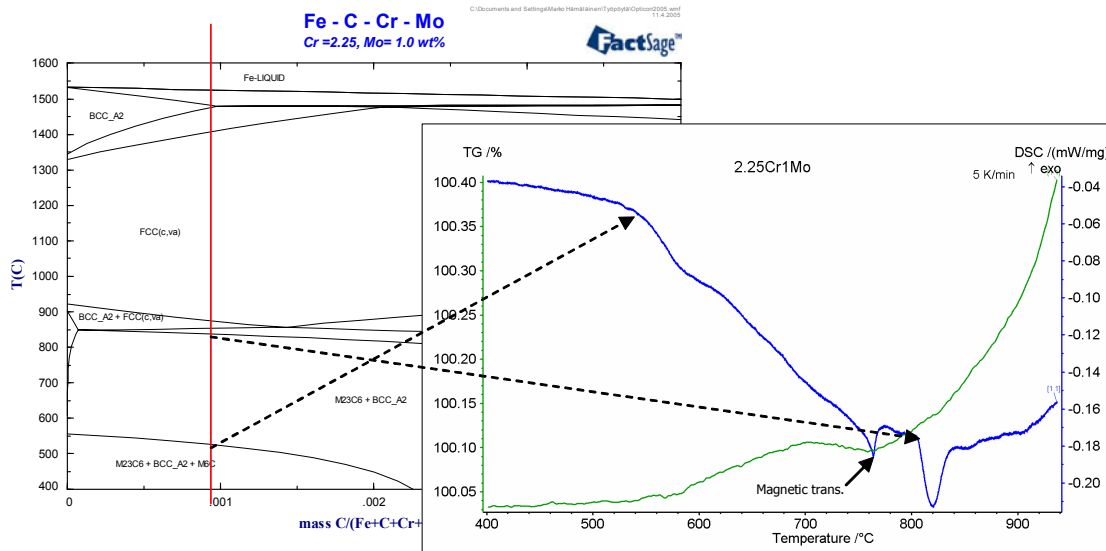*Figure 1.1. Fe-Cr-Mo-C phase diagram and a corresponding TG/DSC curves for the 2.25Cr/1Mo ferritic alloy with phase changes indicated.*
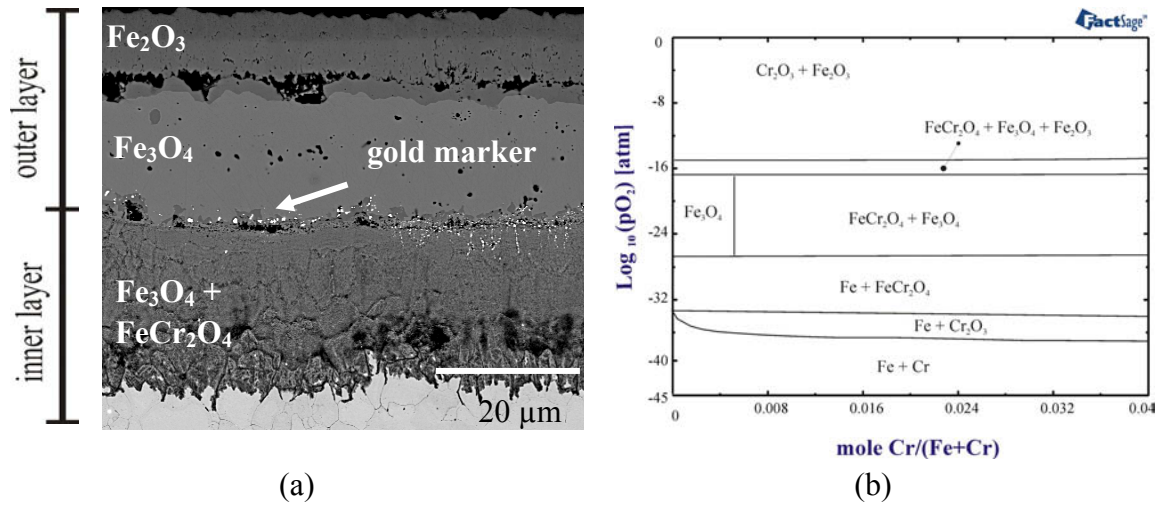
*Figure 1.2. (a) Oxide scale on a low alloy steel (grade X60) after exposure at $550^oC$ to laboratory air for 72h, (b) Fe-Cr-O stability diagram for $T = 550^oC$[7].*

---

[7] V.B. Trindade, U. Krupp, S. Yang and H.-J. Christ, Sonderbände der Praktischen Metallographie, 36, (2004), pp. 243–248.

# 2. Thermodynamic programs and data

(Klaus Hack – GTT-Technologies)

In this chapter the basic tool for thermochemical application calculations, a so-called Integrated Thermodynamic Databank System (ITDS), and the necessary thermochemical data are described and results pertaining to the topics of the project are demonstrated and discussed.

The tasks of an ITDS are threefold:

- storage and administration of thermochemical data of various types of phases (here inorganic phases),

- calculation of thermodynamic properties of phases and their constituents, of reactions between stoichiometric substances, of complex equilibria in multi-phase, multi-component systems, of phase diagrams,

- generation of new thermochemical data from experimental thermodynamic information.

The basic data stored in a thermochemical database consist of the Gibbs energies of the various phases of the chemical system for which the database has been set up. These Gibbs energies are in the simple case of pure substances only a function of temperature, $G = G(T)$, assuming that the pressure dependence is negligible for pressures up to some bar. Pure substances in this context are all gas species, but also condensed matter without compositional variability, such as stoichiometric compounds (e.g. $Al_2O_3$), intermetallic compounds (e.g. FeSi) or even elements (e.g. carbon graphite). However, in very many cases the phases of a system are non-ideal condensed solutions for which the Gibbs energy depends on both temperature and composition, $G = G(T,x_i)$, again neglecting the pressure dependence. Such phases are liquid metals, oxides and salts; solid metal matrix phases, (e.g. FCC_A1 for Ni-based alloys or for austenite steels, or BCC_A2 for ferrite steels), intermetallic phases, (e.g. Laves_C14 in Fe-based alloys); solid oxide solutions, (e.g. wustite, which is non-stoichiometric "FeO" with dissolved Mg or other elements, or corundum, which is a substitutional solution of trivalent cat-ions in $(Al,Fe,Cr)_2O_3$; or, solid salt solutions, (e.g. $K_2(SO_4,CrO_4)$).

From the Gibbs energies of the different phases mathematical methods lead to the various results such as chemical potentials, partial or integral enthalpies of mixing, component activities, equilibrium constants, phase amounts in complex equilibria and finally a series of possible phase diagrams. These relationships are summarized in Figure 2.1.
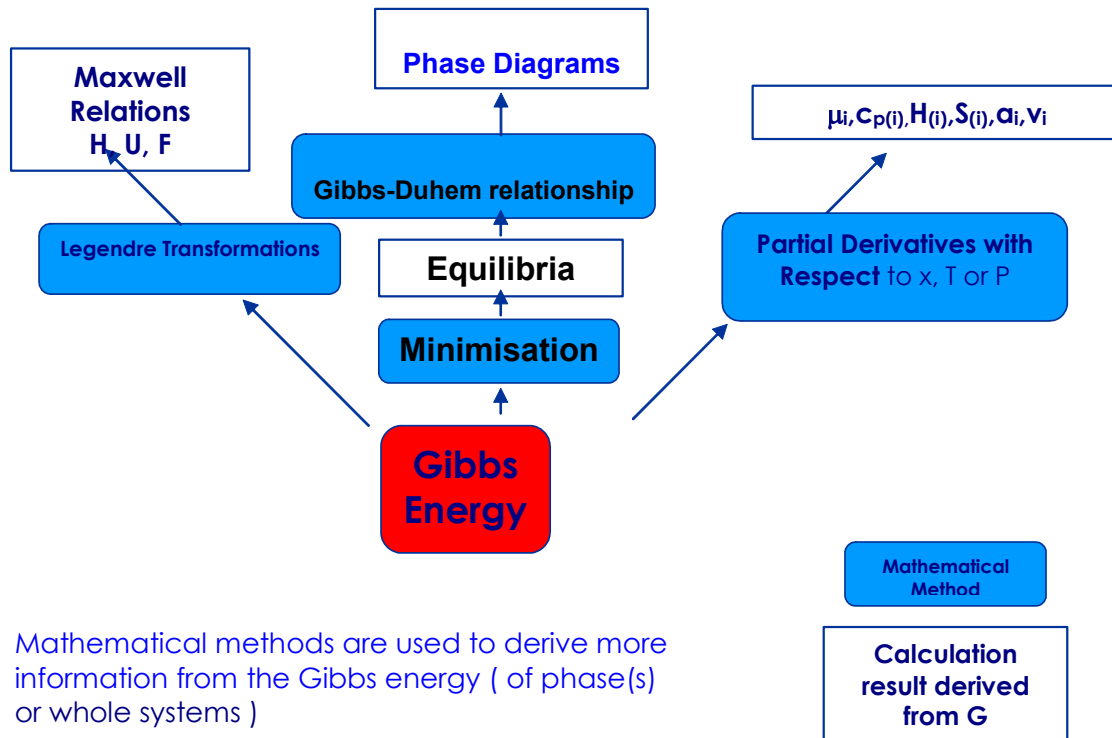
*Figure 2.1. Gibbs energy tree [1].*

## 2.1 Available software

The particular ITDS used for the OptiCorr project is FactSage [2], a joint product of GTT Technologies, Herzogenrath, Germany, and Thermfact, Montreal, Canada. Fact-Sage has modules for the calculation of

- thermodynamic properties of phases and their constituents,
- isothermal and non-isothermal stoichiometric reactions,
- complex equilibrium states under standard conditions and
- with special constraints,
- all types of classical phase diagrams, among these EpH
- diagrams for aqueous systems.

Results can be obtained in tables and plots, and can be exported in files for use in other software, e.g. in Microsoft Office, especially in EXCEL for further calculational exploitation, but also in Word or PowerPoint for presentation of results (especially graphs) in reports.

Especially the modules for the calculation of complex equilibria (called Equilib) and phase diagrams (called Phase Diagram) have been employed for the generation of results in the framework of the OptiCorr project. The data administration has been performed with the Compound and the Solution module respectively, whereas new data have been generated with OptiSage, the latter being a special module for the generation of Gibbs energy data from the assessment of experimental thermochemical data. For more details see www.FactSage.com.

### 2.1.1  Complex equilibrium calculations

Calculations with the Equilib module (complex equilibria) are the most general type of calculation one can perform with FactSage. These calculations are based on the principle of Gibbs energy minimisation at constant temperature and pressure with the constraint that mass balances hold for all independent chemical components of the system.

For example will the program tell for a given overall composition of carbon and oxygen, e.g. $C/O_2 = 1$, whether $CO_2$ is the only stable species (at temperatures up to about 1800K) or whether it will dissociate into CO and $O_2$ or even O (at temperatures well beyond 2000K). Any state in the transitorial temperature range can of course also be calculated. Similarly, alloys, salts or oxides, and also combined states with metals in a corrosive gas atmosphere can be investigated by Gibbs energy minimisation.

Since usually all compositions of a system can be fixed, only temperature and/or pressure are variables for the calculation. Out of these one is given a fixed value and the other is stepped through an interval. Thus results are generated which show the equilibrium state in form of a phase table for each set of fixed temperature, pressure and overall composition. For the phases the equilibrium amounts are given, and if a phase is a solution, then also the phase internal composition is shown. For phases that are not stable at equilibrium the "distance to equilibrium" is shown in form of the activity value that is less than one. The smaller the value the further away from equilibrium is the phase. Quantitatively: $\Delta G = RT \ln a$, with $\Delta G$ the Gibbs energy difference of the particular phase with respect to the equilibrium.

In Table 2.1.1, which is given at the end of this chapter, an example for such an equilibrium table is given for the case of an X20 alloy that is equilibrated with a corrosive gas phase containing Argon, water vapour and oxygen at a temperature of 650°C and under a pressure of 1atm.

The table shows clearly what insight into the behaviour of a complex chemical system can be gained from a complex equilibrium calculation. Not only are all stable phases

shown and their amounts given (Gas, BCC_A2, $M_{23}C_6$, (Mn,Fe)S, Corundum). It is also possible to obtain information about the phase internal composition of the stable phases, both in terms of the phase constituent concentrations (upper part of the table) and also with respect to the element composition (bottom section of the table). Furthermore there is information on the non-stable phases in terms of the phase activities and that phase internal composition which comes closest to equilibrium (see for example the FCC_A1 phase, a = 0.97046 or the Laves_C14 phase, a = 0.89871). For phases that have been treated with a sublattice model the respective sublattice occupation is also available (middle section of the table). It should be noted that the table has already been shortened in order to show only the most relevant information. Altogether more than 20 non-ideal condensed solutions and more than 25 stoichiometric condensed phases have been considered in the calculation. The entire list of solution phases can be found at the bottom the table were the elementary compositions of all phases are given. For the stable phases the values are the true equilibrium values, for the non-stable phases the values relate to the composition that comes closest to equilibrium.

When temperature, pressure or one compositional variable are stepped through an interval the Equilib module permits so-called one-dimensional phase mappings. The calculations are conducted in a way by which permanent checking from step to step is done on the list of stable phases. If no change has occurred, the next step is done; if a change has occurred then the value of the step-variable that leads to the exact transition point is searched for. Thus all phase transitions in the entire step-range are found at their exact point independent of the step size that was chosen. When the calculation is completed a post-processor unit connected to Equilib permits the generation of graphical output of the results. The independent variable of the calculation is chosen as x-axis variable, while a whole range of properties can be selected as y-variable. The most obvious choice for a fixed-composition case would be a phase-amount-versus-T plot, but it is also possible to plot the phase internal composition of condensed solutions or the species distribution in the gas phase as function of temperature. Furthermore, it is possible to plot the phase activities as function of the step variable. This is particularly useful for the monitoring of the phases in the ranges where they are not stable. Small deviations from unity will be indicators for only a slight instability that might disappear for a small change in composition for example. Large deviations from unity indicate that the particular phase has very little tendency to form.

All such plots have been given the collective name one-dimensional phase maps, since in the two-dimensional graphs only one variable, the x-axis variable, was an independent quantity in the calculations while the y-variable is a dependent result of the calculations.

Such diagrams have been employed in the framework of OptiCorr for the investigation of gas internal equilibria of the corrosion gases used in the experiments, the mapping of the phase constitution of the alloys investigated in the experiments and the computational investigation of corrosion experiments between gases and the metals. Results of these calculations are given below.

*Table 2.1.1. Equilibrium between a corrosive gas (0.1 mol) and an X20 alloy (100 g).*

| T = 650.00 C | | | |
|---|---|---|---|
| P = 1.00000E+00 atm | | | |
| V = 6.96915E+00 dm$^3$ | | | |
| | | | |
| **STREAM CONSTITUENTS** | **AMOUNT/mol** | | |
| Ar(g) | 7.7000E-02 | | |
| H$_2$O(g) | 1.5000E-02 | | |
| O$_2$(g) | 8.0000E-03 | | |
| Fe | 8.6837E+01 | | |
| Cr | 1.0280E+01 | | |
| Ni | 7.2000E-01 | | |
| Mo | 8.7000E-01 | | |
| V | 2.6000E-01 | | |
| C | 1.8000E-01 | | |
| Si | 2.3000E-01 | | |
| Mn | 6.2000E-01 | | |
| S | 3.0000E-03 | | |
| | **EQUIL AMOUNT** | **MOLE FRACTION** | **FUGACITY** |
| **PHASE: Gas** | **mol** | | **atm** |
| Ar | 7.7000E-02 | 8.3696E-01 | 8.3696E-01 |
| H$_2$ | 1.5000E-02 | 1.6304E-01 | 1.6304E-01 |
| CH$_4$ | 1.3335E-07 | 1.4495E-06 | 1.4495E-06 |
| H$_2$O | 8.0650E-08 | 8.7663E-07 | 8.7663E-07 |
| HMn | 1.7612E-09 | 1.9144E-08 | 1.9144E-08 |
| H$_2$S | 1.3701E-10 | 1.4892E-09 | 1.4892E-09 |
| CO | 7.2707E-11 | 7.9030E-10 | 7.9030E-10 |
| TOTAL: | 9.2000E-02 | 1.0000E+00 | 1.0000E+00 |
| **PHASE: M$_{23}$C$_6$** | **mol** | **MOLE FRACTION** | **ACTIVITY** |
| CrCrC | 7.9772E-05 | 2.6601E-03 | 3.2224E-10 |
| FeCrC | 2.2813E-05 | 7.6073E-04 | 8.8442E-25 |
| MnCrC | 9.0037E-11 | 3.0024E-09 | 3.4183E-46 |
| NiCrC | 1.1493E-10 | 3.8326E-09 | 7.3338E-66 |
| VCrC | 2.9749E-12 | 9.9201E-11 | 7.7852E-62 |
| CrFeC | 1.4920E-05 | 4.9754E-04 | 2.1084E-12 |
| FeFeC | 4.2668E-06 | 1.4228E-04 | 5.7867E-27 |
| MnFeC | 1.6840E-11 | 5.6156E-10 | 2.2365E-48 |
| NiFeC | 2.1496E-11 | 7.1683E-10 | 4.7984E-68 |
| VFeC | 5.5640E-13 | 1.8554E-11 | 5.0938E-64 |
| CrMnC | 7.2432E-07 | 2.4154E-05 | 1.2943E-15 |
| FeMnC | 2.0714E-07 | 6.9073E-06 | 3.5523E-30 |
| MnMnC | 8.1752E-13 | 2.7261E-11 | 1.3729E-51 |
| NiMnC | 1.0436E-12 | 3.4799E-11 | <1.0000E-75 |
| VMnC | 2.7011E-14 | 9.0073E-13 | 3.1269E-67 |
| CrMoC | 2.3224E-02 | 7.7443E-01 | 2.0468E-03 |
| FeMoC | 6.6414E-03 | 2.2147E-01 | 7.1756E-20 |
| MnMoC | 2.6212E-08 | 8.7407E-07 | <1.0000E-75 |
| NiMoC | 3.3459E-08 | 1.1158E-06 | <1.0000E-75 |
| VMoC | 8.6605E-10 | 2.8880E-08 | <1.0000E-75 |

| | | | |
|---|---|---|---|
| CrNiC | 1.3173E-07 | 4.3927E-06 | 1.4513E-18 |
| FeNiC | 3.7671E-08 | 1.2562E-06 | 3.9832E-33 |
| MnNiC | 1.4868E-13 | 4.9579E-12 | <1.0000E-75 |
| NiNiC | 1.8979E-13 | 6.3288E-12 | 3.3029E-74 |
| VNiC | 4.9124E-15 | 1.6381E-13 | <1.0000E-75 |
| CrVC | 2.0940E-07 | 6.9829E-06 | 5.8298E-18 |
| FeVC | 5.9884E-08 | 1.9969E-06 | 1.6000E-32 |
| MnVC | 2.3635E-13 | 7.8814E-12 | 6.1841E-54 |
| NiVC | 3.0170E-13 | 1.0061E-11 | <1.0000E-75 |
| VVC | 7.8091E-15 | 2.6041E-13 | 1.4084E-69 |
| TOTAL: | 2.9988E-02 | 1.0000E+00 | 1.0000E+00 |
| **PHASE: M$_6$C** | **mol** | **MOLE FRACTION** | **ACTIVITY** |
| FeMoCrC | 0.0000E+00 | 3.0679E-01 | 1.1793E-02 |
| NiMoCrC | 0.0000E+00 | 1.8982E-12 | 1.5391E-23 |
| FeMoFeC | 0.0000E+00 | 4.4327E-02 | 1.9047E-05 |
| NiMoFeC | 0.0000E+00 | 2.7426E-13 | 2.3871E-23 |
| FeMoMoC | 0.0000E+00 | 5.2105E-01 | 2.7362E-02 |
| NiMoMoC | 0.0000E+00 | 3.2239E-12 | 9.8199E-25 |
| FeMoNiC | 0.0000E+00 | 1.3803E-11 | 2.3871E-23 |
| NiMoNiC | 0.0000E+00 | 8.5401E-23 | 2.2544E-27 |
| FeMoVC | 0.0000E+00 | 1.2784E-01 | 2.0477E-03 |
| NiMoVC | 0.0000E+00 | 7.9096E-13 | 1.4135E-30 |
| TOTAL: | 0.0000E+00 | 1.0000E+00 | 7.3130E-01 |
| **PHASE: FCC_A1** | **mol** | **MOLE FRACTION** | **ACTIVITY** |
| CrC | 0.0000E+00 | 2.1042E-06 | 9.5065E-05 |
| FeC | 0.0000E+00 | 1.6556E-05 | 5.4342E-08 |
| MnC | 0.0000E+00 | 4.6676E-07 | 4.2865E-07 |
| MoC | 0.0000E+00 | 9.3988E-08 | 3.2128E-04 |
| NiC | 0.0000E+00 | 4.3763E-07 | 2.1412E-09 |
| SC | 0.0000E+00 | 3.1717E-16 | 2.7465E-18 |
| SiC | 0.0000E+00 | 5.9001E-08 | 5.4427E-14 |
| VC | 0.0000E+00 | 1.8872E-08 | 1.0500E-02 |
| Cr | 0.0000E+00 | 1.0661E-01 | 1.4517E-01 |
| FeVa | 0.0000E+00 | 8.3884E-01 | 8.1688E-01 |
| MnVa | 0.0000E+00 | 2.3649E-02 | 1.1196E-02 |
| MoVa | 0.0000E+00 | 4.7620E-03 | 2.2279E-02 |
| NiVa | 0.0000E+00 | 2.2173E-02 | 1.2011E-02 |
| S | 0.0000E+00 | 1.6070E-11 | 4.0164E-15 |
| SiVa | 0.0000E+00 | 2.9894E-03 | 3.0734E-11 |
| VVa | 0.0000E+00 | 9.5617E-04 | 8.7799E-05 |
| TOTAL: | 0.0000E+00 | 1.0000E+00 | 9.7046E-01 |
| **PHASE: BCC_A2** | **mol** | **MOLE FRACTION** | **ACTIVITY** |
| CrC | 2.3228E-06 | 2.3438E-08 | 1.3520E-35 |
| FeC | 2.0566E-05 | 2.0752E-07 | 7.2701E-34 |
| MnC | 1.4635E-07 | 1.4767E-09 | 1.1199E-15 |
| MoC | 1.8511E-07 | 1.8678E-09 | 3.2835E-27 |
| NiC[3] | 1.7078E-07 | 1.7233E-09 | 5.7174E-31 |
| SC | 2.4535E-15 | 2.4757E-17 | 8.6266E-27 |
| SiC | 5.4555E-08 | 5.5048E-10 | 3.6918E-36 |
| VC | 6.1671E-08 | 6.2228E-10 | 2.5523E-21 |
| CrVa | 9.7926E+00 | 9.8812E-02 | 3.8231E-01 |
| FeVa | 8.6704E+01 | 8.7488E-01 | 8.9020E-01 |
| MnVa | 6.1700E-01 | 6.2258E-03 | 1.0637E-02 |
| MoVa | 7.8040E-01 | 7.8746E-03 | 1.7412E-01 |
| NiVa | 7.2000E-01 | 7.2651E-03 | 5.9244E-03 |
| S | 1.0344E-08 | 1.0437E-10 | 3.5258E-15 |
| SiVa | 2.3000E-01 | 2.3208E-03 | 5.6299E-11 |
| VVa | 2.6000E-01 | 2.6235E-03 | 2.8619E-04 |
| TOTAL: | 9.9104E+01 | 1.0000E+00 | 1.0000E+00 |
| **PHASE: LAVES_PHASE** | **mol** | **MOLE FRACTION** | **ACTIVITY** |
| FeFe | 0.0000E+00 | 2.4663E-02 | 6.3021E-02 |

| | mol | MOLE FRACTION | ACTIVITY |
|---|---|---|---|
| CrFe | 0.0000E+00 | 4.5253E-03 | 2.1348E-07 |
| FeMo | 0.0000E+00 | 8.2030E-01 | 4.8198E-01 |
| CrMo | 0.0000E+00 | 1.5052E-01 | 2.1401E-02 |
| TOTAL: | 0.0000E+00 | 1.0000E+00 | 8.9871E-01 |

**PHASE: CHI_A12          mol    MOLE FRACTION    ACTIVITY**

| | mol | MOLE FRACTION | ACTIVITY |
|---|---|---|---|
| $Fe_{24}Cr_{10}Cr_{24}$ | 0.0000E+00 | 1.8874E-01 | 6.1131E-23 |
| $Fe_{24}Cr_{10}Fe_{24}$ | 0.0000E+00 | 4.4347E-01 | 3.8816E-07 |
| $Fe_{24}Cr_{10}Mo_{24}$ | 0.0000E+00 | 8.3180E-03 | 2.5561E-52 |
| $Fe_{24}Mo_{10}Cr_{24}$ | 0.0000E+00 | 1.0123E-01 | 2.8217E-12 |
| $Fe_{24}Mo_{10}Fe_{24}$ | 0.0000E+00 | 2.3786E-01 | 1.0613E-15 |
| $Fe_{24}Mo_{10}Mo_{24}$ | 0.0000E+00 | 4.4614E-03 | 2.3334E-50 |
| $Cr_{24}Cr_{10}Cr_{24}$ | 0.0000E+00 | 3.0526E-03 | 9.9274E-58 |
| $Cr_{24}Cr_{10}Fe_{24}$ | 0.0000E+00 | 7.1726E-03 | 2.0303E-55 |
| $Cr_{24}Cr_{10}Mo_{24}$ | 0.0000E+00 | 1.3453E-04 | <1.0000E-75 |
| $Cr_{24}Mo_{10}Cr_{24}$ | 0.0000E+00 | 1.6373E-03 | 4.4094E-47 |
| $Cr_{24}Mo_{10}Fe_{24}$ | 0.0000E+00 | 3.8471E-03 | 7.7962E-59 |
| $Cr_{24}Mo_{10}Mo_{24}$ | 0.0000E+00 | 7.2158E-05 | <1.0000E-75 |
| TOTAL: | 0.0000E+00 | 1.0000E+00 | 9.0024E-01 |

**PHASE: $M_2O_3$(Corundum)        mol    MOLE FRACTION    ACTIVITY**

| | mol | MOLE FRACTION | ACTIVITY |
|---|---|---|---|
| $Cr_2O_3$ | 1.0333E-02 | 1.0000E+00 | 1.0000E+00 |
| $Fe_2O_3$ | 6.1103E-11 | 5.9132E-09 | 3.7170E-17 |
| TOTAL: | 1.0333E-02 | 1.0000E+00 | 1.0000E+00 |

**PHASE: (Mn,Fe)S_Q          mol    MOLE FRACTION    ACTIVITY**

| | mol | MOLE FRACTION | ACTIVITY |
|---|---|---|---|
| FeS | 1.4983E-08 | 4.9944E-06 | 7.3830E-06 |
| MnS | 3.0000E-03 | 1.0000E+00 | 1.0000E+00 |
| TOTAL: | 3.0000E-03 | 1.0000E+00 | 1.0000E+00 |

| | mol | ACTIVITY |
|---|---|---|
| $FeCr_2O_4$ | 0.0000E+00 | 2.5531E-02 |
| C_<graphite> | 0.0000E+00 | 2.3023E-04 |
| $NiCr_2O_4$ | 0.0000E+00 | 1.5825E-09 |
| $MoS_2$ | 0.0000E+00 | 1.1912E-09 |
| NiO | 0.0000E+00 | 3.0504E-10 |
| $MoO_2$ | 0.0000E+00 | 1.3402E-10 |

\*\*\*\*\*\*\*\*\*\*\*\*\*\*\*\*\*\*\*\*\*\*\*\*\*\*\*\*\*\*\*\*\*\*\*\*\*\*\*\*\*\*\*\*\*\*\*\*\*\*\*\*\*\*\*\*\*\*\*\*\*\*\*

| Cp_EQUIL | H_EQUIL | S_EQUIL | G_EQUIL | V_EQUIL |
|---|---|---|---|---|
| $J.K^{-1}$ | J | $J.K^{-1}$ | J | $dm^3$ |

\*\*\*\*\*\*\*\*\*\*\*\*\*\*\*\*\*\*\*\*\*\*\*\*\*\*\*\*\*\*\*\*\*\*\*\*\*\*\*\*\*\*\*\*\*\*\*\*\*\*\*\*\*\*\*\*\*\*\*\*\*\*\*

| | | | | |
|---|---|---|---|---|
| 4.77259E+03 | 2.24944E+06 | 6.74516E+03 | -3.97735E+06 | 6.96915E+00 |

**Mole fraction of sublattice constituents in $M_{23}C_6$:**

| Cr | 7.7762E-01 Stoichiometry = 2.0000E+01 |
|---|---|
| Fe | 2.2238E-01 |
| Mn | 8.7768E-07 |
| Ni | 1.1204E-06 |
| V | 2.8999E-08 |

-------------------------------------------------------------

| Cr | 3.4209E-03 Stoichiometry = 3.0000E+00 |
|---|---|
| Fe | 6.3982E-04 |
| Mn | 3.1061E-05 |
| Mo | 9.9589E-01 |
| Ni | 5.6489E-06 |
| V | 8.9798E-06 |

-------------------------------------------------------------

| C | 1.0000E+00 Stoichiometry = 6.0000E+00 |
|---|---|

**Mole fraction of sublattice constituents in $M_6C$:**

| Fe | 1.0000E+00 Stoichiometry = 2.0000E+00 |
|---|---|
| Ni | 6.1873E-12 |

-------------------------------------------------------------

| Mo | 1.0000E+00 Stoichiometry = 2.0000E+00 |
|---|---|

-------------------------------------------------------------

| Cr | 3.0679E-01 Stoichiometry = 2.0000E+00 |
|---|---|
| Fe | 4.4327E-02 |

| | | |
|---|---|---|
| Mo | 5.2105E-01 | |
| Ni | 1.3803E-11 | |
| V | 1.2784E-01 | |

----------------------------------------------------------

| | | |
|---|---|---|
| C | 1.0000E+00 Stoichiometry = 1.0000E+00 | |

**Mole fraction of sublattice constituents in FCC_A1**

| | |
|---|---|
| Cr | 1.0661E-01 Stoichiometry = 1.0000E+00 |
| Fe | 8.3886E-01 |
| Mn | 2.3649E-02 |
| Mo | 4.7621E-03 |
| Ni | 2.2173E-02 |
| S | 1.6070E-11 |
| Si | 2.9894E-03 |
| V | 9.5618E-04 |

----------------------------------------------------------

| | |
|---|---|
| C | 1.9737E-05 Stoichiometry = 1.0000E+00 |
| Va | 9.9998E-01 |

Magnetic properties for FCC_A1:Me(C,Va)#1:
Neel temperature = -150.41 C
Average magnetic moment/atom = 5.4573E-01


**Mole fraction of sublattice constituents in BCC_A2:**

| | |
|---|---|
| Cr | 9.8812E-02 Stoichiometry = 1.0000E+00 |
| Fe | 8.7488E-01 |
| Mn | 6.2258E-03 |
| Mo | 7.8746E-03 |
| Ni | 7.2651E-03 |
| S | 1.0437E-10 |
| Si | 2.3208E-03 |
| V | 2.6235E-03 |

----------------------------------------------------------

| | |
|---|---|
| C | 2.3720E-07 Stoichiometry = 3.0000E+00 |
| Va | 1.0000E+00 |

Magnetic properties for BCC_A2:
Curie temperature = 726.82 C
Average magnetic moment/atom = 1.8702E+00


**Mole fraction of sublattice constituents in LAVES_PHASE:**

| | |
|---|---|
| Fe | 8.4496E-01 Stoichiometry = 2.0000E+00 |
| Cr | 1.5504E-01 |

----------------------------------------------------------

| | |
|---|---|
| Fe | 2.9188E-02 Stoichiometry = 1.0000E+00 |
| Mo | 9.7081E-01 |

**Mole fraction of sublattice constituents in CHI_A12:**

| | |
|---|---|
| Fe | 9.8408E-01 Stoichiometry = 2.4000E+01 |
| Cr | 1.5916E-02 |

----------------------------------------------------------

| | |
|---|---|
| Cr | 6.5089E-01 Stoichiometry = 1.0000E+01 |
| Mo | 3.4911E-01 |

----------------------------------------------------------

| | |
|---|---|
| Cr | 2.9466E-01 Stoichiometry = 2.4000E+01 |
| Fe | 6.9235E-01 |
| Mo | 1.2986E-02 |

Magnetic properties for $M^2O^3$(Corundum):
Neel temperature = -273.15 C
Average magnetic moment/atom = 4.4315E-09

**Mole fraction of system components:**

| | gas_ideal | CEMENTITE | $(Fe,Mn)^5Si^3$ | $M_{23}C_6$ | $M^3C^2$ |
|---|---|---|---|---|---|
| Mo | 4.9878E-28 | 1.9354E-03 | 0.0000E+00 | 1.0302E-01 | 4.5778E-04 |
| Ni | 4.2605E-17 | 1.9956E-04 | 0.0000E+00 | 1.3570E-06 | 0.0000E+00 |

| | | | | | |
|---|---|---|---|---|---|
| Fe | 2.3100E-16 | 8.1160E-02 | 6.2026E-01 | 1.5343E-01 | 0.0000E+00 |
| Mn | 1.6477E-08 | 8.6255E-03 | 4.7414E-03 | 3.8185E-06 | 0.0000E+00 |
| Cr | 6.3118E-16 | 6.3198E-01 | 0.0000E+00 | 5.3664E-01 | 5.5716E-01 |
| V | 7.5028E-23 | 2.6101E-02 | 0.0000E+00 | 9.4895E-07 | 4.2378E-02 |
| Ar | 7.1962E-01 | 0.0000E+00 | 0.0000E+00 | 0.0000E+00 | 0.0000E+00 |
| S | 1.2805E-09 | 0.0000E+00 | 0.0000E+00 | 0.0000E+00 | 0.0000E+00 |
| Si | 8.4117E-16 | 0.0000E+00 | 3.7500E-01 | 0.0000E+00 | 0.0000E+00 |
| O | 7.5441E-07 | 0.0000E+00 | 0.0000E+00 | 0.0000E+00 | 0.0000E+00 |
| C | 1.2470E-06 | 2.5000E-01 | 0.0000E+00 | 2.0690E-01 | 4.0000E-01 |
| H | 2.8037E-01 | 0.0000E+00 | 0.0000E+00 | 0.0000E+00 | 0.0000E+00 |

| | $M_6C$ | $M_7C^3$ | FCC_A1:Me#1 | FCC_A1:Me#2 | BCC_A2 |
|---|---|---|---|---|---|
| Mo | 4.3459E-01 | 6.2335E-03 | 4.7620E-03 | 1.6203E-01 | 7.8746E-03 |
| Ni | 5.7114E-12 | 3.2143E-05 | 2.2173E-02 | 2.5799E-05 | 7.2651E-03 |
| Fe | 2.9838E-01 | 3.9922E-02 | 8.3884E-01 | 2.3613E-03 | 8.7488E-01 |
| Mn | 0.0000E+00 | 4.0382E-03 | 2.3649E-02 | 6.2165E-04 | 6.2258E-03 |
| Cr | 8.7653E-02 | 6.0138E-01 | 1.0661E-01 | 3.5629E-02 | 9.8812E-02 |
| V | 3.6525E-02 | 4.8391E-02 | 9.5617E-04 | 4.0248E-01 | 2.6235E-03 |
| S | 0.0000E+00 | 0.0000E+00 | 1.6070E-11 | 4.4926E-16 | 1.0437E-10 |
| Si | 0.0000E+00 | 0.0000E+00 | 2.9894E-03 | 8.1892E-12 | 2.3208E-03 |
| C | 1.4286E-01 | 3.0000E-01 | 1.9736E-05 | 3.9685E-01 | 7.1159E-07 |

| | LAVES_PHASE | MONI_DELTA | CHI_A12 | KSI_CARBIDE | $(Fe,Mn)^3Si$ |
|---|---|---|---|---|---|
| Mo | 3.2360E-01 | 2.8010E-01 | 6.5565E-02 | 2.0168E-01 | 0.0000E+00 |
| Ni | 0.0000E+00 | 1.9594E-02 | 0.0000E+00 | 0.0000E+00 | 0.0000E+00 |
| Fe | 5.7304E-01 | 7.0025E-01 | 6.9370E-01 | 3.3213E-01 | 7.3688E-01 |
| Mn | 0.0000E+00 | 0.0000E+00 | 0.0000E+00 | 0.0000E+00 | 1.3119E-02 |
| Cr | 1.0336E-01 | 5.8482E-05 | 2.4074E-01 | 2.1618E-01 | 0.0000E+00 |
| Si | 0.0000E+00 | 0.0000E+00 | 0.0000E+00 | 0.0000E+00 | 2.5000E-01 |
| C | 0.0000E+00 | 0.0000E+00 | 0.0000E+00 | 2.5000E-01 | 0.0000E+00 |

| | $(Fe,Mn)^1Si^1$ | $Cr^3Si$ | $CrSi^2$ | SIGMA | MU_PHASE |
|---|---|---|---|---|---|
| Mo | 0.0000E+00 | 0.0000E+00 | 0.0000E+00 | 1.2394E-02 | 3.6916E-01 |
| Ni | 0.0000E+00 | 0.0000E+00 | 0.0000E+00 | 5.2170E-03 | 6.6211E-04 |
| Fe | 4.9925E-01 | 0.0000E+00 | 0.0000E+00 | 6.1575E-01 | 5.5737E-01 |
| Mn | 7.5112E-04 | 0.0000E+00 | 0.0000E+00 | 1.8484E-02 | 0.0000E+00 |
| Cr | 0.0000E+00 | 9.1485E-01 | 9.9996E-01 | 3.4465E-01 | 7.2812E-02 |
| V | 0.0000E+00 | 0.0000E+00 | 0.0000E+00 | 3.5080E-03 | 0.0000E+00 |
| Si | 5.0000E-01 | 8.5150E-02 | 3.9241E-05 | 0.0000E+00 | 0.0000E+00 |

| | FeSpinel | Monoxide | $M^2O^3$(Corund | (Fe,Mn)S_P | (Mn,Fe)S_#1 |
|---|---|---|---|---|---|
| Ni | 0.0000E+00 | 1.2378E-05 | 0.0000E+00 | 0.0000E+00 | 0.0000E+00 |
| Fe | 1.4286E-01 | 4.9996E-01 | 2.3653E-09 | 8.1795E-06 | 2.4972E-06 |
| Mn | 0.0000E+00 | 0.0000E+00 | 0.0000E+00 | 4.9999E-01 | 5.0000E-01 |
| Cr | 2.8571E-01 | 0.0000E+00 | 4.0000E-01 | 0.0000E+00 | 0.0000E+00 |
| S | 0.0000E+00 | 0.0000E+00 | 0.0000E+00 | 5.0000E-01 | 5.0000E-01 |
| O | 5.7143E-01 | 5.0003E-01 | 6.0000E-01 | 0.0000E+00 | 0.0000E+00 |

The cutoff limit for phase or gas constituent activities is 1.00E-10

## 2.1.2  Two-dimensional phase mappings (phase diagrams)

As outlined above one-dimensional mappings lead to graphical representations in which the x-axis variable is an independent and the y-axis variable a dependent quantity. In two-dimensional mappings two independent variables chosen from the set of potential properties of a system and from ratios of the corresponding extensive properties are taken as axes variables.

The relevant potentials are: $\qquad\qquad$ T, P(total), $\mu_i$

The corresponding extensive properties are: $\qquad$ S, –V, $n_i$ (mole numbers)

Ratios of the extensive variables are for example all mole fractions because $x_i = n_i/\Sigma n_j$. In this way one obtains what is generally called phase diagrams, i.e. diagrams which depict the fields of stability of phases or phase combinations under the conditions given by the axes variables plus some additional constant values of further variables depending upon the number of system components.

Such diagrams can be derived from the Gibbs energies of the various phases of a system by making use of the Gibbs-Duhem relationship. Essentially the phase diagram results as a projection from a three-dimensional property diagram with the Gibbs energy plotted along the z-axis while the two phase diagram axes variables are used for x and y.

Figure 2.1.1 shows such a diagram for the binary system Cu-Ni at low temperatures. The miscibility gap in the FCC_A1 phase is depicted in the x-y (mole fraction-temperature) plane, while the Gibbs energy is plotted in z-direction. The equilibria are found searching for the minimum Gibbs energy by way of the common tangent method in a G-versus-mole fraction plane with fixed temperature (and pressure). The equilibrium compositions are projected down into the molefraction-temperature plane thus giving the curve of the miscibility gap.
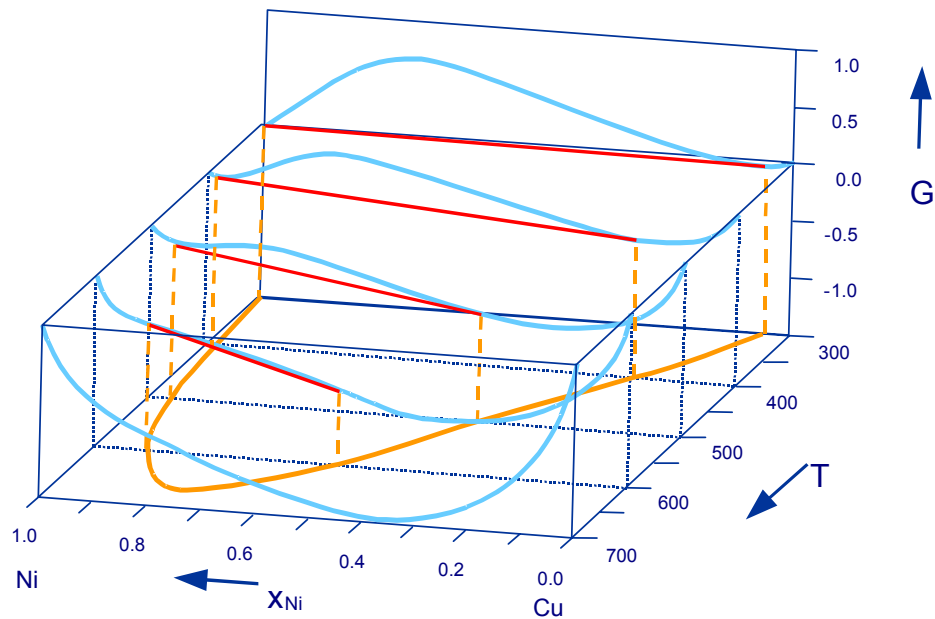


*Figure 2.1.1. G-T-x diagram for the binary system Cu-Ni, p = 1 bar.*

Figure 2.1.2 shows the equivalent diagram for a hypothetical ternary system Fe-C-Me at a fixed temperature and total pressure. Now the equilibria are found by using a tangential plane that touches the Gibbs energy surfaces of the stable phases. The projection of the points of tangency onto the x-y-plane provides the phase boundaries in the Gibbs triangle.
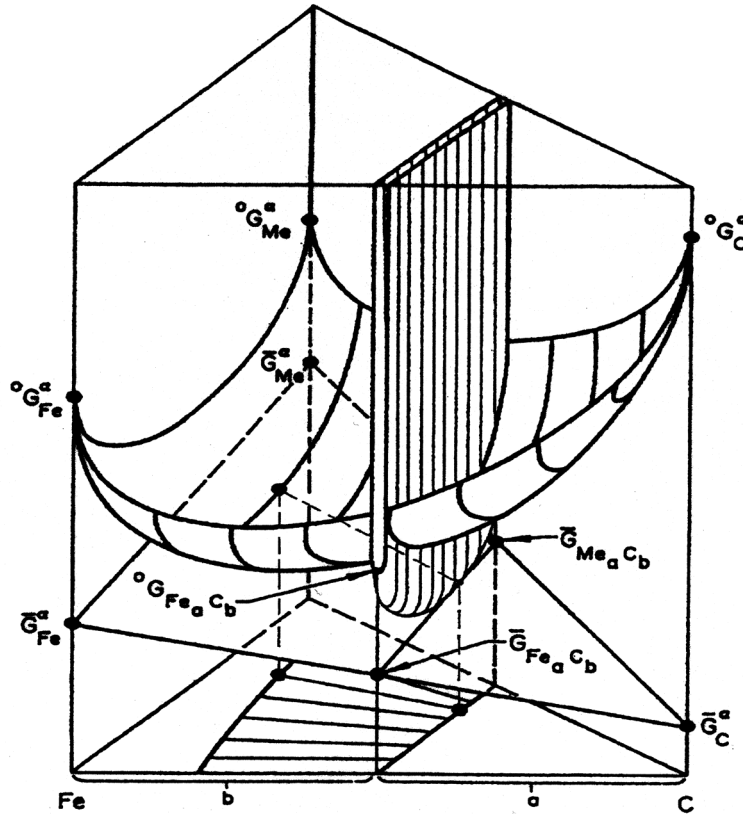


*Figure 2.1.2. G-x-y diagram for the hypothetical system Fe-C-Me, T and P constant.*

For the purposes of the OptiCorr project it has proven useful to apply both types of phase diagrams since temperature-versus-composition plots give insight into the behaviour of the actual alloys, salt or oxide systems involved, while temperature-vs-partial pressure or partial pressure-versus-partial pressure plots related to the practical conditions of reactions of the alloys or salts with a gas phase. Results of such phase diagram calculations are given below.

## 2.2  Thermodynamic database

In order to be able to perform the task of data compilation and assessment for the needs of the OptiCorr project the entire chemical system under investigation has been split into manageable sub-systems of reasonable size and with mutually independent con-

tents. Thus four thermodynamic sub-databases have been created to enable the thermodynamic calculations:

1:  Database for Fe-based alloys
    (Al-C-Ce-Co-Cr-Cu-Fe-Mn-Mo-Nb-Ni-S-Si-V).

2:  Database for Ni-based alloys
    (C-Cr-Fe-Mo-Ni-Si-Ti-W).

3:  Salt-database
    $(K^+,Zn^{+2},Fe^{+2},Fe^{+3},Cr^{2+},Cr^{3+},Ni^{+2}//Cl^-,(SO_4)^{2-},(CrO_4)^{2-})$.

4:  Oxide,sulphate and sulphide-database
    (MeS, MeO, MeSO$_4$, where Me = Al, C, Ce, Co, Cr, Cu, Fe, Mn, Mo, Nb, Ni, Si, Ti, V, W).
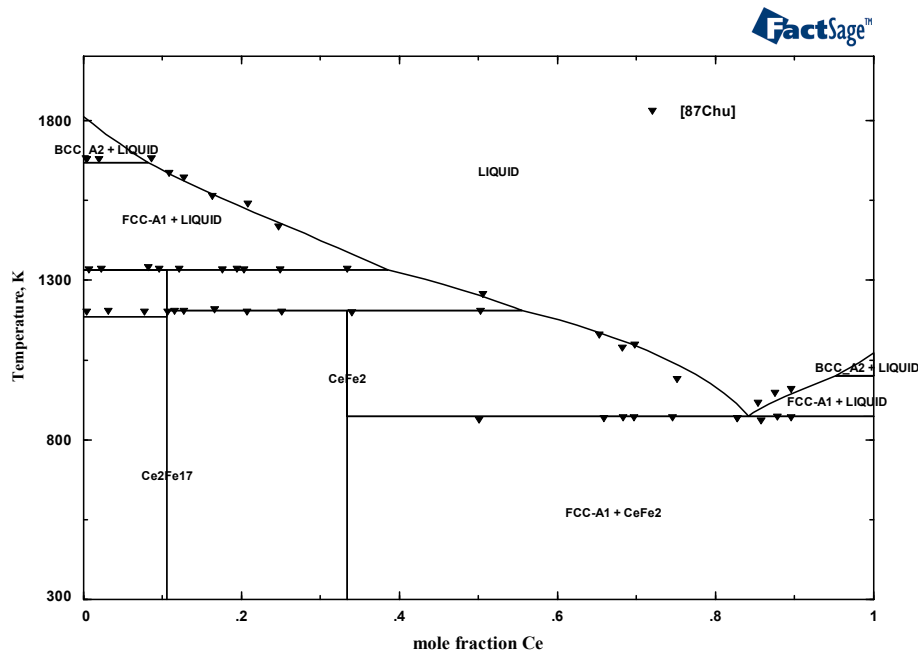


*Figure 2.2.1. The assessed phase diagram for Fe-Ce.*

A significant number of the binary and ternary sub-systems of Fe- or Ni-based alloys have already been thermodynamically assessed. Many of these have been compiled in large databases, for example by SGTE [3]. Several new thermodynamic evaluations, for example for the Ce-Fe, Co-Cr-Fe, Co-Cr-Ni, and Al-Fe-Mn-Si systems have been established in this work using all available experimental data. The calculated phase diagrams and the invariant reactions are in good agreement with experimental results. For example, the Ce-Fe binary system displays two near-stoichiometric phases which form peri-

tectically. Because of the very small homogeneity ranges they were modelled as stoichiometric phases using the formulas $CeFe_2$ and $Ce_2Fe_{17}$ approximating the experimentally determined compositions. The experimentally determined phase diagram by Chuang, Wu and Shao [4] is satisfactorily reproduced by the calculations as shown in Figure 2.2.1.

The calculated activity coefficients of Ce in molten Fe are presented in Figure 2.2.2, where comparison is made with the experimental data due to Teplizkij et al. [5] and Fisher et al. [6]. The agreement is very good, especially when it is kept in mind that the same data also produce a good agreement for the phase diagram.
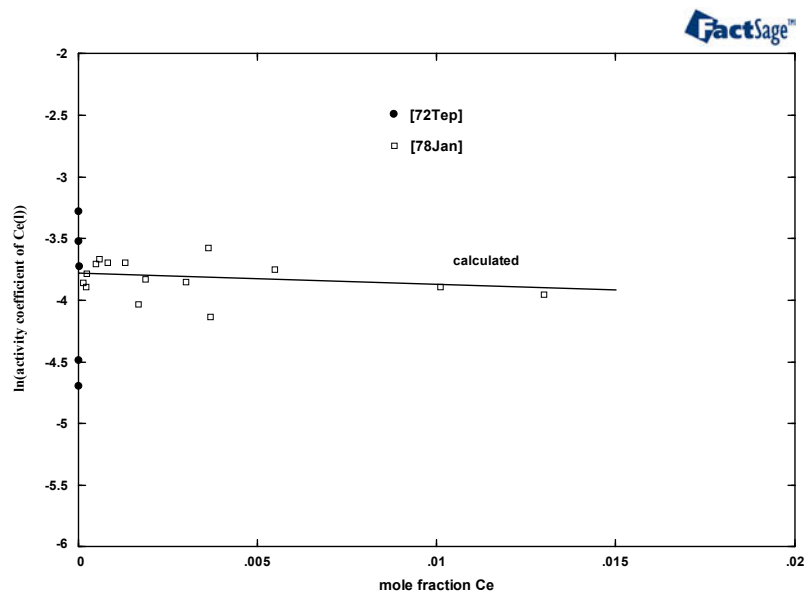


*Figure 2.2.2.  Calculated activity coefficients of Ce in molten Fe.*

As another example, the results on the Co-Cr-Fe system are shown. The isothermal section in the Co-Cr-Fe system at 1373 K has been investigated by two different authors [7, 8]. Figure 2.2.3 shows the calculated isothermal section compared with these experimental data. The comparison between the calculations and experimental determined phase diagrams is good.
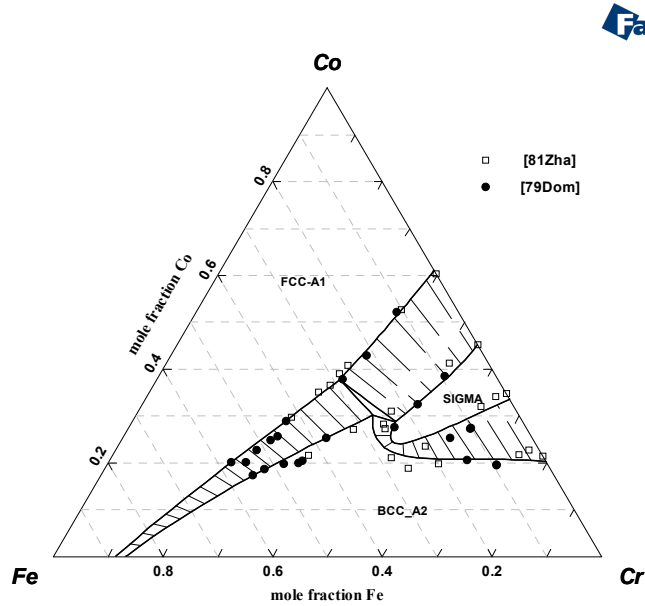
*Figure 2.2.3. Isothermal section in the Co-Cr-Fe system at 1373 K.*

The database created especially for Fe-based alloys contains the thermodynamic data for all the phases significant in commercial alloys, such as carbides $M_{23}C_6$, $M_3C_2$, $M_6C$, $M_7C_3$, MC-eta, nitrides, silicides, Laves phases, P, R, mue and sigma phases.

The salt-database comprises 21 components:

$KCl-ZnCl_2-FeCl_2-FeCl_3-CrCl_2-CrCl_3-NiCl_2-K_2SO_4-ZnSO_4-FeSO_4-Fe_2(SO_4)_3-CrSO_4-Cr_2(SO_4)_3-NiSO_4-K_2CrO_4-ZnCrO_4-FeCrO_4-Fe_2(CrO_4)_3-CrCrO_4-Cr_2(CrO_4)_3-NiCrO_4$.
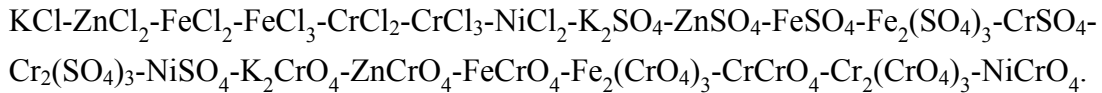
The thermodynamic data for the stoichiometric chlorides as well as some sulphates and chromates could be taken from the FACT database [9]. However, there were also a number of thermodynamic datasets missing, especially for the sulphates and chromates for which work was carried out in this project. The relevant species are listed in Table 2.2.1. Le Van's method was used to estimate the enthalpy of formation of the compounds, Mill's method was employed to estimate the entropy of formation and the method by Kubaschewski and Ünal was used for the estimation of the heat capacity equation. All estimation methods are described in Materials Thermochemistry 6th Edition [10]. The binary systems $KCl-NiCl_2$, $KCl-ZnCl_2$, $KCl-K_2SO_4$, $K_2SO_4-K_2CrO_4$ were evaluated in this work using available experimental data.

The $KCl-NiCl_2$ system displays one near-stoichiometric compound ($KCl.NiCl_2$) that melts peritectically at ~931 K. Figure 2.2.4 shows the calculated and experimentally determined phase diagrams (Tanaka and Katayama [11]), the agreement is good.

24

*Table 2.2.1. Chromates and Sulphates contained in the Salt database.*

| Compound | Solid state | Liquid state |
|---|---|---|
| $K_2SO_4$ | FACT | FACT |
| $K_2CrO_4$ | FACT | FACT |
| $ZnSO_4$ | FACT | estimated |
| $ZnCrO_4$ | estimated | estimated |
| $NiSO_4$ | FACT | estimated |
| $NiCrO_4$ | estimated | estimated |
| $FeSO_4$ | FACT | estimated |
| $FeCrO_4$ | estimated | estimated |
| $Fe_2(SO_4)_3$ | FACT | estimated |
| $Fe_2(CrO_4)_3$ | estimated | estimated |
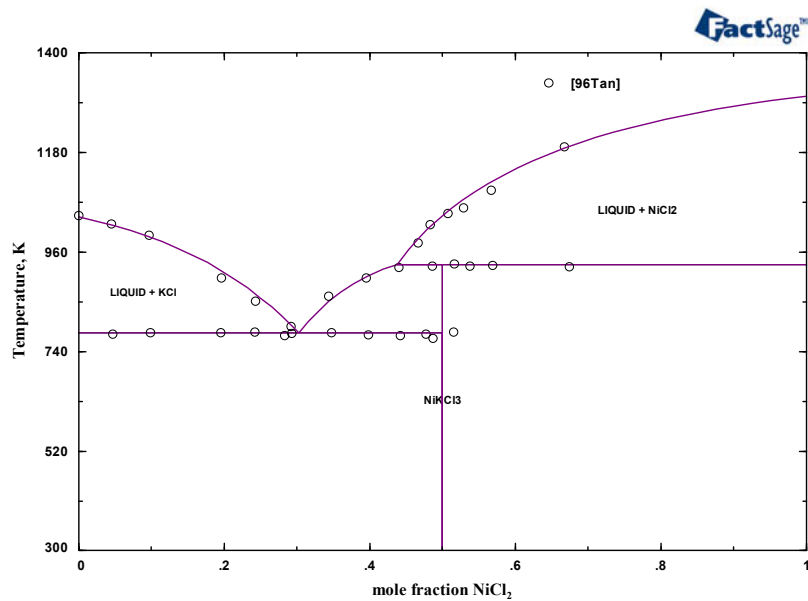


*Figure 2.2.4. Calculated and experimental determined [11] KCl-NiCl$_2$ phase diagrams.*

The system KCl-ZnCl$_2$ was investigated by different authors [12, 13] with the results being in good agreement. There are three near-stoichiometric compounds ($2ZnCl_2.KCl$, $2ZnCl_2.3KCl$ and $ZnCl_2.2KCl$), two of them decompose congruently. The calculated phase diagram is presented in Figure 2.2.5 and the experimental data investigated by Duke and Fleming [12] are shown in Figure 2.2.6, the agreement is satisfactory. The calculated activities of ZnCl$_2$ in the liquid phase for different amounts of ZnCl$_2$ are

compared in Figure 2.2.7 with experimental values carried out by Robertson and Kucharski [13]. Here too the agreement is satisfactory.
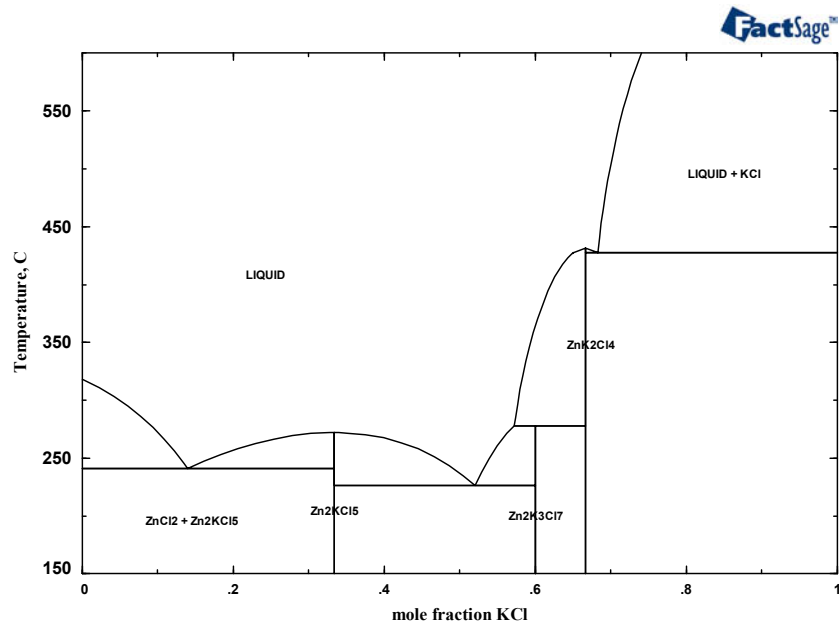


*Figure 2.2.5. Calculated KCl-ZnCl$_2$ phase diagram.*
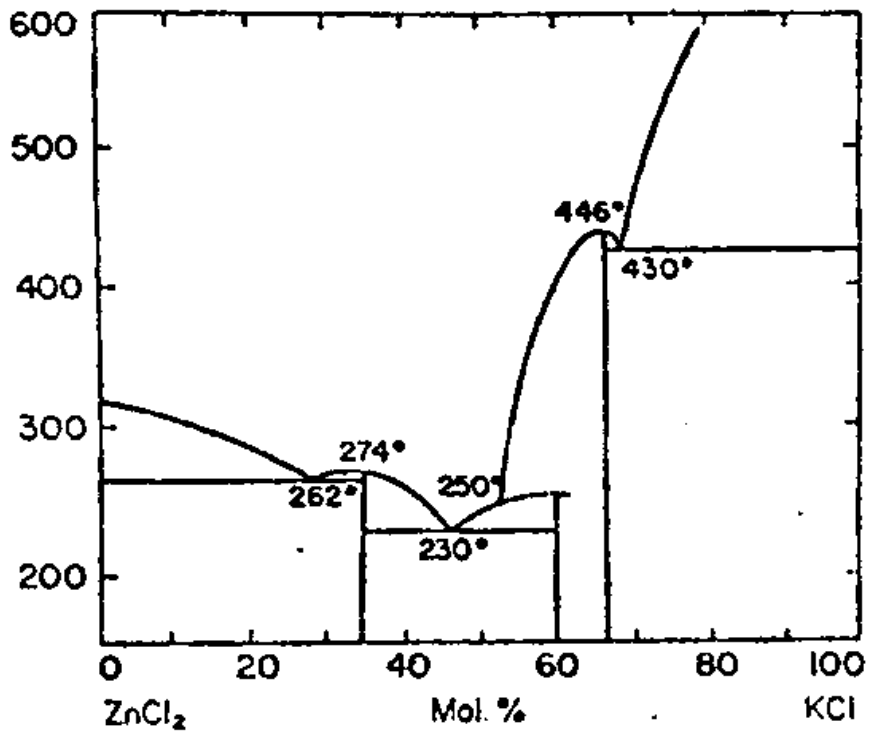


*Figure 2.2.6. Experimental KCl-ZnCl$_2$ phase diagram [13].*
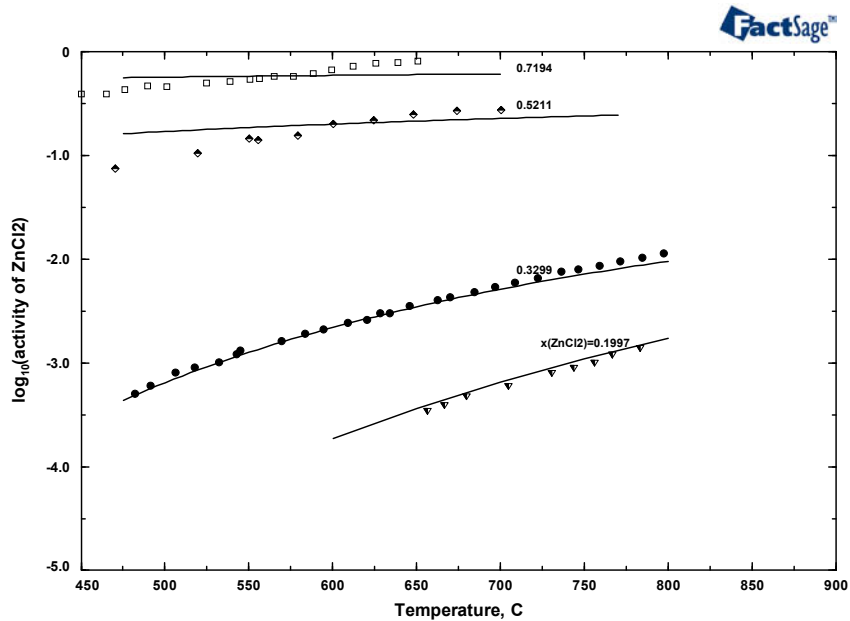
*Figure 2.2.7. Calculated and experimental [13] activities in the KCl-ZnCl₂ system.*

The Oxide sub-database was created using the FACT Pure Substance database [9] and contains the thermodynamic data for all solid oxides, sulphates and sulphides of the elements contained in the databases for Fe-based and Ni-based alloys. In most cases these are stoichiometric solid compounds. However, for Fe-spinel, corundum and wustite (= MeO) solution phase data are available.

## 2.3 Results of the ITDS calculations

In the following chapter results are shown from calculations which employ the databases generated for the OptiCorr project and which are described above in the chapters on one- and two-dimensional phase mappings. The Equilib and the Phase Diagram module of FactSage have been used to obtain these diagrams. They relate to experimental conditions or sample compositions as used in the project.

### 2.3.1 One-dimensional phase mappings

The one dimensional mappings relate to three different kinds of cases: (1) gas equilibria, (2) metal alloy equilibria, and (3) gas metal equilibria.

In the first category plots have been generated which show the thermochemical behaviour of gases used in the corrosion experiments. It should however be noted that instead

of nitrogen as used in the experiments Ar(gon) was used in the calculations since it was found that nitrogen could be considered as inert in all experimental investigations.

In the second category the thermodynamically stable phases for all alloys investigated in the project have been calculated and plotted as functions of temperature. It should be noted that these plots, especially for the austenitic steels may have a certain degree of arbitrariness about them since equilibrium is assumed also for temperatures for which it is well known from practice that frozen-in states from higher temperatures prevail. For the present calculations this fact has not been taken into consideration.

In the third category the phases found for equilibrated gas-alloy systems with certain amounts of corrosive gas species are shown. It is clear that such equilibrium diagrams cannot give the full picture of the real cases since not the entire gas phase and also not the entire alloy amount will participate in the reactions. It is therefore necessary to run case studies with varying ratios of gas to metal in the calculations in order to be able to give limits of the behaviour of the real cases.

A selection of diagrams as described above is shown in Figures 2.3.1 to 2.3.4.
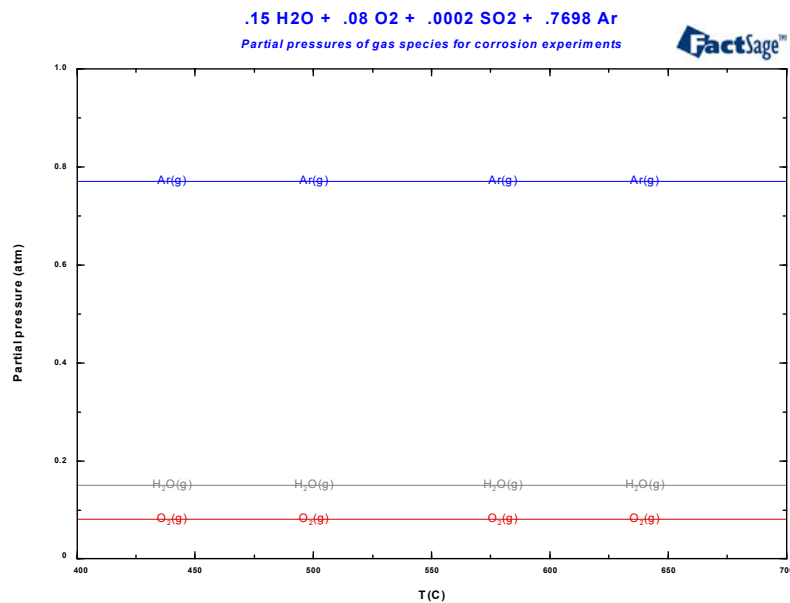


*Figure 2.3.1. The $SO_2$ containing corrosion gas, major constituents.*
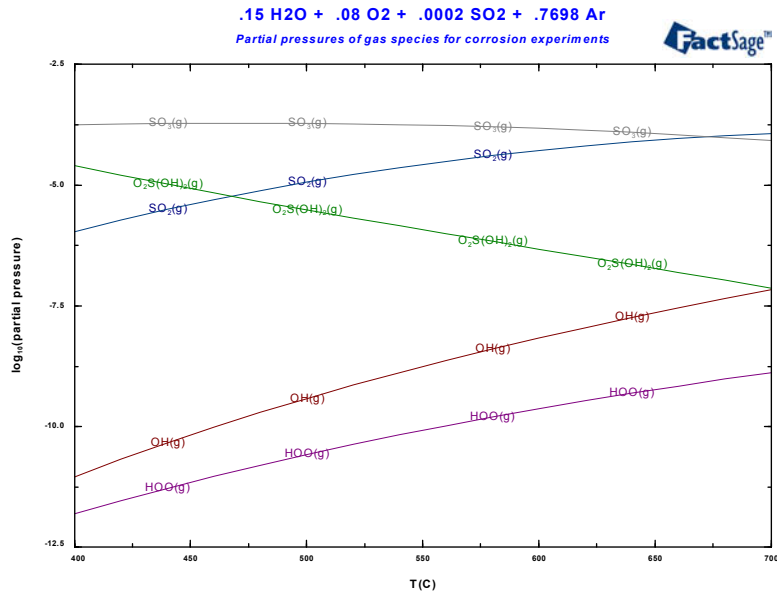
*Figure 2.3.2.  The SO₂ containing corrosion gas, minor constituents.*
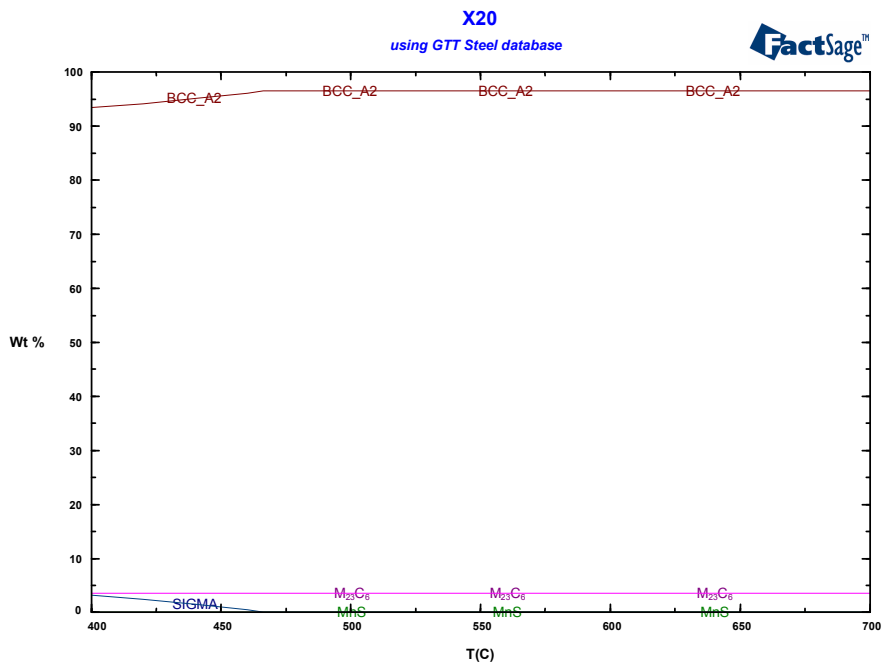


*Figure 2.3.3. Alloy X20, phase distribution versus T.*
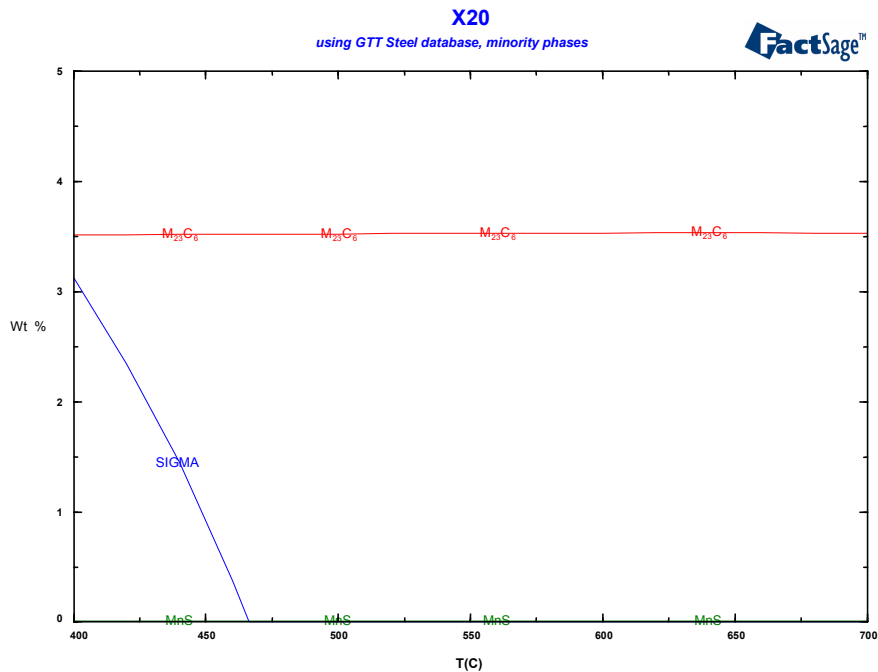
*Figure 2.3.4. Alloy X20, minority phases.*

## 2.3.2 Two-dimensional phase mappings (phase diagrams)

Two-dimensional phase mappings, i.e. classical phase diagrams have been calculated for a multitude of cases pertaining to the OptiCorr project.

On the one hand phase diagrams for the alloy systems have been used in order to check on the quality of the new thermochemical data (see chapter 2.2 above, data assessment). On the other, phase diagrams have also been employed to derive the database for the salt subsystem. Especially the ternary isothermal sections of the $FeCl_x$-KCl-ZnCl2, $CrCl_x$-KCl-ZnCl$_2$ and $NiCl_2$-KCl-ZnCl$_2$ with fixed valency of Fe and Cr respectively (i.e. 2+ or 3+ exclusively) could be used to obtain a much better although qualitative understanding of the differences in the salt corrosion experiments on the pure metal components.

Finally potential diagrams with temperature and partial pressures of oxygen as well as sulphur (or SO$_2$) and chlorine have been generated for various metal subsystems, i.e. alloys, in order to understand the phase formation of the oxides and salts at the surface of the alloys. The diagrams show clearly which phase sequences must be found in reality if for example the oxygen potential is raised from the low values that prevail inside a metal up to the conditions near the surface where the partial pressure of oxygen comes close to the value in the gas phase. An example correlation of this kind is given the chapter Introduction.

A selection of calculated diagrams using the data from the project in the Phase Diagram module of FactSage is shown in Figures 2.3.5–2.3.9.
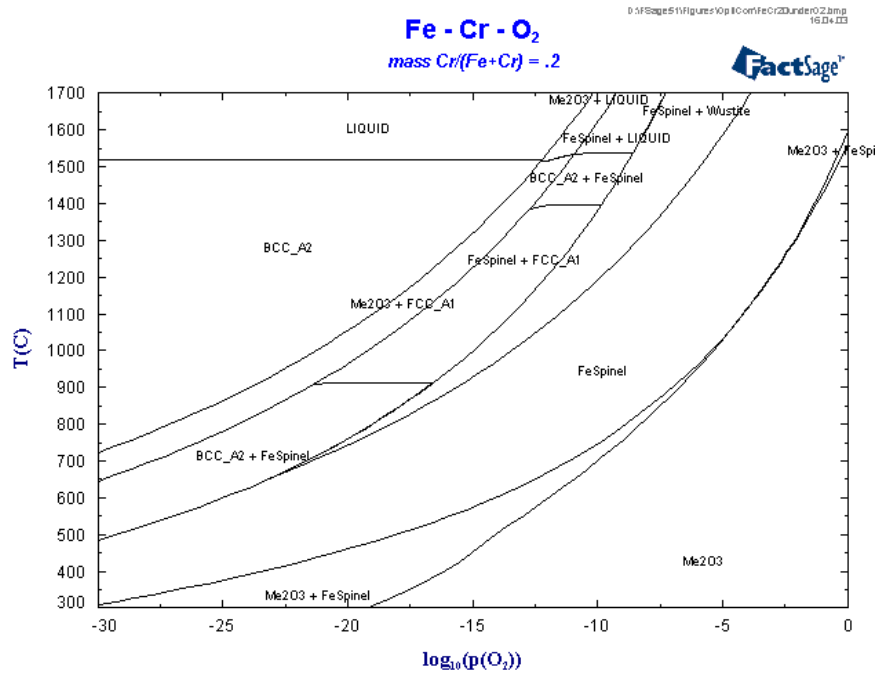


*Figure 2.3.5. The Fe-Cr-O system T-versus log P(O₂). Note that the liquid oxide phase is not part of the present database.*
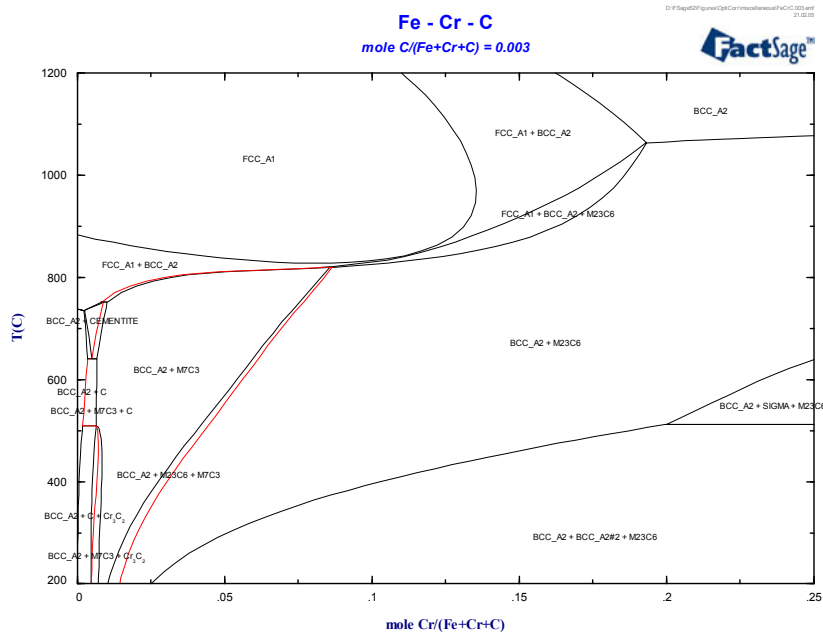


*Figure 2.3.6. The Fe-Cr-C system, T-versus x(Cr) with x(C) = .003 with the stability range of the $M_7C_3$ phase marked.*
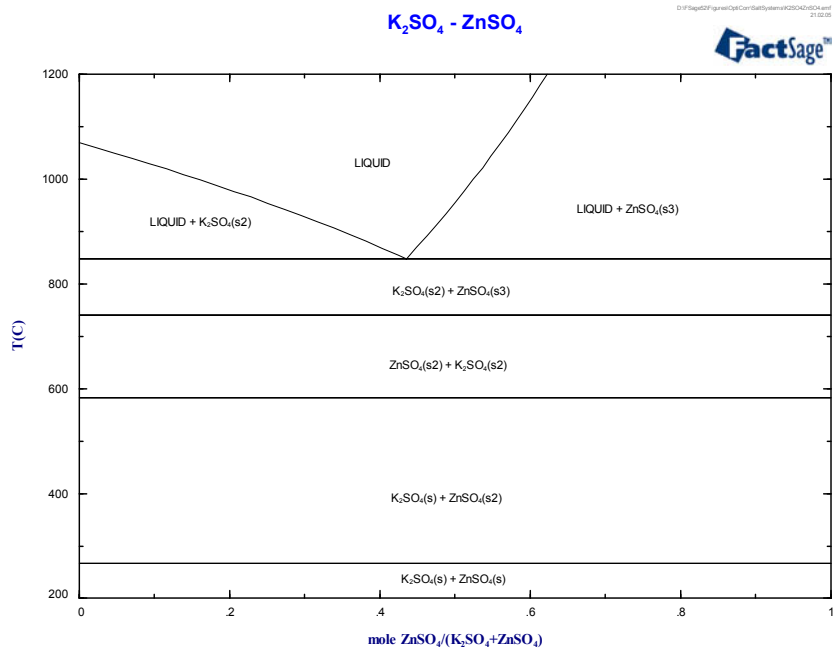
*Figure 2.3.7. The K₂SO₄-ZnSO₄ system, T-versus x(ZnSO₄).*
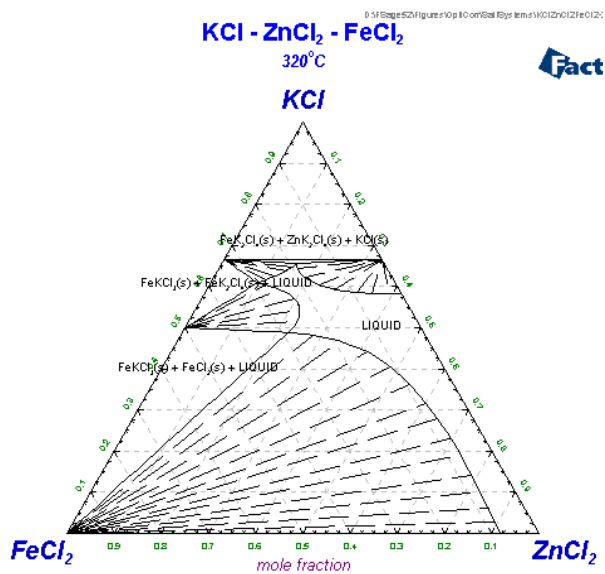


*Figure 2.3.8. The FeCl₂-KCl-ZnCl₂ system, ternary isotherm T = 320°C.*

32
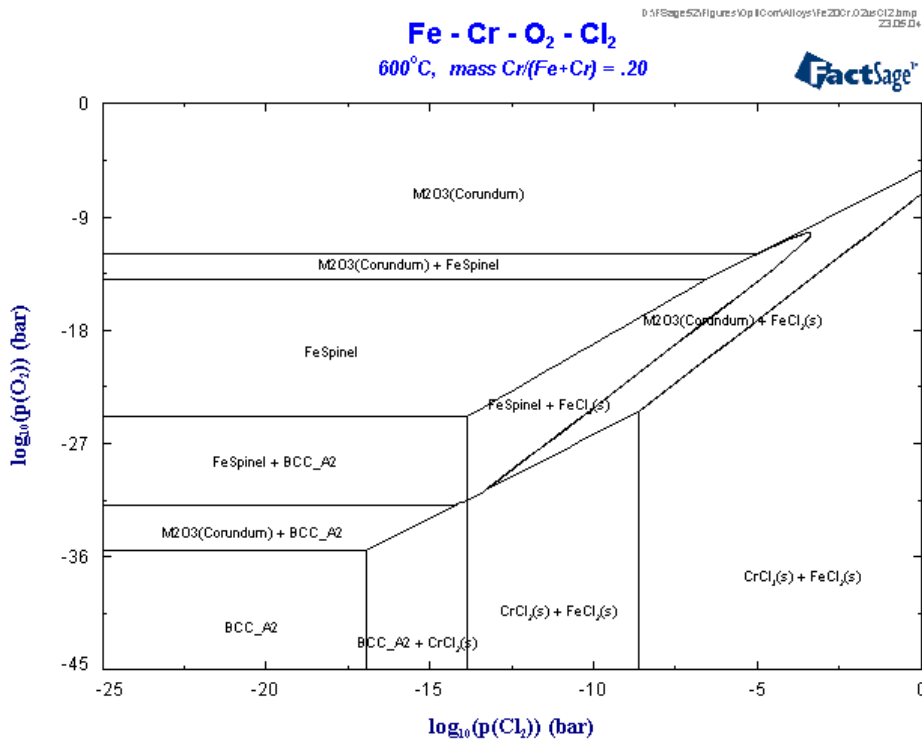
*Figure 2.3.9. The Fe-Cr-$O_2$-$Cl_2$ system, T constant, log $P(Cl_2)$-versus log $P(O_2)$, x(Cr) = .2.*

## 2.4 References

[1]   K. Hack, The SGTE Case Book – Thermodynamics at work, The Institute of Metals, 1996.

[2]   C.W. Bale, P. Chartrand, S.A. Degterov, G. Eriksson, K. Hack, R. Ben Mahfoud, J. Melancon, A.D. Pelton and S. Petersen, CALPHAD, 26(2) (2002), pp. 189–228.

[3]   SGTE Pure Substance Database, Edition 2002 and Solution database, Edition 2004.

[4]   Y.C. Chuang, C.H. Wu and Z.B. Shao, J. Less-Commn Met., 136 (1987), pp. 147–153.

[5]   E.W. Teplizkij and L.P. Wladimirow, Zhurnal fis. chim., 46 (1972), pp. 762–763.

[6]   W.A. Fisher and D. Janke, Arch. Eisenhüttenwesen, 49 (1978), pp. 425–430.

[7]   J. Zhangpeng and B. Jansson, TRITA-MAC-0189, Royal Institute of Technology, Stockholm, May 1981.

[8]   M. Dombre, O.S. Campos, N. Valignat, C. Allibert, C. Bernard and J. Driole, J. Less-Comon Met., 66 (1979), 1.

[9]   FACT Database, Edition 2002.

[10] O. Kubaschweski, C.B. Alcock and P.J. Spencer, Materials Thermo-Chemistry, 6th Edition, Pergamon Press, 1993.

[11] A. Tanaka and H.G. Katayama, Private Communication, 1996.

[12] F.R. Duke and R.A.J. Fleming, J. Electrochem. Soc., 104 (1957), pp. 774–785.

[13] R.J. Robertson and A.S. Kucharski, Can. J. Chem, 51 (1973), pp. 3114–3122.

# 3. Modelling tools

(Introduction by K. Hack – GTT Technologies: individual sections by V.B. Trindade,
U. Krupp & H.-J. Christ – University Siegen; K. Penttilä – VTT Processes;
M. Spiegel & A. Ruh – Max Planck Institute)

As a basis for all process modelling activities in the OptiCorr project the thermodynamic programmer's library ChemApp[1] has been used. ChemApp presents the engine of the Equilib module of FactSage in the form of a set of programmable interface routines between the user's own main program and the actual Gibbs energy minimisation code that is called in the background. The general concept of ChemApp is shown in Figure 3.1. Thus, rigorous Gibbs energy thermodynamics can be employed in a multitude of calculational environments. ChemApp is a commercial product available for general use from GTT-Technologies.
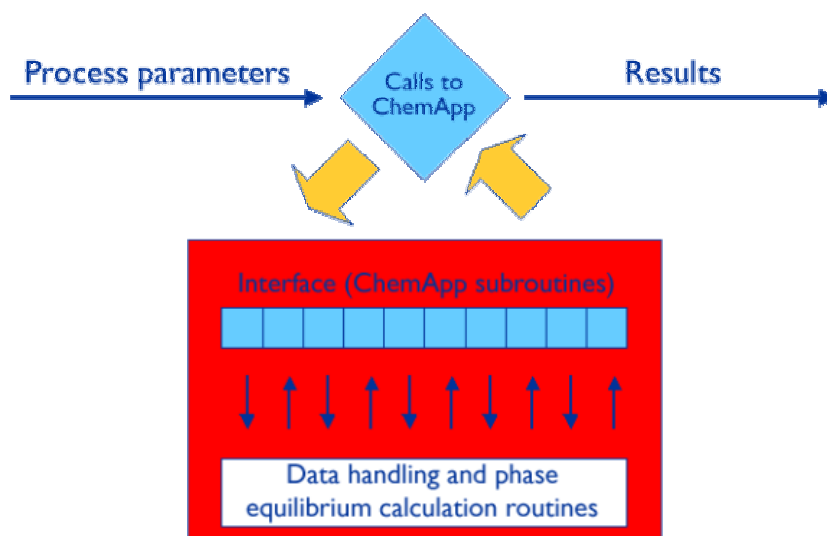


*Figure 3.1. The general principle of the use of ChemApp.*

ChemApp has been integrated as a so-called add-in into EXCEL®[2]. This add-in, named ChemSheet[3] has been the basis of the Liquid-Salt corrosion model on the one hand (see chapter 3.2) and has on the other been employed for setting up a simple precipitation model that permits investigation of the thermochemical behaviour of a combustion gas

---

[1] G. Eriksson, K. Hack and S. Petersen, Werkstoffwoche '96, Symposium 8, Simulation, Modellierung, Informationssysteme Herausgeber: J. Hirsch, DGM Informationsgesellschaft Verlag, 1997.

[2] Microsoft Corporation.

[3] P. Koukkari, K. Pentillä, K. Hack and S. Petersen, Microstructure, Mechanical Properties and Processes Computer Simulation and modelling, EUROMAT 99 – Volume 3 (2000) 323, Wiley-VCH, Weinheim.

that carries a certain aerosol freight in terms of mineral and salt dusts. (see chapter 3.3). ChemSheet is a commercial product available for general use from GTT-Technologies.

ChemApp has also been employed in the framework of a parallel computing package in MatLab™ [4] in order to handle the diffusion model that describes the inward oxide layer formation under oxygen carrying and nitrogen atmosphere (see chapter 3.1).

## 3.1 InCorr: Software for simulation of internal/inwards corrosion processes at high-temperature

(V.B. Trindade, U. Krupp & H.-J. Christ – University Siegen)

For the simulation of internal/inwards corrosion processes at high-temperatures a special tool has been developed which makes use of explicit diffusional kinetics on the one hand and the concept of local equilibrium thermodynamics on the other. For this purpose a link has been established between the numerical environment of MATLAB and the thermochemical library ChemApp.

### 3.1.1 Introduction

For alloys used in high-temperature corrosive atmospheres, the ability to form a protective scale with high density, high stability, good adhesion and low growth rate on the surface of a component is very important. Generally, $Al_2O_3$, $SiO_2$ and $Cr_2O_3$ are expected to protect materials against serious high-temperature degradation. For most materials the formation of a continuous protective scale is not possible due to an insufficient content of protective-oxide-forming elements. If no protective scales are present on the surface, or if cracks or other types of defects allow rapid transport of corrosive species like oxygen, nitrogen, carbon or sulphur through the scale, internal corrosion becomes possible, which decreases the lifetime of components substantially. A reasonable prediction of the service life of structures or equipments operating at high-temperatures in aggressive atmospheres requires a full understanding of the degradation mechanisms of the material due to internal corrosion. The software *InCorr* is an useful tool to simulate such degradation processes under complex conditions and hence, to contribute to new mechanism-based life-prediction methods. The overall objective of this software is to simulate high-temperature corrosion processes under near-service conditions, which requires both, a thermodynamic model to predict phase stabilities for

---

[4] MatLab is a product of Mathworks.

given conditions and a mathematical description of the process kinetics, i.e., solid state diffusion. In ***InCorr*** the thermodynamic program library ChemApp is integrated into a numerical finite-difference diffusion calculation to treat internal oxidation, nitridation, carburisation and sulfidation processes in various commercial alloys. The model is capable to simulate multi-phase internal corrosion processes controlled by solid-state diffusion into the bulk metal as well as intergranular corrosion occurring in polycrystalline alloys due to fast inward transport of the corrosive species along the grain boundaries of the substrate.

In the framework of the EU project OPTICORR the applicability of ***InCorr*** has been extended from pure internal corrosion phenomena, like internal oxidation, carburization and nitridation, to the formation of multi-phase superficial oxide scales, which are formed, e.g. during high-temperature exposure of boiler steels [1].


### 3.1.2  Physical modelling


#### 3.1.2.1  Internal corrosion


A theoretical description of internal corrosion process can be obtained by applying Carl Wagner's classical theory of internal oxidation [2]. When the concentration of a solute B in an alloy AB is lower than a critical value required for transition to superficial scale formation of the nitride, oxide, or carbide, internal precipitation of corrosion products takes place. Assuming a parabolic rate law for the penetration depth $\xi$ and applying Fick´s second law to the diffusion fluxes of solute B and the corrosive species O to the reaction front, kinetics of internal corrosion can be expressed by means of a simple parabolic equation:

$$\xi^2 = \frac{D_O c_O^s}{\nu c_B^0} t \, ,$$  (3.1.1)

where $\xi$ is the penetration depth of internal corrosion products, $c_O^s$ the concentration of the corrosive species at the surface, and $c_B^0$ the initial concentration of the reacting alloying element B. It is assumed that the diffusion coefficient $D_O$ of the corrosive species is substantially higher than the one of the reacting alloying element $D_B$.

For simple systems, Wagner's theory can be applied to predict the penetration depth of internal corrosion as well as the concentration profiles of the solute B and the corrosive species O according to the equations 3.1.2 and 3.1.3 which can be derived from Ficks`s second law:

$$c_O(x,t) = c_O^s \left[ \frac{\operatorname{erfc} \dfrac{x}{2\sqrt{D_O t}}}{\operatorname{erf} \gamma} \right],$$

(3.1.2)

$$c_B(x,t) = c_B^s \left[ \frac{\operatorname{erf} \dfrac{x}{2\sqrt{D_B t}}}{\operatorname{erf} \gamma \sqrt{\Phi}} \right],$$

(3.1.3)

where $\Phi$ is the ratio between the diffusion coefficients of the corrosive species and the solute metal B ($\Phi = D_O/D_B$). The constant $\gamma$ is given by equation 3.1.4:

$$\gamma = \sqrt{\frac{c_O^s}{2 \nu c_B^0}} .$$

(3.1.4)

Figure 3.1.1 shows a schematic representation of the concentration profiles of the species involved in the corrosion process according to Wagner's theory.
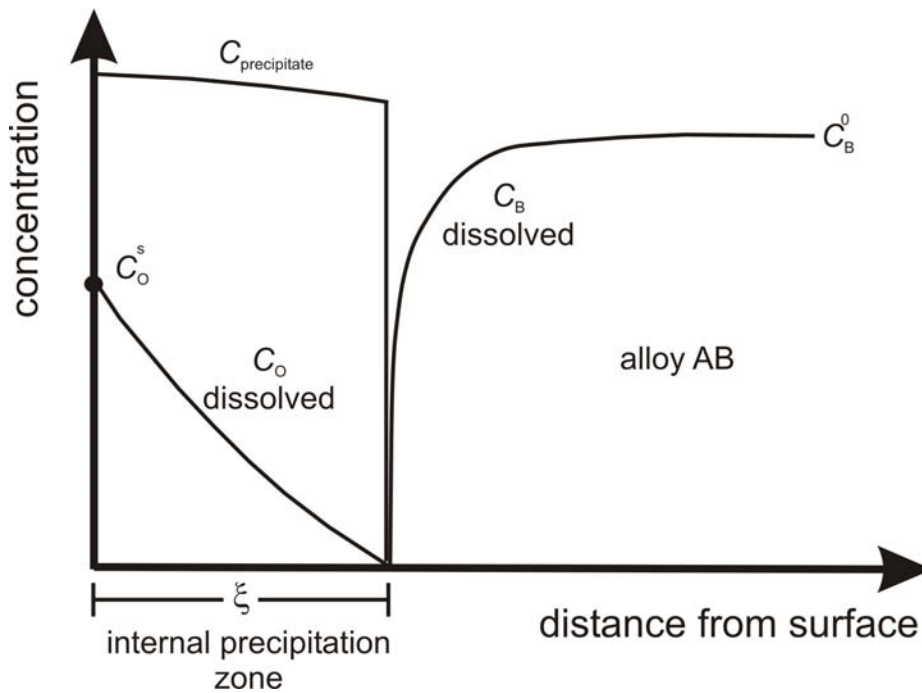


*Figure 3.1.1. Schematic representation of the concentration profiles during internal corrosion.*

A treatment of internal-corrosion problems that involve more than one precipitating species, compounds of moderate stability, high diffusivities of the metallic elements or time-dependent changes in the test conditions, e.g. temperature or interface concentrations, is not possible by applying equations 3.1.1 to 3.1.3. To simulate such systems the application of a numerical method to the diffusion differential equations and the thermodynamics of the system is required.


### 3.1.2.2  Oxidation of steels

The distribution and structure of grain boundaries play an important role for the kinetics of many high-temperature degradation processes since the transport of matter along interfaces is by orders of magnitude faster than throughout the bulk [1]. Therefore, reducing the grain size, i.e., increasing the fraction of fast diffusion paths, may have a detrimental effect, as it is known for the creep behaviour of metals and alloys [3]. On the other hand, the high-temperature oxidation resistance of CrNi 18 8-type stainless steels, which are widely used for superheater tubes in power plants, can benefit from smaller grain sizes. As reported by Teranishi et al. [4] and Trindade et al. [5], the formation of protective, Cr-rich oxides scales ($FeCr_2O_4$ and/or $Cr_2O_3$) is promoted by the fast outward flux of Cr along the substrate grain boundaries. A similar effect can be used by providing nanocrystalline surface layers on Ni-based superalloys. Wang and Young [6] have shown that an increase in the fraction of grain boundaries can decrease the critical Al concentration required for the establishment of a superficial $Al_2O_3$ scale on a material that usually forms a $Cr_2O_3$ scale.

It has been shown [5] that in the case of low-Cr steels, typically used for cooling applications in power generation up to temperatures of approximately 550°C, the beneficial effect of grain refinement disappears. Here, the grain boundaries seem to act as fast-diffusion paths for the oxygen transport into the substrate. As shown in Figure 3.1.2 the parabolic rate growth obviously decreases as the alloy grain size increases. Furthermore, the oxidation kinetics decreases as the Cr content increases for alloys with similar grain size.
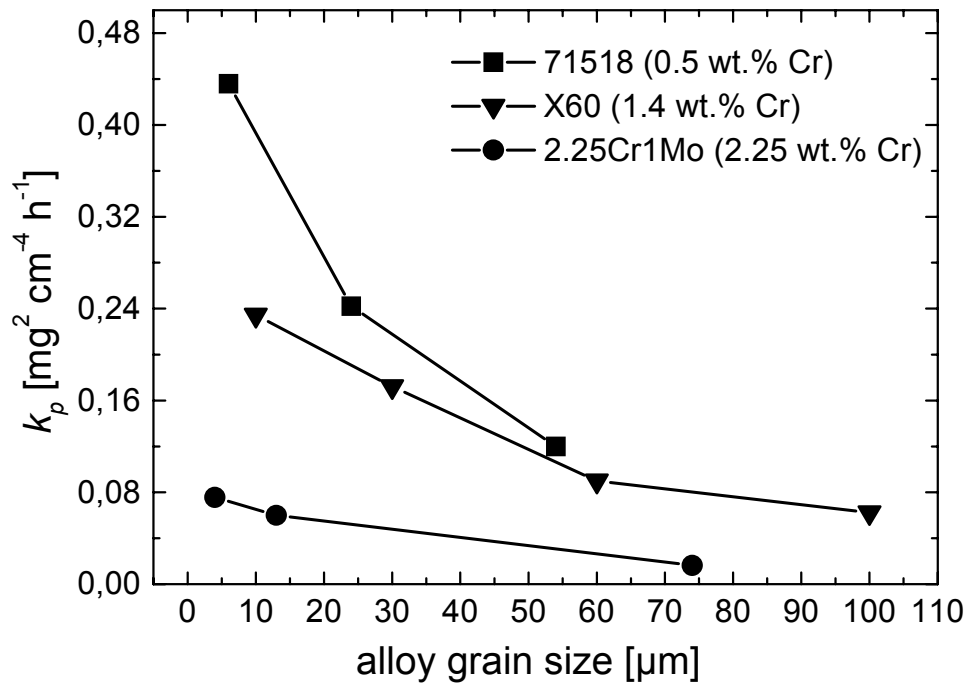
*Figure 3.1.2. Parabolic rate constant $k_p$ of three low-alloy steels oxidized in laboratory air at 550°C for 72 h [5].*

From inert-gold-marker experiments at 550°C (see Figure 3.1.3a) one knows that oxide scale growth occurs by both, outward Fe diffusion leading to the formation of hematite ($Fe_2O_3$, outermost) and magnetite ($Fe_3O_4$) and inward O transport leading to $(Fe,Cr)_3O_4$ formation. As a consequence of the Cr content in the substrate, a gradient in the Cr concentrations establishes reaching from the outer/inner scale interface ($c_{Cr} = 0$) to the inner-scale/substrate interface, where the Cr concentration corresponds to the sole formation of the spinel phase $FeCr_2O_4$. This is in agreement with the thermodynamic prediction using a specific data set developed for these kinds of alloys [7]. The inward oxide growth itself is governed by an intergranular oxidation mechanism (Figure 3.1.3b) that can be described as follows: oxygen atoms that have reached the scale/substrate interface by short-circuit diffusion through cracks, pores (see [8, 9]) or by O anion transport penetrate into the substrate along the grain boundaries leading to the formation of $Cr_2O_3$ and, consequently, $FeCr_2O_4$. Progress of the scale/substrate interface occurs as soon as the bulk of the grains are oxidized completely.
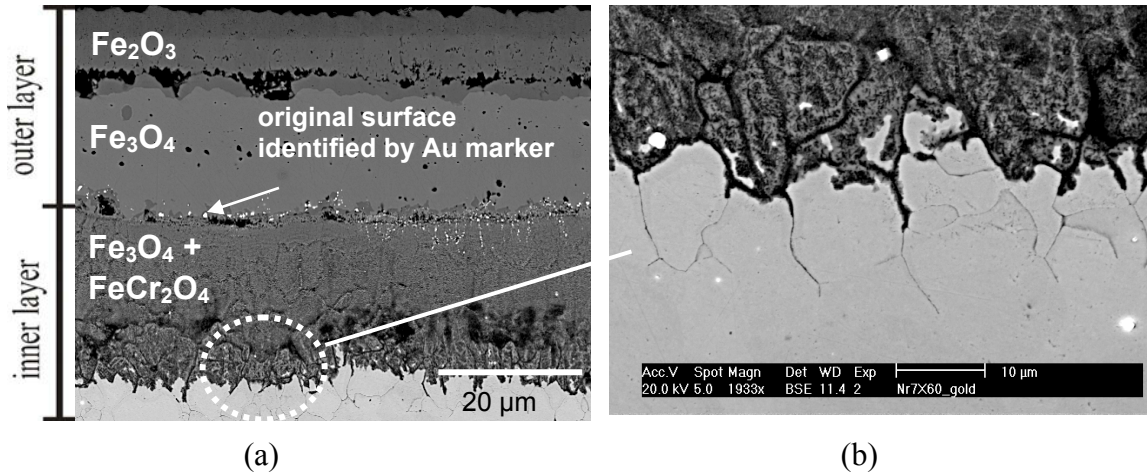
*Figure 3.1.3. (a) Oxide scale on a low alloy steel (grade X60) after expo0sure at 550°C to laboratory air for 72 h and (b) detail, showing the grain boundary attack underneath the interface inner scale/metal [5].*

### 3.1.3  Mathematical modelling and programming

Recently, a numerical model for the diffusive transport processes based on the finite-difference approach has been developed, which distinguishes between fast grain-boundary diffusion and bulk diffusion [11]. Qualitatively, it is capable to predict the relationship between substrate grain size and inward oxide growth kinetics or internal precipitation. Together with the powerful thermodynamic tool ChemApp in combination with a data set for the Fe-Cr-O system (see chapter 2) the mechanism-based simulation of the overall oxidation process of low-Cr steels became possible. In this section, the mathematical background of the model will be described with emphasis on the inward oxide scale formation on low-Cr steels.

Generally, the generic driving force of high temperature corrosion processes can be separated into (i) transport mechanisms, i.e., solid-state diffusion in most cases, and (ii) thermodynamics of chemical reactions. The commonly used, phenomenological way to treat diffusion processes is the application of a second-order partial differential equation (Fick's 2nd law) formulating a relationship between the derivative of the concentration of a species $c$ after the time $t$ and its gradient by means of the location- and temperature-dependent diffusion coefficient $D$, which represents the jump frequency of the species within a substrate.

$$\frac{\partial c}{\partial t} = D \frac{\partial^2 c}{\partial x^2}$$

(3.1.5)

This equation can be rewritten in a simplified form for two-dimensional diffusion problems by neglecting any cross terms in the following form:

$$\frac{\partial c}{\partial t} = D_x \frac{\partial^2 c}{\partial x^2} + D_y \frac{\partial^2 c}{\partial y^2},$$

(3.1.6)

where $D_x$ and $D_y$ are the diffusion coefficients in $x$ and $y$ direction, respectively. Through differential quotients according to the Crank-Nicolson finite-difference scheme [10], here represented in a simplified one-dimensional form:

$$\frac{\partial c}{\partial t} \approx \frac{c(x, t + \Delta t) - c(x, t)}{\Delta t}$$

(3.1.7)

$$\frac{\partial^2 c}{\partial x^2} \approx \frac{D_x}{2} \left( \frac{c(x - \Delta x, t + \Delta t) - 2c(x, t + \Delta t) + c(x + \Delta x, t + \Delta t)}{\Delta x^2} \right.$$
$$\left. + \frac{c(x - \Delta x, t) - 2c(x, t) + c(x + \Delta x, t)}{\Delta x^2} \right)$$

(3.1.8)

By substituting the second derivatives in equation (3.1.6) by the corresponding difference quotients of the concentrations at the locations $x$-$\Delta x$, $x$, and $x$+$\Delta x$, as well as at $y$-$\Delta y$, $y$, and $y$+$\Delta y$, respectively, at the times $t$ and $t$+$\Delta t$, one obtains the implicit Crank-Nicolson scheme of the finite-difference approach for two-dimensional diffusion.

$$\frac{c(x, y, t + \Delta t) - c(x, y, t)}{\Delta t} = \frac{D_x(x, y)}{2} \cdot \frac{c(x - \Delta x, y, t) - 2c(x, y, t) + c(x + \Delta x, y, t)}{\Delta x_l(x, y) \cdot \Delta x_r(x, y)}$$
$$+ \frac{D_x(x, y)}{2} \cdot \frac{c(x - \Delta x, y, t + \Delta t) - 2c(x, y, t + \Delta t) + c(x + \Delta x, y, t + \Delta t)}{\Delta x_l(x, y) \cdot \Delta x_r(x, y)}$$
$$+ \frac{D_y(x, y)}{2} \cdot \frac{c(x, y - \Delta y, t) - 2c(x, y, t) + c(x, y + \Delta y, t)}{\Delta y_l(x, y) \cdot \Delta y_r(x, y)}$$
$$+ \frac{D_y(x, y)}{2} \cdot \frac{c(x, y - \Delta y, t + \Delta t) - 2c(x, y, t + \Delta t) + c(x, y + \Delta y, t + \Delta t)}{\Delta y_l(x, y) \cdot \Delta y_r(x, y)}$$

(3.1.9)

The concept of the finite-difference equation (3.1.9) with locations of variable step widths $\Delta x_l$ and $\Delta x_r$ at the left- and right-hand side of $x$ and $\Delta y_l$ and $\Delta y_r$ at the left- and right-hand side of $y$ is illustrated schematically in Figure 3.1.4.
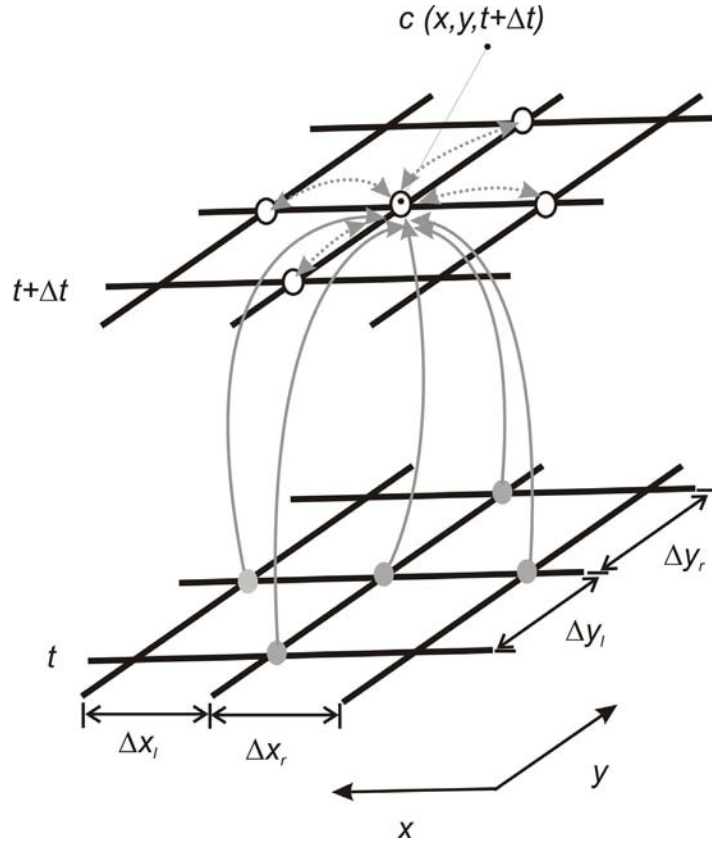
*Figure 3.1.4. Schematic representation of the concentration data points $\vec{c}(t + \Delta t)$ in a two-dimensional finite-difference mesh using the implicit Crank-Nicolson approach.*

If applied to an area of the size $n \cdot \Delta x \cdot m \cdot \Delta y$, equation (3.1.9) can be rewritten as a matrix equation, valid for the concentrations $c(x,y)$ at each location, which can be expressed as concentration vectors $\vec{c}(t)$ and $\vec{c}(t + \Delta t)$ for successive time steps $t$ and $t+\Delta t$. Since the right-hand side of equation (3.1.9) consists of elements of the concentration vectors at different locations according to Figure 3.1.4, it can be expressed by using the complete concentration vectors $\vec{c}(t)$ and $\vec{c}(t + \Delta t)$ multiplied with the corresponding matrices $\mathbf{M_x}$ and $\mathbf{M_y}$. The product of the matrix $\mathbf{B_x}$ and $\mathbf{B_y}$ with the boundary concentration vectors $\vec{c}_b(t)$ and $\vec{c}_b(t + \Delta t)$ is required to establish the boundary conditions in equation (3.1.9), e.g., at locations ahead of the boundary $x_1$ no valid concentration value for $x_1$-$\Delta x$ within the finite-difference mesh does exist, therefore, it has to be defined by $c_b(x_1$-$\Delta x,y,t)$. Finally, the location-dependent diffusion coefficients $D(x,y)$ and the flexible step widths $\Delta x_l$ and $\Delta x_r$, and $\Delta y_l$ and $\Delta y_r$ are expressed by the matrices $\mathbf{R_x}$ and $\mathbf{R_y}$, respectively:

$$\mathbf{R_x} = \mathrm{diag}\left[\frac{D_x(x,y)}{2\Delta x_l \Delta x_r}\right] \text{ and } \mathbf{R_y} = \mathrm{diag}\left[\frac{D_y(x,y)}{2\Delta y_l \Delta y_r}\right] \tag{3.1.10}$$

Then, the matrix equation representing equation (3.1.9) for each location step of the finite-difference mesh can be written as follows:

$$\frac{1}{\Delta t}\left[\vec{c}(t+\Delta t)-\vec{c}(t)\right]=\mathbf{R_x}\left[\mathbf{M_x}\vec{c}(t)+\mathbf{B_x}\vec{c}_b(t)\right]+\mathbf{R_x}\left[\mathbf{M_x}\vec{c}(t+\Delta t)+\mathbf{B_x}\vec{c}_b(t+\Delta t)\right]$$
$$+\mathbf{R_y}\left[\mathbf{M_y}\vec{c}(t)+\mathbf{B_y}\vec{c}_b(t)\right]+\mathbf{R_y}\left[\mathbf{M_y}\vec{c}(t+\Delta t)+\mathbf{B_y}\vec{c}_b(t+\Delta t)\right]$$

(3.1.11)

When the boundary concentrations are assumed as (i) to be homogeneous and (ii) to experience only small changes, i.e., $\vec{c}_b(t)\approx\vec{c}_b(t+\Delta t)$, and the matrices in equation (3.1.11) are multiplied according to $\mathbf{M}=\mathbf{R_x M_x}+\mathbf{R_y M_y}$ and $\mathbf{B}=2(\mathbf{R_x B_x}+\mathbf{R_y B_y})$ one obtains the following governing equation for the concentration vector $\vec{c}(t+\Delta t)$ as a function of the concentration vector at the preceding time step $\vec{c}_b(t)$ and $\vec{c}(t)$:

$$\left[\frac{1}{\Delta t}\mathbf{E}-\mathbf{M}\right]\vec{c}(t+\Delta t)=\left[\frac{1}{\Delta t}\mathbf{E}-\mathbf{M}\right]\vec{c}(t)+\mathbf{B}\vec{c}_b(t),$$

(3.1.12)

with the unit matrix $\mathbf{E}$.

Implemented in the commercial simulation design environment MATLAB, equation (3.1.12) is solved for all species participating in the corrosion reaction and stepwise for the complete reaction time $p\cdot\Delta t$ according to the schematic representation in Figure 3.1.5 (simplified for one-dimensional diffusion) [11].
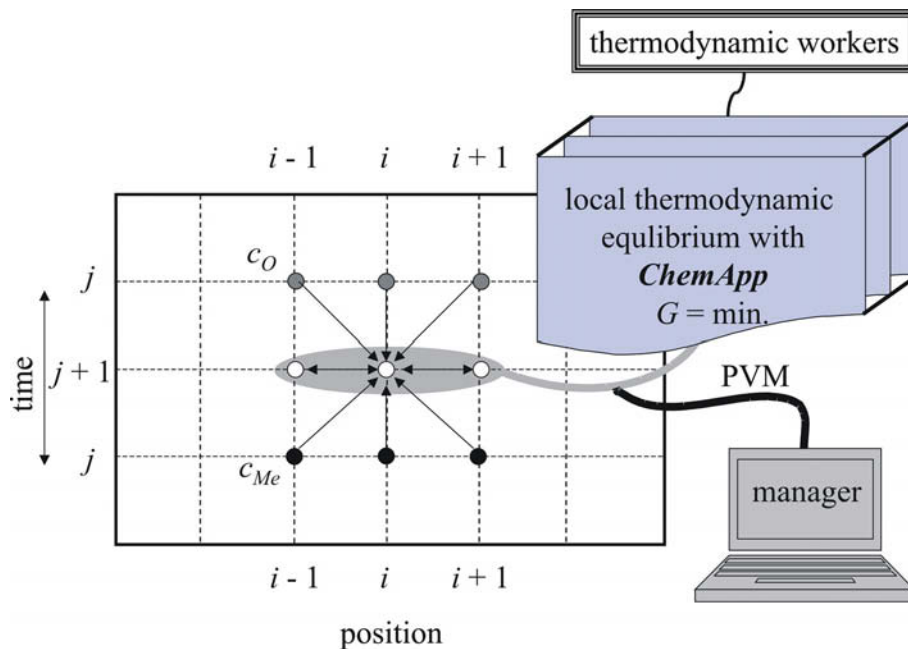


Figure 3.1.5. Schematic representation of the implicit finite-difference technique in combination with the thermodynamic program ChemApp.

To accommodate for the possible chemical reactions of the ongoing corrosion process, the calculated concentrations at $\vec{c}(t + \Delta t)$ ($c_i^{j+1}$ in Figure 3.1.5) must be corrected according to the local thermodynamic equilibrium. For this purpose, the concentrations $\vec{c}(t + \Delta t)$ are transferred into a thermodynamic subroutine ThermoScript, which contains the commercial program ChemApp. ChemApp is based on a numerical Gibbs' energy minimization routine in combination with tailor-made data bases (see chapter 2) . In order to avoid excessive calculation times, the parallel-computing system PVM (parallel virtual machine) is used, i.e., ThermoScript distributes the individual equilibrium calculations to thermodynamic workers according to the schematic representation in Figure 3.1.5. Therefore, by using, e.g., 200 parallel-working processing units (CPUs) the calculation time can be reduced by a factor of up to 200 as compared to a conventional PC. The complete sets of concentrations of all the participating species in local equilibrium form the new starting concentration vector $\vec{c}(t)$ for the application of equation (3.1.9) at the following time step $k+2$.

A simple example is given in order to illustrate the robustness of the software as well as the importance to use parallel computing for the thermodynamic calculations. Figure 3.1.6 shows an one-dimensional discretization containing just 5 nodes.
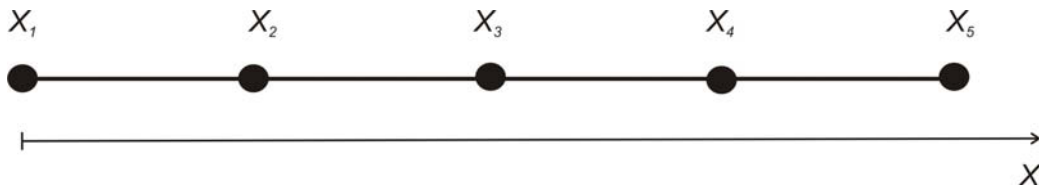


*Figure 3.1.6. One-dimensional discretization.*

The chemical composition of all species must be defined at all nodes (position), which depends on the diffusion step as well as the local thermodynamic equilibrium. Thus, a matrix (eq. 3.1.13) containing those concentrations for the system Fe-Cr-O should have the following format:

$$V_{in} = \begin{array}{c} \\ x_1 \to \\ x_2 \to \\ x_3 \to \\ x_4 \to \\ x_5 \to \\ \\ x_1 \to \\ x_2 \to \\ x_3 \to \\ x_4 \to \\ x_5 \to \\ \cdot \\ \cdot \\ \cdot \end{array} \begin{array}{c} phase \to \\ \left[\begin{array}{ccccccc} O & Fe & Cr & Fe_3O_4 & Cr_2O_3 & FeCr_2O_4 & Fe_2O_3 \\ c_O^s & c_{Fe}^0 & c_{Cr}^0 & 0 & 0 & 0 & 0 \\ 0 & c_{Fe}^0 & c_{Cr}^0 & 0 & 0 & 0 & 0 \\ 0 & c_{Fe}^0 & c_{Cr}^0 & 0 & 0 & 0 & 0 \\ 0 & c_{Fe}^0 & c_{Cr}^0 & 0 & 0 & 0 & 0 \\ 0 & c_{Fe}^0 & c_{Cr}^0 & 0 & 0 & 0 & 0 \\ c_O^s & c_{Fe}^1 & c_{Cr}^1 & c_{Fe3O4}^1 & c_{Cr2O3}^1 & c_{FeCr2O4}^1 & c_{Fe2O3}^1 \\ c_O^2 & c_{Fe}^2 & c_{Cr}^2 & c_{Fe3O4}^2 & c_{Cr2O3}^2 & c_{FeCr2O4}^2 & c_{Fe2O3}^2 \\ c_O^3 & c_{Fe}^3 & c_{Cr}^3 & c_{Fe3O4}^3 & c_{Cr2O3}^3 & c_{FeCr2O4}^3 & c_{Fe2O3}^3 \\ c_O^4 & c_{Fe}^4 & c_{Cr}^4 & c_{Fe3O4}^4 & c_{Cr2O3}^4 & c_{FeCr2O4}^4 & c_{Fe2O3}^4 \\ c_O^5 & c_{Fe}^5 & c_{Cr}^5 & c_{Fe3O4}^5 & c_{Cr2O3}^5 & c_{FeCr2O4}^5 & c_{Fe2O3}^5 \\ \cdot & \cdot & \cdot & \cdot & \cdot & \cdot & \cdot \\ \cdot & \cdot & \cdot & \cdot & \cdot & \cdot & \cdot \\ \cdot & \cdot & \cdot & \cdot & \cdot & \cdot & \cdot \end{array}\right] \end{array} \begin{array}{c} \\ \\ \\ t=0 \\ \\ \\ \\ \\ \Delta t_1 \\ \\ \\ \cdot \\ \cdot \\ \Delta t_n \end{array} \qquad (3.13)$$

This example shows that it is helpful to perform preliminary thermodynamic equilibrium calculations in order to establish the phases which are possible to be in equilibrium at the given state variables (temperature and pressure) and alloy composition. From this knowledge the concentration matrix has to be build up with a dimension that depends on the amount of phases and the discretization in space. At $t = 0$ it is assumed that there are no oxides in the substrate and the oxygen concentration is zero in the bulk and $c_O^s$ on the surface. After the first diffusion time step ($\Delta t_1$) oxygen will diffuse inside the substrate and according to the thermodynamic equilibrium, oxides can be formed. Therefore, the concentration of the metals (Fe and Cr) as well as the oxide will change. The calculations will proceed up to the total calculation time $t_j$, and at every time step the concentration of all species have to be adjusted according to the local thermodynamic equilibrium (see Figure 3.1.7).

The subroutine *ThermoScript* implemented for the calculations using the data banks *OptiCor1.dat*, *OptiCor2.dat*, *FeNi.dat* and *FeCrC.dat* which contains thermodynamic data for the system Fe-Cr-H-O-He, Fe-Cr-Ni-Si-Al-S-H-C-O-N and Fe-Cr-Ni-O-C-Ar, respectively. In this subroutine, which serves as an interface between the diffusion calculation (MatLab) and the thermodynamic program (ChemApp), important parameters must be defined, such as: number of processors that should be used for the thermodynamic calculations (the so-called thermodynamic workers), the permitted phases, an input and an output vector, which are defined by the relevant phases. In this interface the establishment of the PVMs are also defined.
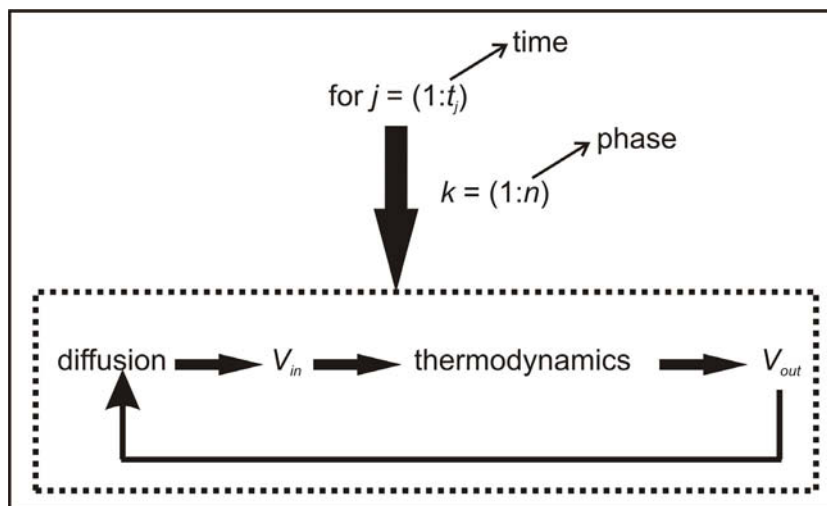
*Figure 3.1.7. Schematic representation of the loop used for the simultaneous diffusion and thermodynamic calculations.*

## 3.2 CorrApp: Salt-melt induced corrosion model

(K. Penttilä – VTT Processes; M. Spiegel & A. Ruh – Max Planck Institute)

A specially adapted version of ChemSheet has been used to execute the model calculations for the corrosion under a salt layer. In this model too diffusion plays an important part, here it is the diffusion of Cl through a salt melt. A detailed description of the model is given below.

### 3.2.1 Introduction

The model described here is part of the study aiming at control and optimization of boiler materials and development of simulation tools for high temperature corrosion. Heat exchanger tubes in waste incinerator boilers are usually attacked by aggressive gases like oxygen, HCl and water vapor as well as molten salts, which cause accelerated corrosion. Most common salt deposits on boiler steels are chloride mixtures.

The CorrApp is a tool for investigating salt-melt induced high temperature corrosion. The kinetics and thermodynamics of corrosion of metals beneath a molten chloride salt are not generally well known. In this project they have been studied by thermogravimetric experiments and these experiments supply the basis for the model.

In CorrApp the thermodynamic program library ChemApp is integrated into a one-dimensional finite-difference diffusion calculation. The model is capable to simulate multi-phase corrosion in different molten salt environments. A typical data-file for pure

metal (iron) consists of a system comprising seven components: Zn-K-Fe-He-O-Cl-H. It contains the gas phase, liquid salt phase, which is composed of soluble chlorides and oxides, and several condensed pure phases (chlorides, oxides and etc.).

### 3.2.2  Physical model

(M. Spiegel & A. Ruh – Max Planck Institute)

A model for the corrosion processes beneath a KCl-ZnCl$_2$ melt is given in Figure 3.2.1 [1, 2]. The substrate metal is covered with a eutectic KCl-ZnCl$_2$ deposit, which melts at 250°C [3]. The model is based on the assumption that dissolution of the metal takes place at the metal – salt melt interface, followed by the formation of iron chloride:

$$Fe + Cl_2 = FeCl_2 \tag{3.2.1}$$

The formation of iron chloride depends on the chlorine partial pressure, established in the molten salt. Disregarding any chlorine in the gas phase, the chlorine source may be the equilibrium content in the molten salt or, if oxygen is present in the gas phase, the chlorine partial pressure may be established for example by the reactions:

$$2KCl + 0.5O_2 = K_2O + Cl_2 \tag{3.2.2}$$

and / or:

$$ZnCl_2 + 0.5O_2 = ZnO + Cl_2 \tag{3.2.3}$$
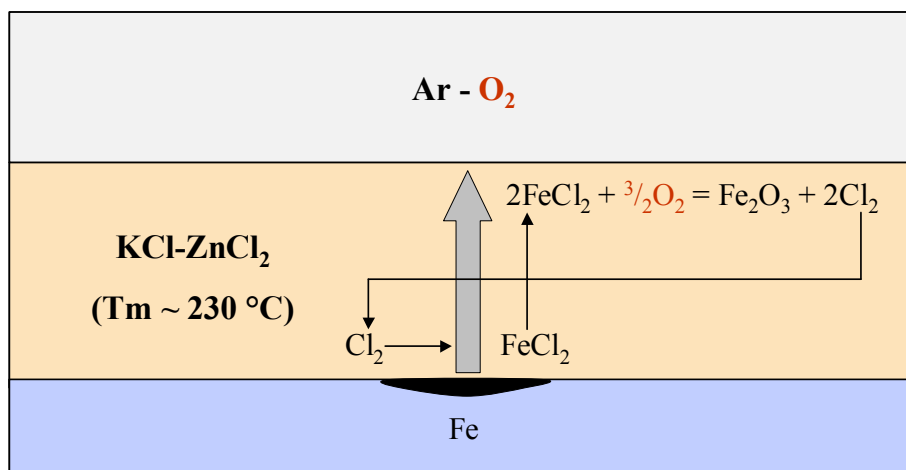


*Figure 3.2.1. Schematic model of high temperature corrosion processes beneath a KCl/ZnCl$_2$ melt [2], showing the transport of gas species and chemical reactions form- ing iron oxide and iron chloride (as described in the text).*

The produced iron chloride from reaction (3.2.1) is mobile in the salt melt and can diffuse outwards to the salt melt/gas atmosphere interface. The outer region of the salt melt is dominated by a higher oxygen partial pressure, which allows the oxidation of $FeCl_2$ to $Fe_2O_3$ due to its favoured thermodynamic stability

$$2FeCl_2 + 1.5O_2 = Fe_2O_3 + 2Cl_2 \qquad\qquad (3.2.4)$$

The released chlorine diffuses back to the metal/salt melt interface and allows a subsequent formation of iron chloride. Chlorine is not consumed and thus this process is catalysed by chlorine. The reaction rate is dependent on the oxygen partial pressure $p(O_2)$ in the atmosphere since it forces reaction (3.2.4) to the right side.

The thermogravimetric experiments with pure iron generally yield data as shown in Figure 3.2.2. Usually three obvious kinetic regimes are observed: an incubation time (A), a linear stage (B) and a stage that is either logarithmic or parabolic (C).
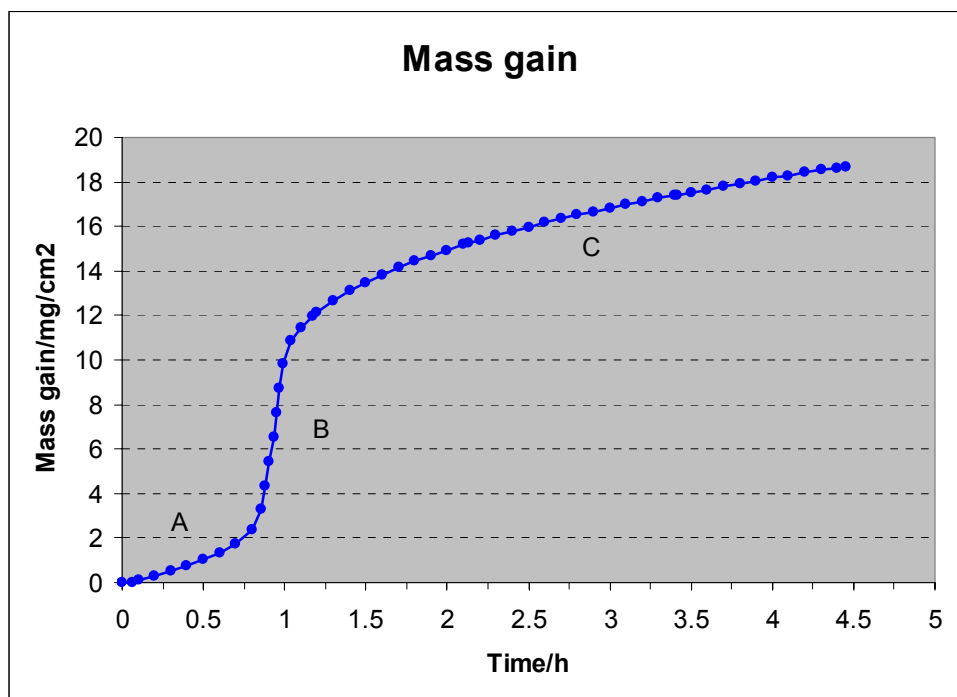


Figure 3.2.2. TG curve for high temperature corrosion (T = 320°C) of pure Fe in an Ar + 8 vol.% $O_2$ atmosphere with 50 mol.% KCl – 50 mol.% $ZnCl_2$ deposit. A, B and C are different kinetic regimes.

Further investigation has shown that the duration of the incubation time depends on the oxygen partial pressure and the thickness of the salt deposit. Experiments with a higher amount of salt deposit have shown that the incubation time increases with increasing amount of salt deposit. In contrast, the duration of the incubation stage decreases with increasing partial pressure of oxygen.

1. The different kinetic regimes can be attributed to different mechanistic steps:
2. Dissolution of metal in the chloride melt at the metal-salt interface.
3. Transport of dissolved chloride species to the melt-gas interface.
4. Precipitation of oxide species in contact with the gas phase.
5. Formation of a porous non-protective scale.

The mobility of metal ions within the salt melt is described by diffusion coefficients of metal ions in chloridic salt melts. Values for iron in chloride melts ($KCl$-$ZnCl_2$) could not be found in literature but typical values of other metal ions like In, Ni, Cu, Pb, Zn, Sn or Cr in chloridic salt melts ($LiCl$-$KCl$, $ZnCl_2$-$NaCl$ or $NaCl$-$KCl$) range between $D = 5*10^{-6}$ and $3*10^{-5}$ $cm^2/s$ for T = 380–700°C [4–11] (see also Table 3.2.1). The rate of iron chloride formation will strongly depend on the amount and the flux of $Cl_2$ to the metal surface. Oxide formation takes place when the oxygen partial pressure is high enough that $\Delta G°$ of its reaction becomes negative. This happens at the outer parts of the salt melt. The formation of $Fe_2O_3$ produces $Cl_2$, which acts as a chlorine source for a subsequent formation of iron chloride, accomplishing a circulation process. Within the salt melt the oxygen partial pressure will decrease towards the metal substrate and the gradient between low oxygen partial pressure in the inner part and higher oxygen partial pressure at the outer part enables an inward oxygen flux.

*Table 3.2.1. Summary about reported diffusion coefficients of metal ions in chloridic salt melts. *): Calculated from Arrhenius equation given in [11].*

| Ion | Salt melt | Temp. | $D$ ($cm^2/s^{-1}$) | Method: | Ref. |
|---|---|---|---|---|---|
| Sn(II) | $ZnCl_2$ + 2NaCl | 450°C | (0.5±0.2) $*10^{-5}$ | Volt. W | [4] |
| | $ZnCl_2$ + 2NaCl | 450°C | (0.6±0.1) $*10^{-5}$ | Volt. GC | [4] |
| | $ZnCl_2$ + 2NaCl | 450°C | (1.0±0.3) $*10^{-5}$ | Semi-int. W | [4] |
| | $ZnCl_2$ + 2NaCl | 450°C | (1.6±0.2) $*10^{-5}$ | Semi-int. GC | [4] |
| | $ZnCl_2$ + 2NaCl | 450°C | (1.1±0.2) $*10^{-5}$ | Chr.p. W | [4] |
| | $ZnCl_2$ + 2NaCl | 450°C | (0.6±0.1) $*10^{-5}$ | Chr.a. W | [4] |
| | $2ZnCl_2$ + 3NaCl | 450°C | (1.0±0.2) $*10^{-5}$ | Volt. W | [4] |
| | $2ZnCl_2$ + 3NaCl | 450°C | (0.7±0.1) $*10^{-5}$ | Volt. GC | [4] |
| | $2ZnCl_2$ + 3NaCl | 450°C | (1.3±0.1) $*10^{-5}$ | Semi-int. W | [4] |
| | $2ZnCl_2$ + 3NaCl | 450°C | (1.1±0.2) $*10^{-5}$ | Semi-int. GC | [4] |
| | $2ZnCl_2$ + 3NaCl | 450°C | (0.9±0.1) $*10^{-5}$ | Chr.p. W | [4] |
| | $2ZnCl_2$ + 3NaCl | 450°C | (0.9±0.2) $*10^{-5}$ | Chr.a. W | [4] |
| | $ZnCl_2$ + NaCl | 450°C | (0.6±0.2) $*10^{-5}$ | Volt. W | [4] |
| | $ZnCl_2$ + NaCl | 450°C | (0.9±0.1) $*10^{-5}$ | Volt. GC | [4] |
| | $ZnCl_2$ + NaCl | 450°C | (1.3±0.2) $*10^{-5}$ | Semi-int. W | [4] |
| | $ZnCl_2$ + NaCl | 450°C | (1.7±0.4) $*10^{-5}$ | Semi-int. GC | [4] |
| | $ZnCl_2$ + NaCl | 450°C | (0.9±0.1) $*10^{-5}$ | Chr.p. W | [4] |
| | $ZnCl_2$ + NaCl | 450°C | (0.8±0.2) $*10^{-5}$ | Chr.a. W | [4] |
| | | | | | |
| Ni (II) | LiCl + KCl (eut.) | 450°C | 1.5 $* 10^{-5}$ | Rot. Disc.el. | [5] |
| | | | | | |

| | | | | | |
|---|---|---|---|---|---|
| Cu (I) | $ZnCl_2$ + 2NaCl | 450°C | $(1.9\pm0.2) *10^{-5}$ | Volt. | [6] |
| | $ZnCl_2$ + 2NaCl | 450°C | $(2.3\pm0.3) *10^{-5}$ | Semi-int. | [6] |
| | $ZnCl_2$ + 2NaCl | 450°C | $(2.0\pm0.3) *10^{-5}$ | Chr.p. | [6] |
| | $ZnCl_2$ + 2NaCl | 450°C | $(1.8\pm0.4) *10^{-5}$ | Chr.a. | [6] |
| | $ZnCl_2$ + 2NaCl | 450°C | $(1.2\pm0.1) *10^{-5}$ | Volt. | [6] |
| | $ZnCl_2$ + 2NaCl | 450°C | $(2.3\pm0.3) *10^{-5}$ | Semi-int. | [6] |
| | $ZnCl_2$ + 2NaCl | 450°C | $(1.8\pm0.2) *10^{-5}$ | Chr.p. | [6] |
| | | | | | |
| Pb (II) | $ZnCl_2$ + 2NaCl | 450°C | $(7.8\pm0.3) *10^{-6}$ | Volt. | [7] |
| | $ZnCl_2$ + 2NaCl | 450°C | $(7.2\pm0.3) *10^{-6}$ | Semi-int. | [7] |
| | $ZnCl_2$ + 2NaCl | 450°C | $(8.3\pm0.2) *10^{-6}$ | Chr.p. | [7] |
| | $ZnCl_2$ + 2NaCl | 450°C | $(6.5\pm0.5) *10^{-6}$ | Chr.a. | [7] |
| | | | | | |
| In (III) | $ZnCl_2$ + 2NaCl | 450°C | $(5.8\pm0.3) *10^{-6}$ | Volt. | [8] |
| | $ZnCl_2$ + 2NaCl | 450°C | $(5.1\pm0.3) *10^{-6}$ | Semi-int. | [8] |
| | $ZnCl_2$ + 2NaCl | 450°C | $(6.4\pm0.2) *10^{-6}$ | Chr.p. | [8] |
| | $ZnCl_2$ + 2NaCl | 450°C | $(5.3\pm0.7) *10^{-6}$ | Chr.a. | [8] |
| | | | | | |
| In (II) | $ZnCl_2$ + 2NaCl | 450°C | $(6.1\pm0.4) *10^{-6}$ | Volt. | [8] |
| | $ZnCl_2$ + 2NaCl | 450°C | $(7.2\pm0.5) *10^{-6}$ | Semi-int. | [8] |
| | $ZnCl_2$ + 2NaCl | 450°C | $(6.2\pm0.8) *10^{-6}$ | Chr.p. | [8] |
| | $ZnCl_2$ + 2NaCl | 450°C | $(5.5\pm0.3) *10^{-6}$ | Chr.a. | [8] |
| | | | | | |
| $WO_4^{2-}$ | LiCl + KCl (eut.) | 450°C | $(1.2\pm0.2) *10^{-5}$ | Rot-r.d.el. + Pot. sweep | [9] |
| | | | | | |
| Zn (II) | NaCl + KCl | 700°C | $(3\pm0.2) *10^{-5}$ | Diff. | [10] |
| | | | | | |
| Cr (III) | LiCl + KCl (eut.) | 380°C | $4.9 *10^{-6}$ *) | Pulse techn. | [11] |
| | | 400°C | $6.2 *10^{-6}$ *) | Pulse techn. | [11] |
| | | 450°C | $1.1 *10^{-5}$ *) | Pulse techn. | [11] |
| | | 500°C | $1.8 *10^{-5}$ *) | Pulse techn. | [11] |
| | | 550°C | $2.7 *10^{-5}$ *) | Pulse techn. | [11] |
| | | | | | |
| Cr (II) | LiCl + KCl (eut.) | 380°C | $5.2 *10^{-6}$ *) | Pulse techn. | [11] |
| | | 400°C | $6.5 *10^{-6}$ *) | Pulse techn. | [11] |
| | | 450°C | $1.1 *10^{-5}$ *) | Pulse techn. | [11] |
| | | 500°C | $1.7 *10^{-5}$ *) | Pulse techn. | [11] |
| | | 550°C | $2.5 *10^{-5}$ *) | Pulse techn. | [11] |

Abbreviations:
Volt:            Voltammetry
Semi-int:        Semi-integral
Chr.p.:          Chronopotentiometry
Chr.a.:          Chronoamperometry
W:               Tungsten electrode
GC:              Glassy carbon electrode
Rot. Disc.el.:   Rotating disk electrode
Rot-r.d.el.:     Rotating ring-disk electrode
Pot. Sweep:      Potential sweep method
Diff.:           different methods
Pulse techn.:    Pulse techniques

### 3.2.3 Mathematical model

(K. Penttilä – VTT Processes)

The developed model is used to simulate stationary salt melt consisting of liquid salt and formed solid phases. Salt melt undergoes changes in its composition and volume due to mass transfer and chemical reactions. Also gaseous species may be formed.

In case of an isothermal and isobaric system the relation between flux and concentration gradient is given by Fick's first law:

$$J = -D\frac{\partial c}{\partial x}$$

(3.2.5)

where $J$ is the diffusion flux i.e. the amount of diffusing species that passes per unit time and unit area of a plane perpendicular to the x-axis, $c$ is the concentration of the species and $D$ is its diffusivity.

Fick's second law is given as:

$$\frac{\partial c}{\partial t} = \frac{\partial}{\partial x}(-J) = \frac{\partial}{\partial x}\left(D\frac{\partial c}{\partial x}\right)$$

(3.2.6)

The salt melt may be represented as one-dimensional slab with uniform or non-uniform mesh size (see Figure 3.2.3). The boundary conditions for the slab are the interfaces between the gas and the salt (right side boundary in model coordinate system) and salt and the metal (left side boundary in model coordinate system).
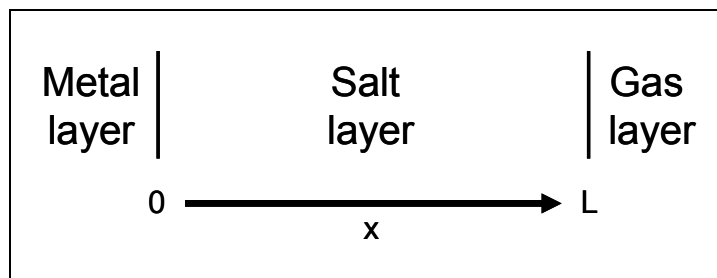


*Figure 3.2.3. Salt melt and its boundary conditions.*

If there is only one solution phase present and the mesh size is uniform, i.e. the distances between all nodal points are the same, then the equation 3.2.6 can be discretized using the backward difference method as follows:

$$\frac{c_i^{m+1} - c_i^m}{\Delta t} = D \frac{c_{i+1}^{m+1} - 2c_i^{m+1} + c_{i-1}^{m+1}}{\Delta x^2}$$

<div align="right">(3.2.7)</div>

where $\Delta t$ is discrete time increment and $\Delta x$ is the distance between discrete nodal points, Figure 3.2.4. Subscript $m$ refers to time and subscript $i$ refers to axial position.
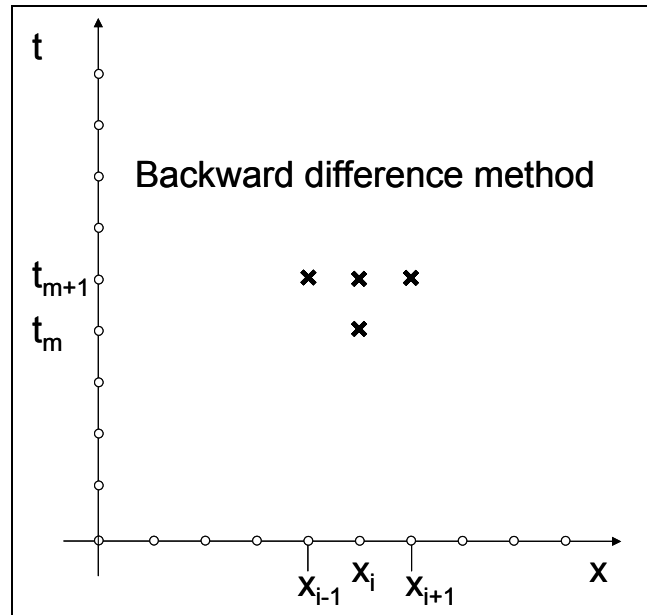


*Figure 3.2.4. Mesh grid (nodal points) in backward difference method.*

When calculating the diffusion between two neighbouring volume elements which contain two or more continuous phases and which could have non-uniform mesh size (Figure 3.2.5), we can use a method analogous to heat conduction between two adjoining and dissimilar materials.
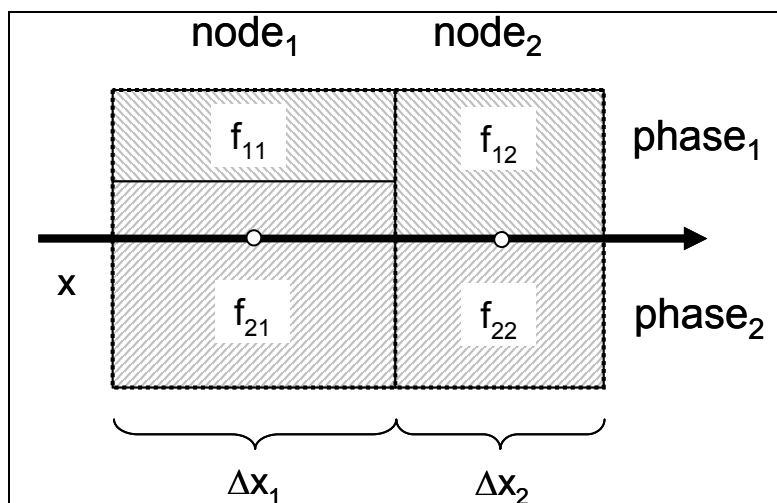


*Figure 3.2.5. Volume fractions of two solution phases in neighbouring volume elements.*

The total resistance to diffusion for constituent $j$ in phase $p$ is given as follows:

$$R_{j12} = \frac{\Delta x_1}{2 f_1^p D_{j1}^p} + \frac{\Delta x_2}{2 f_2^p D_{j2}^p}$$

(3.2.8)

where $f$ is volume fraction of phase, $D$ is the diffusivity of constituent in phase and $\Delta x$ is the thickness of volume element. Subscripts $1$ and $2$ refer to volume element.

The diffusion flux for a phase constituent between volume elements $1$ and $2$ is then given as:

$$J_{12} = \frac{c_1 - c_2}{R_{12}}$$

(3.2.9)

The finite difference equation for a phase constituent in the node is given as:

$$\frac{c_i^{m+1} - c_i^m}{\Delta t} = \frac{1}{\Delta x_i^{m+1}} \left( \frac{c_{i+1}^{m+1} - c_i^{m+1}}{R_{i+1,i}^{m+1}} - \frac{c_i^{m+1} - c_{i-1}^{m+1}}{R_{i,i-1}^{m+1}} \right)$$

(3.2.10)

Equation 3.2.10 is repeated for each phase constituent in each solution phase.

Above equations do not contain any source terms or reactions between phase constituents. Possible reactions are dissolution of metals to salt melt and oxidation of salt melt chlorides to respective oxides. Also gaseous species can be formed which might be again partially soluble to the salt melt. Reactions can be calculated by defining the thermodynamic equilibrium locally in each volume element.

Thermodynamic equilibrium may be solved using Gibbs energy minimization routine, which is non-linear function of given temperature, pressure and initial composition of the system. As a result of the minimization routine the equilibrium composition of the phases and phase constituents is obtained.

In order to calculate the thermodynamic equilibrium the medium must be described as a thermodynamic system consisting of phases and phase constituents, i.e. species. Each constituent consists of linear set of system components, which normally are elements.

As elements are independent variables in the thermodynamic system they may be used as variables in the diffusion model instead of phase constituents. In order to use this method the thermodynamic equilibrium in a volume element must first be calculated

using the known component amounts. Then the concentrations of phase constituents may be calculated from the equilibrium amounts and used in diffusion equation (3.2.10). Finally the diffusion fluxes of phase constituents between the volume elements are converted to fluxes of components using the stoichiometric matrix:

$$J_k = \sum_p \sum_j a_{jk}^p J_j^p$$

(3.2.11)

where stoichiometric matrix $a_{jk}^p$ gives the molar amount of component $k$ in constituent $j$ of phase $p$.

This method reduces considerably the dimensions of the diffusion model as the thermodynamic system may contain many times more phase constituents than the components.

Simplified simulation algorithm is shown in the Figure 3.2.6.
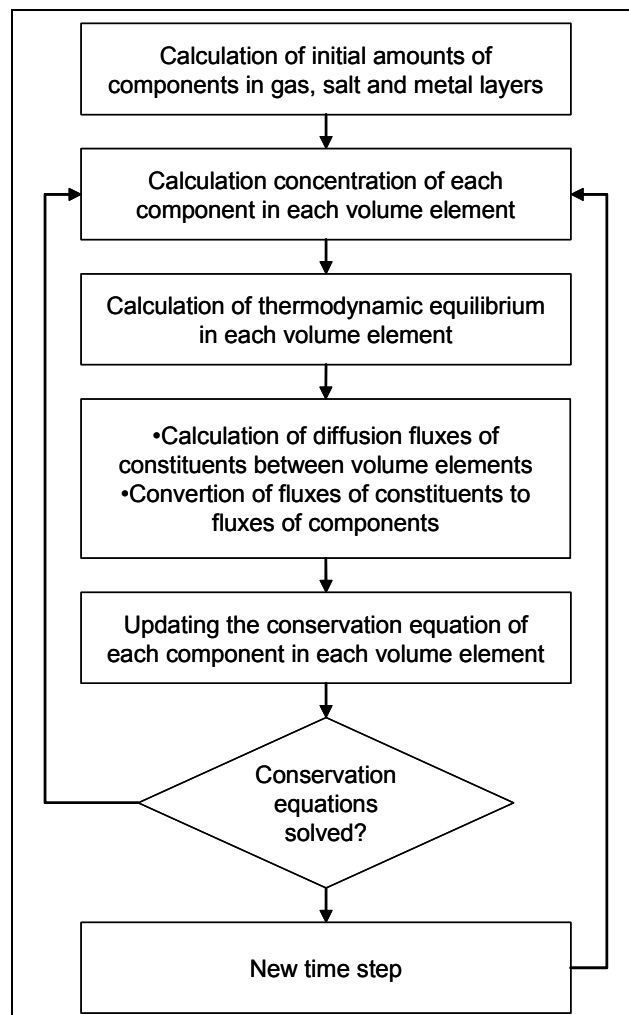


*Figure 3.2.6. Simplified simulation algorithms.*

In order to solve the diffusion model initial and boundary conditions must be given. Initial concentrations of the gas, the salt melt and the metals is given by the user as input. It is generally required that initial concentration is either in equilibrium or does not generate volatiles in the salt melt or metal alloy when equilibrium is calculated.

Boundary conditions of gas constituents at gas-salt interface are given as:

$$J = \frac{\partial c}{\partial x}\bigg|_{t, x=x_{gas}} = k_g \left( c_\infty - c_s \right) \qquad\qquad 3.2.12$$

where $k_g$ is the mass transfer coefficient, $c_\infty$ is the concentration of bulk gas and $c_s$ is the concentration of gas at salt melt surface, which is defined by the local equilibrium.

Boundary conditions of constituents in metal phase at metal-salt interface are given as:

$$J = \frac{\partial c}{\partial x}\bigg|_{t, x=x_{metal}} = k_s \left( c_{MeCl_x, eq} - c_{MeCl_x} \right) \qquad\qquad 3.2.13$$

where $k_s$ is the mass transfer coefficient, $c_{MeCl_x, eq}$ is the saturation concentration and $c_{MeCl_x}$ is the concentration of soluble metal chloride at metal/salt interface.

### 3.2.4  Simulation software

(K. Penttilä – VTT Processes)

The simulation program of the corrosion model is a win32 console application and it is compiled with a Fortran 90 compiler. It uses the thermodynamic programming library ChemApp. The input parameters to the program are given by a text file. To facilitate the use of the program there is a separate user interface for operating it. The user interface is made using Visual Basic and it operates under Excel, Figure 3.2.7. The user interface is used to define the input parameters for the simulation and to start the simulation, which is then executed as a background process. This is important as the simulation could take several hours.

The defined input parameters are stored within the Excel workbook. When the simulation is started the input parameters are written to a text file that is red by the simulation program. During the simulation the results for the selected time steps are saved to a file that is named after the name of the Excel workbook. After the simulation the results can be viewed in Excel in a new automatically generated workbook.
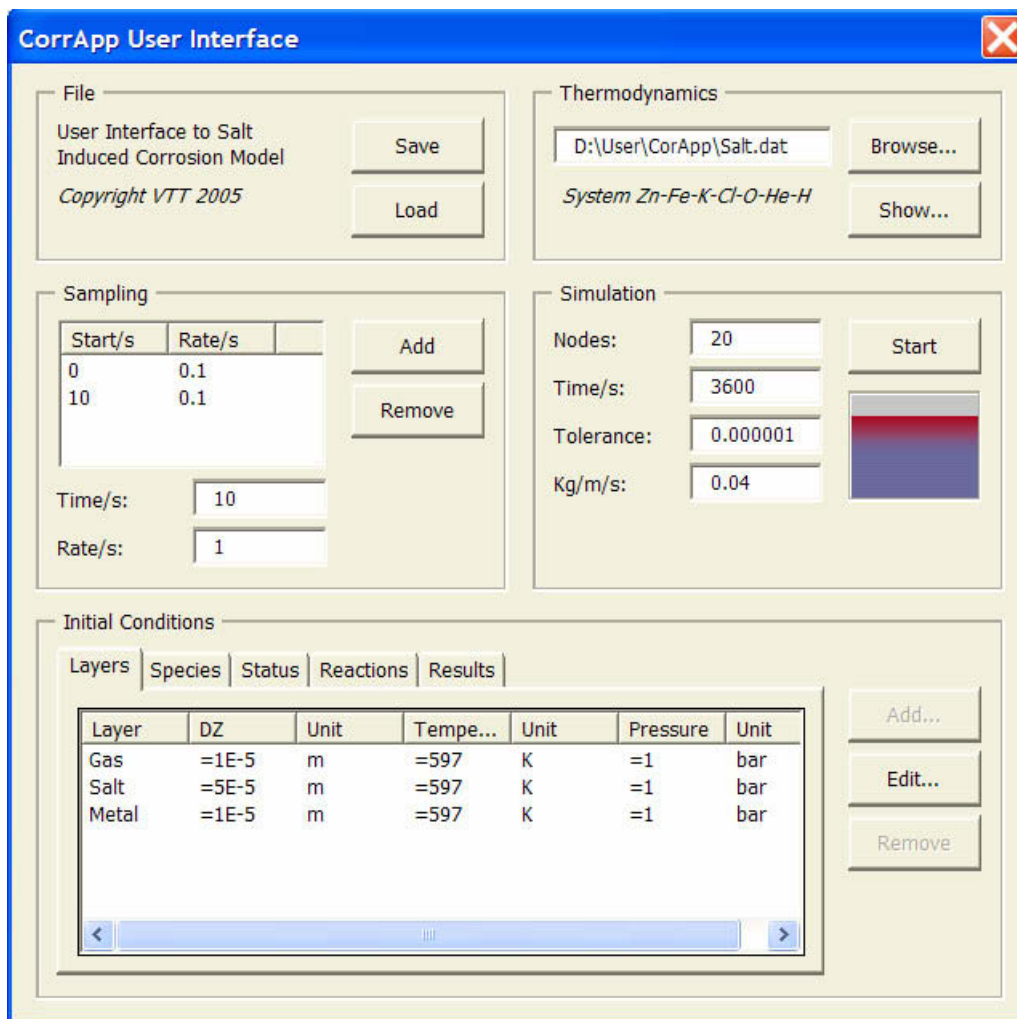
*Figure 3.2.7. The main dialog of the CorrApp User Interface.*

**Thermodynamics** group contains the name of the thermodynamic data-file. It contains the parameters of the thermodynamic system which consists of the gas phase, one or more solution phases, and number of pure liquid and solid phases. The first solution phase after the gas phase should represent the salt melt. The thermodynamic data-file uses ChemSage 4.0 format. There should also be a separate file consisting of diffusion data for the phases and phase constituents. It has the same base name as the thermodynamics data-file but a different extension name (*.dif). The diffusion data consists of porosity of phases, densities and temperature dependent diffusivity parameters of phase constituents.

**Simulation** group contains general parameters like the number of grid nodes in the simulation and the duration of the simulation. Parameter **Kg** defines the mass transfer rate between gas and the surface of the salt melt.

57

**Sampling** group contains parameters that define the rate at which the simulation results are saved. A long simulation could contain several thousands of time steps and usually it is not needed to save the results for each of them.

**Initial Conditions** group contains the parameters that define the geometry and the initial composition of the corrosion model. It also contains the parameters for generating the tables and charts for the simulation results.

List items on different tab pages in **Initial conditions** can be added and edited on separate dialogs.

In the **Layer** dialog (see Figure 3.2.8) user can define the thickness, temperature and pressure of the three layers in the model: gas layer, salt layer and metal layer. The gas layer and the metal layer define the boundary conditions for the calculation as their composition is constant during the simulation. Thickness of the gas layer is only used when the results are shown. The thickness of the metal layer is important as it defines the total amount of the metal present in the simulation. User needs to make sure that its thickness is large enough so that there is enough metal to be dissolved into salt layer for the whole duration of the simulation. The composition of the metal layer is constant but its absolute amount is decreased as the metal is dissolved. The thickness of the metal layer is also used when the results are shown. The bottom of the metal layer is used as the origin of the x-axis (see Figure 3.2.13). This way it is easy to see any volumetric changes in the metal and salt layers when viewing the results.
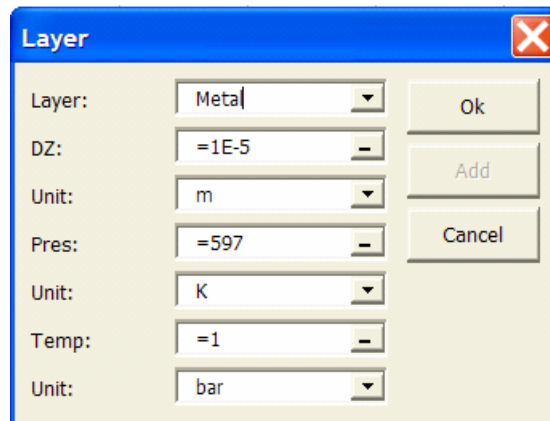


*Figure 3.2.8. Layer dialogue.*

In the **Species** dialog (see Figure 3.2.9) user can define the initial composition of the gas, salt and metal layers. **Phase** list contains the phases that are defined in the thermodynamic data-file. The **Constituent** list contains the constituents in the selected phase. The **Value** is a relative value. The absolute values depend on the volumes of the layers and are calculated when the simulation is started.
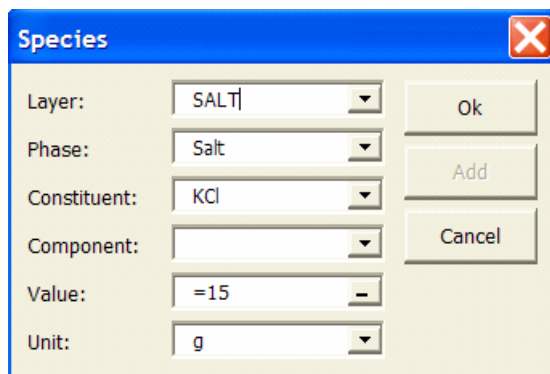
*Figure 3.2.9. Species dialogue.*

The **Status** dialog (see Figure 3.2.10) contains parameters to set the status of phases and phase constituents in a selected layer. This way they can be eliminated from the calculation without editing the thermodynamic data-file.
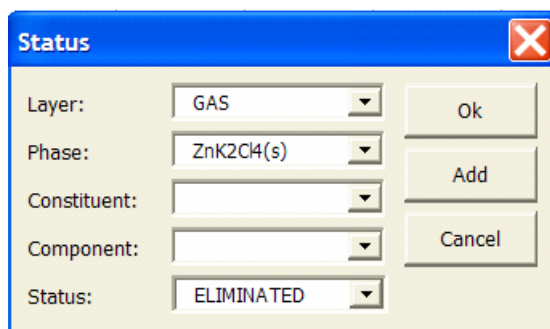


*Figure 3.2.10. Status dialogue.*

The **Result** dialog (see Figure 3.2.11) contains parameters for defining various results for the simulation. After the simulation these parameters are used to generate tables and charts in a new excel workbook. There can be any number of results.
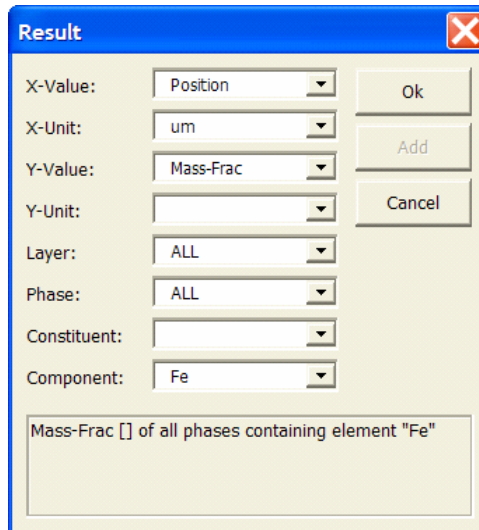
*Figure 3.2.11. Result dialogue.*

There are two different types of results. In the first the x-axis represents the axial-position in the salt melt. In the second the x-axis is the simulation time, an example of this is presented in Figure 3.2.12.
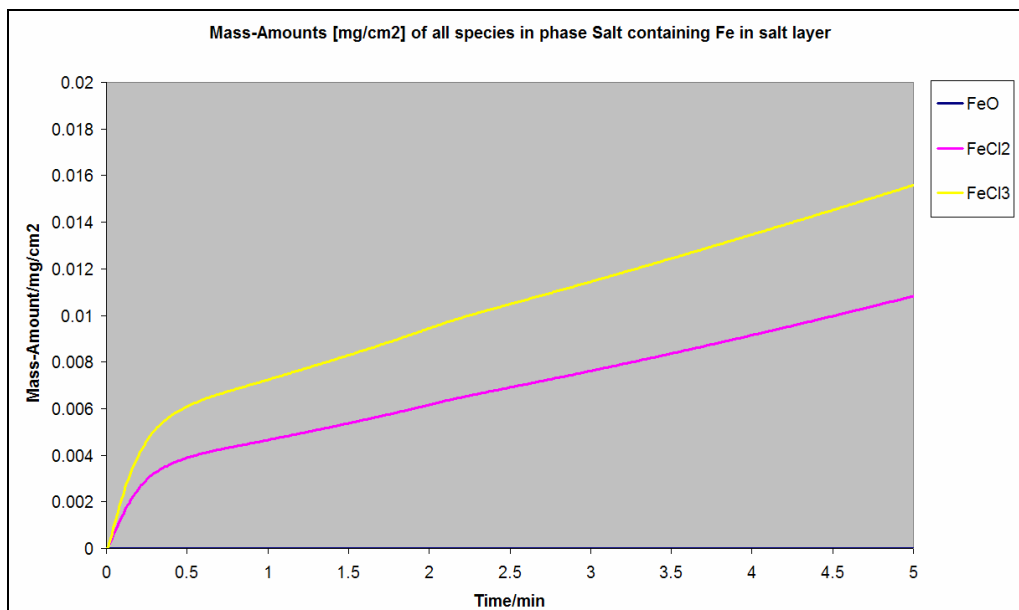


*Figure 3.2.12. Result where the x-axis is the simulation time and the y-axis values are the masses of all species in a salt phase that contains the element Fe. The masses are for the whole salt layer.*

If the x-axis in a result is the axial position, then that result can be animated in the generated workbook. That means that the x-axis and y-axis values are changed as a function of the simulation time. The time change is defined by the sampling rate parameters.
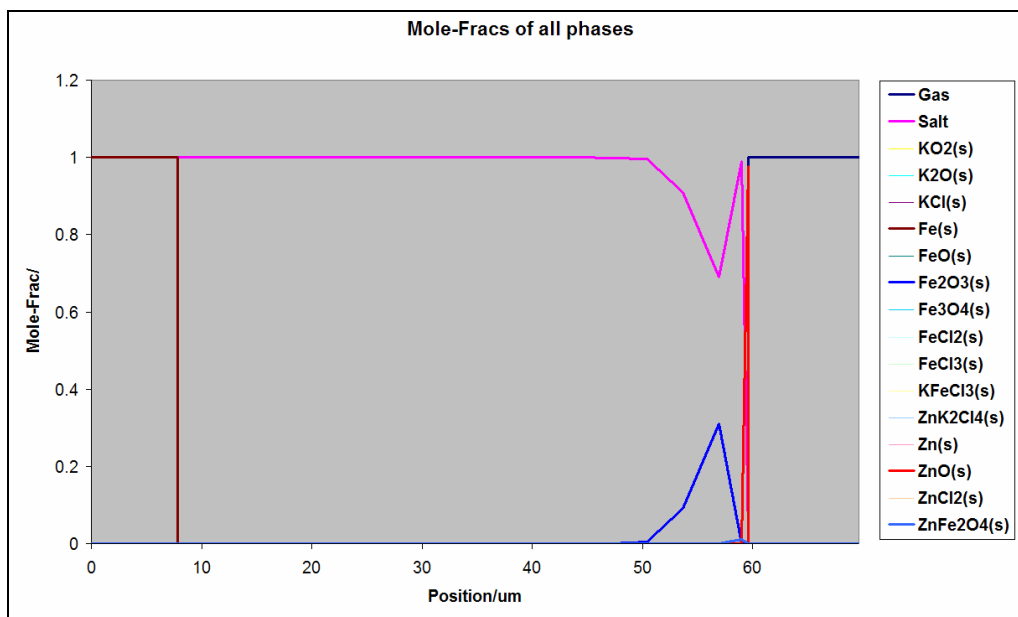
*Figure 3.2.13. Result where the x-axis is the axial position in the salt melt and the y-axis values are the mole fractions of the phases. The metal-salt interface is on the left hand side and the salt-gas interface is on the right hand side. The origin of the x-axis is the bottom of the metal layer. The chart represents the composition of the salt melt after 400 seconds.*

User can choose between several y-axis values: "mole-amount", "mass-amount", "mole-fraction", "mass-fraction", "mole-concentration", "mass concentration". All y-axis values can be applied to one or all phases, or to one or all species in the selected phase. Component can be used to mask those phases or species that contain the given component. Y-axis values can also be applied to one or all components when no phase is selected. Depending on the values in **X-Value** and **Layer** fields, the result applies to each axial position (grid nodes), an axial position at given depth from salt-gas interface, or to whole salt layer.

## 3.3  Gas precipitation model using ChemSheet

(K. Hack – GTT-Technologies)

Although the OptiCorr project was mainly oriented towards the generation of verifiable and reproducible information from dedicated corrosion experiments its link to the chemical behaviour of the "gas phase" in real power plants has also been given some attention. "gas phase" has been put in quotes intentionally since the gas that leaves the combustion chamber of a power plant does not contain gaseous species only. It is in fact a gas-plus-aerosol two phase flow. A ChemSheet model has been set up which permits, on the basis

of a given overall gas-plus-aerosol composition, investigation of the formation of precipitates from the combustion gas on cooling (see Figures 3.3.1 to 3.3.5)

The user may set the temperature range for the cooling by way of the process variable "StepIndex". This variable is increased by one after each calculation. With the total number of steps defined prior to calculation the temperature in each step can be decreased (or increased) using a simple formula (see Figure 3.3.4). The user may furthermore influence the calculation by way of a "transfer coefficient" for the aerosols and of a "sticking factor" for the precipitates (Figure 3.3.5). The former permits control of the amount of aerosols that is transferred from the combustion chamber by the gas phase (range: 0 to 1) while the latter permits in a course way to control the amount of precipitates extracted from the gas through sticking on the walls or pipes of the heat exchangers (range: 0 to 1). The calculation is activated with the toolbar "Calculate" button, Figure 3.3.6. Thus the user can investigate the influence of the amount of carry-over dusts from the combustion chamber to the heat exchangers and the level of wall-sticking of precipitates in the higher temperature range on the precipitates in the lower temperature range.

| | Input Gases | Moles | | Input Solids | Moles | Moles transfer |
|---|---|---|---|---|---|---|
| | N2 | 2.50E+08 | | SiO2(trid) | 1.94E+05 | 1.74E+05 |
| | H2O | 4.48E+07 | | Fe2O3 | 5.42E+04 | 4.88E+04 |
| | O2 | 2.79E+07 | | Al2Ca2SiO7 | 2.06E+04 | 1.86E+04 |
| | CO2 | 2.62E+07 | | Al6Si2O13 | 7.16E+03 | 6.45E+03 |
| | HCl | 2.22E+05 | | Zn2SiO4 | 2.08E+03 | 1.87E+03 |
| | NO | 8.02E+04 | | NiFe2O4 | 1.44E+02 | 1.30E+02 |
| | SO2 | 4.26E+04 | | Cr2O3 | 6.19E+01 | 5.57E+01 |
| | NaCl | 8.67E+03 | | | | |
| | HF | 7.71E+03 | | Transfer Coefficient. | 0.9 | |
| | ZnCl2 | 2.81E+03 | | | | |
| | SO3 | 1.49E+03 | | | | |
| | Cl | 1.03E+03 | | | | |
| | NO2 | 5.45E+02 | | Temperature: | 800 | |
| | Cl2 | 2.05E+01 | | Pressure: | 1 | |
| | O | 1.69E+01 | | | | |
| | CO | 1.36E+01 | | | | |
| | H2 | 1.32E+01 | | | | |
| | ClO | 8.80E+00 | | | | |
| | NiCl2 | 7.14E+00 | | | | |
| | Na2Cl2 | 5.74E+00 | | | | |
| | N2O | 5.10E+00 | | | | |
| | NaOH | 3.4122 | | | | |
| | FeCl2 | 2.0613 | | | | |
| | Zn | 1.499 | | | | |
| | H2O2 | 0.6754 | | Evaluate Graphs | | |
| | NOCl | 0.48321 | | | | |
| | NaF | 0.40719 | | | | |
| | Na2SO4 | 0.19992 | | | | |
| | Fe(OH)2 | 0.18922 | | | | |
| | AlOH | 0.16732 | | 1-Sticking Coeff.: | 0.9 | |

| Salt-liquid/NaF mol/s | Salt-liquid/NaCl mol/s | Salt-liquid/NaOH mol/s | Salt-liquid/Na2SO4 mol/s | Salt-liquid/Na2CO3 mol/s | Salt-liquid/NaNO3 mol/s | AlkCl-ss/NaC mol/s |
|---|---|---|---|---|---|---|
| 0 | 0 | 0 | 0 | 0 | 0 | |
| 0 | 0 | 0 | 0 | 0 | 0 | |

*Figure 3.3.1. The ChemSheet input screen for the gas precipitation model.*

Note: The values for the composition of the gas and the aerosol in Figure 3.3.2 and 3.3.3 have been taken from a process model for a waste incinerator. (Courtesy of M. Modigel and D. Liebig, Institut für Verfahrenstechnik, RWTH Aachen).

Figure 3.3.2. The composition of the combustion gas.



Figure 3.3.4. The temperature input box and the step formula using StepIndex.



Figure 3.3.5. The input boxes for the Transfer Coefficient of the aerosol and the sticking coefficient (1-value).
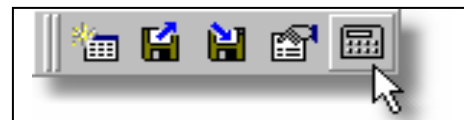


Figure 3.3.6. The ChemSheet toolbar with the "Calculate" button.



Figure 3.3.3. The composition of the aerosol.

# 3.4 References

[1]    V.B. Trindade, U. Krupp, H.-J. Christ, S. Yang and J. Gegner, Proc. 3rd International Conference on Mathematic Modeling and Computer Simulation of Materials Technologies, MMT3, 6.–10. September, Ariel, Israel (2004), 1.38–1.45.

[2]    C. Wagner, Zeitschrift für Physikalische Chemie, 1933, 21, 25.

[3]    A.P. Sutton and R.W. Balluffi, Interfaces in Crystalline Materials, Oxford University Press, Oxford 1995.

[4]    H. Teranishi, Y. Sawaragi and M. Kubota, The Sumitomo Research, 1989, 38, 63.

[5]    V.B. Trindade, U. Krupp, Ph. E.-G. Wagenhuber and H.-J. Christ, Materials and Corrosion, 2005, in press.

[6]    F. Wang and D.J. Young, Oxidation of Metals, 1997, 48, 497.

[7]    L. Heikinheimo, D. Baxter, M. Spiegel, K. Hack, U. Krupp, M. Hämäläinen and M. Arponen, Proc. 6th International Symposium on High Temperature Corrosion and Protection of Materials, Les Embiez, France, Vol. 461–464, 2004.

[8]    R.Y. Chen and W.Y.D. Yuen, Oxidation of Metals, 2003, 59, 433.

[9]    M. Schütze, online Journal of Corrosion Science and Engineering, 2003, 6.

[10]   J. Crank, The Mathematics of Diffusion, 2nd edition, Clarendon Press, Oxford 1986.

[11]   U. Krupp, V.B. Trindade, H.-J. Christ, U. Buschmann and W. Wiechert, Materials and Corrosion. 2005, in press.

# 4. Case studies – Simulation and verification

## 4.1 Use of stability diagrams

(K. Hack – GTT Technologies)

Diagrams generated with the new databases have been collected in this chapter in order to show their relevance for various aspects of the experiments in the project and also in relation to conditions in real power plants. The number of possible diagrams in the range of alloy compositions, temperatures and partial pressures is infinite. So the user has to recur to the software and databases to obtain the figure that relates exactly to his conditions. However, the present set of selected diagrams shows the versatility of the method of Gibbs energy thermodynamics in conjunction with the databases generated in the OptiCorr project.

### 4.1.1 Gas equilibria

In this section the results of equilibrium calculations for the various gases that have been used in the corrosion experiments are shown. The diagrams demonstrate that for some of the gases the assumed overall composition and thus the partial pressures of the main components, i.e. their chemical potentials, are not changed by phase internal equilibration while for others the equilibrium gas differs markedly from the nominal composition.
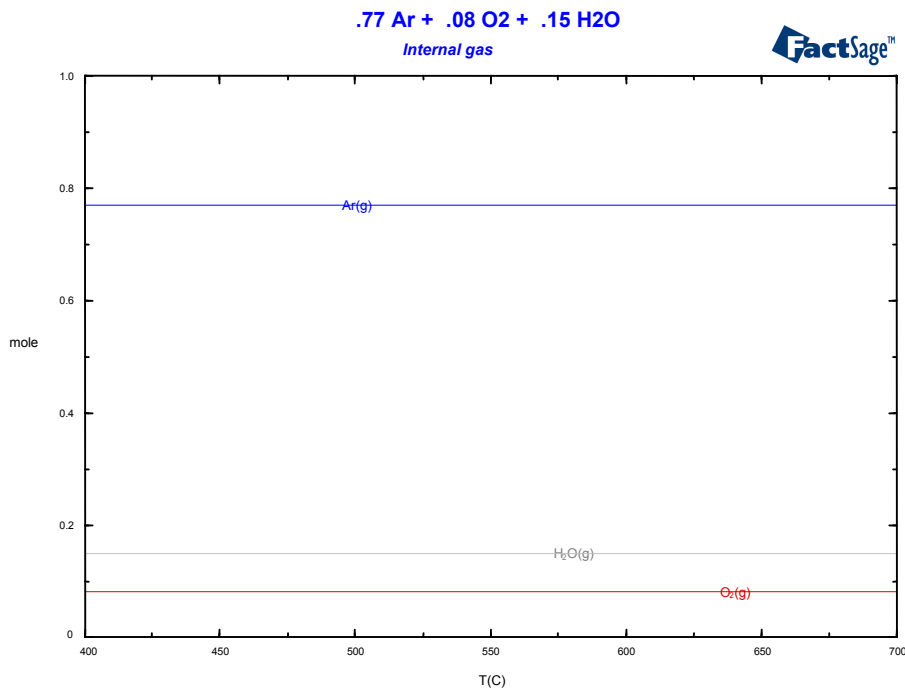


Figure 4.1.1. Gas 1 (Argon, water vapour and oxygen), major constituents.
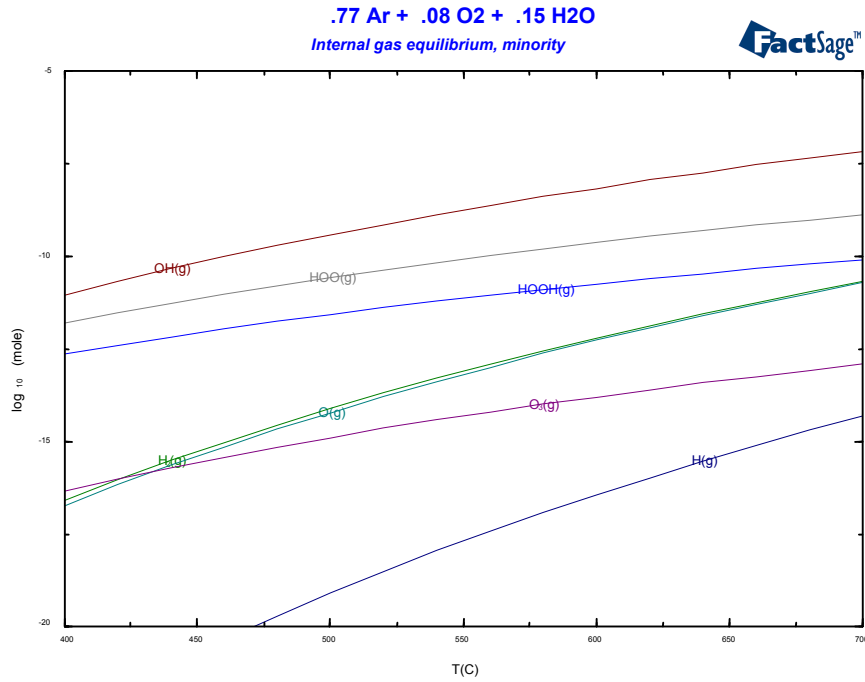
*Figure 4.1.2. Gas 1 (Argon, water vapour and oxygen), minor constituents.*

For the simple gas mixture Argon (speak nitrogen) with water vapour and oxygen the two Figures 4.1.1 and 4.1.2 show that there are no important gas internal equilibria which would require adjustment of the assumption that the gas produces an oxygen potential as set by the input amounts.
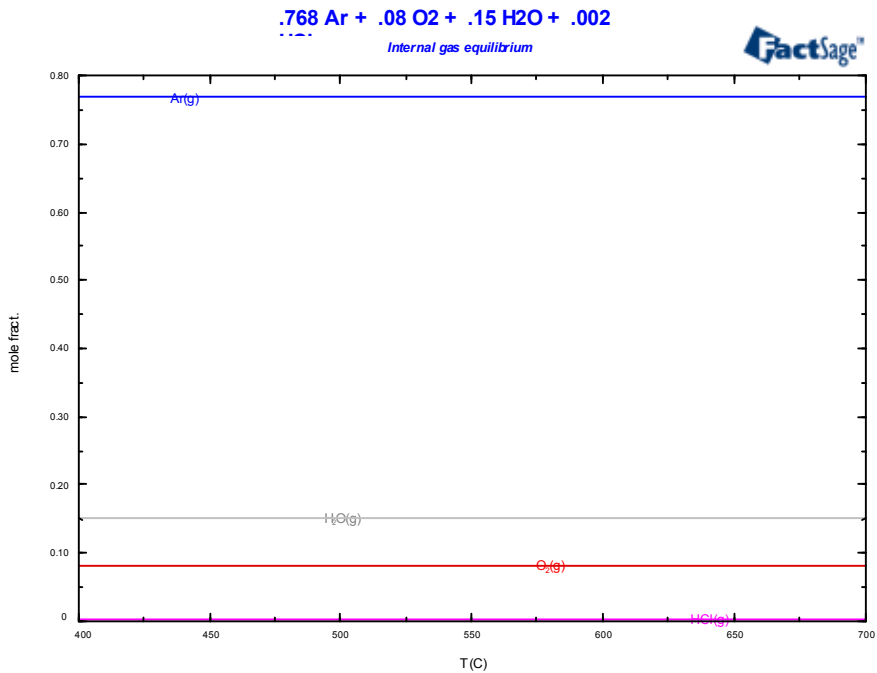


*Figure 4.1.3. Gas 2 (Argon, water vapour, oxygen and HCl), major constituents.*
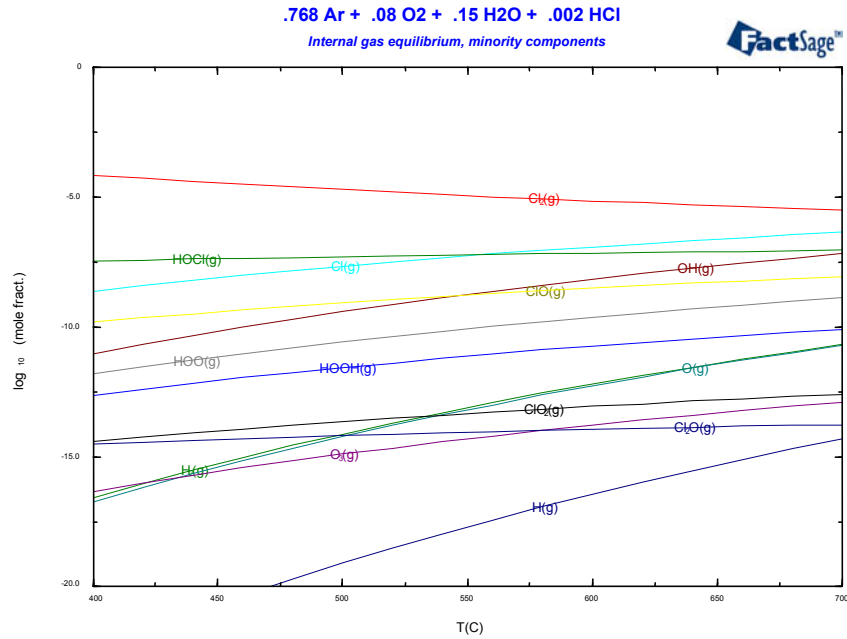
*Figure 4.1.4. Gas 2 (Argon, water vapour, oxygen and HCl), minor constituents.*

Figures 4.1.3 shows that the assumed partial pressure of HCl is kept constant throughout the entire temperature range. It must however also be noted that the resulting $Cl_2$ potential (Figure 4.1.4) is only approximately constant, its value dropping from slightly above $10^{-5}$ atm to just below the temperature range considered.
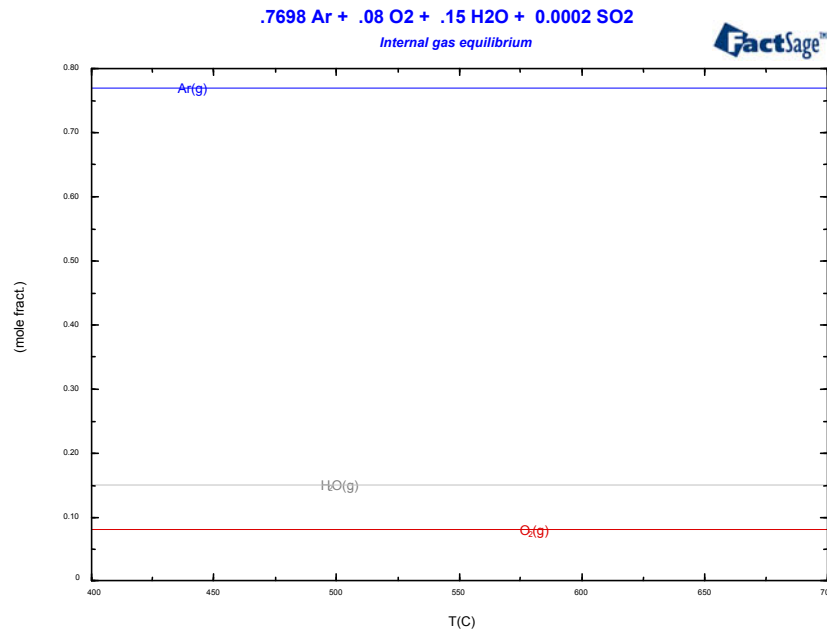


*Figure 4.1.5. Gas 3 (Argon, water vapour, oxygen and SO₂), major constituents.*
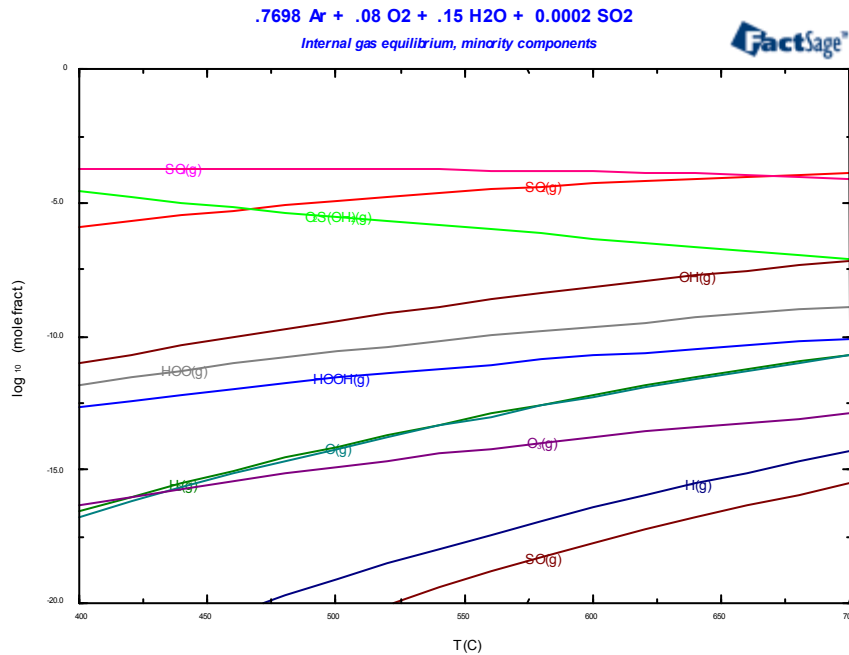
*Figure 4.1.6. Gas 3 (Argon, water vapour, oxygen and SO₂), minor constituents.*

Figures 4.1.5 and 4.1.6 show the phase internal behaviour of a gas with Argon, water vapour, oxygen and $SO_2$. For Argon, $H_2O$ and $O_2$ the partial pressures are constant throughout the temperature range (Figure 4.1.5), however, the behaviour of $SO_2$ is strikingly different from what is assumed (P($SO_2$)=$2*10^{-4}$ atm). It is the $SO_3$ partial pressure which is almost constant (~$1.5 \ 10^{-4}$) while the $SO_2$ pressure ranges from ~$10^{-6}$ to ~$1.19 \ 10^{-4}$ across the T-range.

## 4.1.2 Alloy phase mappings

In this section the one-dimensional phase mappings for selected alloys used in the project are shown. For the calculations it was assumed that full equilibration will take place, also at low temperatures. Thus some of the austenitic alloys show behaviour that may differ from the real case because in reality the room temperature state is usually a frozen-in equilibrium from some higher temperature.

The alloys shown here are X20 (a 10.28Cr ferritic steel), Alloy 625 (a Ni based 19Cr8.9Mo alloy), Sanicro28 (an Fe26.65Cr30.60Ni alloy) and a ferritic 2.25Cr steel 2.25Cr-1Mo(3GH).

The phase mappings for steel X20 are presented in Figures 4.1.7–4.1.12.
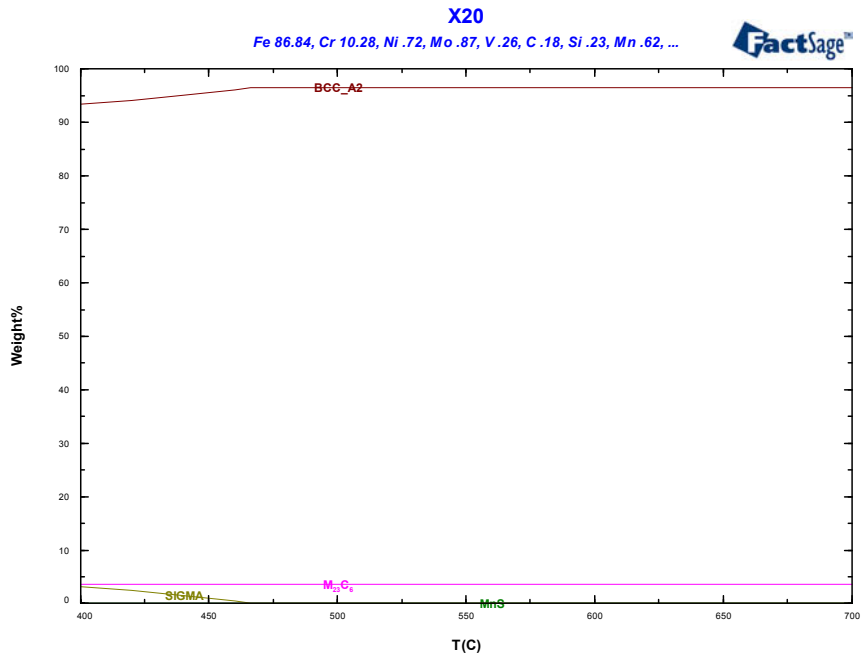


*Figure 4.1.7. The major phases of the X20 steel.*
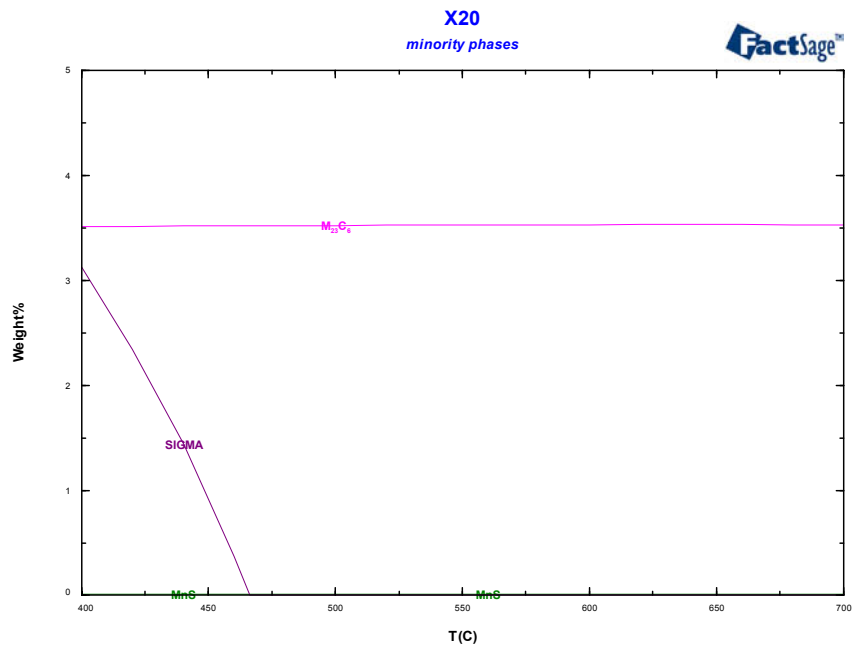


*Figure 4.1.8. The major phases of an X20 steel, details.*
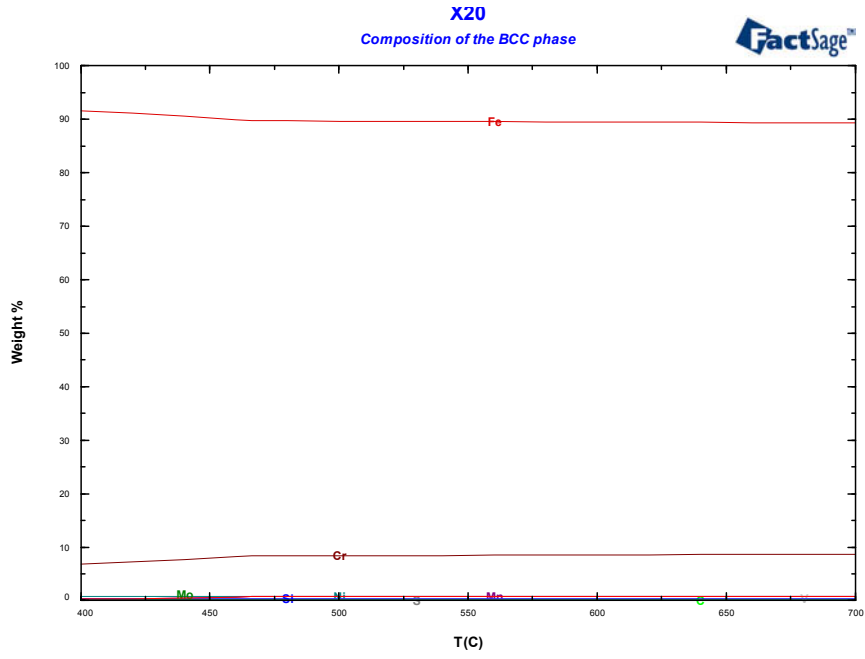
*Figure 4.1.9. The composition of the BCC phase in an X20 steel.*
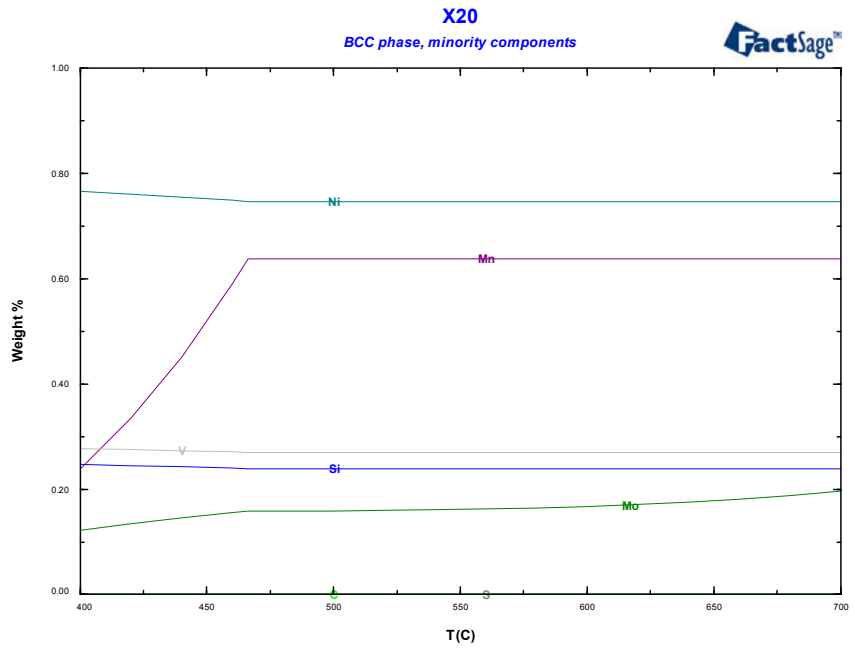


*Figure 4.1.10. The composition the BCC phase in an X20 steel, minor constituents.*
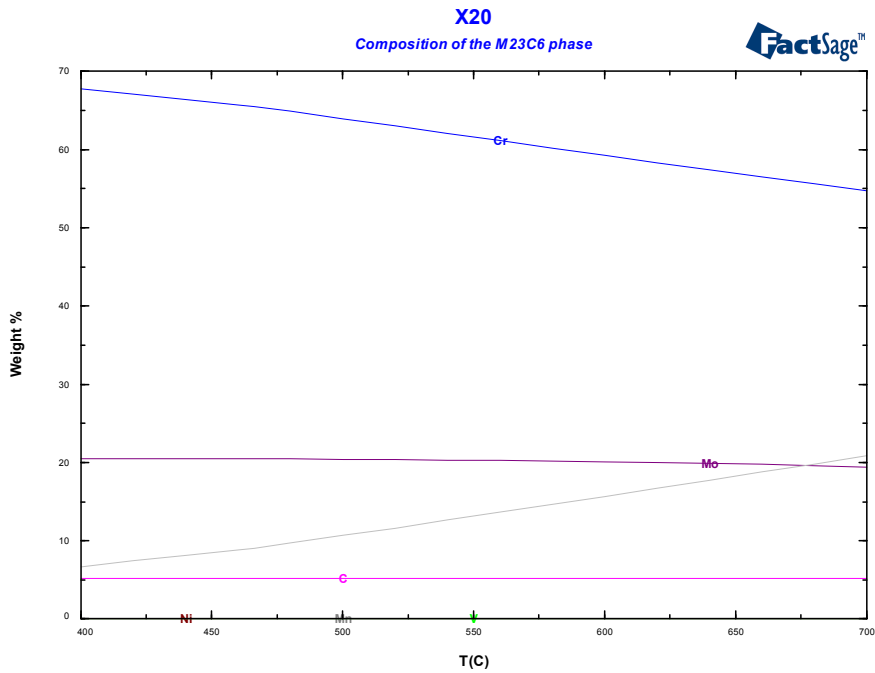
*Figure 4.1.11. The composition of the $M_{23}C_6$ phase in an X20 steel.*
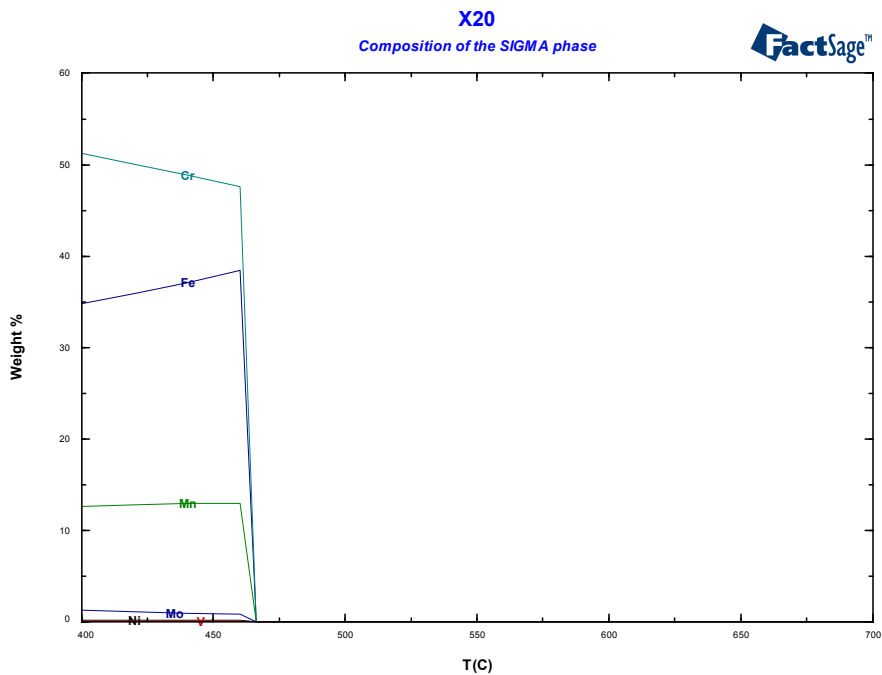


*Figure 4.1.12. The composition of the SIGMA phase in an X20 steel.*

The X20 steel shows a classical ferrite steel behaviour with a BCC_A2 matrix. The precipitates $M_{23}C_6$ and MnS are very constant throughout the entire temperature range while the small amount of SIGMA phase that forms under equilibrium conditions at lower temperatures will most likely not occur in practice since the temperatures are too low for equilibration.

The phase mappings for alloy 625 are presented in Figures 4.1.13–4.1.16.
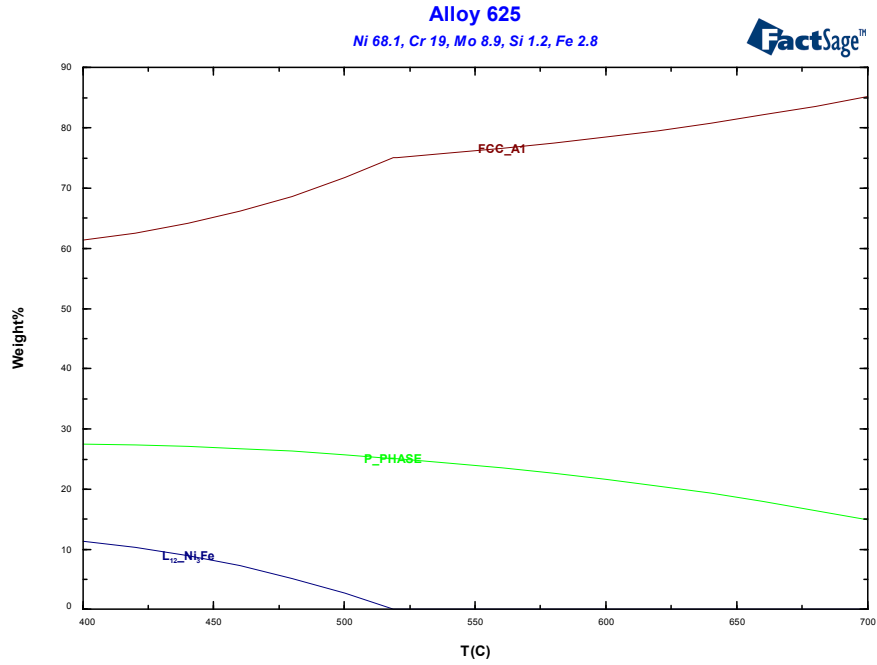


*Figure 4.1.13. The major phases of Alloy 625 (Ni-based Cr-Mo alloy).*
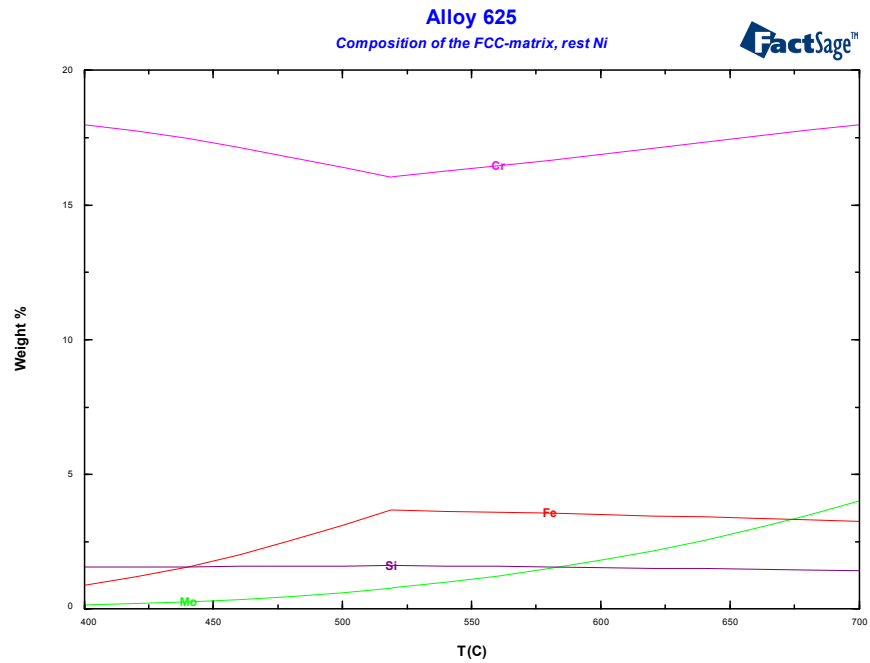


*Figure 4.1.14. The composition of the FCC phase in Alloy 625 (Ni-based Cr-Mo alloy).*
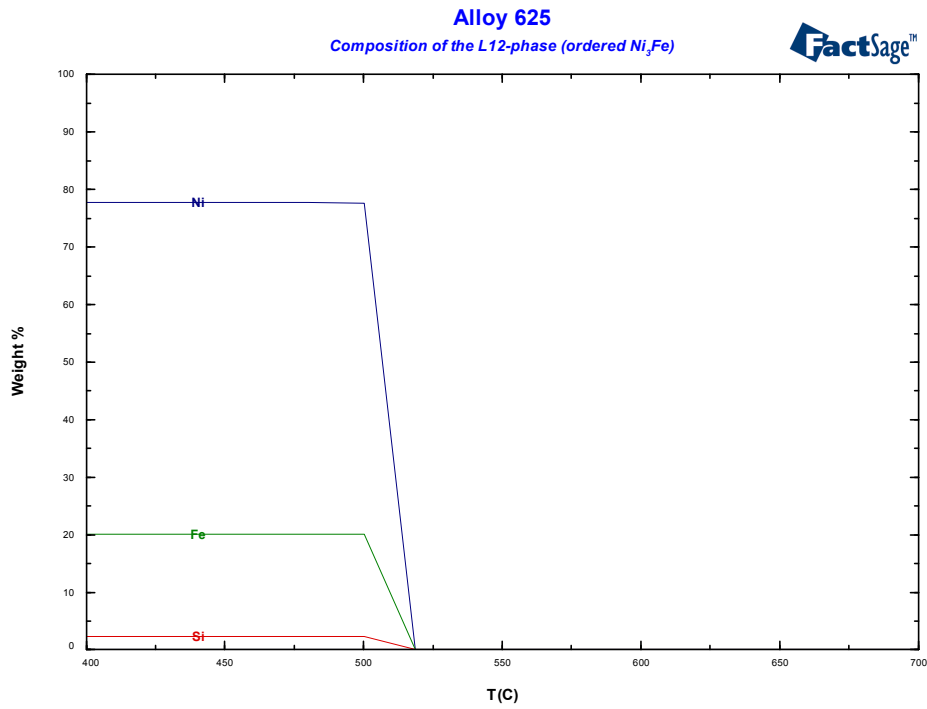
*Figure 4.1.15. The composition of the L12 phase in Alloy 625 (Ni-based Cr-Mo alloy).*
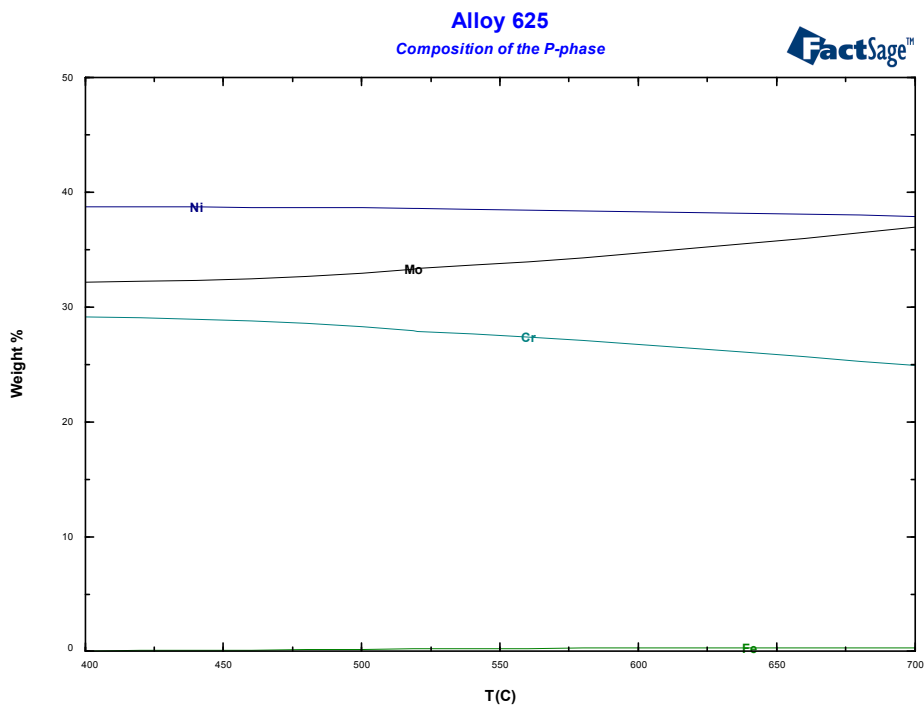


*Figure 4.1.16. The composition of the P-phase in Alloy 625 (Ni-based Cr-Mo alloy).*

The phase mappings for Sanicro 28 are presented in Figures 4.1.17–4.1.22.
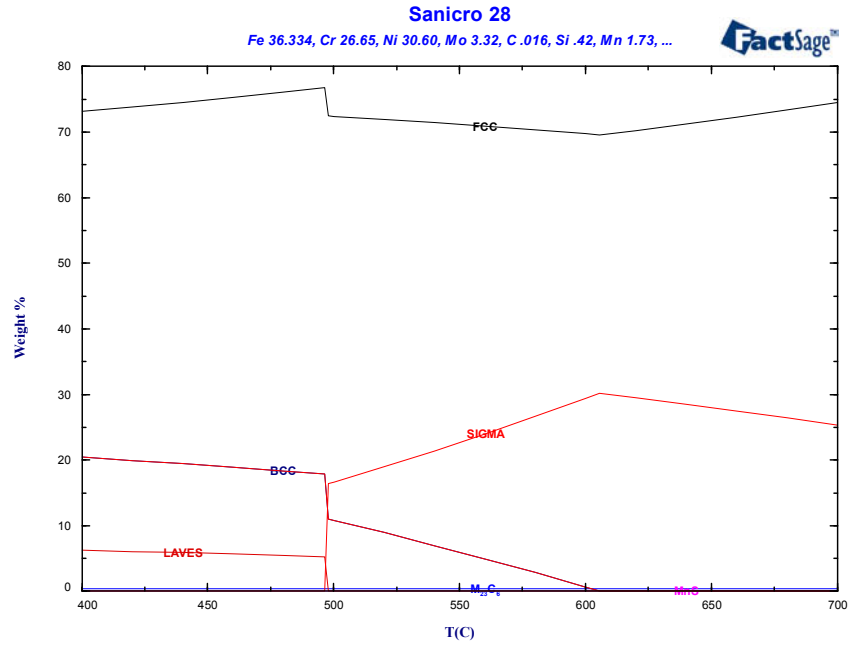


Figure 4.1.17. The major phases of Sanicro 28 (FeCrNi-based alloy).
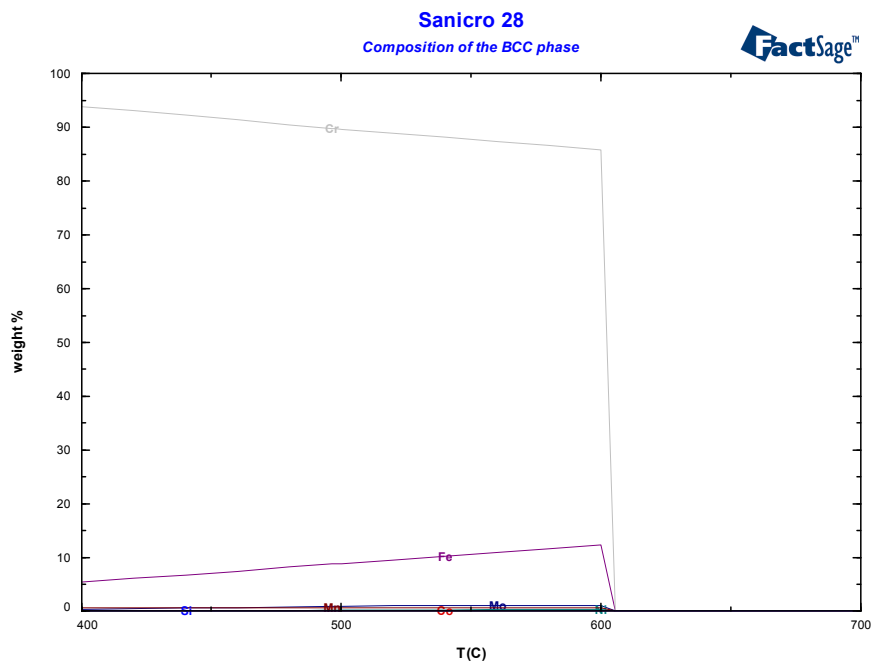


Figure 4.1.18. The composition of the BCC phases in Sanicro 28 (FeCrNi-based alloy).
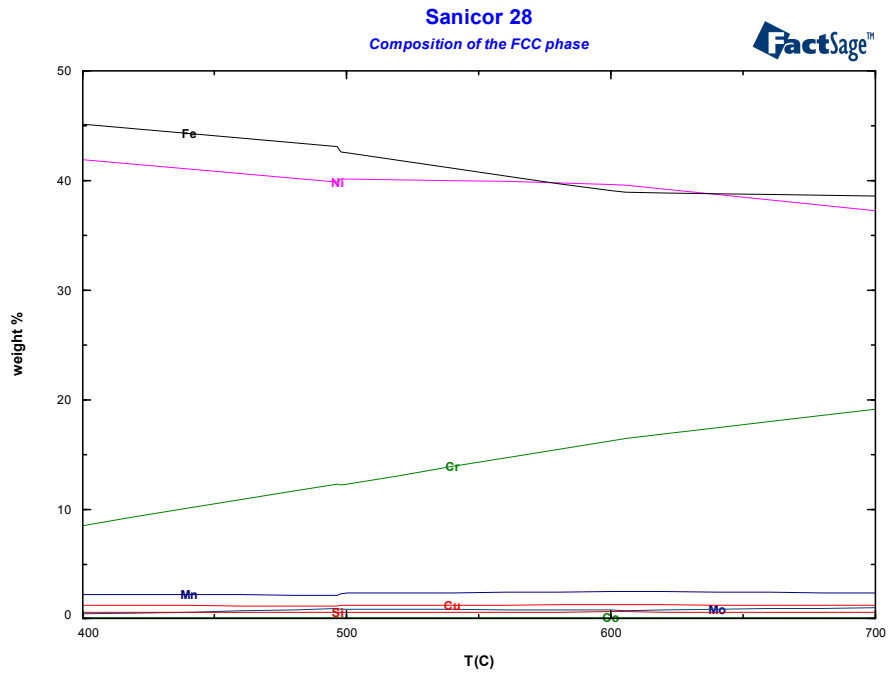
*Figure 4.1.19. The composition of the FCC phase in Sanicro 28 (FeCrNi-based alloy).*
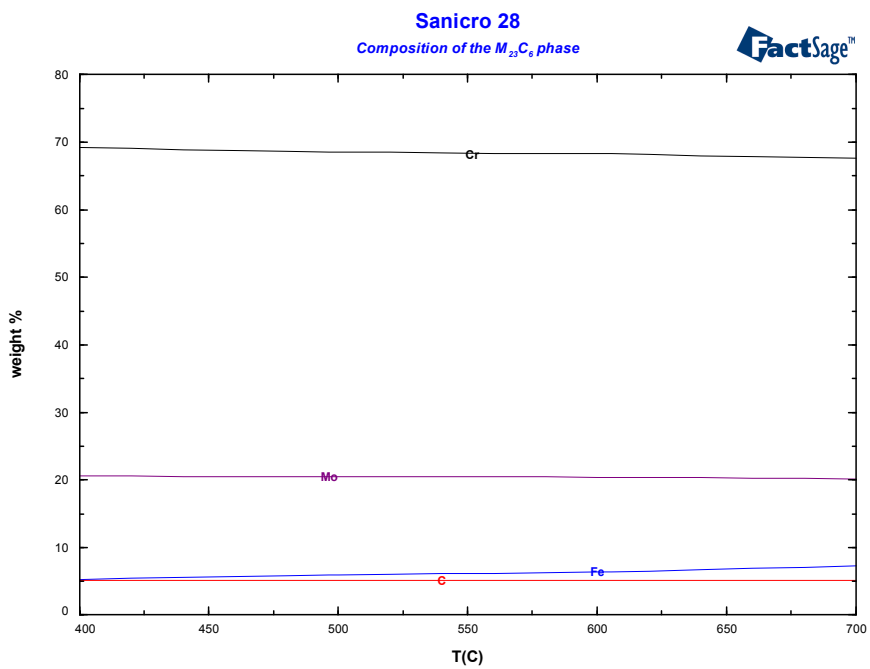


*Figure 4.1.20. The composition of the $M_{23}C_6$ phase in Sanicro 28 (FeCrNi-based alloy).*
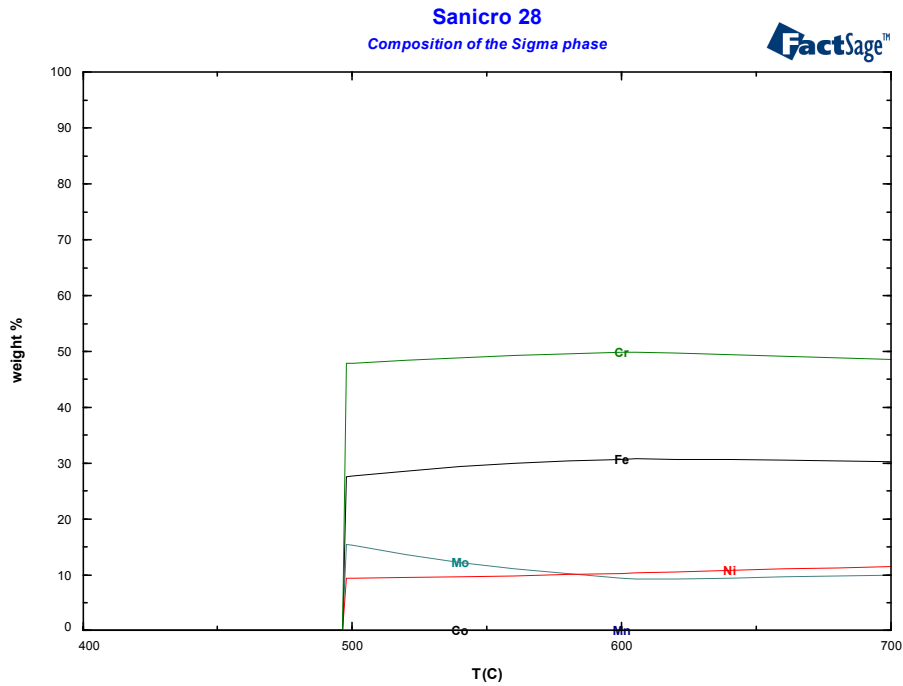
*Figure 4.1.21. The composition of the SIGMA phase in Sanicro 28 (FeCrNi-based alloy).*
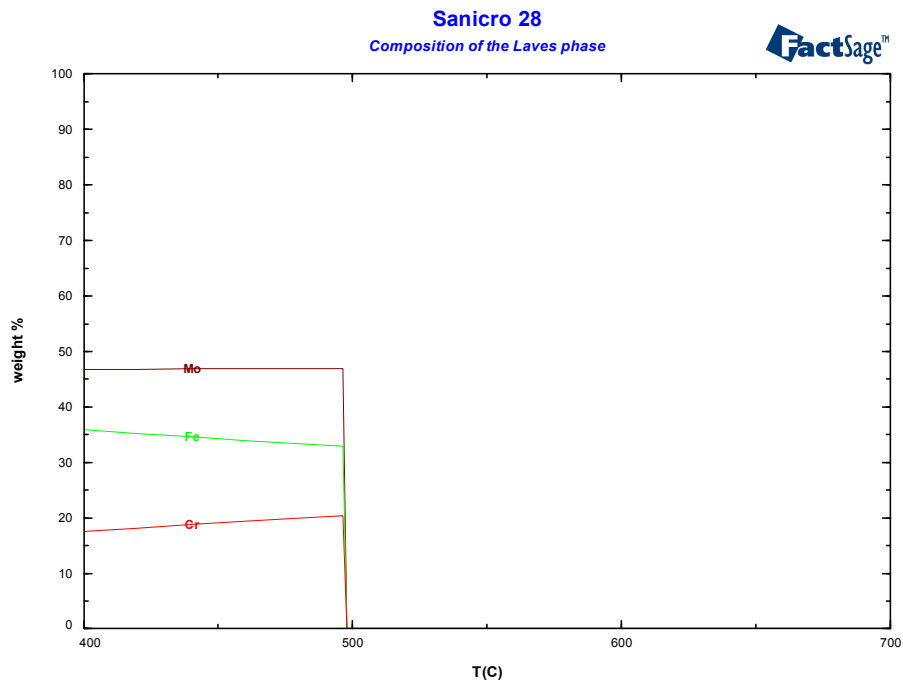


*Figure 4.1.22. The composition of the Laves phase in Sanicro 28(FeCrNi-based alloy).*

Sanicro 28 is a complex alloy because of its fairly high amounts of three major components. The phase distribution shows this very clearly (Figure 4.1.17). Under equilibrium conditions an appreciable amount of Sigma phase will occur at higher temperatures

while at lower temperatures other intermetallic phases, e.g. the Laves phase, occur. However, in practice this alloy is given elaborate heat treatment at higher temperatures. The frozen-in state is Sigma free. Furthermore, practical tests showed that if the sigma phase forms at lower temperatures it precipitates in very small particles, which might even have a hardening effect similar to the carbides that are formed.

The 2.25Cr-1Mo steel, with only 2.25% Cr and all other alloying components under 1%, is a classical low alloyed ferritic boiler steel. The figure series 4.1.23 to 27 shows that under equilibrium conditions at higher temperatures a constant amount of $M_{23}C_6$ will be formed while at lower temperatures a small amount of $M_6C$ will form. In addition the small amount of S in the alloy is sufficient to bind Mn in the MnS phase.
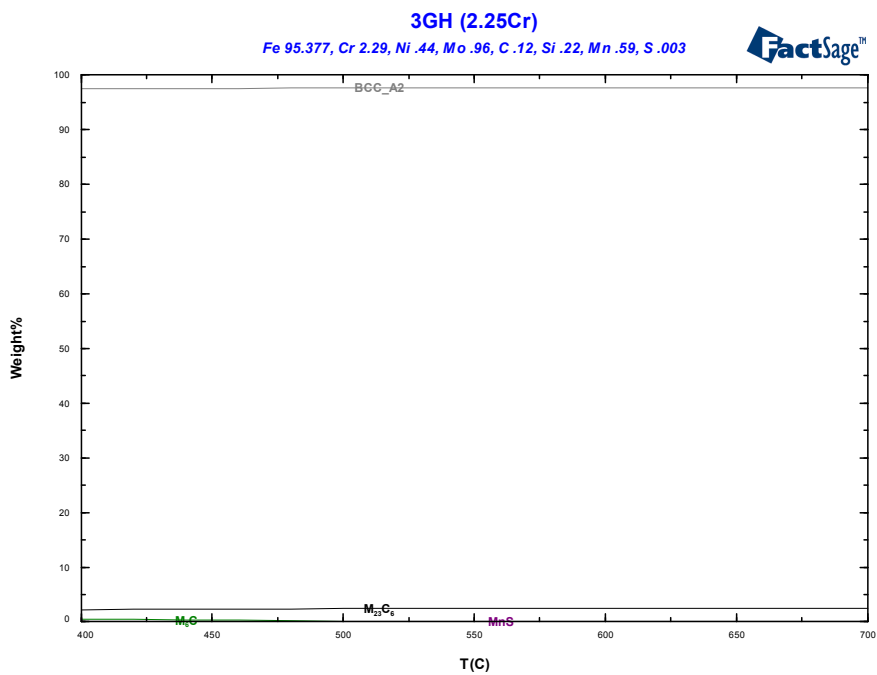


*Figure 4.1.23. The major phases of 2.25Cr-1Mo (a ferritic steel).*
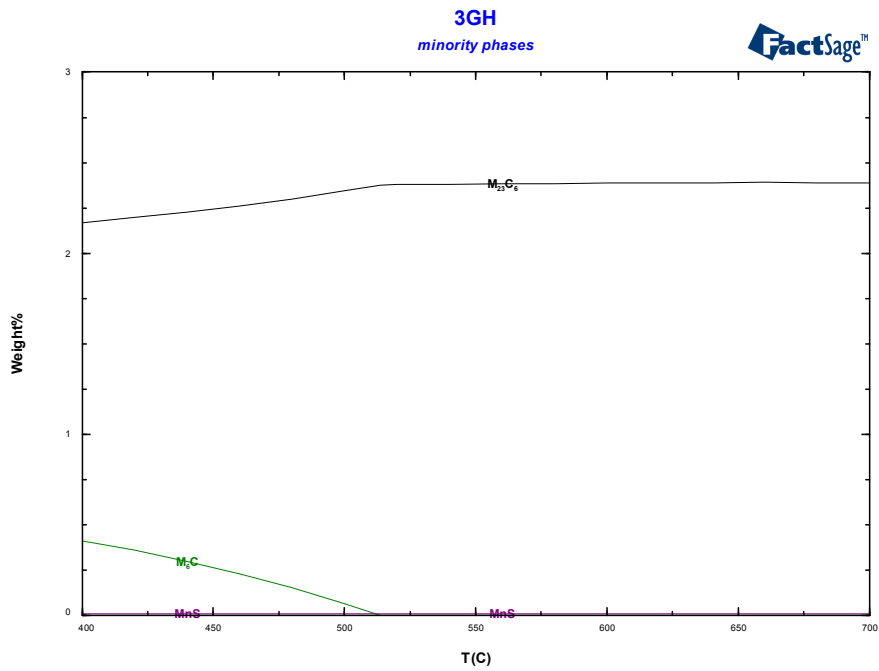
*Figure 4.1.24. The minor phases of 2.25Cr-1Mo (a ferritic steel).*
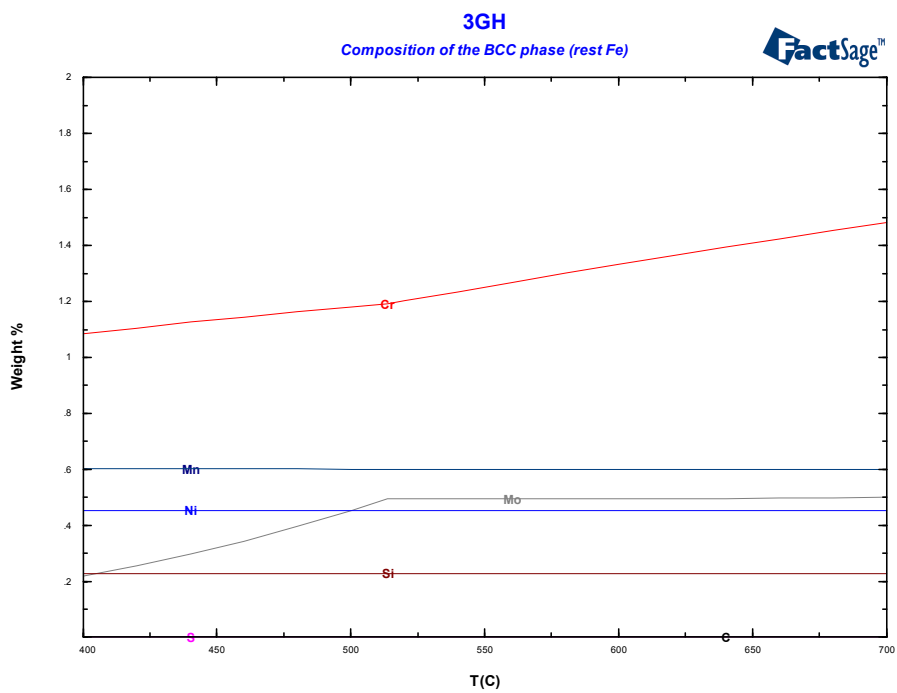


*Figure 4.1.25. The composition of the BCC phase in 2.25Cr-1Mo (a ferritic steel).*
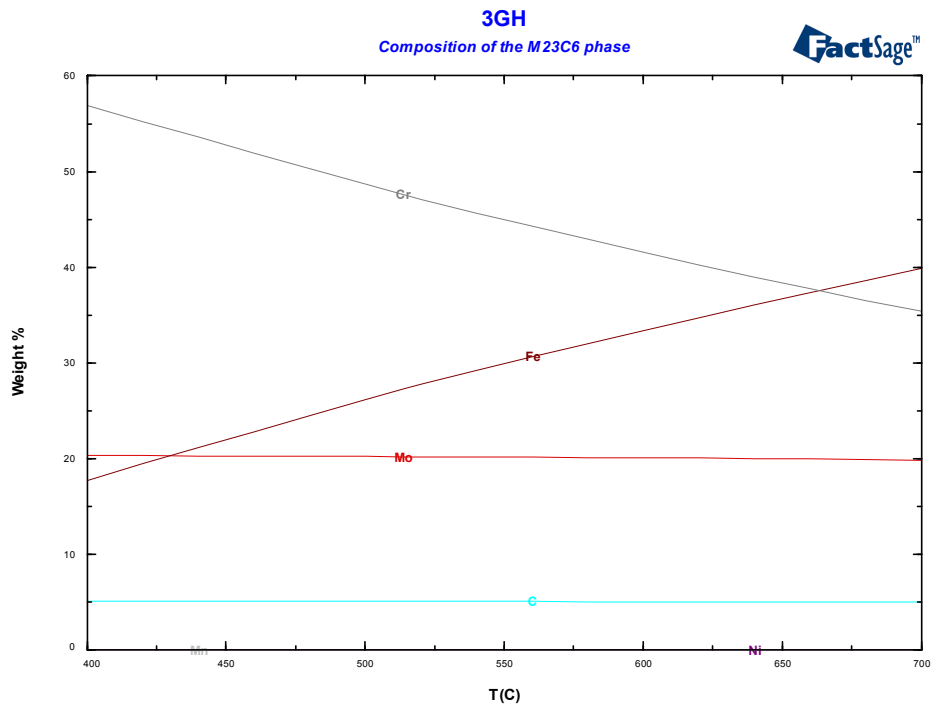
*Figure 4.1.26. The composition of the $M_{23}C_6$ phase in 2.25Cr-1Mo (a ferritic steel).*
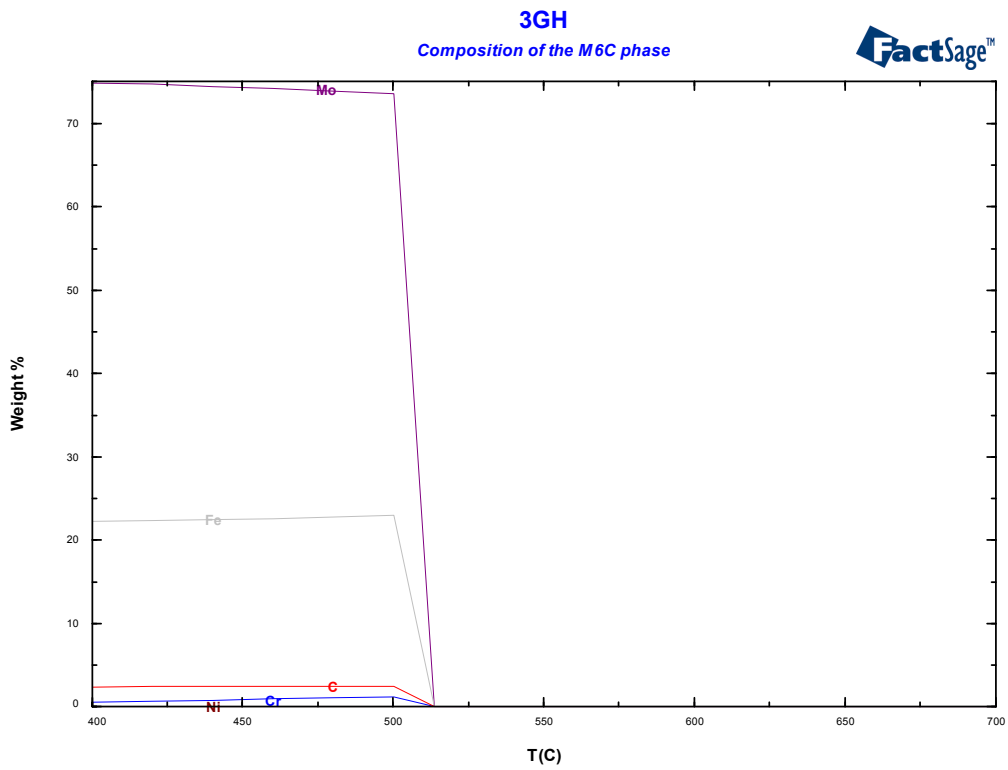


*Figure 4.1.27. The composition of the $M_6C$ phase in 2.25Cr-1Mo (a ferritic steel).*

## 4.1.3  Salt phase diagrams

In this section two-dimensional phase mappings for two and three component salts as used in the experiments of the OptiCorr project are shown. Especially with respect to the MeClx-KCl-ZnCl$_2$ systems with Me = Fe, Cr and Ni the phase diagrams correlate very well with the trends found in the corrosion experiments. The higher the solubility of the respective MeClx the greater the tendency for corrosion. For Fe it is considerably higher than for Cr, while Ni shows virtually no corrosion under a salt layer.

Figures for mixed salts, e.g. chlorides with sulphates, are given here to show the potential of the method. Corresponding experimental conditions have not been investigated in the project.
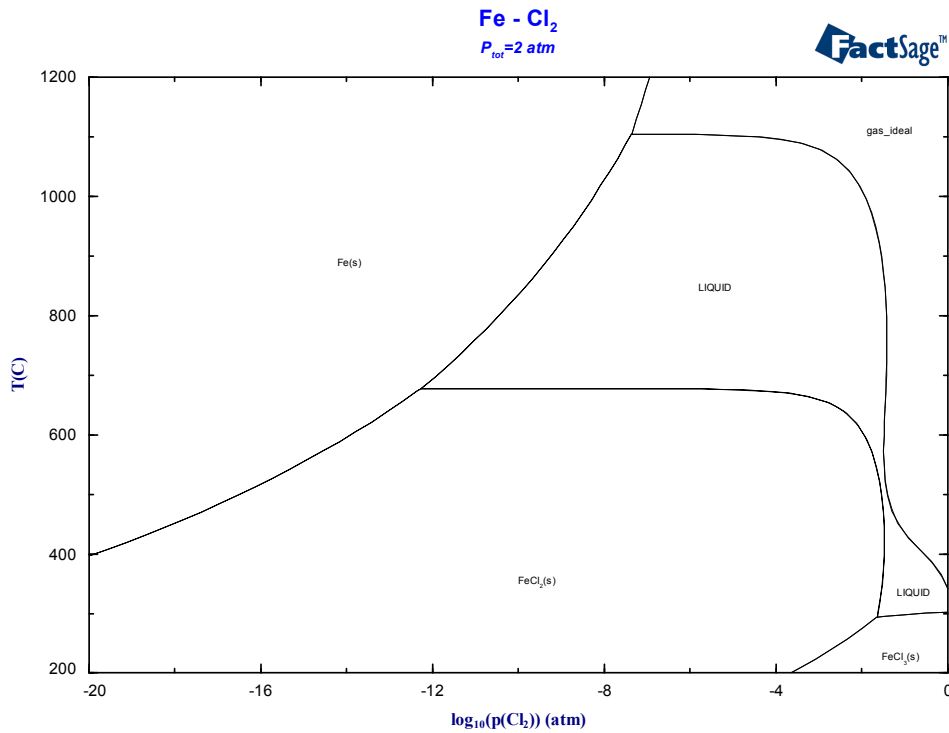


*Figure 4.1.28. The Fe-Cl system with T vs P(Cl$_2$) and a total pressure of 2 atm.*

Figure 4.1.28 shows the behaviour of pure iron under a Cl$_2$ atmosphere and variable temperatures. In the temperature range shown Fe will be solid BCC_A2 while the resulting salts may be either solid (stoichiometric FeCl$_2$ or FeCl$_3$). The liquid that is formed is a single phase two-component solution which contains both di-valent and tri-valent Fe simultaneously. The amounts of these two species depend strongly upon the Cl$_2$-partial pressure. It should be noted that the compositions along the vertical range of the liquid-solid curve are mainly dominated by tri-valent Fe while the horizontal part is mainly di-valent. This can unfortunately not be seen directly from the diagram, but the

FactSage program permits point calculations inside the diagram that revealed this behaviour (see Table 4.1.1).

*Table 4.1.1. Equilibrium composition of the salt melt in the Fe-Cl$_2$ system for T = 317.31, log p(Cl$_2$) = -1.444 and P$_{total}$ = 2 atm.*

```
T = 317.31 C
P = 2.00000E+00 atm
V = 0.00000E+00 dm³

STREAM CONSTITUENTS      AMOUNT/mol
Fe                 1.0000E+00
*Cl₂               1.4329E+00

                  EQUIL AMOUNT  MOLE FRACTION    FUGACITY
PHASE: gas_ideal       mol                atm
Fe₂Cl₆           0.0000E+00   9.3749E-01    5.6217E-01
Cl₂              0.0000E+00   5.9931E-02    3.5938E-02
FeCl₃            0.0000E+00   2.5801E-03    1.5472E-03
FeCl₂            0.0000E+00   4.5962E-09    2.7561E-09
Cl               0.0000E+00   4.1307E-09    2.4770E-09
Fe₂Cl₄           0.0000E+00   2.6218E-11    1.5722E-11
FeCl             0.0000E+00   2.1034E-39    1.2613E-39
Fe               0.0000E+00   6.0309E-51    3.6165E-51
TOTAL:           0.0000E+00   1.0000E+00    2.9983E-01
PHASE: LIQUID      mol      MOLE FRACTION    ACTIVITY
FeCl₂            1.3422E-01   1.3422E-01    4.0943E-02
FeCl₃            8.6578E-01   8.6578E-01    8.4554E-01
TOTAL:           1.0000E+00   1.0000E+00    1.0000E+00
                   mol              ACTIVITY
FeCl₂(s)         0.0000E+00          8.6543E-01
FeCl₃            0.0000E+00          6.8875E-01
Fe_BCC_A2        0.0000E+00          7.6388E-23
Fe_FCC_A1        0.0000E+00          4.2165E-23
******************************************************************
 Cp_EQUIL    H_EQUIL    S_EQUIL    G_EQUIL    V_EQUIL
  J.K-1       J       J.K-1      J        dm³
******************************************************************
 1.30140E+02 -3.20498E+05  2.81515E+02  -4.86721E+05  0.00000E+00

Mole fraction of the ionic constituents in LIQUID:
Fe[2+]            1.3422E-01   Stoichiometry calculated
Fe[3+]            8.6578E-01
-------------------------------------------------------------
Cl               1.0000E+00   Stoichiometry calculated
```

The following three figures (4.1.29 to 31) show the relevant binary subsystems of the FeCl$_2$-KCl-ZnCl$_2$ ternary salt system. These have been treated like normal binaries and combined into a "normal" ternary. However, as can be seen from Figure 4.1.28 the transition from di-valent to tri-valent Fe is dependent upon the chlorine partial pressure. Thus for a complete understanding of the Fe-K-Zn-Cl system it is also necessary to have information on the FeCl$_3$-KCl-ZnCl$_2$ system. This information has been generated in the

OptiCorr project. Thus the ternary system FeClx-KCl-ZnCl$_2$ can be calculated for a fixed partial pressure of Cl$_2$. Figures 4.1.32–4.1.34 show the behaviour of the system at very low P(Cl$_2$) where it is equivalent to the classical FeCl$_2$-KCl-ZnCl$_2$ diagram. Figure 4.1.32 show the system for P(Cl$_2$) = 10$^{-5}$ atm. In this partial pressure range the liquid does indeed contain an appreciable amount of trivalent Fe while the solid chloride is still FeCl$_2$.
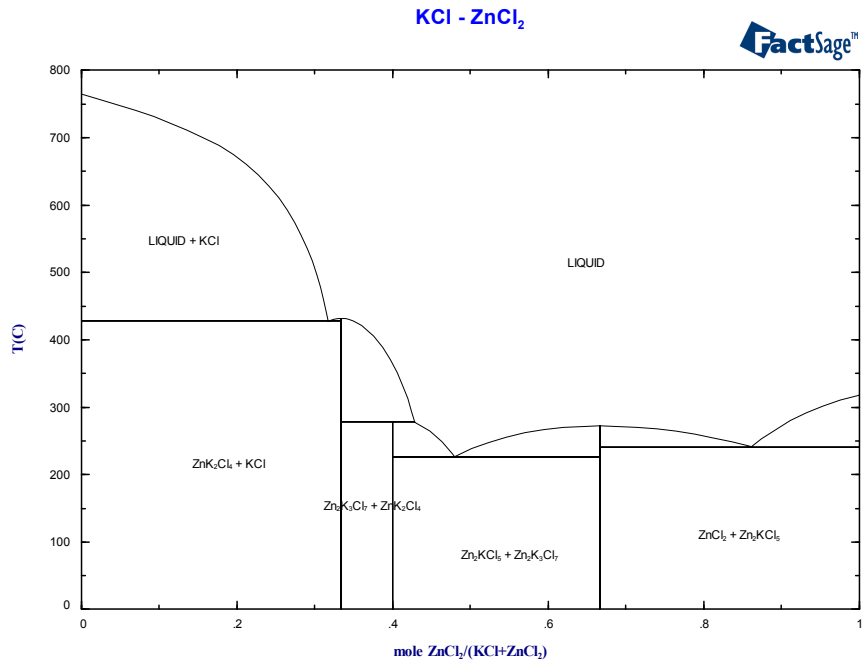


*Figure 4.1.29. KCl-ZnCl$_2$ calculated from present database.*
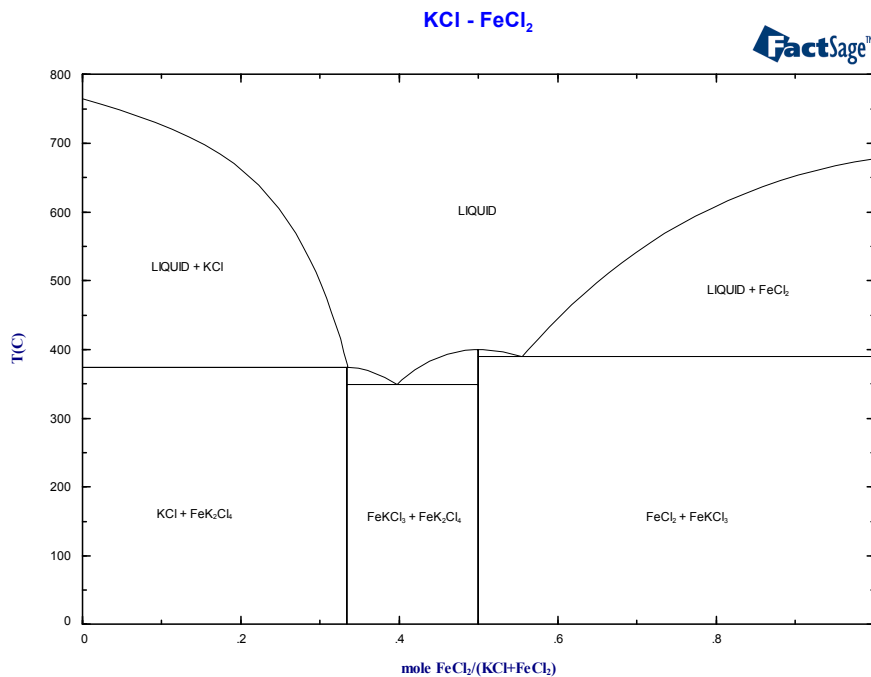


*Figure 4.1.30. KCl-FeCl$_2$ calculated from the present database.*
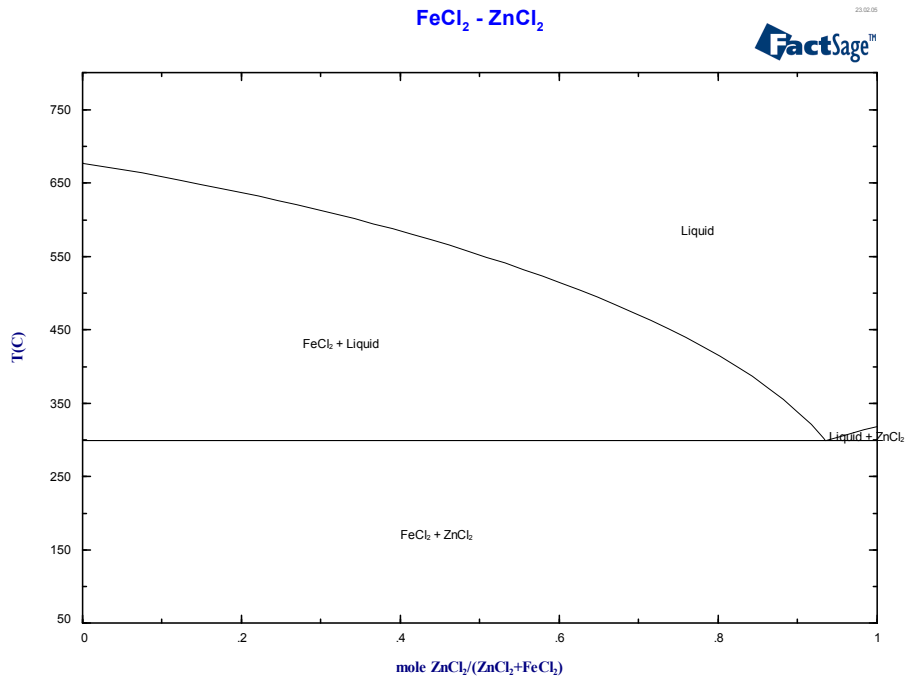
*Figure 4.1.31. FeCl₂-ZnCl₂ calculated from the present database.*
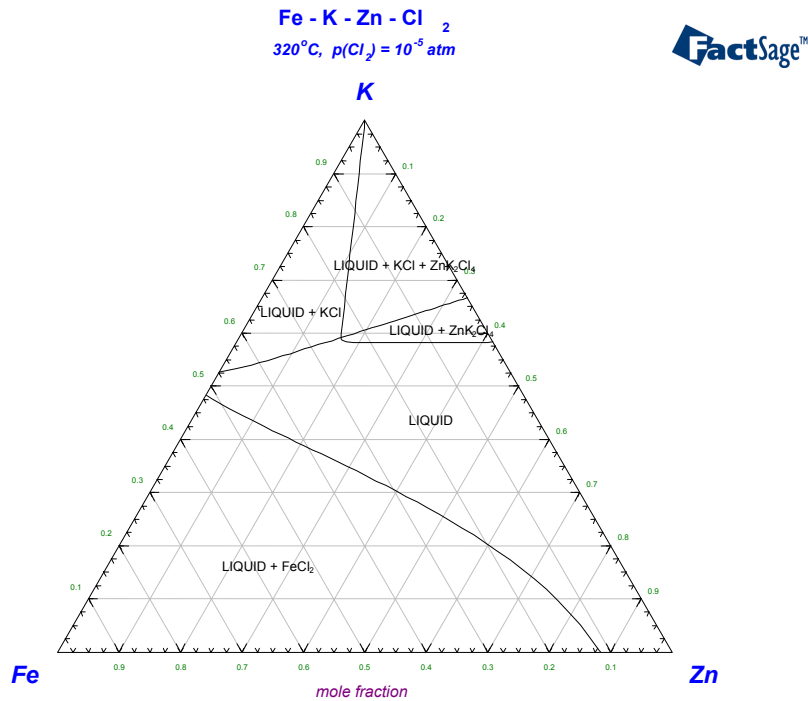


*Figure 4.1.32. FeClₓ-KCl-ZnCl₂, T = 320°C with fixed P(Cl₂) = 10⁻⁵ atm.*

The above figure represents a realistic value for the $Cl_2$ partial pressure and incorporates for the liquid phase a composition that contains both di-valent and tri-valent iron.

83
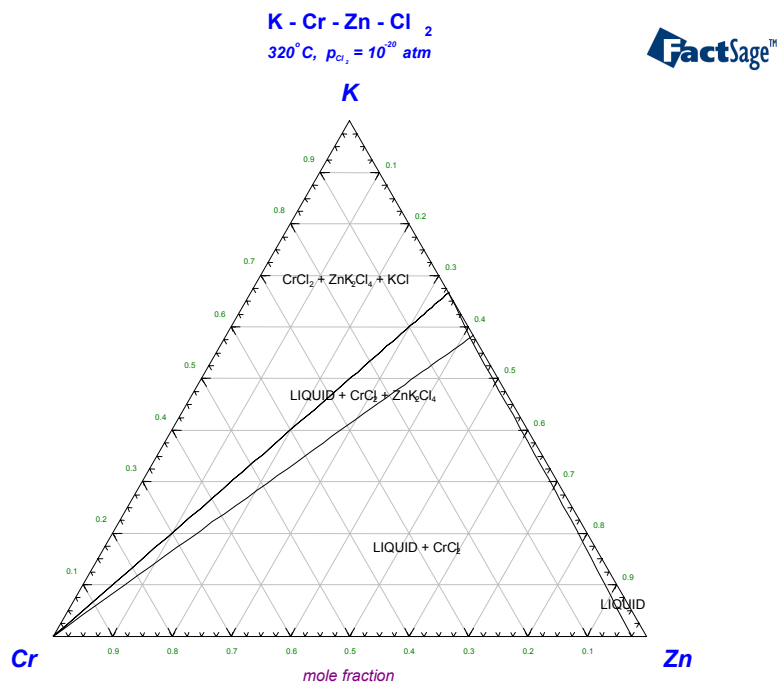
*Figure 4.1.33. CrClx-KCl-ZnCl$_2$, T = 320°C with fixed P(Cl$_2$) = 10$^{-20}$ atm.*

Figure 4.1.33 shows the behaviour of the K-Cr-Zn-Cl$_2$ system for 320°C and a very small chlorine partial pressure of 10$^{-20}$ atm. The very small pressure was chosen to be able to show a clearly visible range of stability of the pure liquid phase. The figure can be read as the KCl-CrCl$_2$-ZnCl$_2$ system. Under normal condition of the chlorine potential (~10$^{-5}$) there is hardly a range for the pure liquid state visible.

**KCl - NiCl₂ - ZnCl₂**
*Liquidus Surface between 300 and 1000 °C*
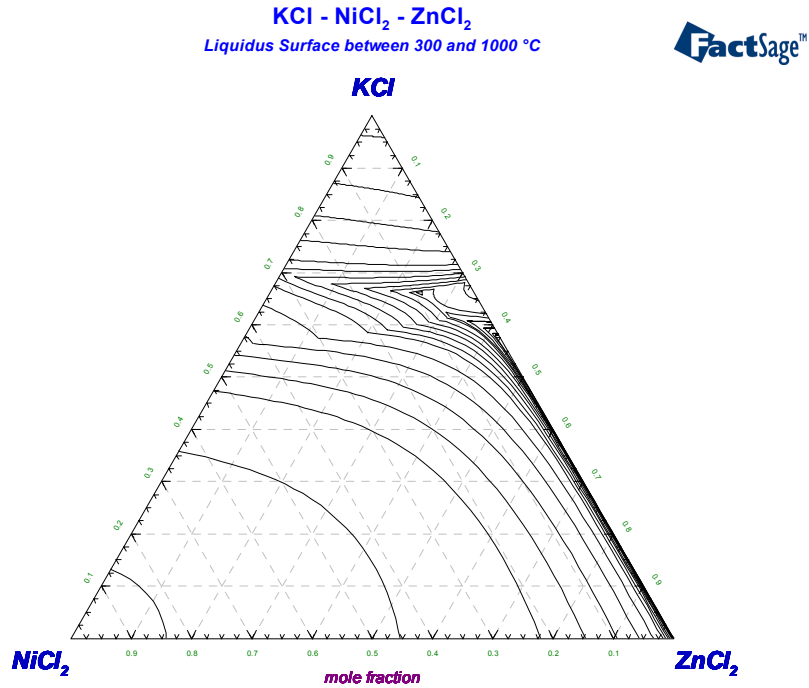
*Figure 4.1.34. NiCl₂-KCl-ZnCl₂, liquidus projection, 300C < T/°C < 1000.*

Figure 4.1.34 has been generated to show the melting behaviour of the entire KCl-NiCl₂-ZnCl₂ system. It also demonstrates the capabilities of the Phase Diagram module of FactSage.

It is possible to select a single phase for plotting although all phase equilibria are calculated. Thus by selection of the Liquid phase as the phase for plotting all phase boundaries are shown which relate to the primary fields of solidification. For the KCl-NiCl₂-ZnCl₂ system it is obvious that at high temperatures the primary phase field for NiCl₂ dominates the system while at lower temperatures KCl and later the double salts are important. However, the lowest temperatures of stable liquid occur along the KCl-ZnCl₂ edge where the liquid does only dissolve very small amounts of NiCl₂. This is fully consistent with the corrosion behaviour of pure Ni as investigated in the project. It was found that virtually no corrosion occurs in finite times.

The present database also permits the interaction of the major alloying components under salt forming conditions to be investigated. This is shown for the combination Fe and Cr in Figure 4.1.35 where the temperature versus log partial pressure plot for a given Cr mole fraction is depicted.
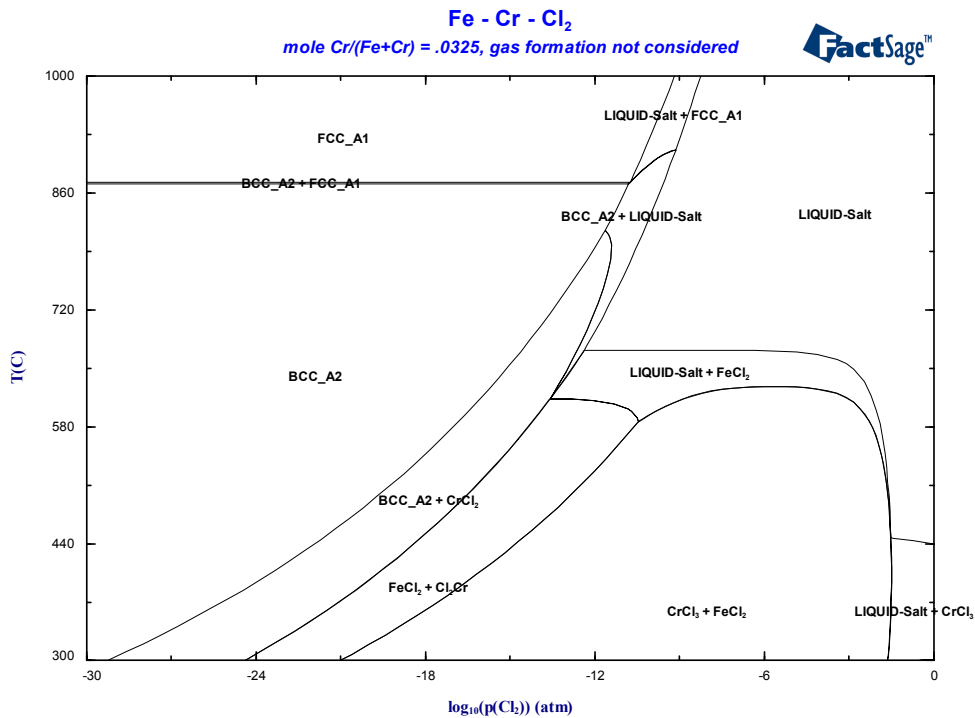
*Figure 4.1.35. An Fe 3.25Cr alloy in a chlorine atmosphere with variable temperature.*
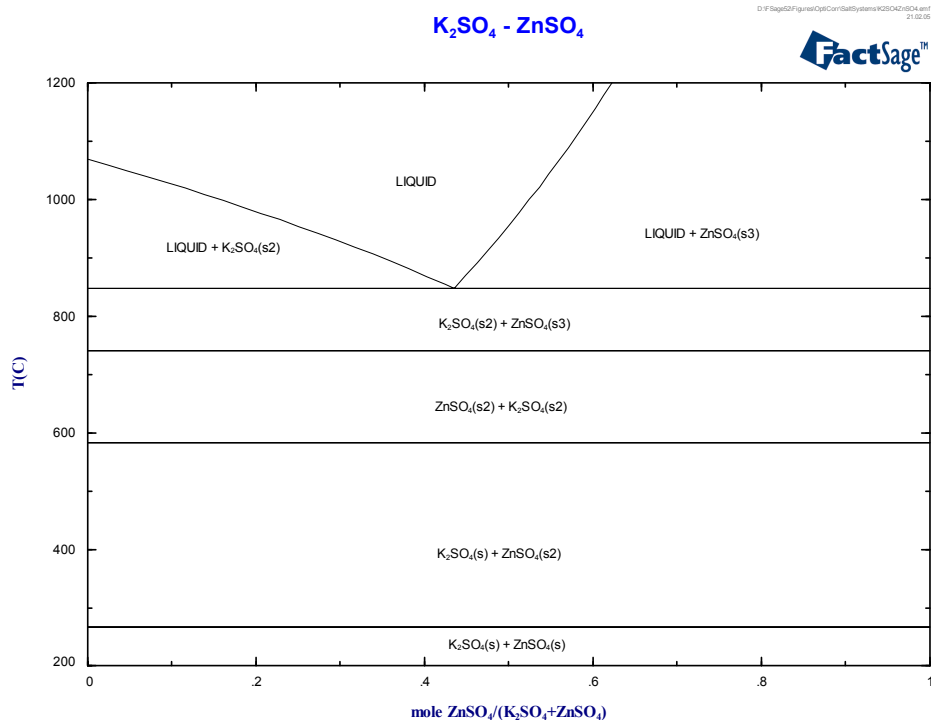


*Figure 4.1.36. The K₂SO₄-ZnSO₄ phase diagram calculated from the present database.*
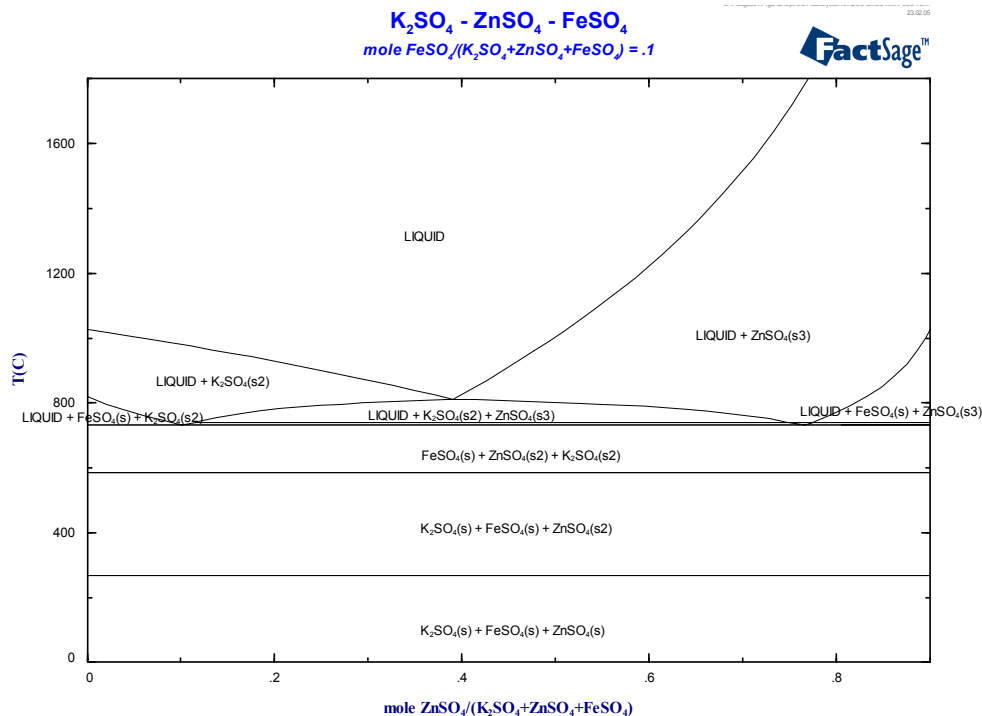
*Figure 4.1.37. The K2SO4-ZnSO4 phase diagram with small amounts of Fe in the system.*

Figures 4.1.36 and 4.1.37 show results from calculations which make use of the present salt database. In these the changes in the melting behaviour of the binary $K_2SO_4$-$ZnSO_4$ system (Figure 4.1.36) under the influence of small amounts of $FeSO_4$, i.e. di-valent Fe, (Figure 4.1.37) are shown. These effects have however not been part of the experimental work of the present project. Nevertheless, they are important for the future full modelling of the salt behaviour in deposits of heat exchangers.

### 4.1.4  Predominance area and other diagrams with gases

There are two types of diagrams possible in this category. In both cases the temperature ad the total pressure are constant. If more than two alloy components are considered then the additional component amounts are kept constant. In the first type of diagram one axis relates to the composition of the second alloy component and the other to the partial pressure of the corrosive gas component. The second type of diagram both axes relate to partial pressures of corrosive gas components.

The first type is particularly useful if the influence of the alloy composition is to be investigated while the second is well suited if the behaviour of alloys with given composition is to be investigated for complex gas atmospheres with more then one corrosive component. For the second type it should be noted that the alloys are considered to react with the gases, i.e. their amounts and compositions change when reaction products are

formed. This is different from the classical type of diagrams where the overall composition of the alloys is used to calculate the component activities that are then *not* changed in the calculations.
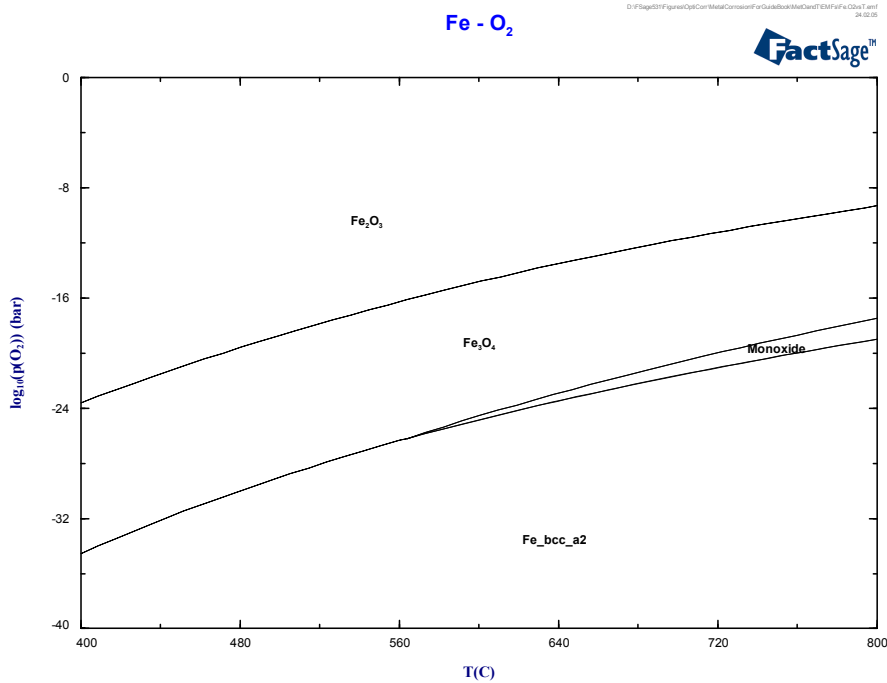


*Figure 4.1.38. The Fe-O₂ system with variable oxygen potential and variable temperature as calculated from the present database.*
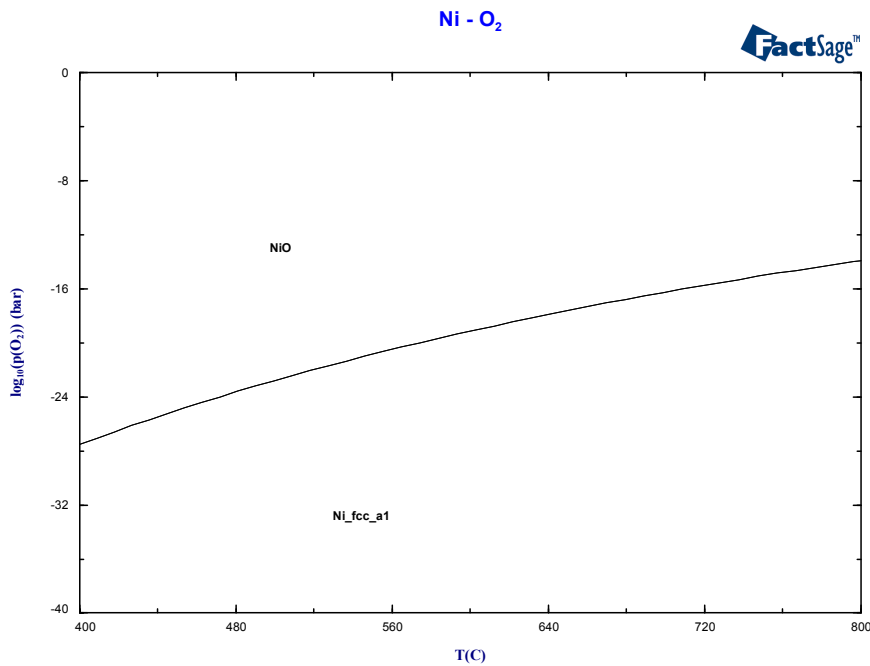


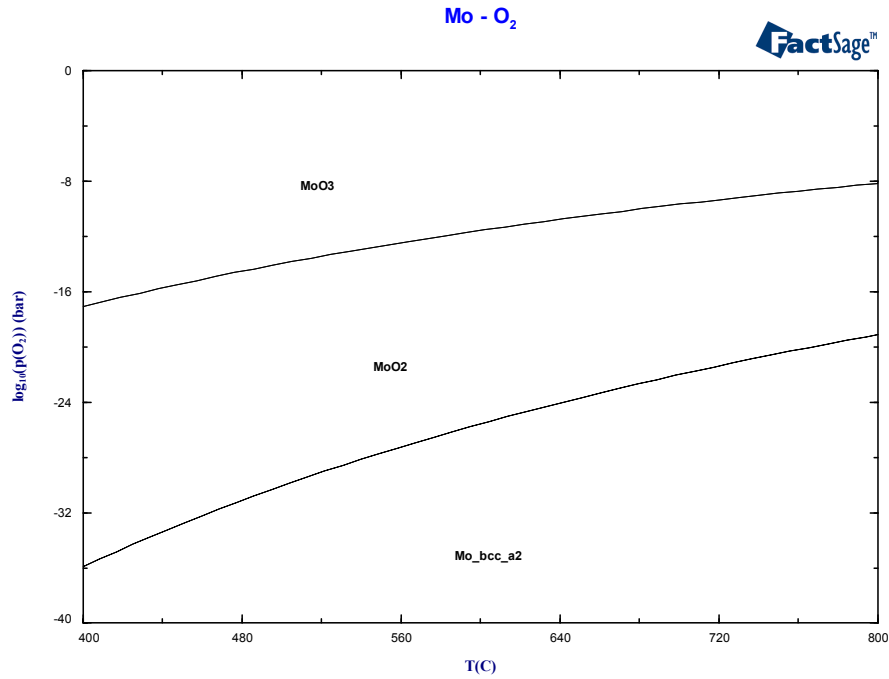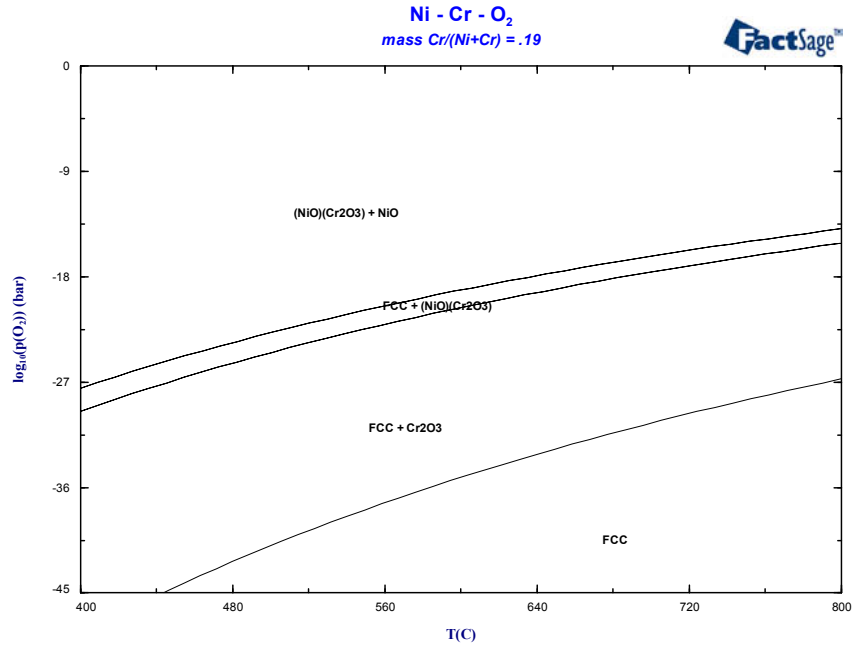*Figure 4.1.39. The Ni-O₂ systems for variable oxygen potential and temperature as calculated from the present database.*

*Figure 4.1.40. The Mo-O₂ systems for variable oxygen potential and temperature as calculated from the present database.*

Figures 4.1.38 to 40 show clearly that all major alloying components will be oxidised in the temperature and oxygen potential range that is possible in heat exchangers. It is thus a question of preferred oxidation in the alloy when all components are together with given relative amounts. This behaviour is shown in the following series of figures.
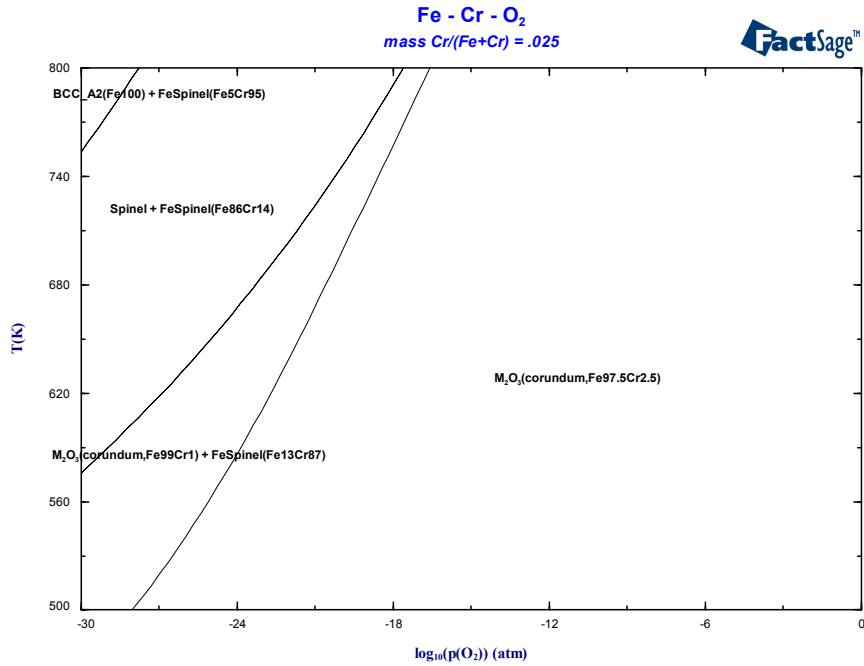
*Figure 4.1.41. A Fe 2.5%Cr alloy for variable oxygen potential and temperature as calculated from the present database.*
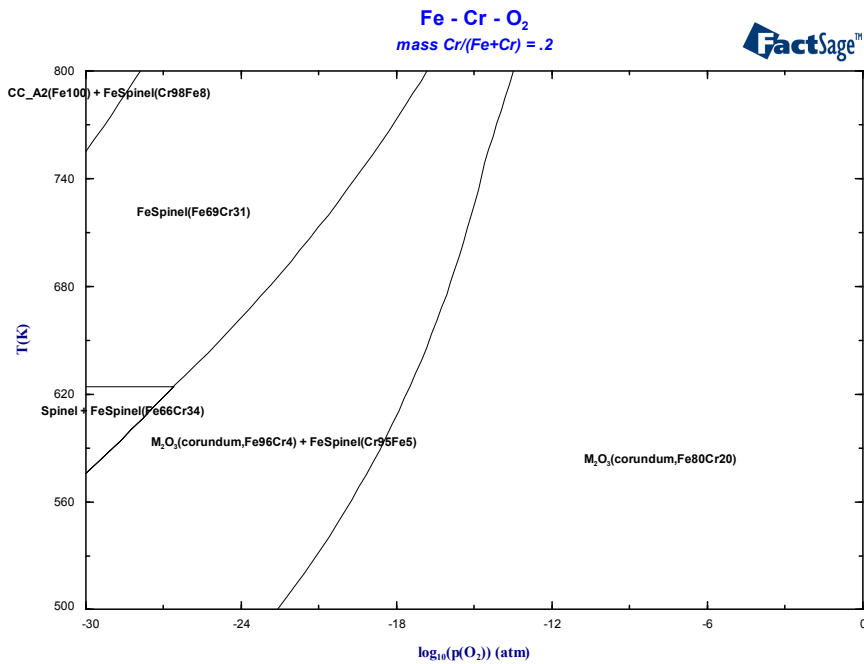


*Figure 4.1.42. A Fe 20%Cr alloy for variable oxygen potential and temperature as calculated from the present database.*

Figures 4.1.41–4.1.42 show that the basic behaviour of the phases formed in Fe-Cr alloys are the same no matter whether small or large amounts of Cr are added. However, a

detailed comparison of the curves shows that the boundary of complete oxidation of the alloy is shifted towards higher oxygen potentials. Also the compositions of the mixed oxides differ from one diagram to the other.



*Figure 4.1.43. A Ni 19%Cr alloy for variable oxygen potential and temperature as calculated from the present database.*
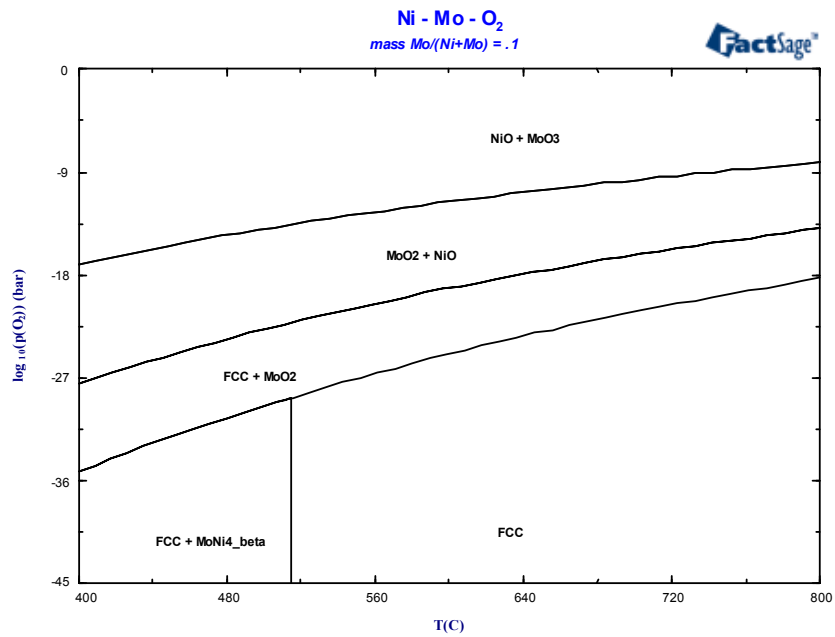


*Figure 4.1.44. A Ni 9%Mo alloy for variable oxygen potential and temperature as calculated from the present database.*
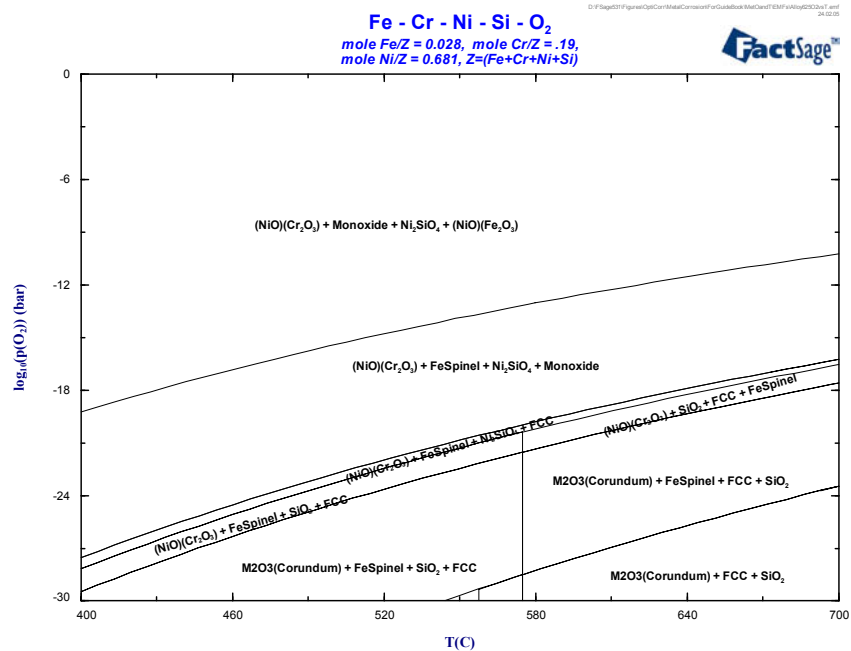
*Figure 4.1.45. A Ni 20%Cr 2.8%Fe Si alloy for variable oxygen potential and temperature as calculated from the present database.*

The figure series 4.1.43 to 4.1.45 shows the oxidation behaviour of various pure and alloyed metals thus giving the temperature and oxygen potential limits for formation of corrosion products for the different pure metals but also for important combinations of these.
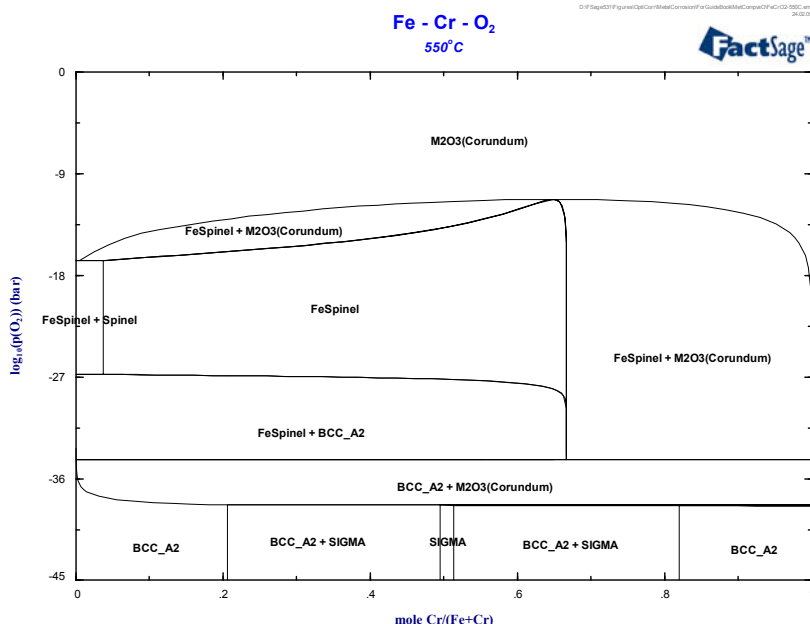


*Figure 4.1.46. Fe-Cr alloys with variable composition under variable oxygen potential and fixed temperature as calculated from the present database.*

Figure 4.1.46 shows for the Fe-Cr system the influence of the Cr composition and the oxygen potential on the phase stability fields for a fixed temperature (320°C). It is obvious from the above that Chromium in the alloy will first react with the oxygen thus depleting the alloy.
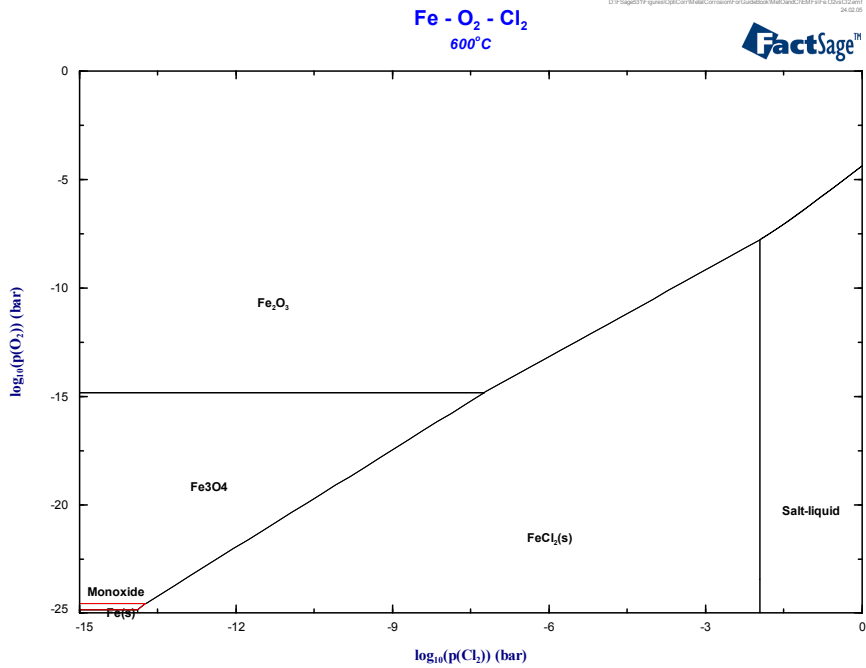


*Figure 4.1.47. The Fe-O-Cl system for a fixed temperature and for variable oxygen and chlorine potential as calculated from the present database.*
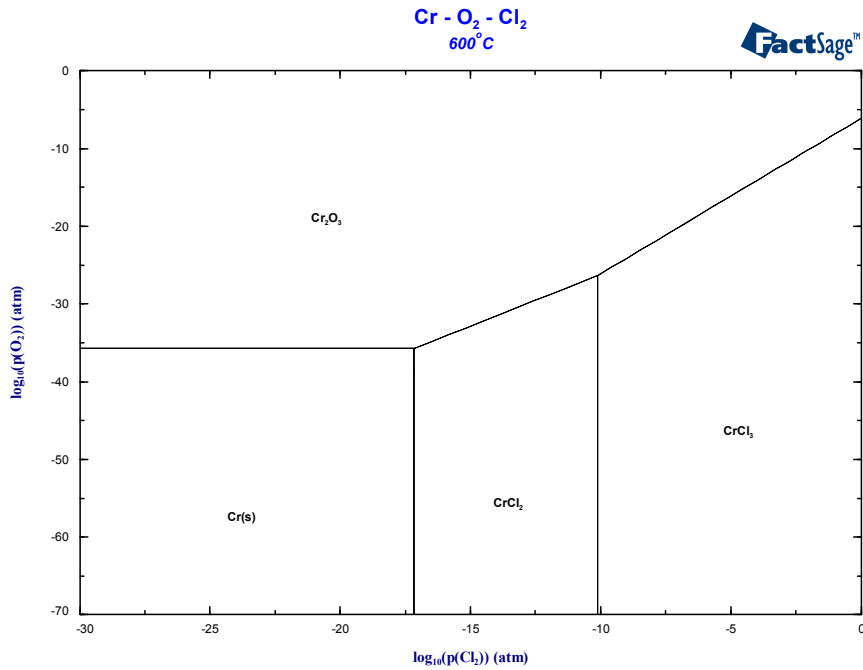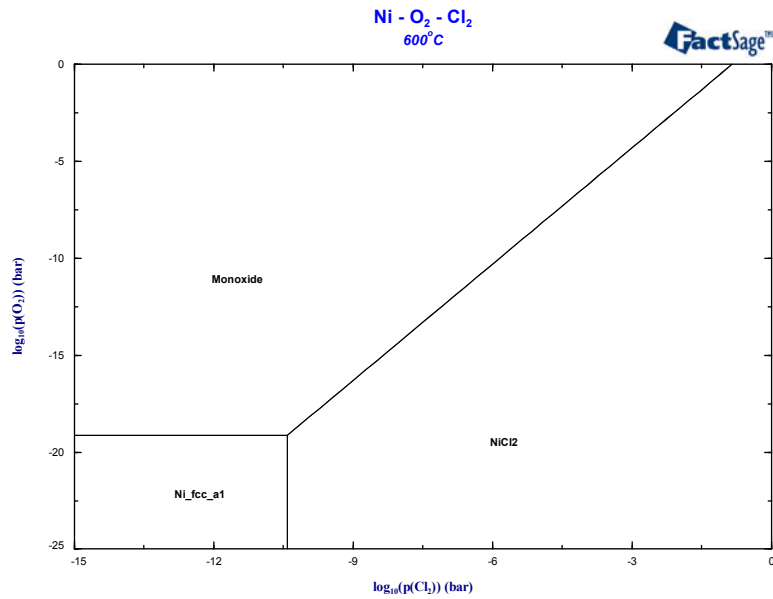


*Figure 4.1.48. The Cr-O-Cl system for a fixed temperature and for variable oxygen and chlorine potential as calculated from the present database.*

*Figure 4.1.49. The Ni-O-Cl system for a fixed temperature and for variable oxygen and chlorine potential as calculated from the present database.*
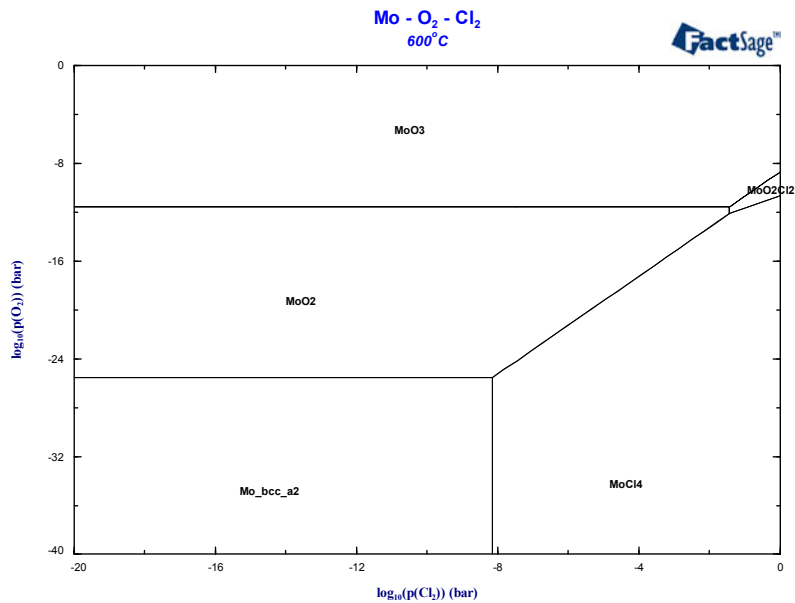


*Figure 4.1.50. The Mo-O-Cl system for a fixed temperature and for variable oxygen and chlorine potential as calculated from the present database.*

The series of Figures 4.1.46 to 4.1.50 above shows the isothermal (600°C) phase relations of the basic metals used for the productions of heat exchanger materials (Fe and Ni) as well the major alloying components (Cr and Mo) in an atmosphere containing oxygen and chlorine. The general behaviour is comparable in all cases but the limits for formation of the first corrosion product may differ markedly.
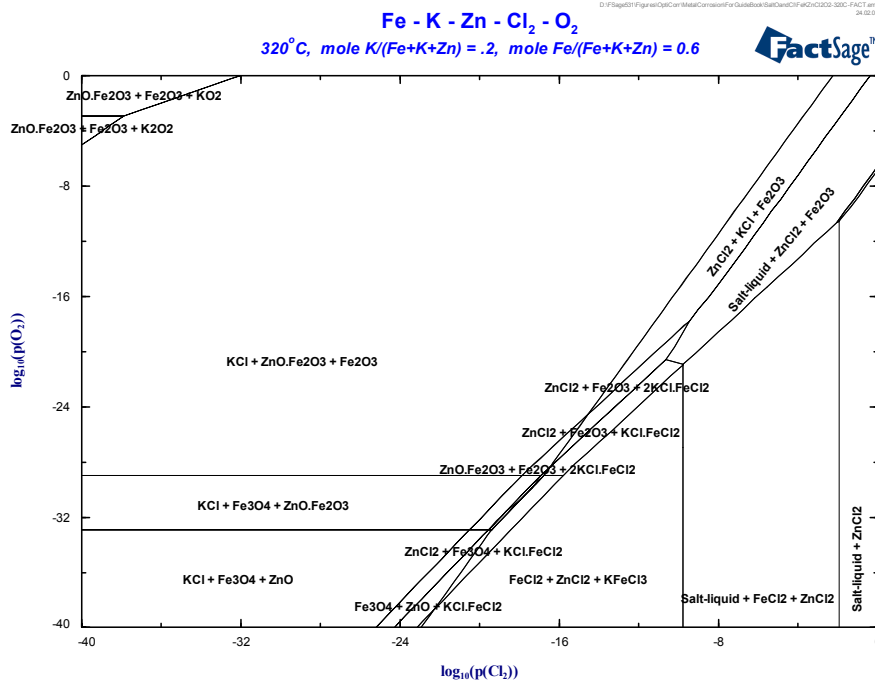
*Figure 4.1.51. The Fe-K-Zn system for a fixed temperature and for variable oxygen and chlorine potential as calculated from the present database.*

Figure 4.1.51 shows the combined reactions of the Fe-K-Zn system (ratio Fe/(K+Zn)=4) with an atmosphere of oxygen and chlorine with variable partial pressures for a fixed temperature of 320°C (as used in the experimental of the project). It can be seen that for very low oxygen and chlorine potential both Fe and Zn will be oxidised while potassium will form KCl. Only at very high oxygen potentials and low chlorine partial pressure will potassium also be oxidised. On the other hand will an increase of the chlorine partial pressure at low oxygen potential first lead to chlorination of Fe while Zn will follow next. A further increase of the chlorine potential will then lead to the formation of a liquid salt phase. An increase of the oxygen partial pressure with high chlorine potential will lead to the formation of $Fe_2O_3$. This behaviour is in good qualitative agreement with the experimental findings of the salt corrosion experiments with pure iron.
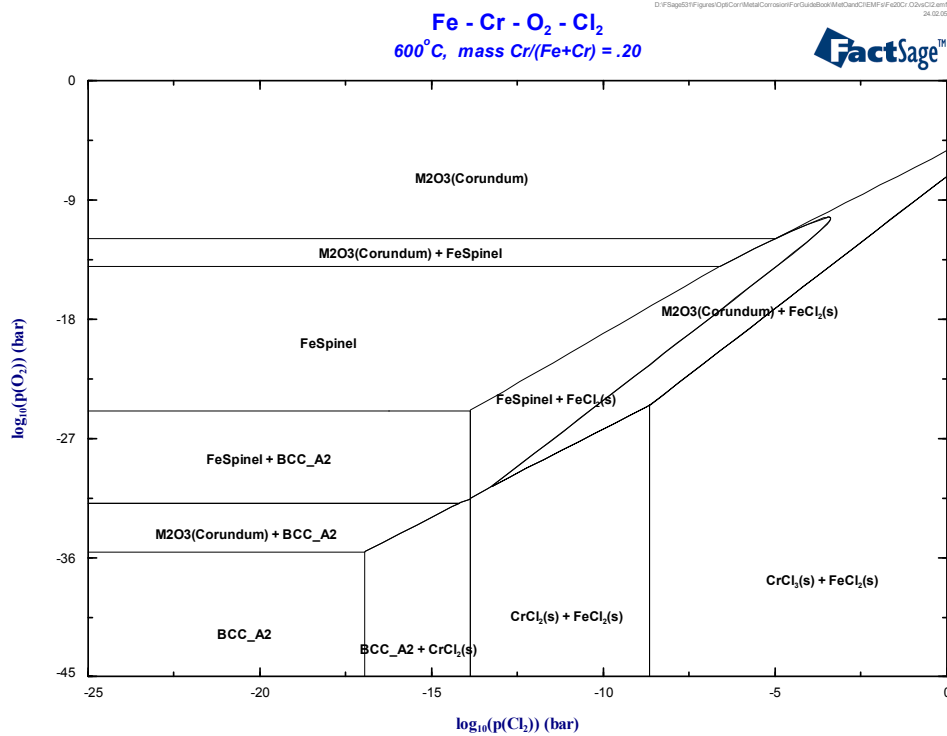
*Figure 4.1.52. An Fe-20Cr alloy in a chlorine-oxygen atmosphere at 600°C.*

Figure 4.1.52 shows that both with respect to oxygen and to the chlorine reactions it will be first the alloying component chromium that will form new phases with the gases. The alloy will in turn loose some of its chromium. If the phases formed, e.g. corundum, result in a dense layer this will act as a protective barrier for further corrosion in reality. The calculations of the phase diagram do however not take this effect into account. Instead corrosion is assumed to proceed, which in the end will lead to Fe-spinel and/or $FeCl_2$ formation, i.e. complete consumption of the alloy.
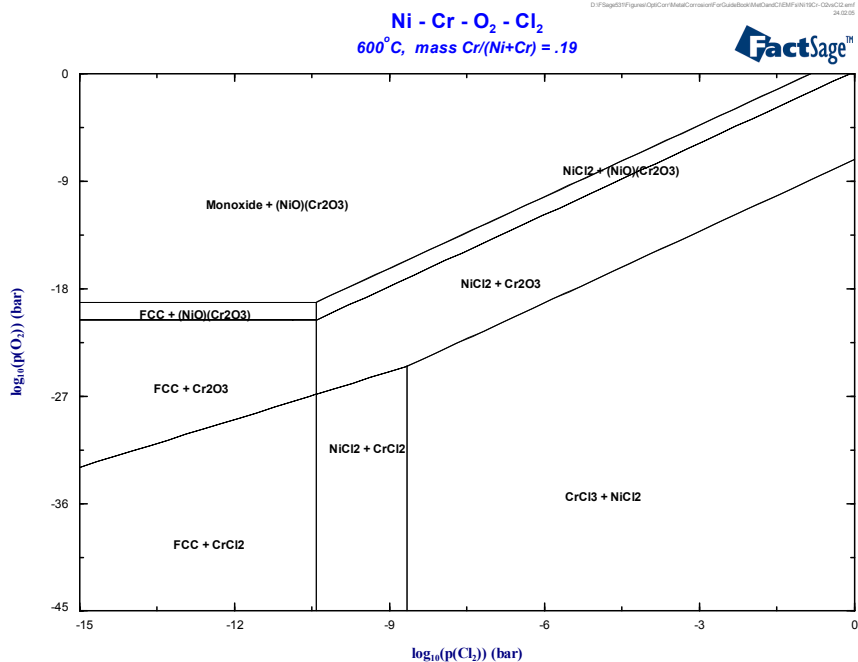
*Figure 4.1.53. A Ni-19Cr alloy in a chlorine-oxygen atmosphere at 600°C.*

Chromium will also in Ni-based alloys be the first component to react with oxygen and/or chlorine from a gas atmosphere. In great similarity to the Fe-based alloys discussed above Cr will form oxide and/or chloride before the matrix metal Ni starts to react with the gas phase. Here too the formation of dense protective layers is possible which is however not considered in the diagram.
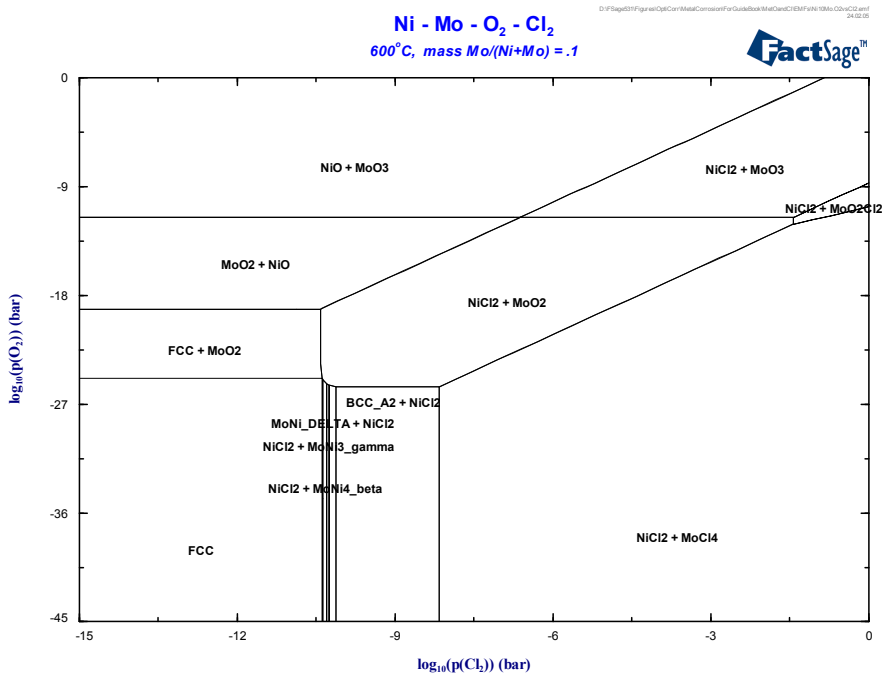


*Figure 4.1.54. A Ni-9Mo alloy in a chlorine-oxygen atmosphere at 600°C.*

97

Figures 4.1.53 and 4.1.54 show that Mo and Cr have a very similar behaviour when used as alloying components for Ni-based alloys. Both alloying components will react first with oxygen and/or chlorine from the gas phase before finally also the matrix material Ni is attacked by the gas.
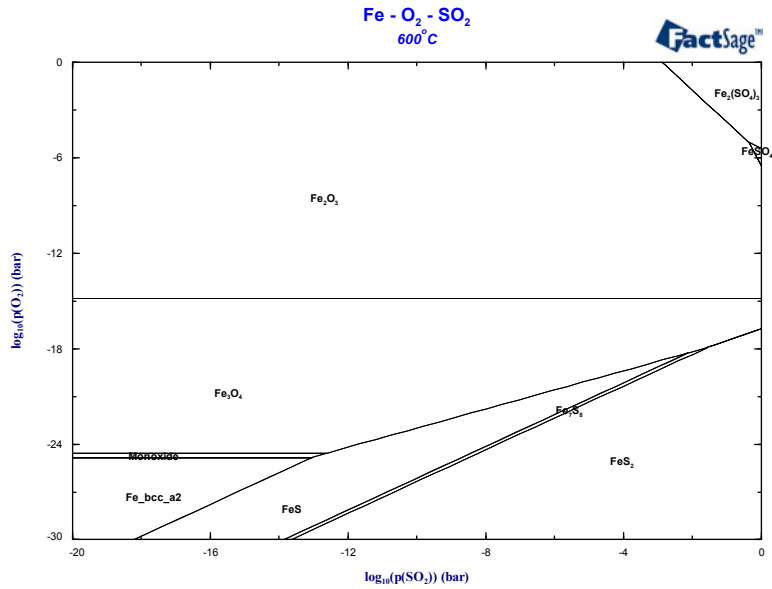


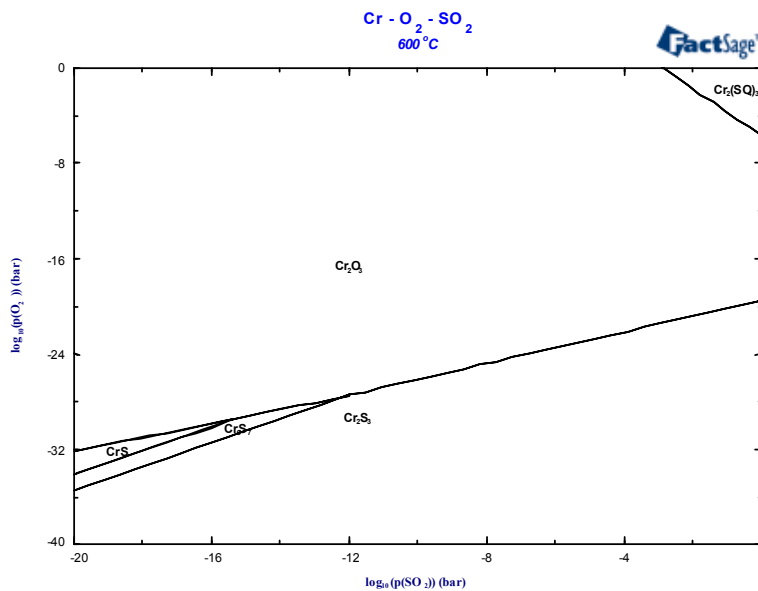*Figure 4.1.55. Pure Fe in an oxygen-SO2 atmosphere at 600°C.*



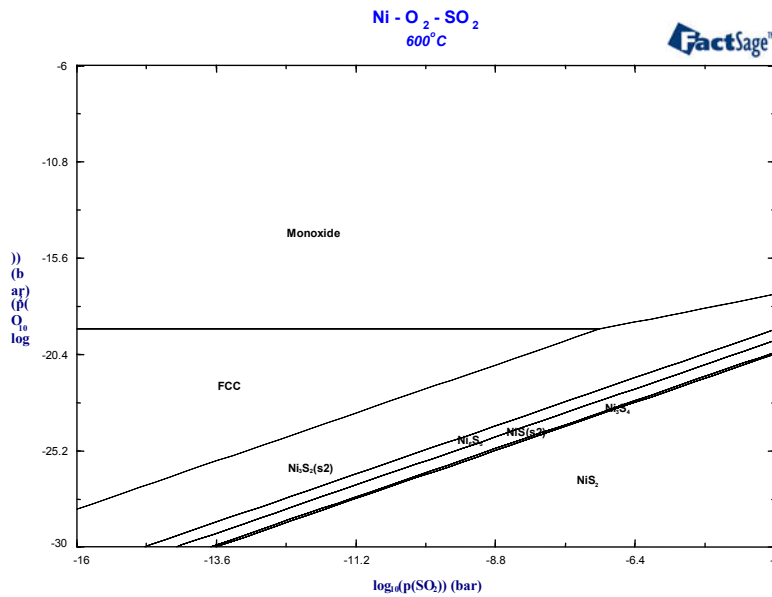*Figure 4.1.56. Pure Cr in an oxygen-SO2 atmosphere at 600°C.*

*Figure 4.1.57.  Pure Ni in an oxygen-SO₂ atmosphere at 600°C.*
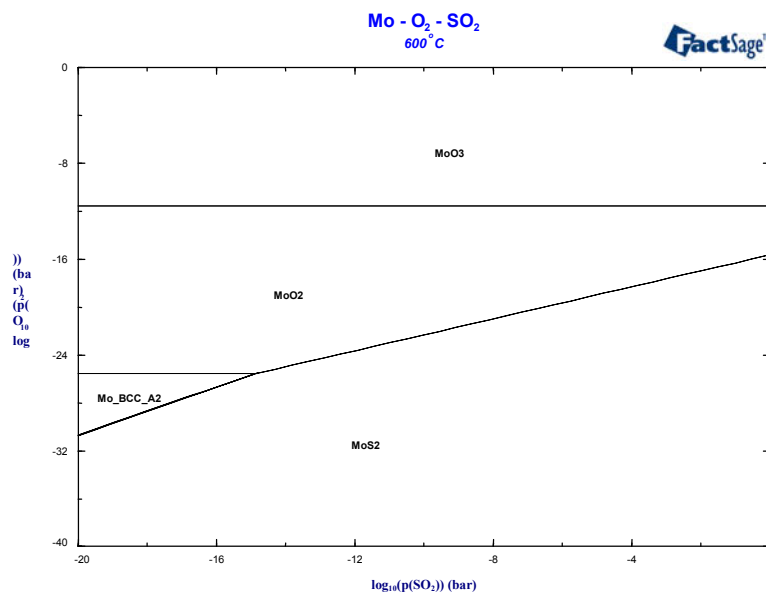


*Figure 4.1.58. Pure Mo in an oxygen-SO₂ atmosphere at 600°C.*

The figure series 4.1.55 to 4.1.58 shows the behaviour of the major pure metal components in a combined oxygen/SO₂ atmosphere. Comparison of the ranges of stability shows that similar to the O₂/Cl₂ systems Cr and Mo will react first and thus lead to protective layers as is in accord with practical experience.
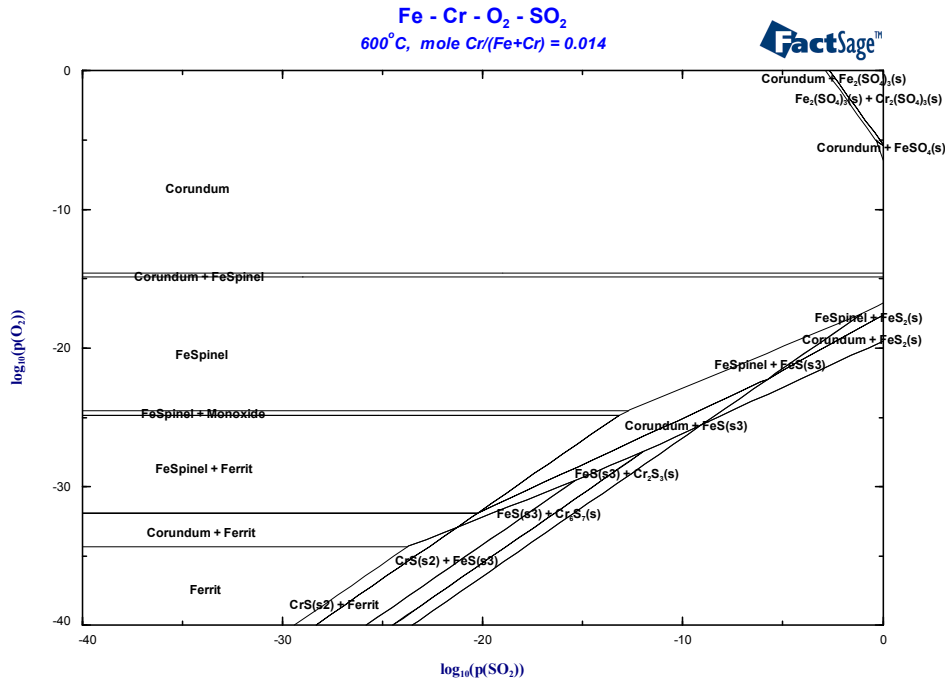
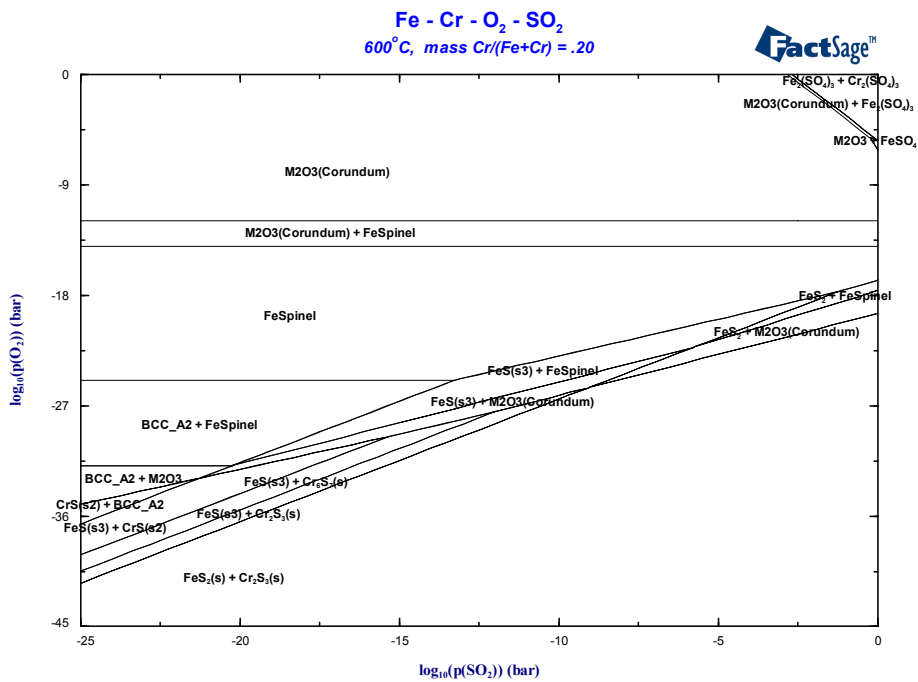*Figure 4.1.59. An Fe-1.4Cr alloy in an oxygen and SO₂ atmosphere, T = 600°C.*



*Figure 4.1.60. An Fe-20Cr alloy in an oxygen and SO₂ atmosphere, T = 600°C.*
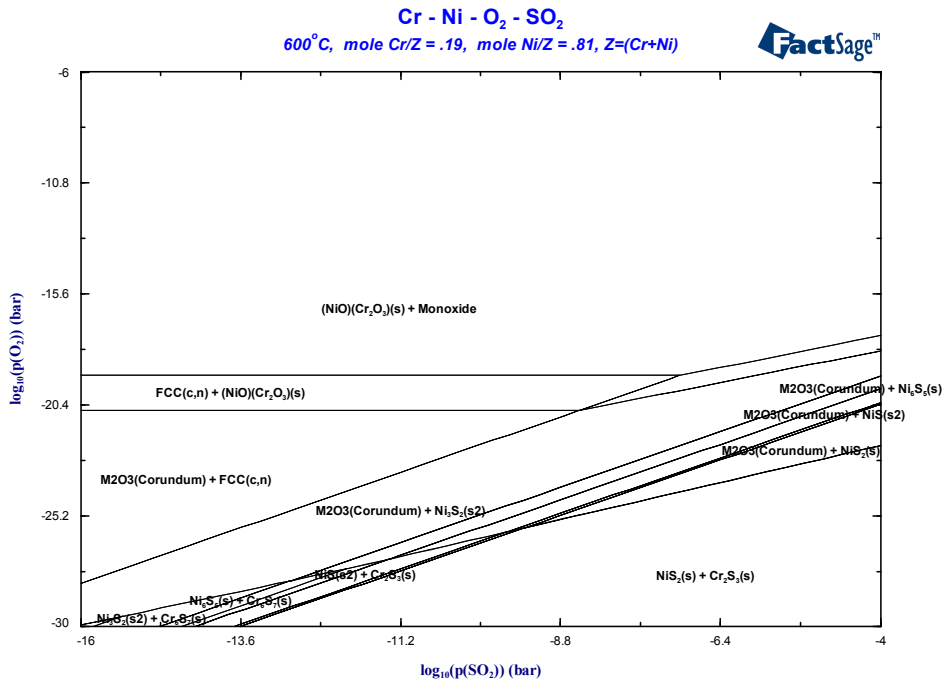
*Figure 4.1.61. A Ni-19Cr alloy in an oxygen and $SO_2$ atmosphere, T = 600°C.*
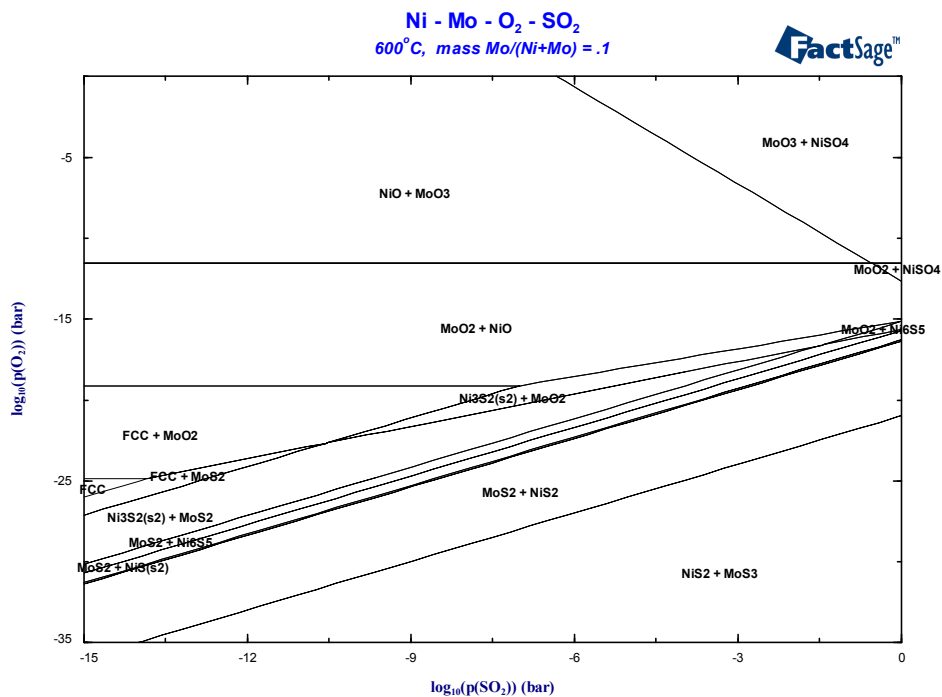


*Figure 4.1.62. A Ni-10Mo alloy in an oxygen and $SO_2$ atmosphere, T = 600°C.*

The figure series 4.1.59 to 4.1.62 shows that the similar to the $O/Cl_2$ systems discussed earlier an increase in oxygen potential will first lead to an oxide based on the alloying components (here Cr and Mo). However, the increase in $SO_2$ potential will first lead to a sulphide based on the alloying component. Only simultaneous very high levels oxygen and $SO_2$ potential will lead to sulphate formation.

## 4.2 Modelling of internal oxidation/corrosion

(V.B. Trindade, U. Krupp & H.-J. Christ – University Siegen)

### 4.2.1 Introduction

MATLAB provides the application M-file that allows to develop a graphical user interface (GUI). The entire code, including the callbacks, is contained in the application M-file. Each callback is implemented as a subfunction in the M-file. This approach enables the M-file to have a single entry point that can initialise the GUI or can call the appropriate callback, or any helper subfunction which shall be used in the GUI [1].

A user-friendly interface using GUI was developed for the OPTICORR modelling tools. The versatility of these interfaces permits to carry out simulations using *InCorr* (for calculations on the hot gas / alloy systems) and ChemSheet (for calculations on the salt / alloy systems). On the other hand it can also be used as a data bank for the experimental kinetic data obtained by the consortium and from the open literature as well as for phase diagrams calculated using the software FactSage. Figure 4.2.1 shows examples of interfaces generated using the GUI tool of the MATLAB software package. In the following two sub-chapters 4.2.2 and 4.2.3 examples are given for the application of *InCorr* to external and internal corrosion processes of low- and high-alloyed steels and Ni-base alloys.
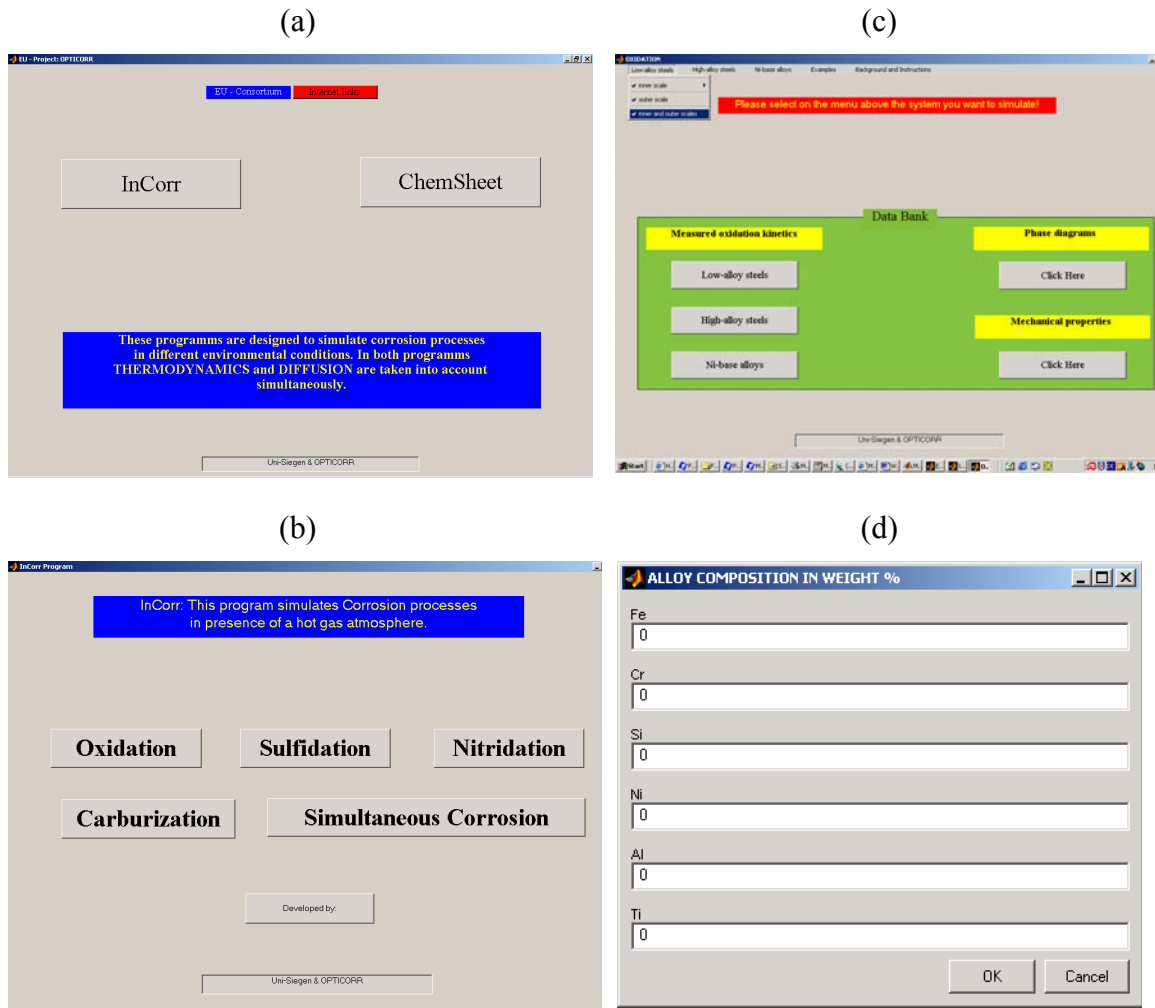
(b)

(d)



*Figure 4.2.1. User-friendly interfaces generated using GUI for InCorr: (a) main window, (b) window to choose the corrosion process, (c) simulation window and (d) input of the alloy composition.*

## 4.2.2  Oxidation of steels

To apply the finite-difference approach mentioned in section 3.1.2.2 to oxidation processes of Cr-containing steels, it has to be taken into account that, generally, the oxide scale consists of three or more separate layers, e.g., in the case of low-Cr steels an outer magnetite scale (below an outermost hematite layer) on top of an inward-growing magnetite/spinel-phase scale and an intergranular oxidation zone below the scale/substrate interface [2].

Since it was shown in the present project that oxidation processes of Cr-containing steels are mainly governed by grain-boundary transport of the reacting species, i.e., Cr and O grain-boundary diffusion, a two-dimensional finite-difference model has been

established that distinguishes between fast diffusion along substrate grain boundaries and slow transport through the bulk. Due to the lack of data available for interface diffusivities, on the base of an estimate value for the grain boundary width [3] of $\delta = 0.5$ nm, the grain-boundary diffusion coefficient was assumed to be 100 times higher than the bulk diffusion coefficient [4], which has a value of $D_b = 5.39 \cdot 10^{-13}$ m²/s for oxygen in iron at $T = 550°C$.

According to the schematic representation for the intergranular oxidation process in low-Cr steels in Figure 4.2.2, oxygen firstly penetrates along the substrate grain boundaries, and hence, the diffusivity elements $D_y$ of the matrix $\mathbf{R_y}$ along the grain boundaries are set to the grain boundary diffusion coefficient $D_{GB}$. At the same time oxygen bulk diffusion takes place driven by the two-dimensional concentration gradient. Hence, the respective elements $D_x$ and $D_y$ of the matrices $\mathbf{R_x}$ and $\mathbf{R_y}$ are set to the bulk diffusion coefficient $D_b$. The first oxidation product that becomes thermodynamically stable during this process is $Cr_2O_3$. The corresponding depletion in Cr in combination with the increase of the oxygen activity leads to the subsequent formation of the Fe-Cr spinel $FeCr_2O_4$. Further Cr depletion manifests itself in a Cr gradient in the $(Fe,Cr)_3O_4$ phase over the inward-growing oxide scale, finally resulting in almost pure magnetite $(Fe_3O_4)$. As soon as the metallic substrate is completely consumed (except the residual Fe in equilibrium with $Fe_3O_4$) the inner-oxide/substrate interface moves one location step inward (see Figure 4.2.2).
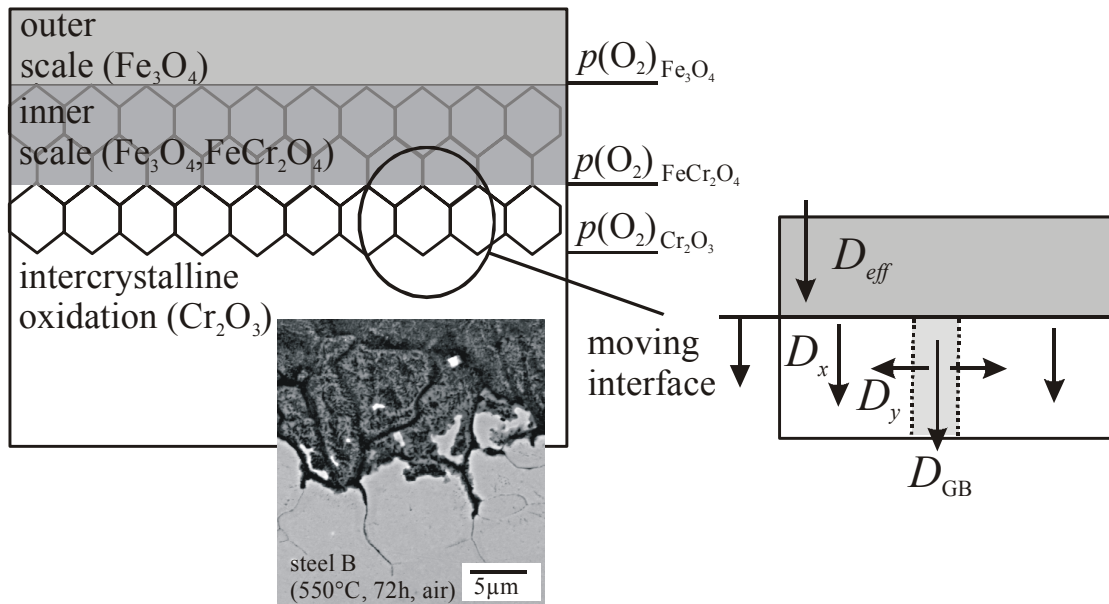


*Figure 4.2.2. Schematic representation of the oxidation process of low-alloy Cr-containing steels and the two-dimensional model using a moving-interface approach and distinguishing between grain-boundary and bulk diffusion.*

Diffusion through the inner $Fe_3O_4/FeCr_2O_4$ scale, the mechanism of which is not fully understood since it strongly depends on the Cr concentration and is affected by the pronounced porosity, is treated in this study by an effective diffusion coefficient $D_{eff}$. The observed value of $D_{eff}$ was estimated by means of the experimentally determined $k_p$ value for the inner-scale growth kinetics in combination with Wagner's theory of oxidation [5].

$$k_p = \int_{p(O_2)Cr_2O_3}^{p(O_2)Fe_3O_4} D_O \, d \ln p(O_2), \tag{4.2.1}$$

where $p(O_2)Fe_3O_4$ is the oxygen partial pressure at the outer/inner scale interface (see Figure 4.2.2) and $p(O_2)Cr_2O_3$ the estimated, respective pressure at the scale/substrate interface.

Figure 4.2.2 summarizes the concept of the simulation procedure: (i) the origin of the grid is starting at the outer/inner scale interface, where the spinel phase completely disappears; (ii) inward growth of the inner scale is defined by the condition that the metallic substrate is completely consumed, and finally, (iii) the depth of the intercrystalline oxidation attack depends on the $Cr_2O_3$ equilibrium.

The concept of the simulation program, that has been developed within the present project is shown in Figure 4.2.3, highlighting the main elements of the model.
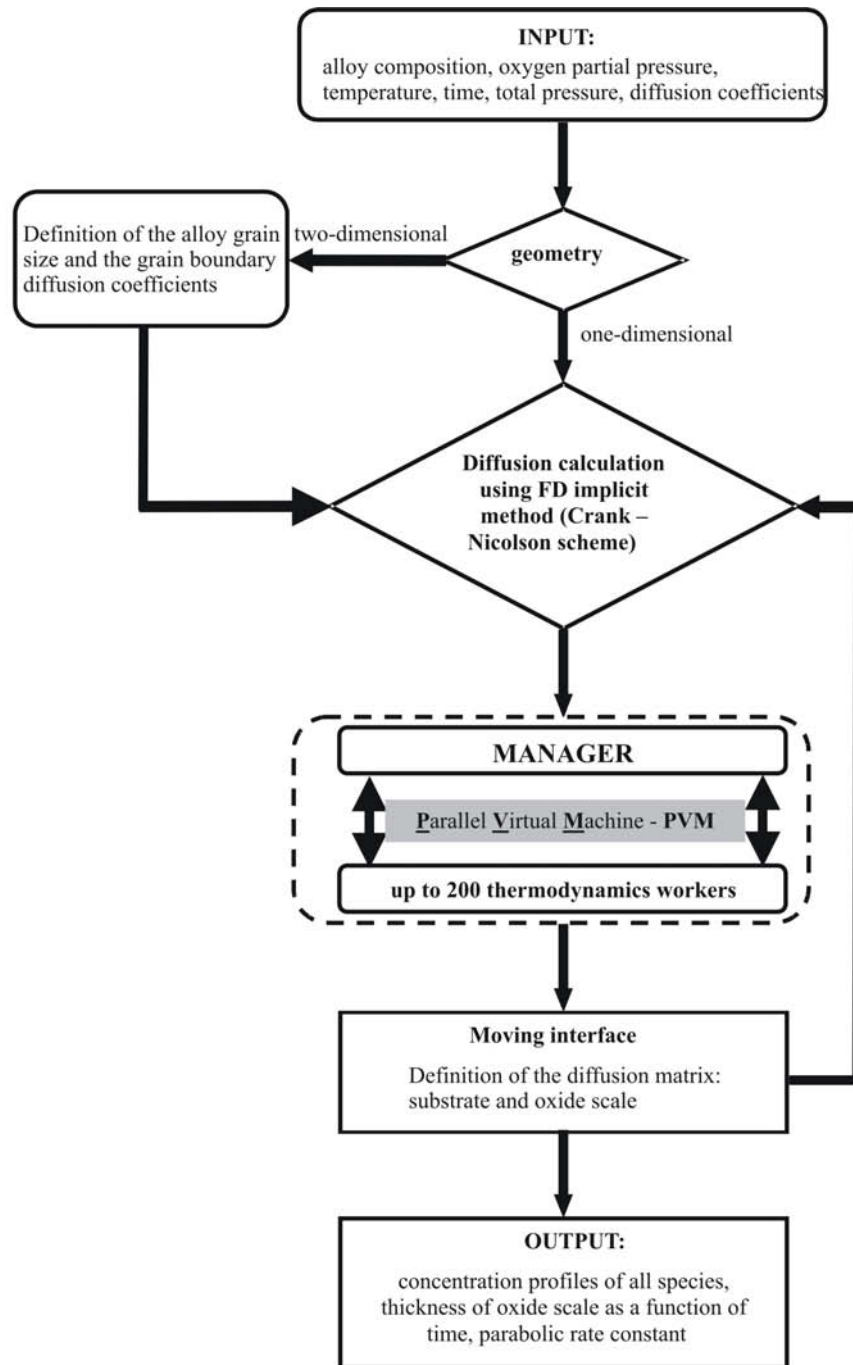
*Figure 4.2.3. Main elements of the computer model to simulate the inner oxide scale growth on Cr-containing steels.*

To distinguish the lattice diffusion (volume diffusion) from the diffusion along grain boundaries the diffusion coefficient matrix (equation 4.2.2) has to be set up before starting of the calculations.

$$D_{ij} = \begin{bmatrix} D_{11} & D_{12} & D_{13} & D_{14} & D_{15} \\ D_{21} & D_{22} & D_{23} & D_{24} & D_{25} \\ D_{31} & D_{32} & D_{33} & D_{34} & D_{35} \\ D_{41} & D_{42} & D_{43} & D_{44} & D_{45} \\ D_{51} & D_{52} & D_{53} & D_{54} & D_{55} \end{bmatrix}$$ (4.2.2)

In this case the definition of the real diffusion coefficient matrix is:

$$D_{ij} = \begin{cases} D_b & \text{; if } (i,j) \text{ is located inside the grain} \\ D_{GB} & \text{; if } (i,j) \text{ is located along grain boundaries} \end{cases}$$

However, when the parent element, e.g. iron, oxidizes, than it is necessary to distinguish also between the diffusion in the oxide and diffusion in the substrate bulk and along grain boundaries. This has been realized by implementation of a moving interface which is shown schematically in Figure 4.2.4 for the calculation of inward scale formation in steels.
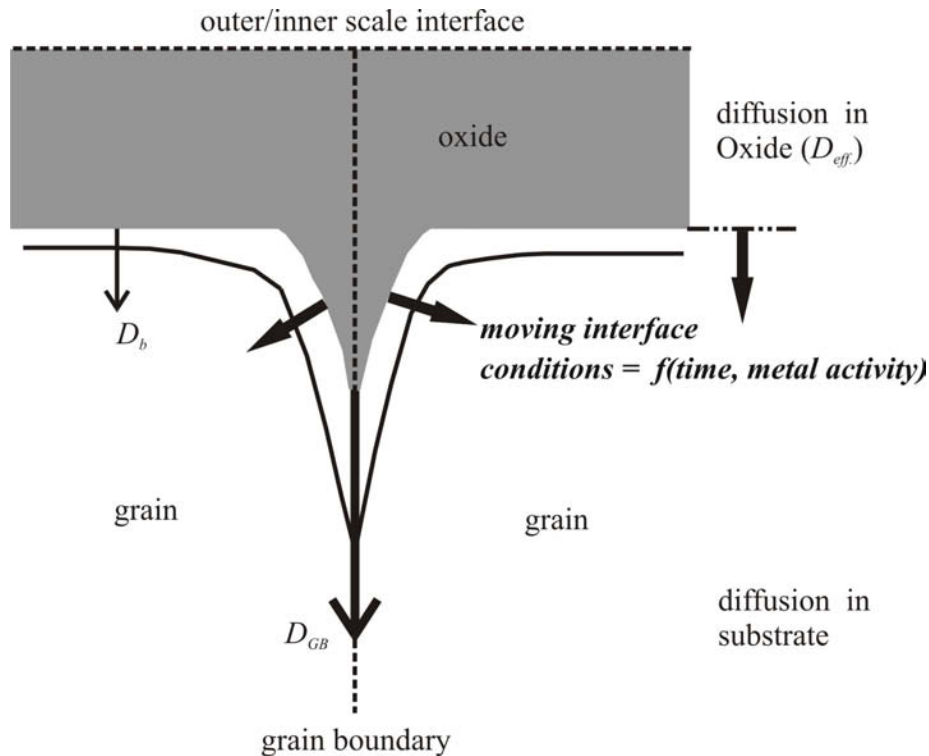


*Figure 4.2.4. Schematic representation of the moving boundary interface used for calculation of the inward scale growth in steels.*

For this more complex case the diffusion matrix becomes:

$$D_{ij} = \begin{cases} D_b & \text{; if } (i,j) \text{ is located inside the grain and } c_{Fe}>0 \\ D_{GB} & \text{; if } (i,j) \text{ is located along grain boundaries and } c_{Fe}>0 \\ D_{oxide} & \text{; if } (i,j) \text{ is located in the region where } c_{Fe}=0 \end{cases}$$

The numerical model described in chapter 3 was applied to the oxidation processes of low- and high-Cr steels as discussed in part 1 of this guide book using diffusion data given by Heuman [4]:

- $D_{\text{O in } \alpha\text{-Fe}} = 2.8 \times 10^{-4} \exp(-251\text{kJ/R}T)$,
- $D_{\text{Cr in } \alpha\text{-Fe}} = 3.59 \times 10^{-6} \exp(-179\text{kJ/R}T)$,
- $D_{\text{Fe in } \alpha\text{-Fe}} = 3.78 \times 10^{-7} \exp(-92.1\text{kJ/R}T)$.

Figure 4.2.5 shows the calculated two-dimensional concentration profiles for magnetite ($Fe_3O_4$), the Fe-Cr spinel phase ($FeCr_2O_4$) and chromia ($Cr_2O_3$) for steel X60 containing 1.44wt.% Cr and having a grain size of $d = 30$ μm. It should be mentioned here that the thermochemical database of the system treats $Fe_3O_4$ and $FeCr_2O_4$ as separate but coexisting phases, i.e., an increase in the Cr concentration leads to a relative increase in the fraction of the spinel phase $FeCr_2O_4$.

Fe₃O₄ [at.%]

FeCr₂O₄ [at.%]

Cr₂O₃ [at.%]

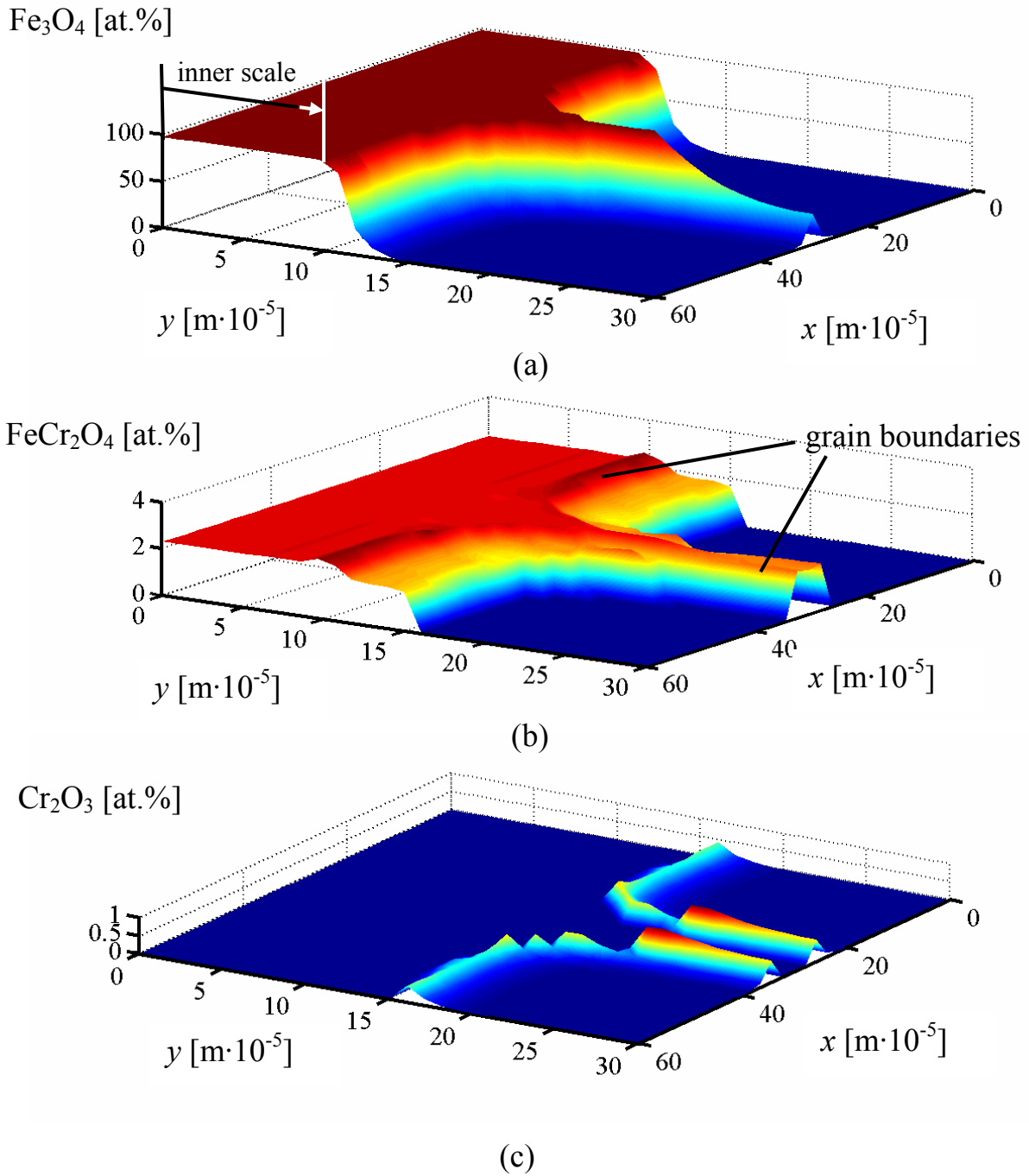*Figure 4.2.5. Simulated lateral concentration profiles of the oxide phases (a) Fe₃O₄, (b) FeCr₂O₄, and (c) Cr₂O₃ formed during exposure of the low-alloy steel X60 ($c_{Cr}$ = 1.44 wt.%) with a grain size of d = 30 μm at T = 550°C to air (y = 0 corresponds to the original inner-scale/metal interface at t = 0s).*

The results support the experimental observation that the first oxide phase being formed is $Cr_2O_3$ along the substrate grain boundaries, followed by $FeCr_2O_4$ and finally, $Fe_3O_4$. Since oxygen penetration into the alloy occurs by both, grain-boundary as well as bulk diffusion, the oxidation process proceeds from the grain boundaries into the bulk until the complete metallic phase is consumed. This situation defines the progress of the inner oxide scale (see arrow in Figure 4.2.5a).

The simulated growth kinetics of the inner oxide scale as a function of the exposure time is shown in Figure 4.2.6 for three different grain sizes. In the case of the material with a grain size of $d = 10\mu m$ it could be demonstrated that the simulated data are in excellent agreement with the experimentally determined values of the inner-scale thickness for various exposure times.
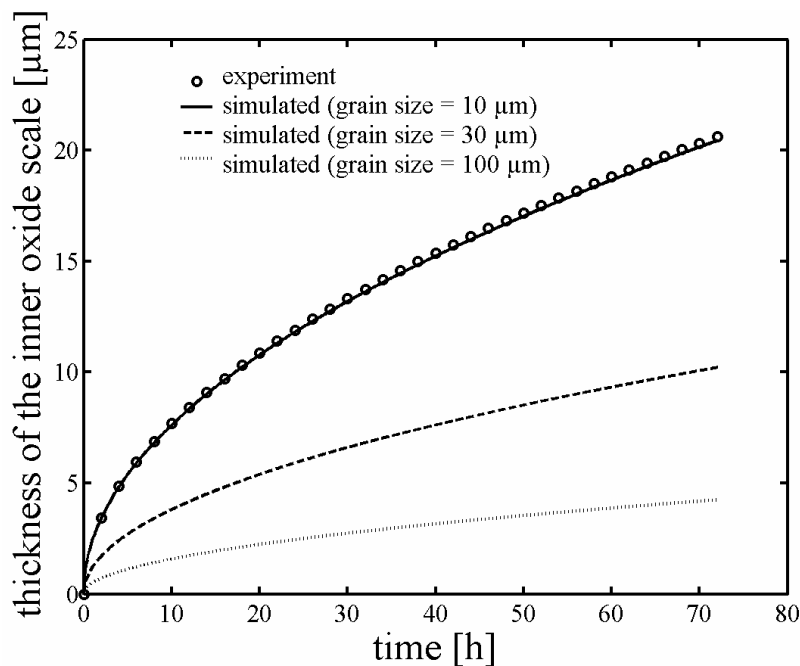


Figure 4.2.6. Comparison of the simulated inner-oxide growth kinetics for the low alloy steel X60 ($c_{Cr} = 1.44$ wt.%) with three different grain sizes and with the experimentally measured inner-oxide thickness for specimens having a grain size of d = 10 μm.

While for low-alloy steels with initial Cr concentrations between 0.5 and 2.3 wt.% an increase in the grain size results in a decrease in the oxidation kinetics, high-Cr austenitic steels exhibit a contrary effect: a smaller grain size results in an increase of the outward Cr transport and hence, to a transition in the oxidation mechanism from non-protective magnetite/spinel phase $(Fe,Cr)_3O_4$ to protective chromia $(Cr_2O_3)$ formation. Experimental observations revealed that on top of the fine-grained specimens (d = 4 and 11 μm) a very thin protective $Cr_2O_3$ scale was formed. However, locally the oxide scale was not totally protective leading to the formation of iron oxide nodules, which grow outward and inward. Generally, the formation of a protective $Cr_2O_3$ scale on specimens with a small grain size is favoured

by a higher Cr flux from the bulk to the substrate/oxide interface as a consequence of the higher grain boundary density. This is supported by first simulation results using the two-dimensional finite-difference approach as already described in combination with diffusion data taken from Kaur et al. [6]. Figure 4.2.7a shows qualitatively the Cr enrichment and gradient along a substrate grain boundary for high-temperature exposure of the austenitic stainless steel TP347. Indeed, the simulation revealed for an increase in the grain size, while keeping all the other parameters the same, that instead of pure $Cr_2O_3$ a mixture of oxide phases is formed as it is shown in Figure 4.2.7b.
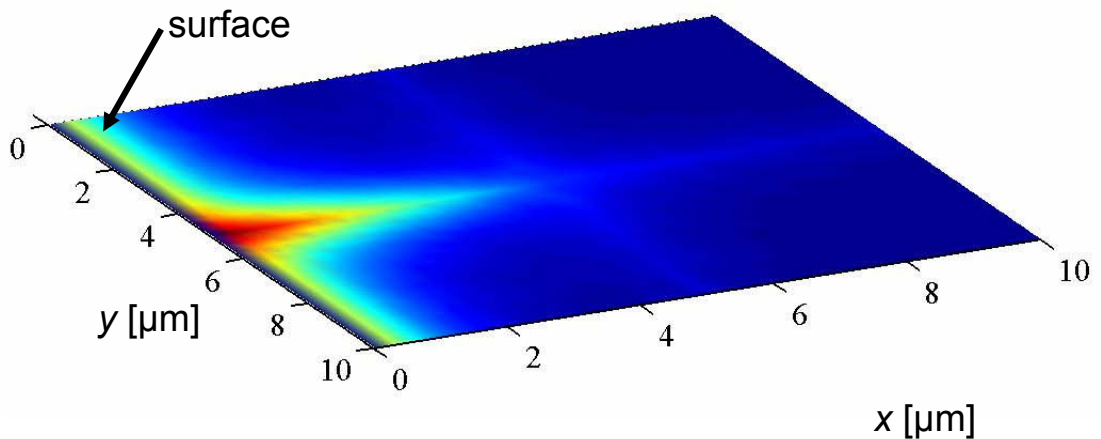


(a)
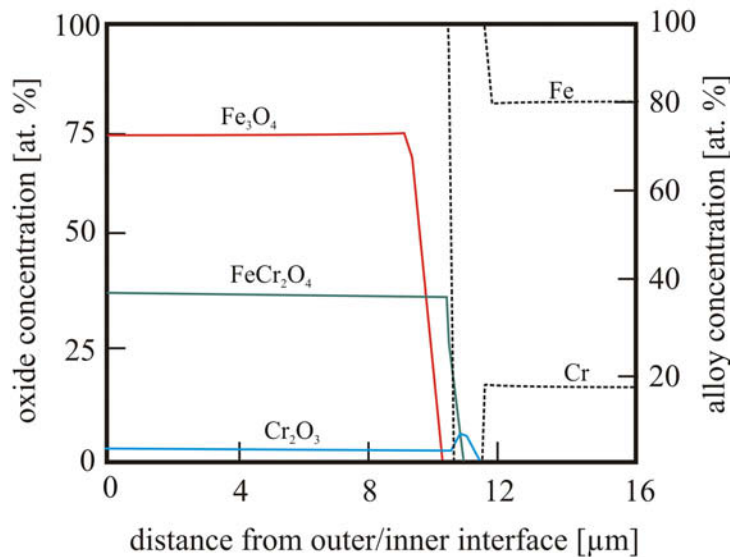


(b)

*Figure 4.2.7. (a) Qualitative Cr enrichment along substrate grain boundary on a fine-grained material (d = 5 µm) forming a superficial $Cr_2O_3$ scale and (b) one-dimensional concentration profiles of the oxidation products and the metallic elements of a coarse-grained specimen (d = 65 µm).*

## 4.2.3  Nitridation and oxidation of Ni-based alloys (after ref. [7])

Generally, internal nitridation takes place, when the alloying elements differ strongly in their affinity to nitrogen and if the concentrations of the elements with high nitrogen affinity are below critical values, so that no superficial nitride scale can be formed. Internal nitridation of those engineering alloys which do develop a protective oxide scale is attributed to instabilities in the outer scale as a result of erosion, growth stress within the surface layer, crack formation from cyclic creep, and superimposed thermal cycling [7]. Figure 4.2.8 summarizes schematically the microstructural changes that are caused by internal nitridation.



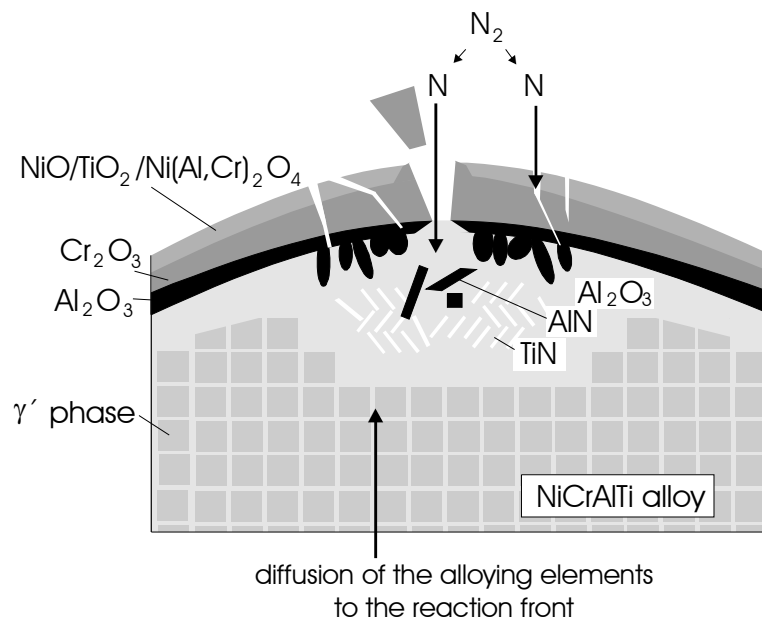*Figure 4.2.8. Internal nitridation of Ni-base superalloys caused by cracks and pores in the oxide scale [7].*

Figure 4.2.9 gives an example for an ***InCorr*** calculation of the concentration profiles (Figure 4.2.9b) of the species involved in simultaneous internal precipitation of Ti and Al nitrides in a Ni-20Cr-2Al-2Ti alloy during high-temperature exposure in a nitrogen-based atmosphere.
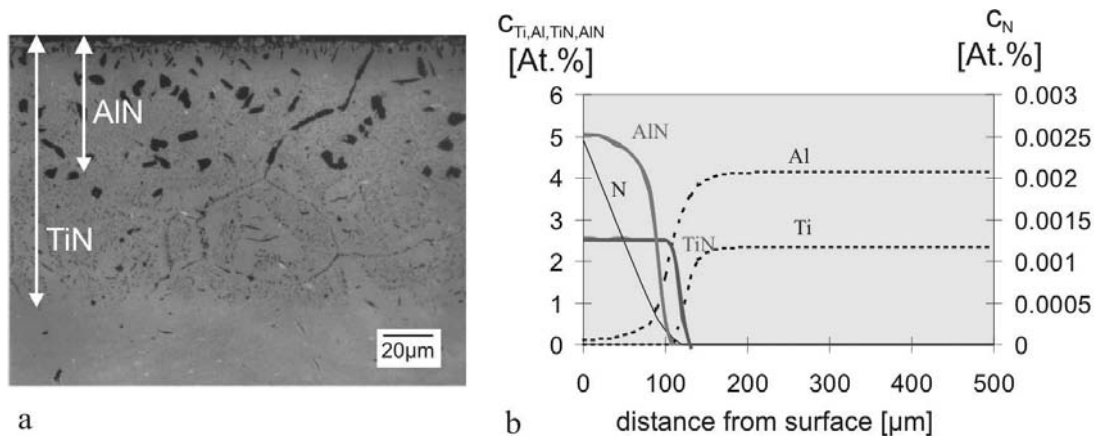
*Figure 4.2.9. Simultaneous internal nitridation by TiN and AlN in Ni-20Cr-2Al-2Ti (100 h, 1000°C, nitrogen): (a) experimental result and (b) corresponding calculated concentration profiles [7].*

A further example for internal corrosion degradation of Ni-based alloys as it is often observed under in-service conditions, is internal oxidation occurring mainly along alloy grain boundaries [8]. Figure 4.2.10a shows a cross section of Inconel 625Si after 90 h of exposure to laboratory air at 1000°C. A continuous external $Cr_2O_3$ oxide scale is formed on the surface of both alloys. In the case of Inconel 625Si a discontinuous $SiO_2$ scale is formed underneath the $Cr_2O_3$ scale (Figure 4.2.10a), which is probably responsible for the relatively low oxidation rate. Internal oxidation was observed in both alloys, occurring preferentially along alloy grain boundaries, enhanced by the fast oxygen diffusion along these short-circuit diffusion paths. Figure 4.2.10b shows the simulated concentration profiles of Al and $Al_2O_3$, which are in good agreement with the experimentally observed intergranular oxidation characteristics, when considering higher oxygen diffusivity along alloy grain boundaries as compared to bulk.
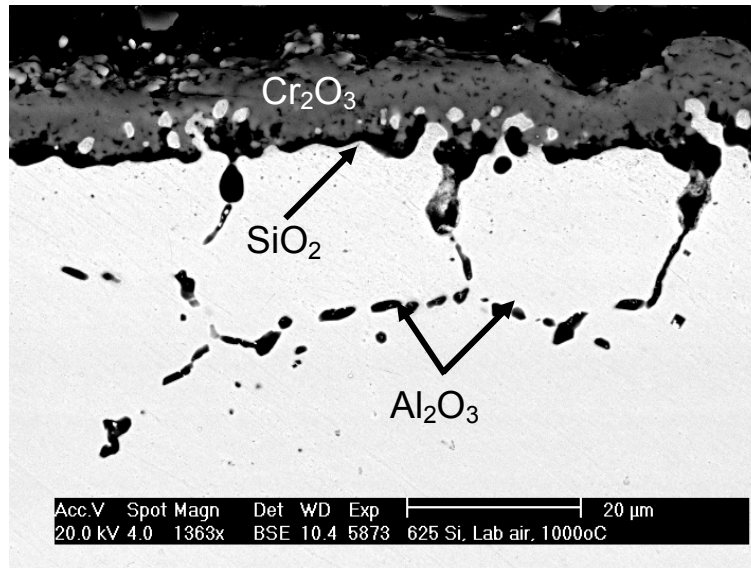
(a)
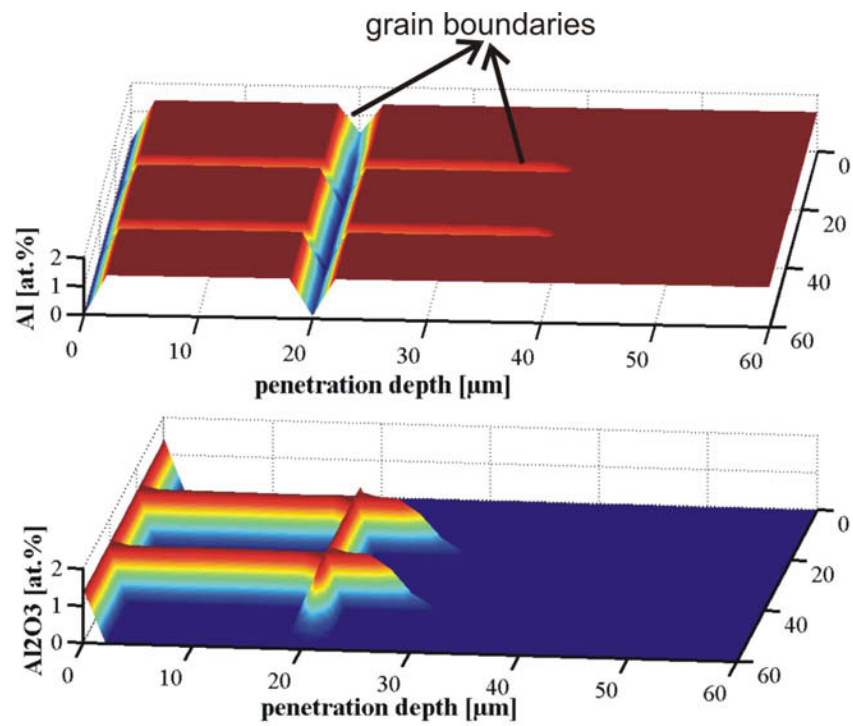


(b)

*Figure 4.2.10. Internal oxidation of the Ni-based alloy Inconel 625Si in laboratory air at 1000°C after 90 h: (a) SEM micrograph of the cross-section and (b) simulated concentration profiles of Al and Al₂O₃.*

### 4.2.4  Concluding remarks

The examples presented above demonstrate the applicability of the combination of the finite-difference technique and computational thermodynamics to complex corrosion processes which depend substantially on the material's microstructure. Of course, much more experimental work is required to describe in detail the variety of possible transport processes, e.g., taking place within the porous inner oxides scale and along the substrate grain boundaries. Strictly spoken, the structure of the interfaces should change as soon as the grain boundaries are covered by an oxide phase which is in contact with the matrix on both sides. Also, the actual value of the grain-boundary thickness and its implementation in the finite difference approach remains an open question. In the present approach, the grain-boundary thickness is assumed as to be $\delta = 0.5$ nm according to Fisher [3] and the segregation factor as to be $s = 1$.

### 4.2.5  References

[1]    http://www.matlabgui.com/

[2]    U. Krupp, V.B. Trindade, H.-J. Christ, U. Buschmann and W. Wiechert, Diffusion and Defects Forum, 2004, Vol. 237–240, pp. 946–951.

[3]    J.C. Fisher, Journal of Applied Physics, 1951, 22, 74.

[4]    T. Heumann, Diffusion in Metallen, Springer-Verlag, Berlin Heidelberg, Germany 1992.

[5]    C. Wagner, Zeitschrift für Physikalische Chemie, 1933, 21, 25.

[6]    I. Kaur, W. Gust and L. Kozma, Handbook of Grain and Interphase Boundary Diffusion Data, Ziegler Press, Stuttgart, Germany 1989.

[7]    U. Krupp, H.-J. Christ, Oxidation of Metals, 52 (1999), 277.

[8]    V.B. Trindade, U. Krupp, Ph. E.-G. Wagenhuber and H.-J. Christ, *Materials and Corrosion*, 2005, in press.

# 4.3  Modelling of salt melt induced corrosion

(K. Penttilä – VTT Processes; M. Spiegel – Max Planck)

## 4.3.1   Pure Fe-metal

Experiments on Pure iron covered by a 50 mol.% $ZnCl_2$ – 50 mol.% KCl melt show accelerated corrosion. According to the corrosion model (chapter 3.2.2, Figure 3.2.1) the reason for the accelerated corrosion rate is the diffusion of the dissolved iron chloride toward to the salt melt – gas atmosphere interface. Due to the higher $p(O_2)$ on the outer part, oxidation of iron chloride to iron oxide takes place. Figure 4.3.1 shows the stability diagram of the system Fe – $O_2$ – $Cl_2$ at 320°C. An important parameter for this type of corrosion is the solubility of the metal chloride in the molten chloride mixture (50 mol.% $ZnCl_2$ – 50 mol.% KCl; Figure 4.3.2). At 320°C about 15 mol.% $FeCl_2$ can be dissolved in a 50 mol.% $ZnCl_2$ – 50 mol.% KCl melt. The diffusion rate of the dissolved portion of iron chloride will be higher than is the case of solid iron chloride, yielding a higher corrosion rate due to oxidation of iron chloride to iron oxide at the upper part of the salt melt. Experiments that have been stopped after a few hours of corrosion confirm the formation of iron chloride (Figure 4.3.4). A comparison of two thermogravimetric experiments show the influence of $p(O_2)$ on the corrosion kinetics (Figure 4.3.5).
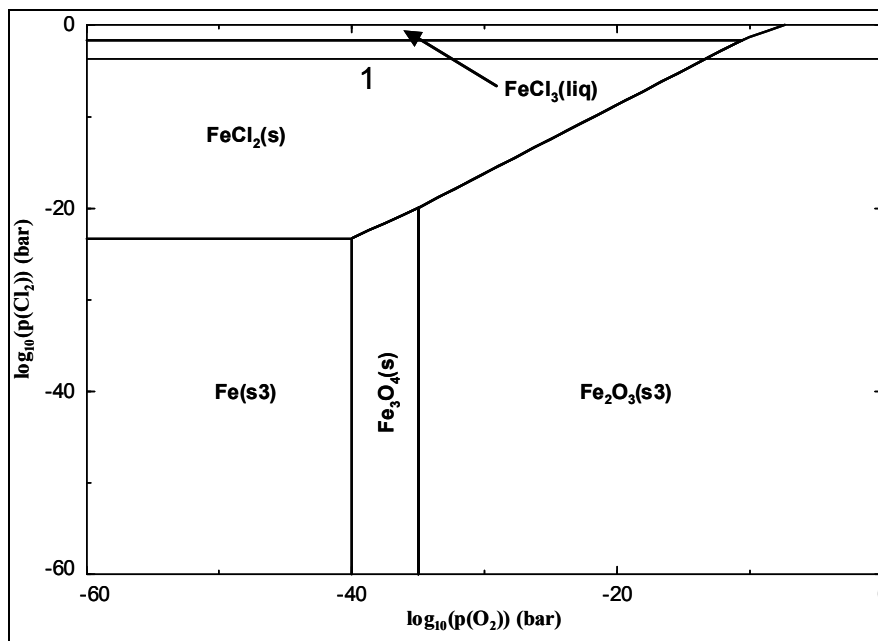


*Figure 4.3.1. Phase diagram of the system Fe–$Cl_2$–$O_2$ at T = 320°C. The chlorine partial pressure established by the oxidation of $ZnCl_2$ at 8 vol.% $O_2$ is indicated with "1". Close to the metal/salt melt interface iron chloride is stable. Close to the salt melt/gas atmosphere interface hematite is stable. Calculated with FactSage.*
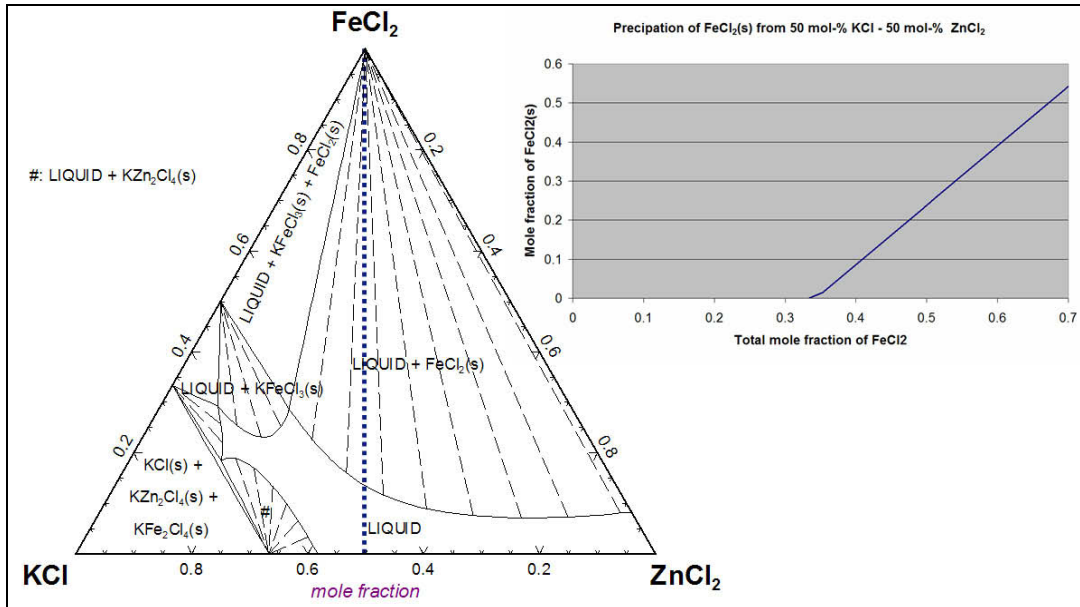
*Figure 4.3.2. Phase diagram of the FeCl₂-KCl-ZnCl₂ system (T = 320°C).*

Figure 4.3.3 shows the thermodynamic data-file used in all the simulations. It is compiled from the data evaluated by Klaus Hack (see chapter 2.2). It contains 10 elements, three solution phases (gas, salt and metal alloy) and 22 solid phases. It can be used to simulate pure Fe, Ni, Cr metals or their alloy under different salts in contact with atmosphere containing Ar, $O_2$, HCl, $H_2O$ and $SO_2$.

| Gas IDMX | | Salt SUBG | BCC SUBLM | Solids PURE | | Elements |
|---|---|---|---|---|---|---|
| Ar | $Cr_2$ | KCl | Fe | Fe(s) | NiO*Cr2O3(s) | •Zn |
| H | CrO | $FeCl_2$ | Ni | FeO(s) | NiO*Fe2O3(s) | •Ni |
| $H_2$ | $CrCl_2$ | $FeCl_3$ | Cr | $Fe_2O_3$(s) | NiSO4(s) | •Fe |
| $O_2$ | $CrCl_3$ | $ZnCl_2$ | S | $Fe_3O_4$(s) | NiS(s) | •Cr |
| OH | Fe | $NiCl_2$ | | $FeCl_2$(s) | Cr(s) | •K |
| $H_2O$ | FeO | $CrCl_2$ | | $FeCl_3$(s) | $Cr_2O_3$(s) | •Cl |
| $S_2$ | $FeCl_2$ | $CrCl_3$ | | $FeKCl_3$(s) | $CrCl_2$(s) | •S |
| $H_2S$ | Fe(OH)2 | $K_2SO_4$ | | $FeK_2Cl_4$(s) | $CrCl_3$(s) | •O |
| $SO_2$ | Ni | $FeSO_4$ | | $FeCrO_4$(s) | $CrSO_4$(s) | •Ar |
| $SO_3$ | NiO | Fe2(SO_4)_3 | | $FeSO_4$(s) | $Cr_2(SO_4)_3$(s) | •H |
| $H_2SO_4$ | $NiCl_2$ | $ZnSO_4$ | | FeS(s) | $Cr_2S_3$(s) | |
| $Cl_2$ | Ni(OH)_2 | $NiSO_4$ | | $KO_2$(s) | Zn(s) | |
| HCl | Zn | $CrSO_4$ | | $K_2O$(s) | ZnO(s) | |
| HOCl | $ZnCl_2$ | $Cr_2(SO_4)_3$ | | KCl(s) | $ZnCl_2$(s) | |
| K | | $K_2CrO_4$ | | $K_2CrO_4$(s) | $ZnK_2Cl_4$(s) | |
| KOH | | $FeCrO_4$ | | $K_2SO_4$(s) | $Zn_2KCl_5$(s) | |
| KCl | | $Fe_2(CrO_4)_3$ | | K2S(s) | $Zn_2K_3Cl_7$(s) | |
| | | $ZnCrO_4$ | | Ni(s) | $ZnFe_2O_4$(s) | |
| | | $NiCrO_4$ | | NiO(s) | $ZnCrO_4$(s) | |
| | | $CrCrO_4$ | | $NiCl_2$(s) | $ZnSO_4$(s) | |
| | | $Cr_2(CrO_4)_3$ | | NiKCl3(s) | ZnS(s) | |
| | | $Cl_2$(l) | | | | |

*Figure 4.3.3. The thermodynamic data file used in the simulation.*

117
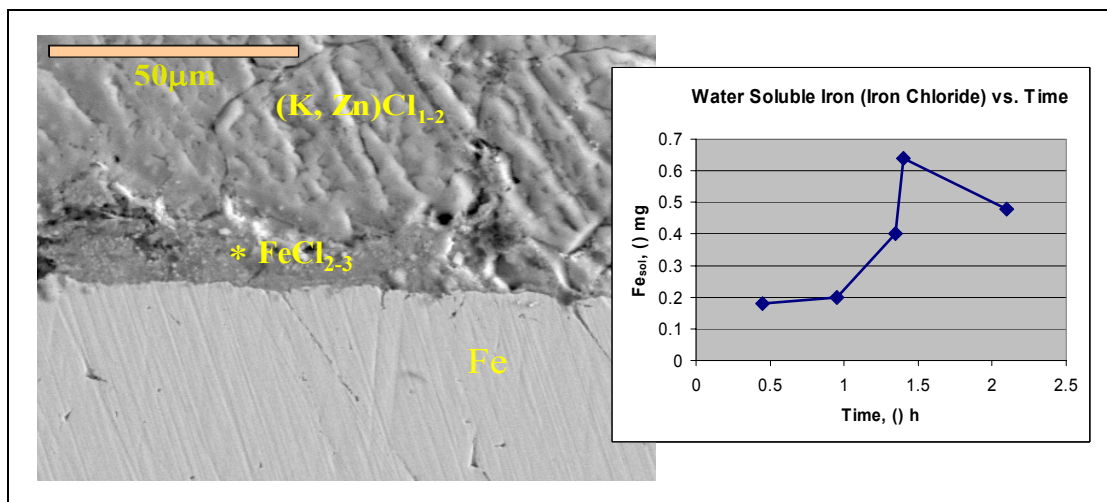
*Figure 4.3.4. Iron Chloride formation during incubation time (A. Ruh, M. Spiegel [2]). T = 320°C, Ar – 4 vol.% $O_2$, KCl 50 mol.%, $ZnCl_2$ 50 mol.%.*



*Figure 4.3.5. Thermogravimetric curves for high temperature corrosion (T = 320°C) of pure Fe covered with 50 mol.% KCl – 50 mol.% $ZnCl_2$ (15 mg/cm$^2$) in Ar – $O_2$ atmosphere (8 and 16 vol.% $O_2$).*

Simulated composition of salt phase species is shown in Figure 4.3.7. $Fe_2O_3(s)$ and $Zn_2Fe_2O_4(s)$ are formed at salt/gas interface at position where iron chloride mass fraction is lowered drastically (see Figure 4.3.8). Soluble chloride ($Cl_2(l)$) is formed from reactions between zinc chloride and oxygen and iron chlorides and oxygen at salt/gas interface. It diffuses to metal/salt interface where metal iron is dissolved to salt (see Figure 3.2.1).

118
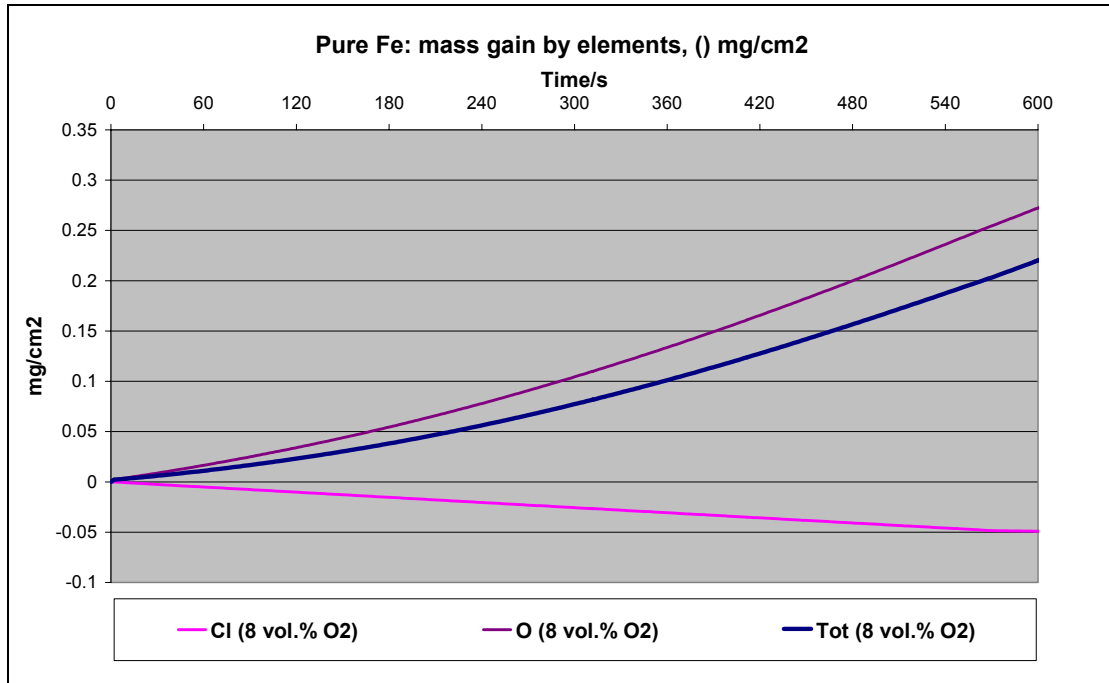
*Figure 4.3.6. Simulated mass gain curves of pure Fe covered with 50 mol.% KCl – 50 mol.% ZnCl$_2$ (15 mg/cm$^3$) in Ar – O$_2$ atmosphere (8 vol.% O$_2$).*
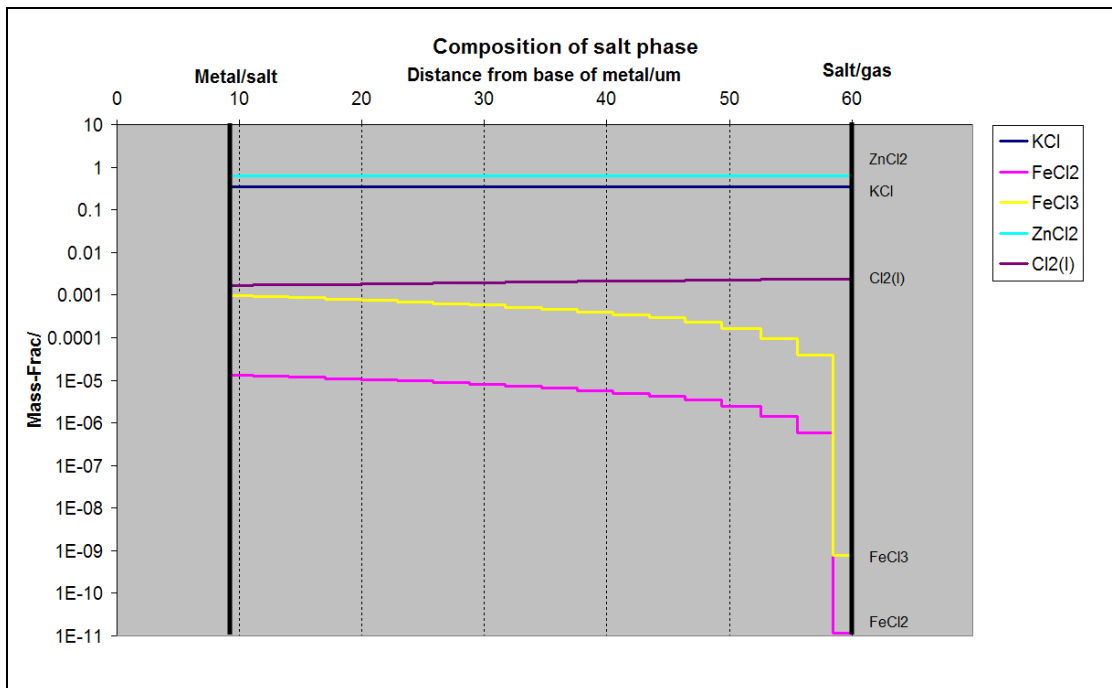


*Figure 4.3.7. Simulated composition of salt phase species after 5 minutes. Pure Fe covered with 50 mol.% KCl – 50 mol.% ZnCl$_2$ (15 mg/cm$^3$) in Ar – O$_2$ atmosphere (8 vol.% O$_2$).*
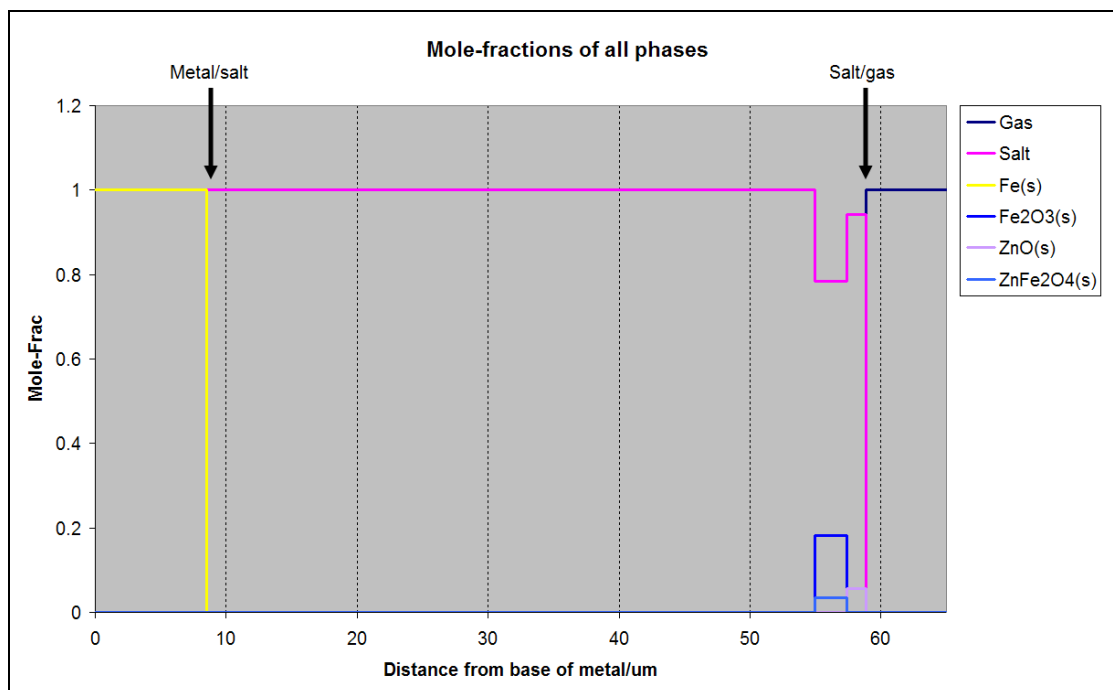
*Figure 4.3.8. Simulated oxide formation after 10 minutes. Pure Fe covered with 50 mol.% KCl – 50 mol.% ZnCl$_2$ (15 mg/cm$^3$) in Ar – O$_2$ atmosphere (8 vol.% O$_2$).*

Experiments with pure Fe in Ar – O$_2$ – HCl atmosphere

TG experiments have been carried out on pure Fe covered with a 50 mol.% KCl – 50 mol.% ZnCl$_2$-mixture (15 mg/cm$^2$) in an Ar – O$_2$ – HCl atmosphere. The HCl content has been varied (500–2000 vppm). TG curves of these experiments are shown in Figure 4.3.9. A TG curve from an experiment without HCl is given for comparison [2]. HCl containing atmospheres yield a higher mass gain. For 2000 vppm HCl a mass loss can be observed after about 55 hours of corrosion due to evaporation of iron chloride (and ZnCl$_2$).

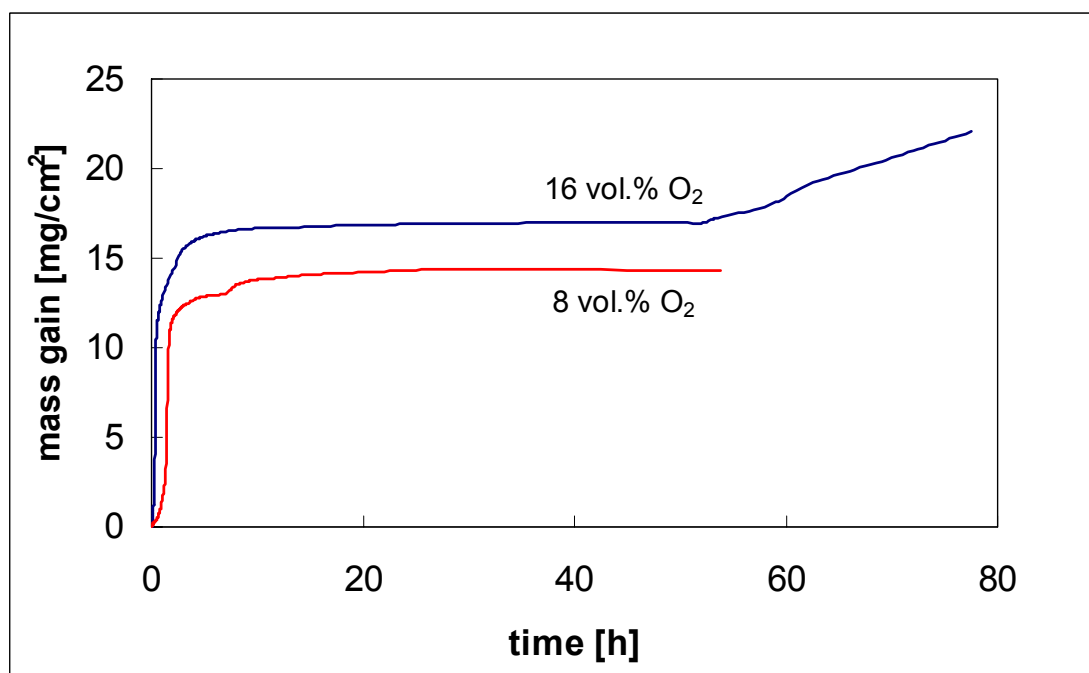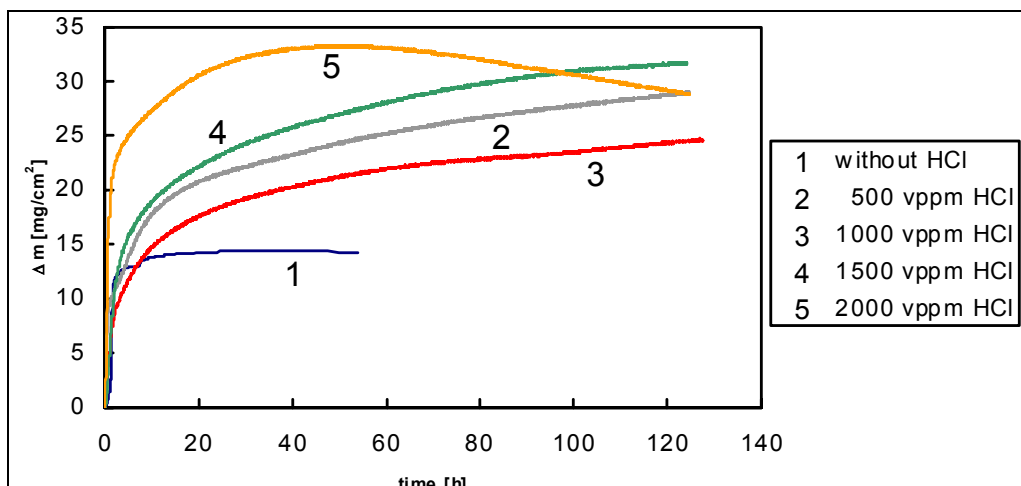*Figure 4.3.9. TG curves for high temperature corrosion (T = 320°C) of pure Fe covered with a 50 mol.% KCl – 50 mol.% ZnCl₂ deposit in Ar – 8 vol.% O₂ – HCl (0–2000 vppm). TG curve of the experiment without HCl is taken from [2]. In comparison to HCl-free atmospheres the mass gain of HCl containing atmospheres is clearly enhanced. At 2000 vppm a mass loss occurs after about 55 hours indicating evaporation of chloride.*

While the start of the curve with an incubation phase is obvious in the experiment without HCl gas, this phenomena is only evident for experiments in Ar – O₂ – HCl atmospheres with lower HCl (500 vppm) contents (Figure 4.3.10). For higher HCl contents the incubation phase disappears so that the TG curve starts with a linear stage.
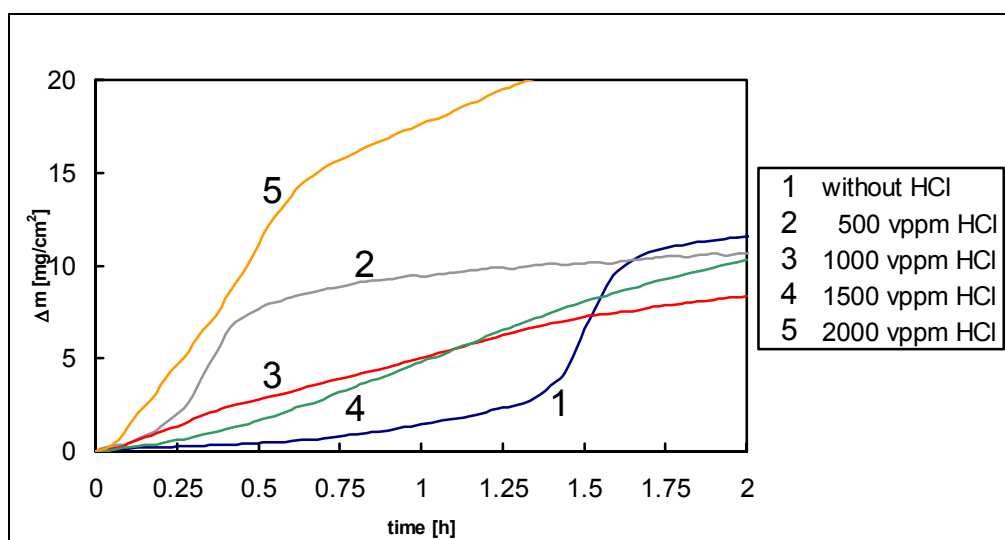


*Figure 4.3.10. TG curves for high temperature corrosion (T = 320°C) of pure Fe covered with a 50 mol.% KCl – 50 mol.% ZnCl₂ deposit in Ar – 8% O₂ – HCl (0–2000 vppm) showing the first two hours of corrosion. TG curve of the experiment without HCl is taken from [2]. It shows a relative long incubation time. An incubation phase can also be observed at 500 vppm HCl but it disappears at higher HCl contents. The slope of the linear stage is greater when an incubation phase is present.*

121

## 4.3.2 Pure Ni-metal

Nickel shows a relatively low corrosion rate (Figure 4.3.11). This is due to relatively high stability of $NiCl_2$ in comparison to NiO (Figure 4.3.12). $NiCl_2$ is also more stable in comparison to $FeCl_2$, $FeCl_3$ (Figure 4.3.1) or $CrCl_3$ (Figure 4.3.16) even at somewhat higher $p(O_2)$. On the other hand $NiCl_2$ is almost insoluble in the KCl – $ZnCl_2$ melt (Figure 4.3.13). Therefore, the diffusion rate of $NiCl_2$ will be lower as well as the corrosion rate. For low corrosion rate as for Ni the evaporation of the chloride deposit must be taken into account. Generally, enhanced mass gain was observed when either a higher amount of salt deposit or oxygen was applied.



*Figure 4.3.11. Thermogravimetric curves for high temperature corrosion (T = 320°C) of pure Ni covered with 50 mol.% KCl – 50 mol.% $ZnCl_2$ (15/30 mg/cm$^2$) in Ar – $O_2$ atmosphere (8 and 16 vol.% $O_2$) and for evaporation of KCl / $ZnCl_2$ on Pt and Fe at 320°C in Ar.*

*Figure 4.3.12. Phase diagram of the system Ni–Cl₂–O₂ at T = 320°C. The chlorine par-tial pressure established by the oxidation of ZnCl₂ at 8 vol% O₂ is indicated with "1". At this p(Cl₂) NiO will be formed at the outermost part of the chloride melt, close to the salt melt/gas atmosphere interface, only. Calculated with FactSage.*
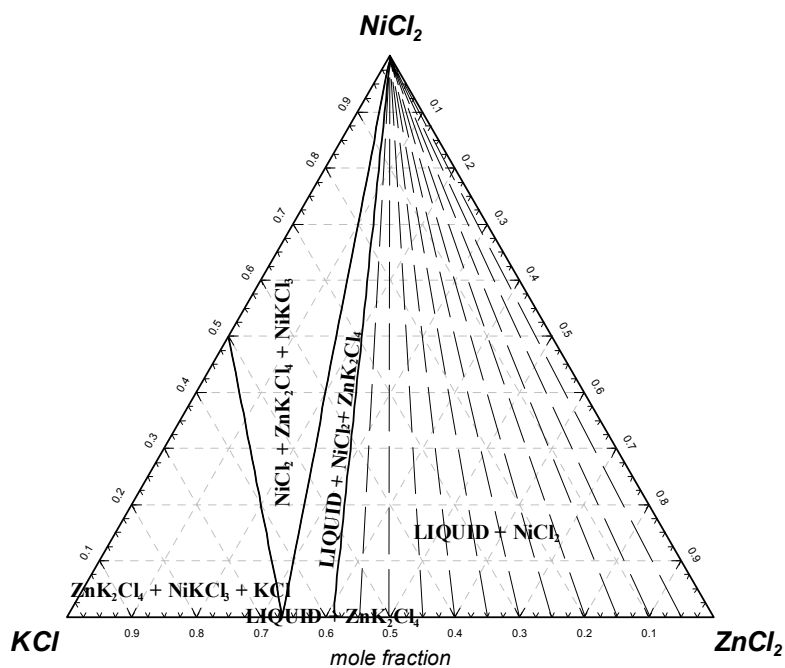


*Figure 4.3.13. Phase diagram of the NiCl₂-KCl-ZnCl₂ system (T = 320°C).*
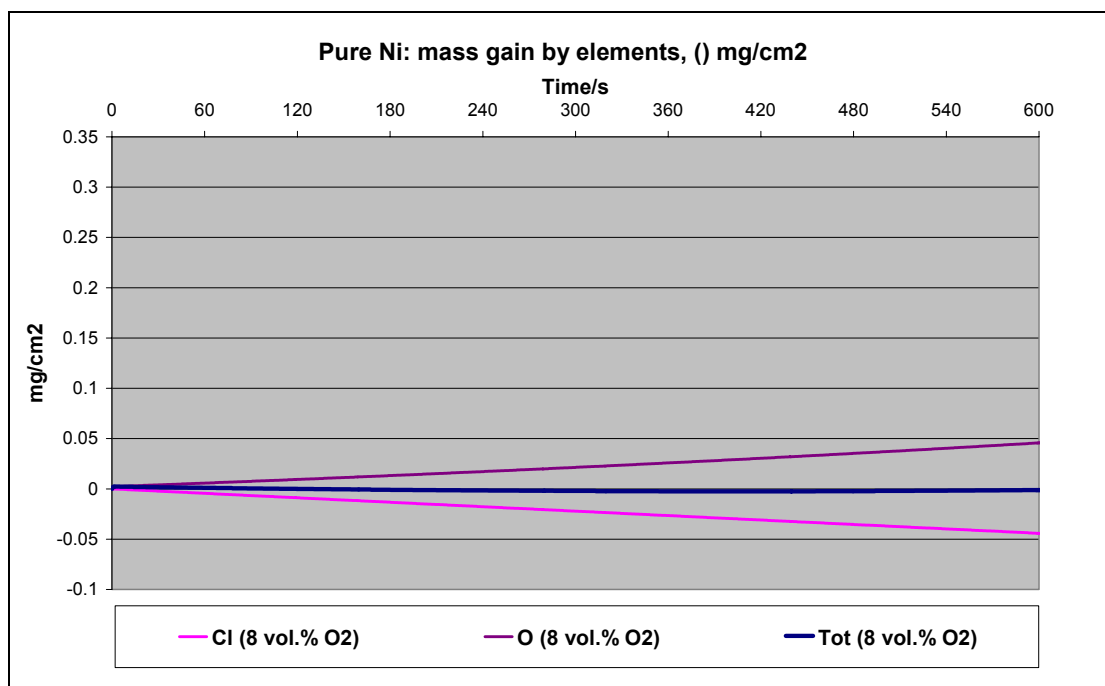
*Figure 4.3.14. Simulated mass gain curves (T = 320°C) of pure Ni covered with 50 mol.% KCl – 50 mol.% ZnCl$_2$ (15 mg/cm$^3$) in Ar – O$_2$ atmosphere (8 vol.% O$_2$).*

### 4.3.3 Pure Cr-metal

For thermogravimetric experiments on pure Cr in Ar – O$_2$ (8–16 vol.%) atmospheres the samples were covered by a 50 mol.% KCl – 50 mol.% ZnCl$_2$-mixture (15–30 mg/cm$^2$). The TG curves of these experiments are shown in Figure 4.3.15. The mass gain is enhanced when either a higher amount of salt deposit or oxygen was applied, similar to Ni. In this experimental series the evaporation rate of the KCl-ZnCl$_2$ deposit should be considered. The corrosion of pure Cr beneath molten KCl – ZnCl$_2$ is characterised by low mass gains. Even Cr$_2$O$_3$ is stable over a wide p(O$_2$) – p(Cl$_2$) range (Figure 4.3.16) the corrosion rate is quite low, indicating a less accelerated oxidation rate. A reason for this behaviour might be the low solubility of CrCl$_3$ in molten KCl – ZnCl$_2$ (Figure 4.3.17), similar to NiCl$_2$.
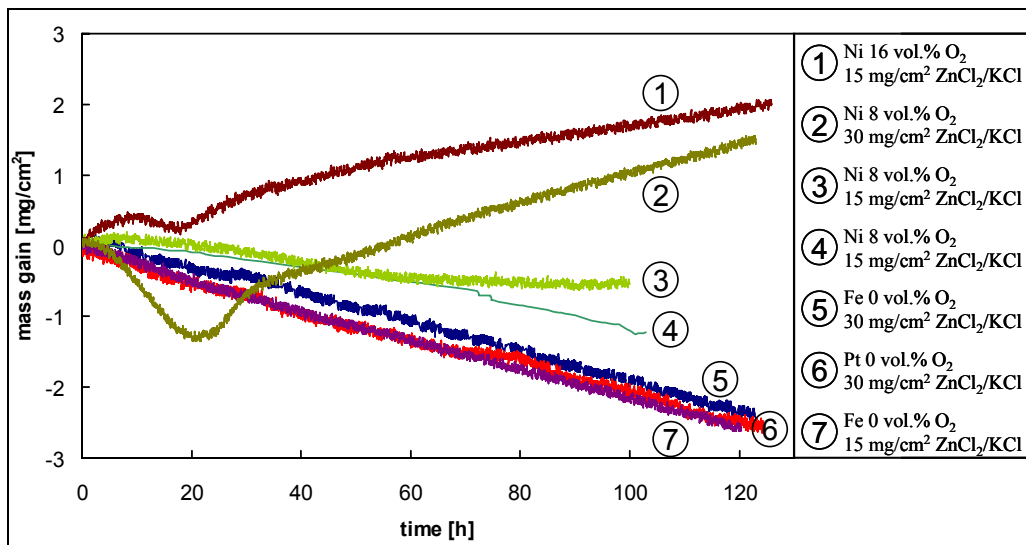
*Figure 4.3.15. Thermogravimetric curves for high temperature corrosion(T = 320°C) of pure Cr covered with 50 mol.% KCl – 50 mol.% ZnCl$_2$ (15/30 mg/cm$^2$) in Ar – O$_2$ atmosphere (8 and 16 vol.% O$_2$) and for evaporation of KCl / ZnCl$_2$ on Pt and Fe at 320°C in Ar.*
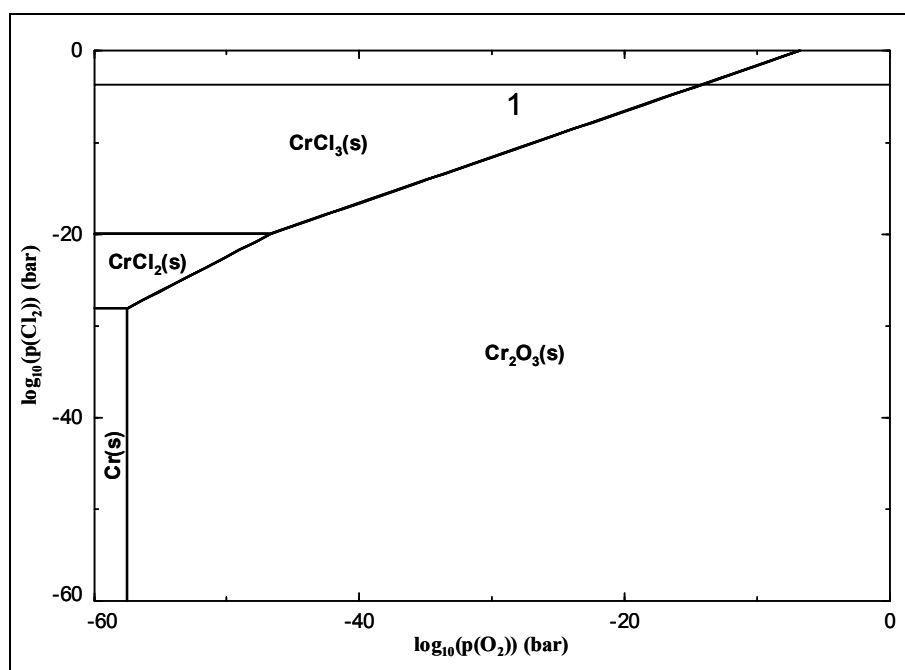


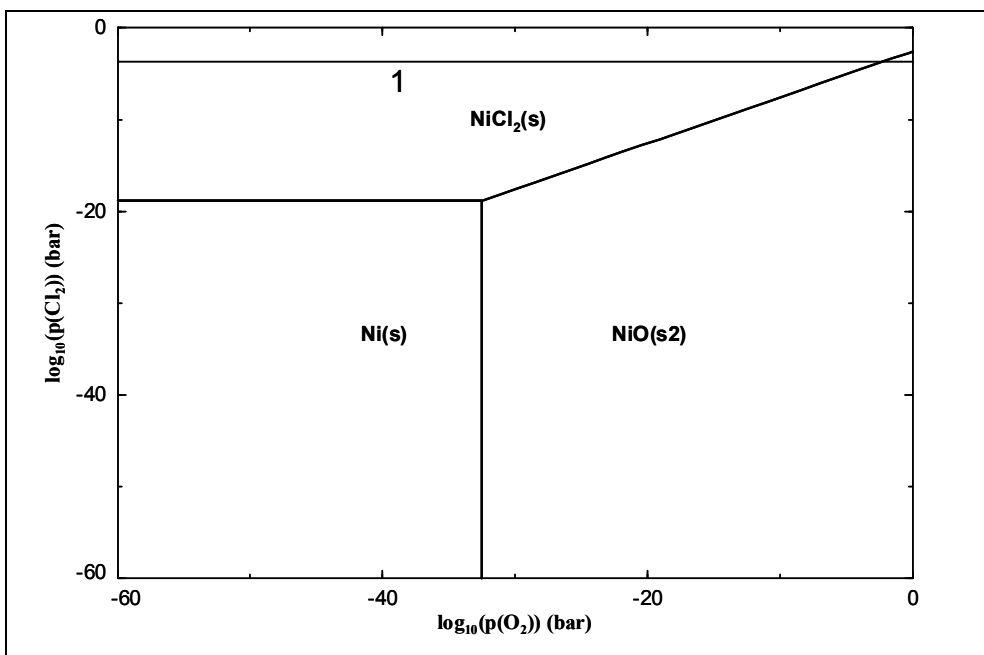*Figure 4.3.16. Phase diagram of the system Cr–Cl$_2$–O$_2$ at T = 320°C. The chlorine partial pressure established by the oxidation of ZnCl$_2$ at 8 vol% O$_2$ is indicated with "1". Calculated with FactSage.*

125
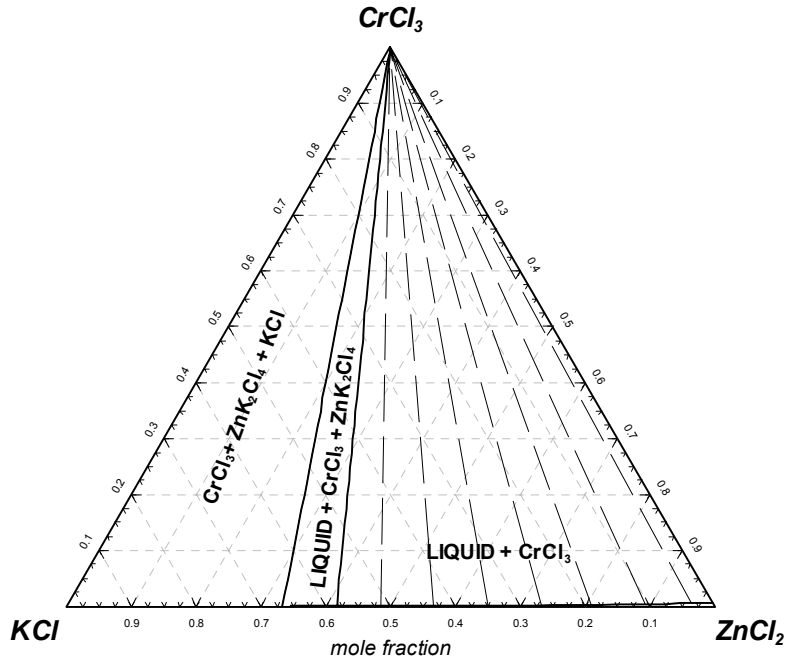
*Figure 4.3.17. Phase diagram of the CrCl$_3$-KCl-ZnCl$_2$ system (T = 320°C).*
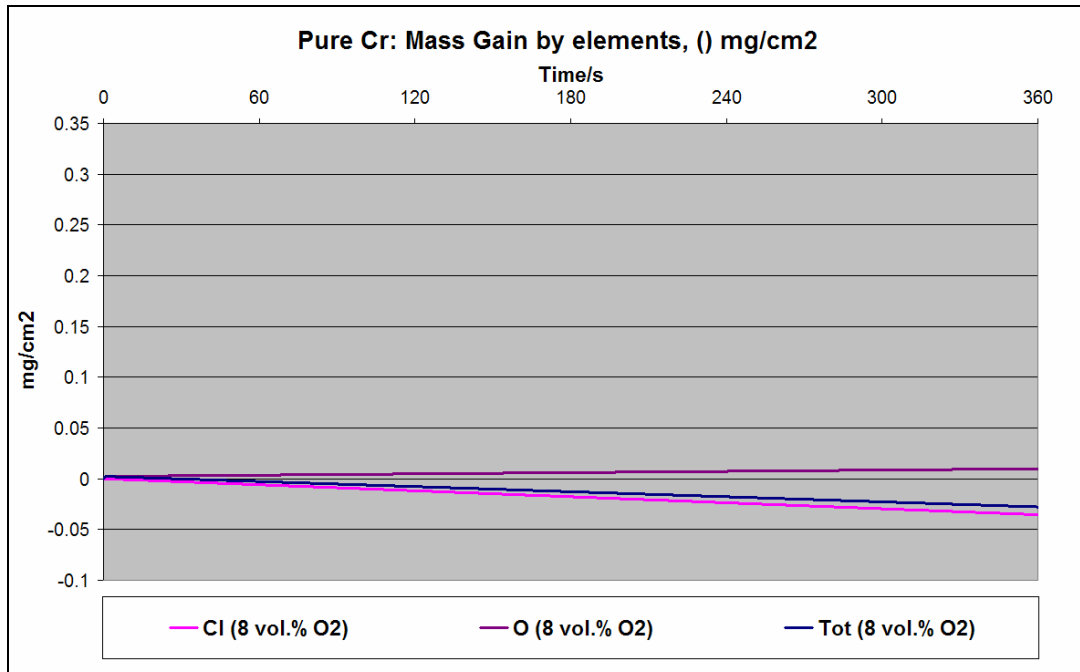


*Figure 4.3.18. Simulated mass gain curves (T = 320°C) of pure Cr covered with 50 mol.% KCl – 50 mol.% ZnCl$_2$ (15 mg/cm$^3$) in Ar – O$_2$ atmosphere (8 vol.% O$_2$).*
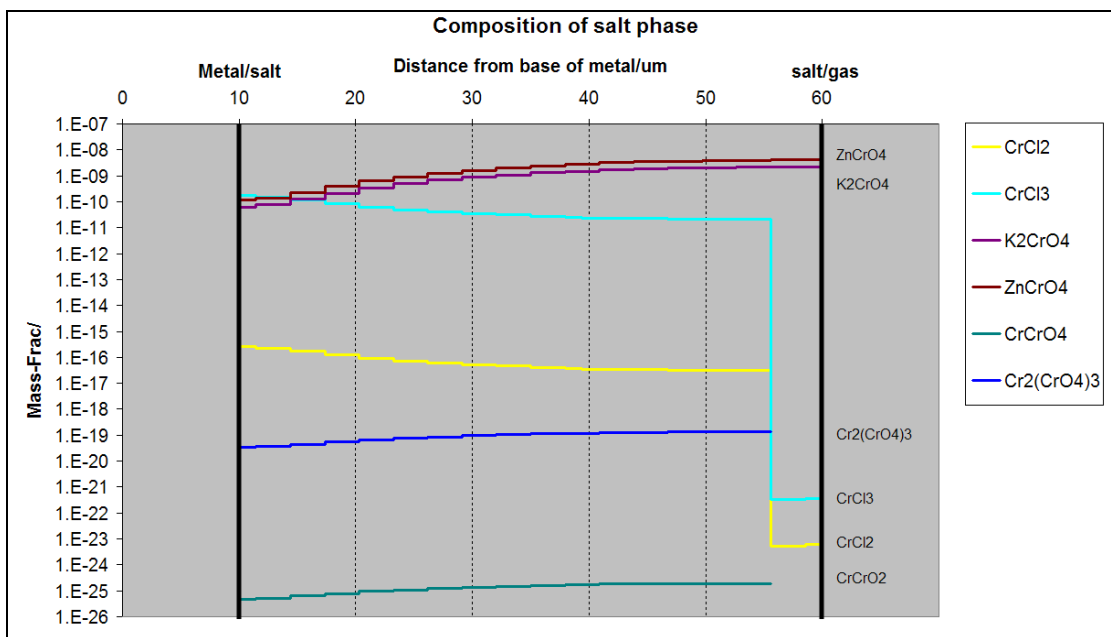
*Figure 4.3.19. Simulated composition of salt phase species that contain chromium after 5 minutes. Pure Cr covered with 50 mol.% KCl – 50 mol.% ZnCl₂ (15 mg/cm³) in Ar – O₂ atmosphere (8 vol.% O₂).*

Simulated composition of salt phase species containing chromium is shown in Figure 4.3.19. Some $Cr_2O_3(s)$ if formed at salt/gas interface at position where chromium chloride mass fraction is lowered drastically but due to very low solubility of $CrCl_3$ to salt its amount is negligible.

### 4.3.4  2.25Cr1Mo-alloy

The corrosion behaviour of 2.25Cr1Mo resembles the behaviour of pure Fe. Thermogravimetric experiments carried out on 2.25Cr1Mo yield similar curves to pure Fe (Figure 4.3.5). The curves show an incubation phase, a linear stage and a stage that is either parabolic or logarithmic. The process seems to be controlled by Fe. Cr and Mo most likely do not have any influence on the corrosion resistance of 2.25Cr1Mo. Table 4.3.1 illustrates the kinetic data for 2.25Cr1Mo and pure Fe for comparison.
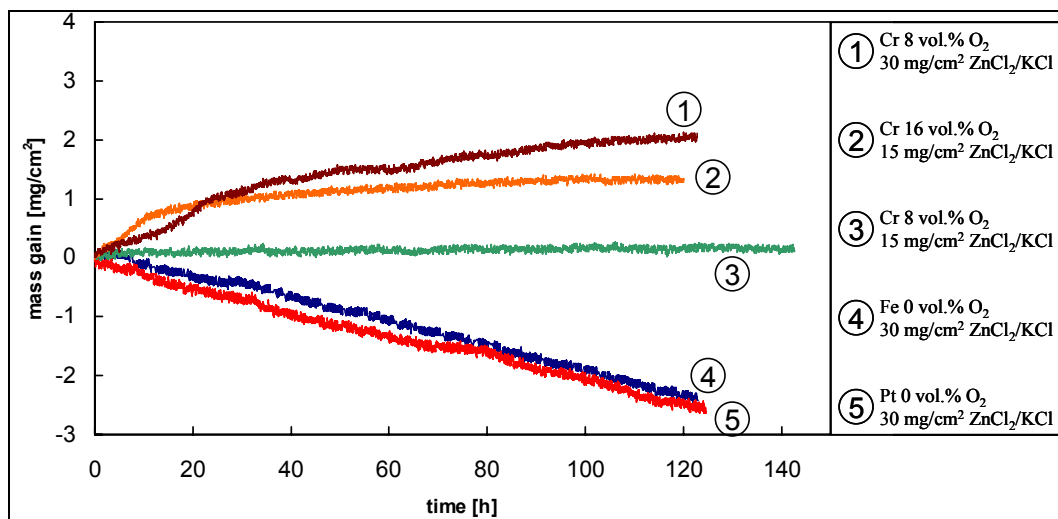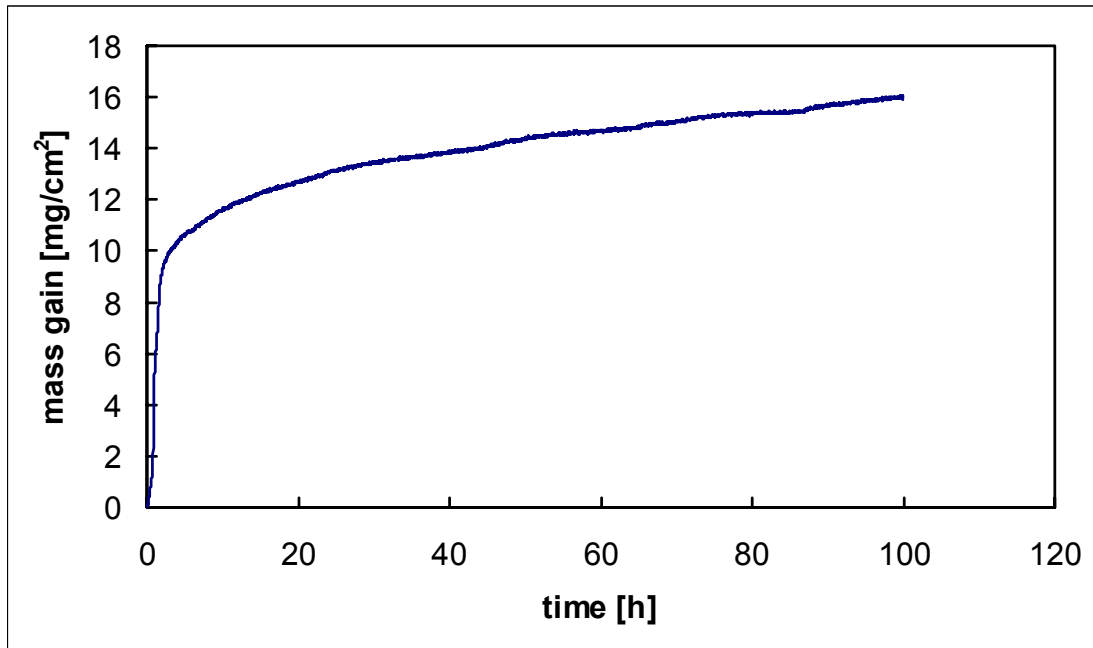
*Figure 4.3.20. Thermogravimetric curve for high temperature corrosion (T = 320°C) of 2.25Cr1Mo-Alloy covered with 50 mol.% KCl – 50 mol.% ZnCl$_2$ (15 mg/cm$^2$) in Ar – O$_2$ atmosphere (8 vol.% O$_2$).*

*Table 4.3.1. Kinetic data of corrosion studies on 2.25Cr1Mo and pure Fe at T = 320°C in an Ar – 8 vol.% O$_2$ atmosphere beneath 50 mol.% ZnCl$_2$ – 50 mol.% KCl (15 mg/cm$^2$).*

|  | 2.25Cr1Mo | Pure Fe |
|---|---|---|
|  |  |  |
| Incubation time [h] | 0.82 | 1.16 |
| K$_{lin}$ [mg/(cm$^2$*t)] | 22.48 | 35.97 |
| Total mass gain [mg/cm$^2$] | ∼ 15–16 | ∼ 14–15 |

### 4.3.5  References

[1]    M. Spiegel, Molten Salt Forum, Vol. 7, (2003), 253.

[2]    A. Ruh and M. Spiegel, EUROCORR 2003, Budapest, Hungary (CD-ROM), (2003).

[3]    G. Sorrell, Materials at High Temperatures, Vol. 14, No. 3, (1997), 207.

[4]    Y. Castrillejo, M.A. García, A.-M. Martinez, C. Abejón, P. Pasquier and G. Picard , J. Electroanal. Chem., 434, (1997), 43.

[5]   J. Bouteillon and M.-J. Barbier, J. Electroanal. Chem., 56, (1974), 399.

[6]   Y. Castrillejo, C. Abejón, M. Vega, R. Pardo and E. Barrado, Electrochim. Acta, 42 (1997), 1495.

[7]   Y. Castrillejo, S. Palmero, M.A. García, L. Debán and P. Sanchez Batanero, Electrochim. Acta, 41, (1996), 2461.

[8]   Y. Castrillejo, M.A. García, E. Barrado, P. Pasquier and G. Picard, Electrochim. Acta, 40, (1995), 2731.

[9]   H. Yabe, S. Hikino, K. Ema and Y. Ito, Electrochim. Acta, 35, (1990), 1233.

[10]  M. Taoumi, J. Bouteillon and M.J. Barbier, Electrochim. Acta 31, (1986), 837.

[11]  F. Lantelme, K. Benslimane and M. Chemla, J. Electroanal. Chem., 337, (1992), 325.

## 4.4  Results from the gas precipitation model

(K. Hack – GTT Technologies)

The simple ChemSheet-based model for the calculation of precipitate formation in a combustion gas with a variable aerosol freight has been used for parameter studies concerning the values of the "transfer coefficient" (initial aerosol freight) and the "sticking coefficient" (adhesion of precipitates on walls or pipes). The temperature range has been the same in all calculations assuming cooling between 800 and 300 K in steps of 25 K. The input composition of the gas and the aerosol have been taken as introduced in Chapter 3.3. It should be noted again at this point that these values come from a simulation of a waste incinerator. They are thus not representative for a very wide range of combustion power plants. Nevertheless, the results of the simulation calculations as shown below indicate what thermochemical modelling can do in complex cases such as those discussed here.
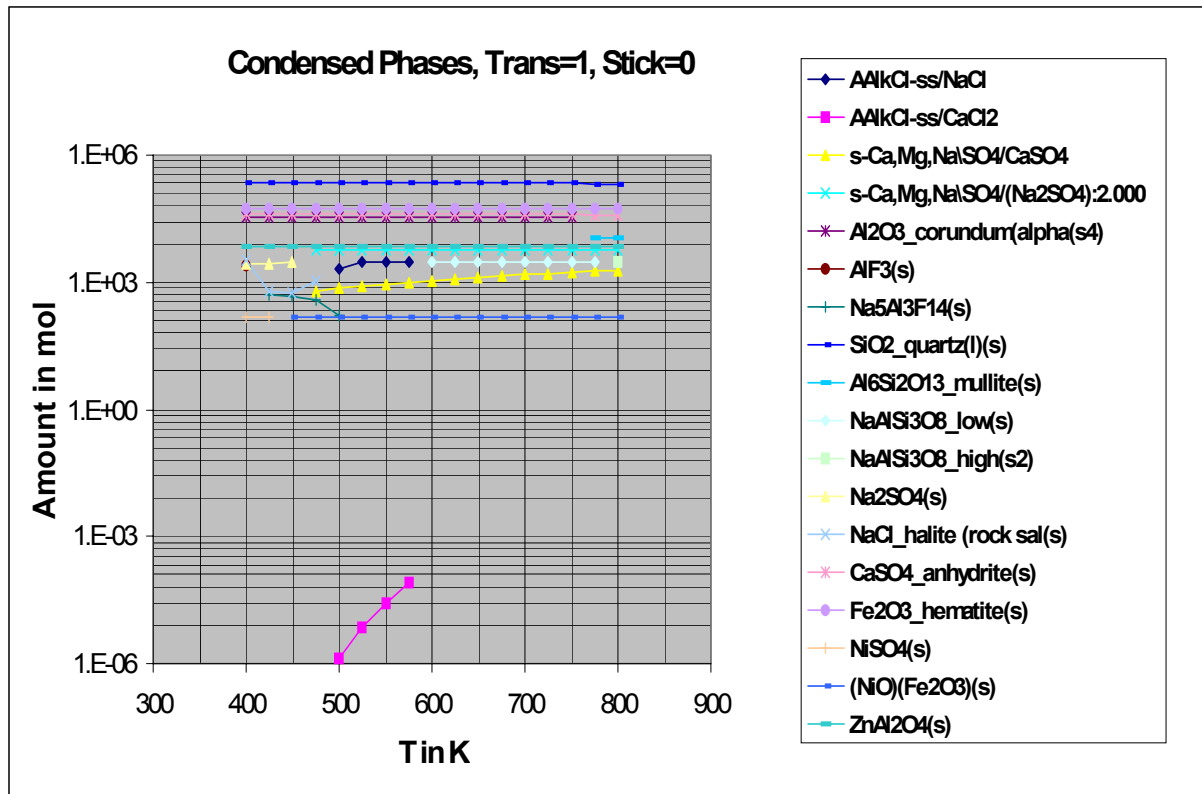
*Figure 4.4.1. Condensed Phases for the case of full aerosol transfer and no wall sticking.*

Figure 4.4.1 shows the result of a kind of reference calculation: this calculation contains all gas species and all condensed phases for each of the temperatures covered in the calculations. There are no material losses through sticking on the walls. Thus the chemical composition of the system is the same throughout the entire temperature range. Nevertheless, a first "feel" for the chemistry of such a complex system can be gained. Chlorides are formed at temperatures between 500 and 600 K, fluorides occur at temperatures below 550 K, while sulphates can be found in the entire range; at higher temperatures as a solid solution between $Na_2SO_4$ and $CaSO_4$, at lower temperatures as pure $Na_2SO_4$, $CaSO_4$ and also $NiSO_4$. Quartz, alumina, hematite, and Zn-aluminate are found at all temperatures, while mullite only occurs at high temperatures (775 to 800 K). These oxide phases are mainly due to the aerosol freight that is assumed at the start of the cooling sequence.

This first calculation cannot be related directly to the reality in a power station since it is known that some of the condensed matter transported by the gas and some of the condensed matter that precipitates from the gas on cooling sticks to the walls and heat exchanger pipes. Material has to be taken out of the calculation stepwise in order to simulate this behaviour. The following figures will give a first view on that situation.
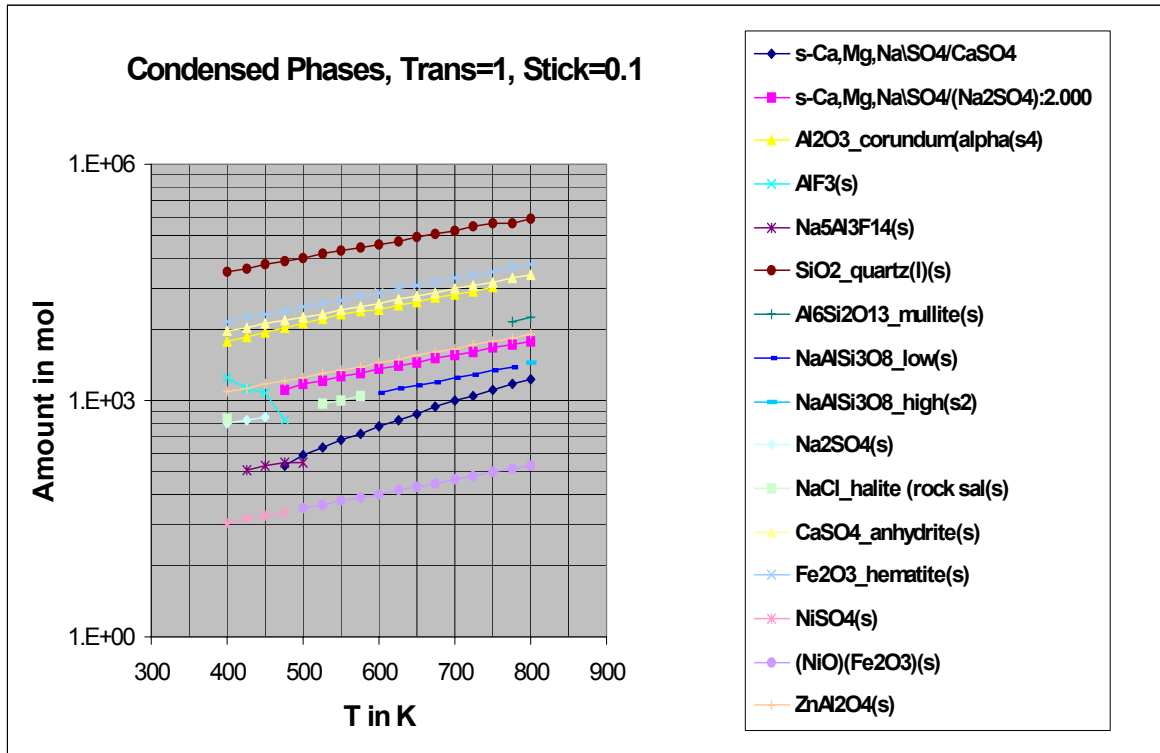
*Figure 4.4.2. Condensed Phases for the case of full aerosol transfer and 10% wall sticking.*

In Figure 4.4.2 is shown how the condensed phases will behave if all matter that is in aerosol form in the combustion chamber is transferred to the cooling stages and if 10% of the condensed material that is formed at each temperature step is taken out of the calculation before the next step thus simulating wall sticking. The condensed phases formed are both salts and mineral oxides with the oxides occurring at all temperatures as in the first calculation, Fig 4.4.1. Concerning the salts it can be seen that the sulphates form again the majority with a small temperature window between 575 and 525 K in which NaCl forms. The fluorites $AlF_3$ and $5NaF.3AlF_3$ are present again at low temperatures.
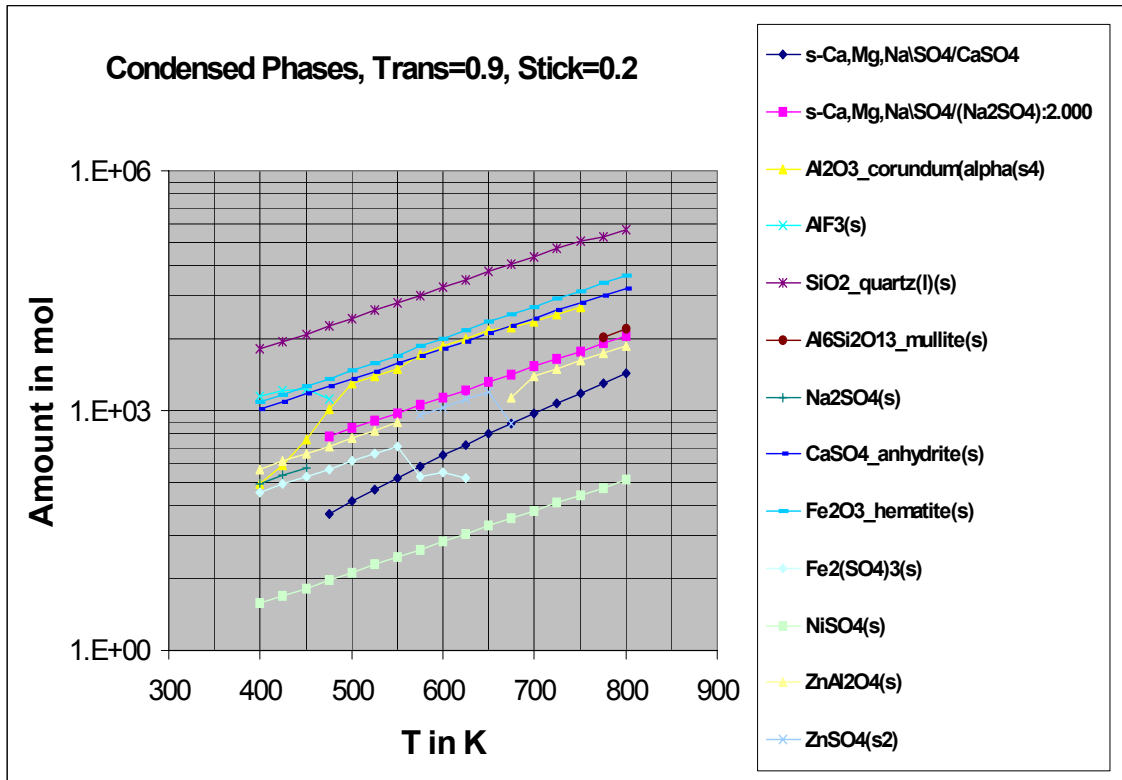
*Figure 4.4.3. Condensed phases for restricted transfer (90%) and 20% sticking.*

In Figure 4.4.3 is shown a situation similar to that for Figure 4.4.2, but with a slightly higher sticking coefficient and the additional assumption that not all of the aerosol is transferred to the cooling sequence, i.e. there is also some wall sticking already in the combustion chamber. It is interesting to note how much of a change in the phase con-stellation and also in the temperatures of stability is brought about by such a relatively small change in the sticking coefficient. No chloride formation is found in these calcula-tions and the only fluoride is AlF3 at low temperatures. In the other hand there is $ZnSO_4$ formation in an intermediate temperature range. This result, in comparison to that in Figure 4.4.2, shows that the sticking factor clearly has an influence on the results. It will therefore be very important for the future development of modelling of the heat ex-changer processes to know in more detail the sticking behaviour of the condensed phases.
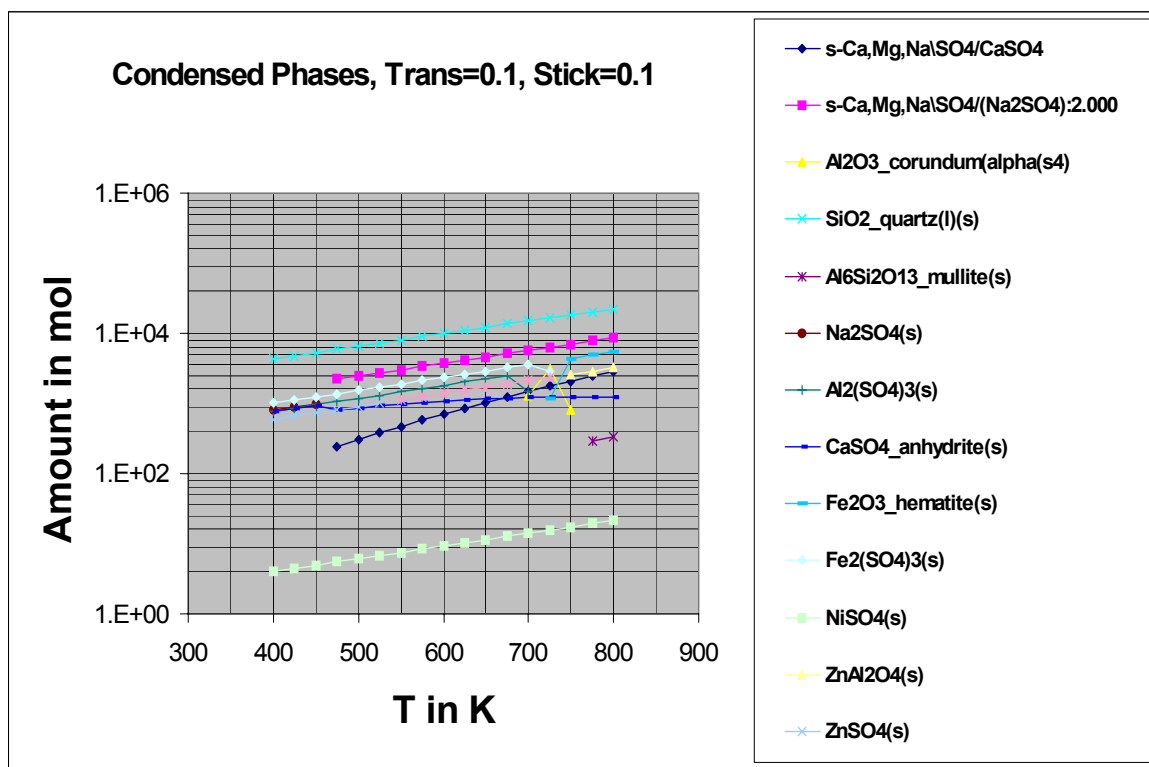
*Figure 4.4.4. Condensed phases low transfer(10%) and low sticking (10%).*

From Figures 4.4.4 it is obvious (low transfer coefficient and low sticking factor) that a certain aerosol freight is necessary in order for some precipitation to occur. The precipitates are a mix of oxides (minerals) and salts with the salts being sulphates. It must be assumed that the chance to find salts from a mere condensation effect are small. They form mainly as a result of reactions with other solids already present as aerosols. This holds particularly for the chlorides which do not occur if the aerosol amount is assumed to be low.
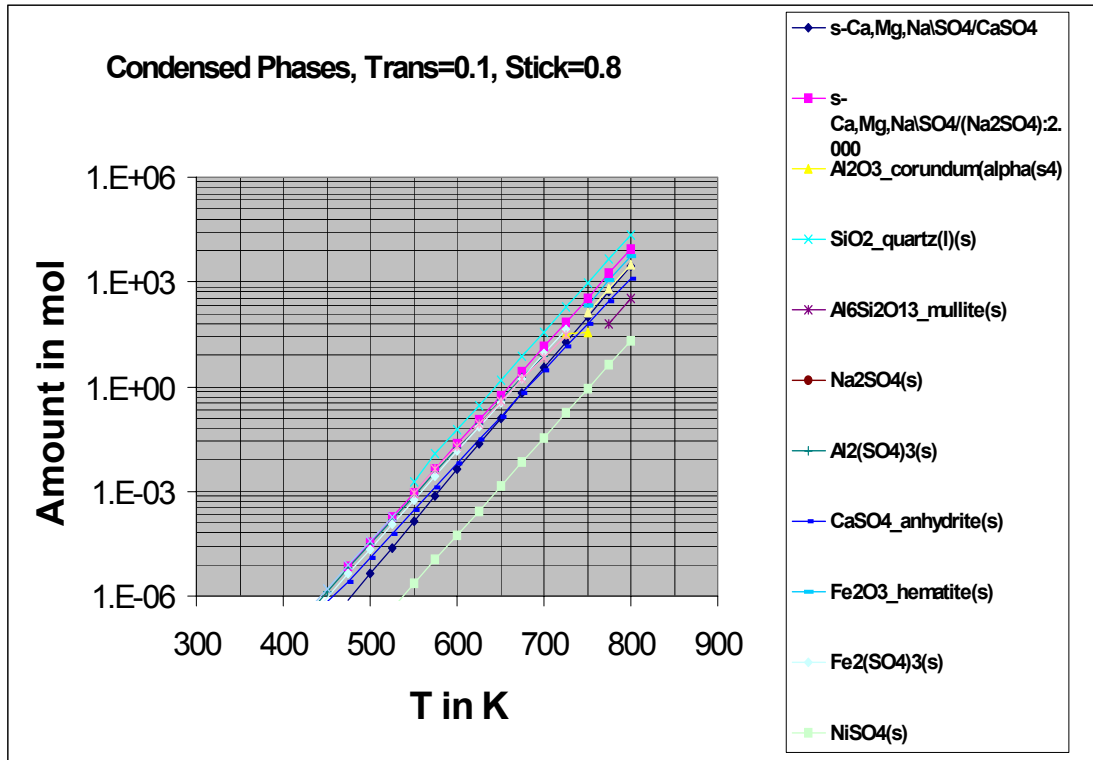
*Figure 4.4.5. Condensed phases for very low transfer (10%) and very high sticking (80%).*

Figure 4.4.5 has been generated for the very extreme case of almost no transfer of aerosol (10%) from the combustion chamber to the cooling sequence and for very high sticking (80%) of the precipitates formed. In contrast to all previous simulations there is now a strictly linear decrease of the amounts of precipitates with decreasing temperature. This is due to the extreme choice of the simulation parameters. This choice is not very likely to be close to the real case.

# 5. Key laboratory oxidation and corrosion data

In the OPTICORR project a set of experimental tests were carried out to investigate high temperature oxidation and corrosion under simulated bio/waste-fuelled boiler atmospheres and temperatures. The work was carried out to provide data for thermodynamic and kinetic modelling and to propose or verify the chemical reactions taking place in the studied systems. Therefore, the aims of the experimentation can be summarised:

- Collecting a comprehensive data set on high temperature active oxidation (gas-metal reactions) and on high temperature salt induced corrosion (gas-salt-metal reactions).

- Understanding of HT corrosion and oxidation mechanisms of steels and alloys under service conditions typical of biomass and waste combustion plants.

The OPTICORR project included four technical work packages, where two first produced data for modelling of corrosion kinetics. The kinetics of high temperature oxidation and corrosion were determined from laboratory TG-tests and multi sample corrosion exposure tests. The materials studied are typical of boiler tubes and fin-steels: ferritic alloys, austenitic steel T347, X10, X20, Sanicro 28, AC66 and Ni-based alloy Inconel 625. Rautaruukki has supplied ferritic steels and made characterisation of the test materials (Table 5.1).

The exposure gases are dry air, air with 15 vol-% $H_2O$, and with 2000 ppm HCl and 200 ppm $SO_2$ and a mixture of these all. The salt deposits used are based on KCl-$ZnCl_2$ and Ca-, Na-, K-, Pb- and Zn-sulfates. The test temperatures for exposures with deposits are 320, 420°C and for gas exposures 500, 550 and 600°C, however some tests were carried out at 420°C as well. The tests have been carried out by partners VTT, JRC-IE, MPIE and University of Siegen, summary in Table 5.2.

The project work summarised by the partners is in the following:

- **HUT (Marko Hämäläinen):** The work consisted of TG-experimentation under dry air (2 reference steels) with various heating speeds and cycles. The possibility to derive models for oxidation kinetics of multi-oxide systems has been studied. Also a substantial input to the collection and evaluation of thermodynamic data has been carried out.

- **VTT (Satu Tuurna & Liisa Heikinheimo):** The work contributed to the exposure tests according to split of the exposure test matrix in the project. The results cover 3 different mixed atmospheres and 4 temperatures (420 to 600°C) forming a consistent data set for active oxidation modelling.

-   **UNISiegen (Vicente B Trindade):** The work contributed to exposure tests according to split of the test matrix in the project. The exposure tests have supported the InCorr model development and verification of the demonstration cases with this tool, mainly the effects of grains size of austenitic and ferritic steels on oxidation kinetics. Also thermal cycling effects (RT – 550$^{o}$C for 20 min) have been studied and the results show that this yields to a very aggressive corrosion.

-   **JRC IE (Szymon Sroda & David Baxter):** The work has contributed to both the exposure test series and to TG test series. The gas atmospheres were similar in both test series, mixed gases, according to split of the exposure test matrix in the project. The results will form a wide data set with the results of VTT for active oxidation under simulated combustion atmospheres.

-   **MPIE (Andreas Ruh & Michael Spiegel):** The work contributed to salt induced high temperature corrosion studies and modelling according to the project work plan. The main work has been carried out to study the hot corrosion of Fe, Cr and Ni. Also a set of exposure tests with the test steels has been carried out using the defined salt deposits and gas atmospheres (split of the exposure test matrix in the project). The results are forming a data set of reaction kinetics and data and corrosion mechanisms for the modelling of salt induced corrosion with HTApp.

*Table 5.1. Composition of all alloys used in the experimental work of OPTICORR.*

| Steel grade | Form* | C | Si | Mn | P | S | Al | Cr | Cu | Mo | Ni | V | Other |
|---|---|---|---|---|---|---|---|---|---|---|---|---|---|
| **Pure metals (MPIE)** | | | | | | | | | | | | | |
| **Fe** | P | | | | | | | | | | | | Fe 99.99 |
| **Cr** | P | | | | | | | 99.99 | | | | | |
| **Ni** | P | | | | | | | | | | 99.99 | | |
| **Ferritic alloys (Rautaruukki, VTT, JRC)** | | | | | | | | | | | | | |
| 71439 | P | 0.0724 | 0.487 | 0.469 | 0.085 | 0.0098 | 0.035 | 0.723 | 0.335 | | 0.145 | 0.004 | Ce = 0.003 |
| 71518 (Mod Ni) | P | 0.074 | 0.386 | 1.04 | 0.004 | 0.005 | 0.09 | 0.59 | 0.40 | 0.002 | 0.79 | 0.032 | Ce = 0.004 |
| 71518 (Mod Ni +Si) | P | 0.075 | 1.01 | 1.07 | 0.004 | 0.005 | 0.092 | 0.59 | 0.39 | 0.003 | 0.78 | 0.032 | Ce = 0.004 |
| 4X60 | P | 0.06 | 0.2 | 0.6 | 0.01 | <0.01 | 0.04 | 1.4 | 0.01 | - | 0.04 | 0.00 | Nb 0.05 |
| 7X60 | P | 0.06 | 0.2 | 0.6 | 0.01 | <0.01 | 0.04 | 1.4 | 0.01 | - | 0.04 | 0.00 | Ce 0.03, Nb 0.05 |
| 4X60 – b | P | 0.056 | 0.17 | 0.58 | 0.004 | 0.005 | 0.08 | 1.4 | 0.026 | 0.002 | 0.069 | 0.002 | Nb 0.047 (Ce 0,001) |
| 7X60 – b | P | 0.054 | 0.116 | 0.5 | 0.004 | 0.002 | 0.09 | 1.39 | 0.021 | 0.003 | 0.068 | 0.001 | Ce 0.014, Nb 0.046 |
| 2.25Cr1Mo | R | 0.09 | 0.23 | 0.59 | 0.015 | 0.015 | 0.013 | 2.29 | 0.15 | 0.96 | 0.44 | 0.01 | W <0.01, Ti 0.003, Co 0.03, Nb 0.02 |
| 2.25Cr1Mo (Ce) | P | 0.08 | 0.15 | 0,55 | 0.005 | 0.003 | 0.025 | 2.28 | 0.16 | 1.00 | 0.46 | 0.01 | Ce 0.026, Nb 0.022 |
| X10 | T | 0.10 | 0.38 | 0.48 | | | 0.01 | 8.7 | | 0.97 | 0.26 | | |
| X20 | T | 0.87 | 0.23 | 0.62 | | | | 12.8 | | 0.87 | 0.72 | | |
| **Austenitic alloys (VTT, JRC)** | | | | | | | | | | | | | |
| TP347H | T | 0.048 | 0.29 | 1.84 | 0.026 | 0.013 | | 17.58 | | | 10.70 | | Nb 0.56 |
| Sanicro 28 | T | 0.02 | 0.42 | 1.73 | | | | 26.7 | 0.87 | 3.32 | 30.6 | | |
| AC66 | T | 0.06 | 0.21 | 0.64 | | | 0.01 | 27.3 | | | 32.2 | | |
| **Ni-based alloy (MPIE)** | | | | | | | | | | | | | |
| Alloy 625Si | P | 0.01 | 1.2 | 0.07 | 0.01 | 0.01 | 0.24 | 19.0 | <0.01 | 8.9 | bal | <0.01 | W 0.07, Ti 0.28, Co 0.04, Fe 2.8, Nb 0.02 |

* delivery condition: P – plate, T – tube, R – rod (cast)

*Table 5.2. OPTICORR test matrix.*

| Test gas species | $O_2$-$H_2O$ | $O_2$-HCl-$H_2O$ | $O_2$-$SO_2$-$H_2O$ | $O_2$-HCl-$SO_2$-$H_2O$ | KCl-$ZnCl_2$ | Ca, Na, K, Pb, Zn-Sulfate | Chloride : Sulfate 1:1 |
|---|---|---|---|---|---|---|---|
| Test temperature | 420 / 500 / 550 / 600°C | 420 / 500 / 550 / 600°C | 420 / 550 / 600°C | 550 / 600°C | 320°C (wet/dry) | 420°C (wet/dry) | 420°C (wet/dry) |
| **Materials** (Table 1) | | | | | | | |
| Rautaruukki Materials | Siegen JRC VTT | JRC VTT | JRC VTT | VTT | MPIE | MPIE | MPIE |
| Fe | - | - | - | - | MPIE | MPIE | MPIE |
| Cr | - | - | - | - | MPIE | MPIE | MPIE |
| Ni | - | - | - | - | MPIE | MPIE | MPIE |
| 2.25Cr-1Mo | Siegen JRC VTT | JRC VTT | JRC VTT | VTT | MPIE | MPIE | MPIE |
| TP 347 | Siegen JRC VTT | JRC VTT | JRC VTT | VTT | MPIE | MPIE | MPIE |
| AC 66 / X10 / X20 | Siegen JRC | JRC | JRC | | MPIE | MPIE | MPIE |
| Alloy 625 | Siegen JRC VTT | JRC VTT | JRC VTT | VTT | MPIE | MPIE | MPIE |

Gas phase containing carrier gas $N_2$ or He as appropriate, amounts is according to EU-PREWIN definition:
$O_2$: 8 vol.%, HCl: 2000 vppm, $SO_2$: 200 vppm, $H_2O$: 15 vol.%

Salt compositions according to EU-PREWIN definition:
50 mol.% KCl- 50 mol.% $ZnCl_2$; Ca-Na-K-Pb-Zn-Sulfate (20 wt.% each) Chloride : sulfate mixture 1:1 of both.

Test duration:
72, 360 and 720 h exposure tests
TG tests 100h max.

Standard sample preparation in tests:
Sample size: 10mm x 10 mm x 2–5mm
Special size for GDOES[1]: 15 mm x 15 mm x 2–5mm
Surface finish: 1000 grit SiC paper, all faces

---

[1] GDOES = Glow Discharge Optical Emission Spectroscopy

# 5.1  Details of tests

## 5.1.1  Thermogravimetric tests

The aims of the thermogravimetric experiments (TG) were:

- to investigate the corrosion behaviour of different steels

- to get a basic understanding of the corrosion processes

- to obtain experimental data for kinetic modelling: (MPIE → VTT)

- to investigate the presence of corrosion products (phases) for thermodynamic modelling: (MPIE → GTT).

TG experiments have been carried out on different samples covered by a 50 mol.% $ZnCl_2$ − 50 mol.% KCl mixture, which is molten at the process temperature (320°C). Different atmospheres have been used in order to get basic information about the salt melt induced corrosion process:

I.   $\underline{Ar − O_2\ atmospheres:}$ Experiments in $Ar − O_2$ atmospheres have been carried out on Fe, Cr, Ni, TP 347 H, 2.25Cr1Mo, 2.25Cr1Mo-mod. Ce in order to study the effects of $p(O_2)$ and the amount (thickness) of the salt deposit.

II.  $\underline{Ar − O_2 − HCl\ atmospheres:}$ Experiments in $Ar − O_2 − HCl$ atmospheres have been carried out on Fe, Cr and Ni in order to investigate the effects of $p(O_2)$ and $p(HCl)$ on the corrosion kinetics and products as well as the resulting $p(Cl_2)$.

III. $\underline{Ar − O_2 − H_2O\ atmospheres:}$ Experiments in $Ar − O_2 − H_2O$ atmospheres have been carried out on Fe in order to investigate the effects of $p(H_2O)$ on the corrosion kinetics. The effect of water vapour on the equilibrium gas atmosphere has also been studied.

Corrosion products have been analysed after the experiments using different methods (chemically, SEM − equipped with an EDX detector or XRD). The determination of corrosion products formed during the corrosion processes might give important information for thermodynamic models.

## 5.1.2  Multisample exposure tests

The multi-sample exposure tests were carried out at VTT Industrial Systems under isothermal conditions at temperatures of 420, 550 and 600°C in moist oxidising atmospheres up to 360 hours. Exposure temperature areas are shown in Fe-O phase diagram, Figure 5.1.1. Table 5.1.1 presents the gas compositions used in the exposures. The tests were carried out in a horizontal tube furnace, the tube diameter of 75 mm. The flow

rates of gases were controlled by mass-flow controllers and the total gas flow was 6 l/h. The $N_2$-$O_2$ gas was passed through a humidifying unit containing deionised water before the furnace thereby adding 15% of moisture to the gas mixture. Exhaust gases were neutralised using NaOH gas scrubbers.

## Fe-O
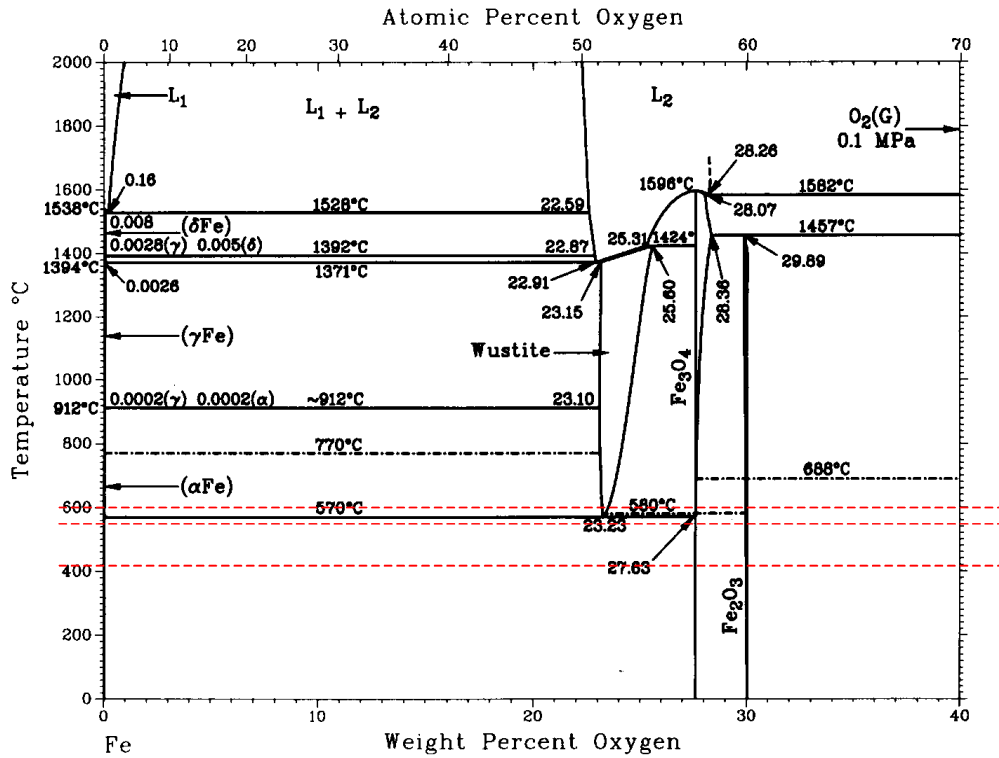


Figure 5.1.1. Fe-O phase diagram and used exposure temperatures [1].

Table 5.1.1. Gases used in exposure tests. All gas compositions are in volume percent.

| Gas 1 | 8% $O_2$ - 15% $H_2O$ - $N_2$ |
|-------|-------------------------------|
| Gas 2 | 200 ppm $SO_2$ - 8% $O_2$ - 15% $H_2O$ - $N_2$ |
| Gas 3 | 2000 ppm HCl - 8% $O_2$ - 15% $H_2O$ - $N_2$ |
| Gas 4 | 200 ppm $SO_2$ - 2000 ppm HCl - 8% $O_2$ - 15% $H_2O$ - $N_2$ |

The multi-sample exposure tests were carried out at JRC Petten under isothermal conditions at a temperature of 500°C in $N_2$-8% $O_2$-15% $H_2O$, $N_2$-8% $O_2$-15% $H_2O$-200 vppm $SO_2$ and $N_2$-8% $O_2$-15% $H_2O$-2000 vppm HCl atmospheres up to 360 hours. The exposure tests were carried out in a vertical tube furnace, tube diameter 80 mm. The gas flow was set

140

at 10 l/h. Before entering the furnace, the gas was passed through the humidifier at an appropriate temperature to obtain 15 vol.% water vapour in the gas mixture. The samples were hung on the platinum wire. An alumina crucible was placed underneath each sample to collect the possible spalled products.

Multisample exposure tests were also carried out at MPIE, Düsseldorf on a set of different steels with different salt compositions in dry / moist atmospheres. The samples were covered with 15 mg/cm$^2$ of the salt mixtures. These tests have been done to compare the corrosion resistances of different steels, but also to study the effects of salt composition and the composition of the reaction gas. Another point of interest was the formation of corrosion products. The information about species formed during the corrosion process might be helpful for thermodynamic models. Table 5.1.2 gives an overview about the experimental conditions of the exposure tests. Table 5.1.3 shows the steels used for the different experiments.

*Table 5.1.2. Overview about multisample exposure tests, carried out at MPIE, Düsseldorf.*

| No. | salt mixture | Temp. [°C] | $N_2$ [vol.%] | $O_2$ [vol.%] | HCl [vppm] | $SO_2$ [vppm] | $H_2O$ [vol.%] |
|-----|------|------|------|------|------|------|------|
| A1 | S1 | 320 | bal. | 8 | 2000 | 200 | - |
| A2 | S2 | 420 | bal. | 8 | 2000 | 200 | - |
| A3 | S3 | 420 | bal. | 8 | 2000 | 200 | - |
| A4 | S1 | 320 | bal. | 8 | 2000 | 200 | 15 |
| A5 | S2 | 420 | bal. | 8 | 2000 | 200 | 15 |
| A6 | S3 | 420 | bal. | 8 | 2000 | 200 | 15 |

Gas flow: 2.5 ml/s     test duration: 360 h

Salt deposit: S1: 50 mol.% $ZnCl_2$ – 50 mol.% KCl     amount: 15 mg/cm$^2$

               S2: Ca-Na-K-Pb-Zn sulfate (20 wt.% each component)   15 mg/cm$^2$

               S3: 50 wt.% of S1 – 50 wt.% of S2       15 mg/cm$^2$

*Table 5.1.3. Alloys and pure metals used for multi-sample exposure tests.*

| Tests | A1–A3 | A4–A6 |
|---|---|---|
| **Material** | Fe | Fe |
| | Cr | Cr |
| | Ni | Ni |
| | 66557 | 66557 |
| | 70252 | 71439 |
| | 71439 | 71518 |
| | 71518 | 71518 (Mod Ni) |
| | 71612 | 71518 (Mod Ni + Si) |
| | 73213 | 4X60 |
| | 4X60 | 7X60 |
| | 7X60 | 8, WSB |
| | 8, WSB | 9, WSB |
| | 9, WSB | 2.25Cr1Mo |
| | 2.25Cr1Mo | 2.25Cr1Mo (Mod Ce) |
| | TP347H | TP347H |
| | AC 66 | AC 66 |
| | Alloy 625Si | Alloy 625Si |

## 5.2 Summary of main results

### 5.2.1 Oxidation and active oxidation

The active oxidation results are summarised for common ferritic and austenitic materials for boiler applications:

- The presence of HCl in moist air at temperature above 500°C accelerates the oxidation rate of the studied materials.

- The SEM/EDS studies suggest that, in HCl-containing atmospheres the corrosion mechanism is "active oxidation".

- The presence of $SO_2$ generally suppresses the oxidation rate, especially for ferritic materials.

- Suppression of the oxidation rate in an $SO_2$ containing atmosphere could be due to the presence of sulphides at metal/scale interfaces, which probably influences ion transport through the oxide scale. If it is assumed that the oxidation reaction is surface controlled, then it can be concluded that the sulphates presented on the surface influence the absorption process of the oxygen.

New low-alloyed steels developed by Rautaruukki:

- Addition of HCl and $SO_2$ to the corrosion atmosphere increases the corrosion rate of steels studied.

- Ni and Si alloying elements have no significant influence on corrosion rate in HCl and $SO_2$ containing atmospheres. The addition of Ni and Si could improve the corrosion resistance of studied steels in moist air.

- The Ce alloying element enhance the corrosion rate of studied steels, especially in HCl-containing atmospheres.


### 5.2.2  Salt induced corrosion

The observations and results of TG experiments confirm the model initially described by Spiegel [M. Spiegel, Molten Salt Forum, Vol. 7 (2003) 253]. Therefore, the corrosion sequence can be subdivided into three different parts that correspond to the kinetic steps observed in the experiment:

- Dissolution of metal in the chloride melt at the melt scale interface

- Transport of dissolved chloride to the gas/melt interface

- Precipitation of oxide in contact with the gas phase

- Formation of a porous oxide scale.

From the salt deposited exposure samples it could be concluded that in general excellent corrosion resistances could be observed for Ni- and Cr based materials (Ni, Cr, Alloy 625Si and AC 66) covered with any salt deposit. The corrosion behaviour beneath chloride deposits seems to be influenced by the presence of Ni. Cr mainly contributes to corrosion resistance beneath sulfate deposits. Steel TP 347 shows higher mass losses due to a higher amount of Fe. Pure Fe and ferritic steels generally tend to sustain worse corrosion with higher mass losses. Exceptions are the Rautaruukki steels number 71518 and number 4, which show a better corrosion resistance when covered by a sulfate deposit. For many steels there does not seem to exist any dependence on the salt chemistry (Fe, 66557-021, 70252, 71439, 73213, 9) but for others, especially for 2.25Cr1Mo, the resistance just degrades in the presence of both salts.


## 5.3  Reference

1. ASM handbook, Vol. 3. Alloy Phase Diagrams. Ed. by Hugh Baker. ASM International, Materials Park, USA, 1992.

## 5.4 Public reporting of OPTICORR project results

The test results have been published in several conferences and workshops during the project work (2001–2005). The list of relevant publications is in the following chapter.

1. Hack, K. Development of Toolboxes for the Modelling of Hot Corrosion of Heat Exchanger components (EU-project OPTICORR). European Federation of Corrosion (EFC) Novel Approaches to the Improvement of High Temperature Corrosion Resistance, Workshop, October 2004.

2. Hämäläinen, M., Friman, M., Braga, H., Lourenço, N., Malheiros, L. Evaluation of the oxide phase behaviour of boiler steels in high temperature corrosion (EU-project OPTICORR). European Federation of Corrosion (EFC) Novel Approaches to the Improvement of High Temperature Corrosion Resistance, Workshop, October 2004.

3. Heikinheimo, L., Baxter, D., Hack, K., Spiegel, M., Hämäläinen, M., Krupp, U., Arponen, M. Optimisation of in-service performance of boiler steels by modelling high temperature corrosion. EU-project OPTICORR. European Federation of Corrosion (EFC), Novel Approaches to the Improvement of High Temperature Corrosion Resistance, Workshop, October 2004.

4. Heikinheimo, L., Baxter, D., Spiegel, M., Hack, K., Krupp, U., Hämäläinen, M., Arponen, M. Optimisation of in-service performance of boiler steels by modelling high temperature corrosion. 6th International Symposium on High Temperature Corrosion and Protection of Materials, 16.5.2004.

5. Heikinheimo, L., Penttilä, K., Hämäläinen, M., Krupp, U., Trindade, V., Spiegel, M., Ruh, A., Hack, K. High temperature oxidation and corrosion modelling using thermodynamic and experimental data. BALTICA VI. International Conference of Life Management and Maintenance for Power Plants, 8.6.2004.

6. Krupp, U., Trindade, V.B., Hanjari, B.Z., Yang, S., Christ, H.-J., Buschmann, U., Wiechert, W. Experimental analysis and computer simulation of inward oxide growth during high-temperature corrosion of low-alloy boiler steels. 6th International Symposium High Temperature Corrosion and Protection of Materials, 16.5.2004.

7. Krupp, U., Trindade, V.B., Yang, S., Christ, H.-J., Buschmann, U., Wiechert, W. The Effect of Grain-Boundary Diffusion during Oxidation of Cr-Containing Steels. DIMAT 2004; Sixth International Conference on Diffusion in Materials, July 2004.

8. Krupp, U., Trindade, V.B., Schmidt, P., Yang, S., Christ, H.-J., Buschmann, U., Wiechert, W. Computer-Based Simulation of Inward Oxide Scale Growth on Cr-Containing Steels at High Temperatures (EU-project OPTICORR). European Federation of Corrosion (EFC) Novel Approaches to the Improvement of High Temperature Corrosion Resistance, Workshop, October 2004.

9. Penttilä, K. et al. Model for Chloride Melt Induced Corrosion of Pure Iron (EU-project OPTICORR). European Federation of Corrosion (EFC) Novel Approaches to the Improvement of High Temperature Corrosion Resistance, Workshop, October 2004.

10. Ruh, A., Spiegel, M. Kinetic investigations on salt melt induced high-temperature corrosion of pure iron. Eurocorr 2003, The European Corrosion Congress. 28.9.2003.

11. Ruh, A., Spiegel, M. Kinetic investigations on salt melt induced high-temperature corrosion of pure metals. 6th International Symposium High Temperature Corrosion and Protection of Materials, 16.5.2004.

12. Ruh, A., Spiegel, M. Influence of gas phase composition on the kinetics of chloride melt induced corrosion of pure iron (EU-project OPTICORR). European Federation of Corrosion (EFC) Novel Approaches to the Improvement of High Temperature Corrosion Resistance, Workshop. October 2004.

13. Ruh, A., Spiegel, M. Influence of HCl and water vapour on the corrosion kinetics of Fe beneath molten $ZnCl_2/KCl$. Eurocorr 2004, The European Corrosion Congress Nice, France, 12–16 September 2004.

14. Sroda, S., Tuurna, S. Laboratory scale tests on corrosion behaviour of boiler materials in simulated combustion atmospheres. European Federation of Corrosion (EFC) Novel Approaches to the Improvement of High Temperature Corrosion Resistance, Workshop, October 2004.

15. Sroda, S., Baxter, D., Arponen, M. The influence of alloying elements on corrosion behavior of ferritic steels in simulated combustion atmospheres. European Federation of Corrosion (EFC) Novel Approaches to the Improvement of High Temperature Corrosion Resistance, Workshop, October 2004.

16. Sroda, S., Tuurna, S., Penttilä, K., Heikinheimo, L. High Temperature Oxidation Behaviour of Boiler Steels under Simulated Combustion Gases. 6th International Symposium High Temperature Corrosion and Protection of Materials, 16.5.2004.

17. Trindade, V.B., Krupp, U., Wagenhuber, Ph. E.-G., Yang, S., Christ, H.-J. The Different Role of Alloy Grain Boundaries on the Oxidation Mechanisms of Cr-Containing Steels and Ni-Base Alloys at High-Temperatures (EU-project OPTICORR). European Federation of Corrosion (EFC) Novel Approaches to the Improvement of High Temperature Corrosion Resistance, Workshop. October 2004.

18. Trindade, V.B., Hanjari, B.Z., Borin, R., Schmidt, P., Yang, S.L., Krupp, U., Christ, H.-J. Effect of Alloy Grain Size on the High-Temperature Oxidation Behaviour of the Austenitic Steel TP347. The 59th Annual ABM International Congress, July 2004.

19. Trindade, V.B., Borin, R., Hanjari, B.Z., Schmidt, P., Yang, S., Krupp, U., Christ, H.-J. High-Temperature Oxidation of Pure Fe and Fe-Cr Alloys The 59th Annual ABM International Congress, July 2004.

20. Trindade, V.B., Krupp, U., Yang, S., Christ, H.-J. Analyse des Hochtemperaturoxidationsverhaltens niedriglegierter Chromstähle mit Hilfe von Markerversuchen und der EBSD-Technik. Metallographie-Tagung, Bochum, September 2004.

21. Trindade, V.B., Krupp, U., Hanjari, B.Z., Yang, S., Christ, H.-J. Analyse des Hochtemperaturoxidationsverhaltens niedriglegierter Chromstählen mittels Markerversuche und EBSD. Metallographie-Tagung, September 2004.

22. Trindade, V.B., Krupp, U., Christ, H.-J., Gegner, J. Simulation of Thermodynamics and Kinetics of Internal Corrosion of Engineering Alloys at High-Temperatures. Third International Conference on Mathematical Modelling and Computer Simulation of Materials Technologies. September 2004.

23. Tuurna, S., Heikinheimo, L., Arponen, M., Hämäläinen, M. Oxidation kinetics of low alloyed ferritic steels in a moist atmosphere Eurocorr 2003, The European Corrosion Congress. 28.9.2003.

24. Tuurna, S., Sroda, S., Heikinheimo, L. The effect of HCl and $SO_2$ on gas phase corrosion of boiler steels. BALTICA VI, International Conference of Life Management and Maintenance for Power Plants, 8.6.2004.

25. Yang, S.L., Krupp, U., Christ, H.-J., Trindade, V.B. The Relationship Between Grain Boundary Character and the Intergranular Oxide Distribution in IN718 Superalloy, Advanced Engineering Materials – accepted.

146

26. Trindade, V.B., Krupp, U., Wagenhuber, Ph. E.-G., Virkar, Y.M., Christ, H.-J. Studying the Role of the Alloy-Grain-Boundary Character During Oxidation of Ni-Base Alloys by Means of EBSD Technique, presented at 6th Conference on Microscopy of Oxidation, will be published in Materials at High-Temperatures.

27. Trindade, V.B., Krupp, U., Christ, H.J., Maurício, M.J., Rizzo, F.C. Experimental Characterization and Computer-Based Simulation of Thermodynamics and Kinetics of Corrosion of Steels at High Temperatures, will be presented at The 1st International Conference on Diffusion in Solids and Liquids, DSL-2005, July 6–8, 2005, University of Aveiro, Aveiro, Portugal.

# Acknowledgements

Author(s)
Baxter, David & Heikinheimo, Liisa (eds.)

Title

# OPTICORR Guide Book - Optimisation of in-service performance of boiler steels by modelling high temperature corrosion

Abstract

This Guide Book is intended to assist the prospective user of a novel range of corrosion modelling software that has been designed to assess potential corrosion under high temperature combustion process conditions. The models described have been developed through the course of the European-funded materials research project, OPTICORR, G5RD-CT-2001-00593.

The corrosion models were based on existing ChemSheet and InCorr software systems. These tools addressed two separate parts of the corrosion process, molten salt corrosion on the surface and internal oxidation/corrosion. The ChemSheet modelling development consists of models for salt-induced high temperature corrosion using the thermodynamic data from within the project. The approach has been to model the salt/gas and salt/metal interfaces. Interaction between the salt and the metal seems to be dependant on the interaction between the salt and the gas.

In the case of internal oxidation/corrosion, the objective was to simulate high temperature corrosion processes under near-service conditions, which requires both a thermodynamic model to predict phase stability for given conditions and a mathematical description of the process kinetics, i.e. solid-state diffusion. The simulation has been achieved by integrating the existing thermodynamic program library ChemApp into a numerical finite difference diffusion calculation. In order to illustrate the application of the modelling tools a number of examples are contained in this Guide Book, including: use of stability diagrams, modelling of internal oxidation / corrosion, modelling of hot salt corrosion and results from the gas precipitation model.

Keywords
corrosion modelling software, corrosion processes simulation, thermodynamic stability calculations, combustion process conditions, combustion plants

This Guide Book is intended to assist the prospective user of a novel range of corrosion modeling software that has been designed to assess potential corrosion under high temperature combustion process conditions. The models described have been developed through the course of the European-funded materials research project, OPTICORR, G5RD-CT-2001-00593.

The corrosion models were based on existing ChemSheet and InCorr basic software systems. These tools addressed two separate parts of the corrosion process, molten salt corrosion on the surface and internal oxidation/ corrosion. In order to illustrate the application of the modelling tools a number of example are contained in this Guide Book, including: use of stability diagrams, modelling of internal oxidation / corrosion, modelling of hot salt corrosion and results from the gas precipitation model.